DISSERTATION

DESIGN & MODELING OF PHASE TRANSFORMING ULTRA-HIGH TEMPERATURE METAL CERAMIC MULTILAYER COMPOSITES

Submitted by

John Carter Stotts

School of Materials Science and Engineering

In partial fulfillment of the requirements

For the Degree of Doctor of Philosophy

Colorado State University

Fort Collins, Colorado

Spring 2025

Doctoral Committee:

Advisor: Christopher R. Weinberger

Martin Gelfand
Kaka Ma
Justin Sambur

ABSTRACT

DESIGN & MODELING OF PHASE TRANSFORMING ULTRA-HIGH TEMPERATURE METAL CERAMIC MULTILAYER COMPOSITES

Ultra-high temperature ceramics are a class of materials that have found use in high-temperature structural applications due to their high melting temperatures and excellent high-temperature mechanical properties. Although this class of materials is well-suited to these applications at high temperature, they suffer from a low fracture toughness at ambient temperatures where component fabrication and assembly takes place. Thus, during the fabrication and assembly process these materials are highly susceptible to catastrophic brittle failure. In this work, we introduce a novel type of composite that significantly improves the low-temperature fracture toughness without sacrificing the excellent high-temperature properties of the ultra-high temperature ceramics.

These novel composites are an innovative approach to metal-ceramic multilayer composites, with the unique ability undergo a phase transformation in the metal layers that results in their disappearance, leaving a single-phase ultra-high temperature ceramic after annealing. In this work, we endeavored to model this phase transformation process and characterize the performance of the composite in order to optimize the material selection and design of the composite. To achieve this goal, we determined the phase transformation time of composites using Finite Element Method simulations and constructed more general, coarse-grained, models of the phase transformation kinetics and toughening.

The key to enabling the phase transformation in these composites is to choose group IV transition metal carbides or nitrides and group V transition metal carbides for the ceramic layers of the composite. This group of materials possess a wide range of homogeneity with respect to carbon/nitrogen content in their monocarbide/nitride phases. Additionally, the phase transformation from metal to ceramic in these materials is controlled by the diffusion of the nonmetal atom (car-

bon/nitrogen) and results in ceramic layer growth with strong adhesion between layers. Thus, a composite can be constructed with a 'frozen-in' non-equilibrium microstructure containing alternating layers of metal and ceramic and be made to transform simply by increasing the temperature ,*i.e.* annealing.

Furthermore, this work contains an investigation into the kinetics of carbon diffusion in sub-stoichiometric titanium carbide. This investigation, motivated by an open question in the literature posed by Sarian in 1968, used a computational approach comprised of Monte Carlo, kinetic Monte Carlo, and Density Functional Theory simulations in order to determine the interconnection of diffusion and vacancy-ordered phases. The investigation was multi-pronged, beginning with simulations on a square lattice and then being extended to three-dimension simulations of the titanium carbide carbon-vacancy sublattice.

ACKNOWLEDGEMENTS

Completion of the work encapsulated in this dissertation would have been impossible if not for the thoughtful advice of my PhD advisor, Dr. Chris Weinberger. I would also like to express gratitude for the discussion, advice, and support of all of members of the Advanced Computational Materials Engineering (ACME) lab during my time at CSU. Dr. Xiaochuan Tang, Brennan Watkins, Hunter Brumblay, Sajjad Hossain, Yuchen Huang, and Ian Anderson have all contributed to this work in meaningful ways. Additionally, I would like to extend a special thanks to the members of my PhD committee: Dr. Justin Sambur, Dr. Kaka Ma, and Dr. Martin Gelfand, who provided constructive feedback and experienced perspectives.

The research contained in the dissertation was support by the Army Research Office under grant No. W911NF2120084. This work utilized the RMACC Summit and Alpine supercomputers, which are supported by the National Science Foundation (awards ACI-1532235 and ACI-1532236), the University of Colorado Boulder and Colorado State University. The RMACC Summit and Alpine supercomputers are a joint effort of the University of Colorado Boulder and Colorado State University. This work also utilized computing resources provided by CSU engineering technology services, especially the ASHA computing cluster.

DEDICATION

I would like to dedicate this dissertation to my wife, Rebecca, whose support has made all of the difference.

TABLE OF CONTENTS

LIST OF TABLES

LIST OF FIGURES

Chapter 1

Introduction

The high temperatures experienced by structural components in hypersonic and space exploration environments demand that structural materials exhibit excellent mechanical properties even at temperatures in excess of $3000^{\circ}\mathrm{C}$. Very few materials exist with the ability to remain solid and even fewer display mechanical properties sufficient for use as structural materials in these conditions. Virtually all of the materials with this combination of properties belong to the group of ceramics known as Ultra-high Temperature Ceramics (UHTCs), which are mainly comprised of the carbides, nitrides, and borides of the group IVB, and VB transition metals of the periodic table. Despite the exception high-temperature properties of UHTCs, these materials ironically suffer from poor mechanical properties, particularly fracture toughness, at ambient temperatures. Due to this poor low-temperature performance, structural components constructed from UHTC materials are often susceptible to brittle failure during manufacturing and assembly. One method used to combat this is to construct UHTC ceramic matrix composite materials, often through the introduction of SiC fibers to the ceramic matrix. This has the effect of increasing the materials resistance to fracture and therefore mitigating the risk of brittle failure at ambient temperatures. Though the former solution can work well, it is not the only solution. Another common way to improve the fracture toughness of ceramic materials is through the addition of ductile metal layers which act in opposition to crack propagation. These composites are known as metal ceramic multilayers (MCMs), with the most common example being pearlite - a layered material forming from a eutectoid in the Fe-C system and being composed of alternating ferrite and cementite layers. Though the existence of metal layers at high-temperature is certainly in opposition to the need for exceptional high-temperature properties, similar composites can be constructed in UHTC systems. In particular, the UHTC materials having the B1 rocksalt crystal structure present a unique opportunity for improving low-temperature properties by creating MCMs due to their wide range of stability with respect to carbon content. In fact, the B1 rocksalt phase in many of the Me-C/N often remains

stable even with the removal of 50% of the non-metal atoms. This leads to these MCM composites having the unique ability to remove their metal layers upon annealing due to a diffusion-controlled phase transformation. In this dissertation, the following questions related to these transforming UHTC MCM composites are addressed using computational techniques:

1. What is the relationship between the initial conditions of a transforming composite (carbon concentration, magnitude of equilibrium concentration difference, ceramic phase fraction), materials properties (carbon diffusivities), and transformation time?

2. If we allow the temperature to increase at a constant rate over the course of a simulation will the parabolic relationship between diffusivity, transformation time, and bilayer length remain? If not, what will be the new relationship between effective diffusivity and temperature?

3. If we allow the carbon diffusivity in the ceramic to change with carbon composition will the activation energy for the phase transformation be dominated by the near-stoichiometric diffusivity far from the interface or by the carbon-depleted diffusivity close to the interface in the ceramic layers?

4. Which combinations of materials, i.e., Me/MeC and volume fractions for a transforming composites result in the greatest amount of toughening and fastest phase transformations?

5. How does a vacancy order-disorder transition affect the diffusivity through the lattice?

Chapter 2

Literature Review

2.1 Applications

Historically, the primary applications of transition metal carbides and nitrides have sought to utilize their high melting points, hardness, and high-temperature strength. These applications have included cutting and drilling tools [10], leading edges, combustors, and thermal protection systems for hypersonic aircraft [11], and wear-resistant surfaces or coatings [12]. More recently, there has been interest in using transition metal carbides and nitrides as inert matrix materials for advanced nuclear reactor fuels specifically due to their resistance against fission product corrosion [6]. Most importantly, these materials have potential applications as high-temperature structural components for use in the aerospace industry, though problems due to unfavorable room-temperature properties, especially low fracture toughness must be overcome before the transition metal carbides and nitrides can find widespread use in these applications [13].

Transition metal carbides and nitrides are often used for hard coatings, especially for applications such as coating the rake surface of cutting and drilling tools [12]. Transition metal carbides and nitrides are excellent choices for this application due to their high hardness and melting temperatures; however, there are other factors that require consideration when selecting materials for hard coatings. Interfacial factors, as an example, must also be considered since strong adherence of the coating to its metal substrate is required. In many cases, multilayer hard coating designs are used in order to meet specific layer-dependent criteria, since strong substrate adhesion is required at the metal-ceramic interface and weak adhesion at the free surface of the hard coating is preferable.

In the nuclear fuel industry, ceramic coatings are often used to cover fuels used in high-temperature reactors. Currently, SiC is the most common coating, but recent studies have indicated that ZrC may possess more favorable properties [6, 14, 15]. For example, ZrC possesses a

melting temperature in excess of $3000\mathrm{K}$, is resistant to corrosion due to fission products, has high thermal conductivity (at elevated temperatures), and has a small cross-section for the absorption of neutrons [6]. The main failure mechanisms for current tri-structural isotropic (TRISO) fuel particles occurs when the structural layers of the particle are thinned, reducing strength and potentially allowing the release of fission products. One cause for this avenue of structural failure is fission product attack wherein the structural layers are degraded due to chemical attacks from fission products such as Cs, Pd, and Co [15]. Additionally, during the reaction of $\mathrm{UO_2}$ oxygen is released and it is thought that the addition of ZrC would act as an oxygen-getter, trapping freed oxygen before harmful oxidative reactions can occur [14].

In the aerospace and defense industries development of materials for high-temperature environments is a top priority. Historically, SiC and oxide ceramics have been the only materials acceptable for use in high-temperature oxidative environments [16]. Despite resistance to oxidation, these materials are not suitable for ultra-high temperatures above $3000^{\circ}\mathrm{C}$. As a result, since the 1960s there has been interest in developing ultra-high temperature ceramics for hypersonic applications. Development of these non-oxide ceramics for hypersonic applications has been, in general, less productive than the simple oxides since these materials are not found in nature and require atmosphere-controlled processing [11]. The UHTCs are ceramics with melting temperatures in excess of $3000^{\circ}\mathrm{C}$ and include the borides, carbides, and nitrides of the group IVB (titanium, zirconium, hafnium) VB (vanadium, niobium, tantalum) metals of the periodic table. Of these materials, the transition metal carbides have the highest melting temperatures and are perhaps most suitable to high-temperature environments, though melting temperature is not the only property of importance. Oxidation resistance, damage tolerance, thermal conductivity, thermal shock resistance, brittle-to-ductile transition temperature, fracture resistance, strength, and creep resistance all affect the performance of materials for hypersonic applications. As such, the development of these materials requires a full characterization of candidate materials.

2.2 Structure and Phases of Transition Metal Carbides

To begin the characterization of the transition metal carbides we must first understand the crystal structure of the phases that exist in these material systems. All of the transition metal carbides exhibit the B1 rocksalt crystal structure at near-stoichiometric carbon compositions. The B1 rocksalt structure is shown in Figure 2.1 and is comprised of two interpenetrating fcc lattices. For each sublattice there is a corresponding species, in other words, there is a sublattice containing only metal atoms and a separate sublattice containing only carbon atoms. The carbon atoms occupy the octahedral interstices of the metal atom sublattice. In this arrangement, there exists covalent bonds between overlapping *d* electrons of metal atoms and *p* electrons of carbon atoms as well as metallic bonds between *d* electrons of neighboring metal atoms [17]. Ionic bonds can also be present in these materials, but they are usually characterized primarily by a mixture of covalent and metallic bonds. In contrast, many of the other materials that exhibit the B1 rocksalt crystal structure are purely ionic ceramics such as the prototypical NaCl.

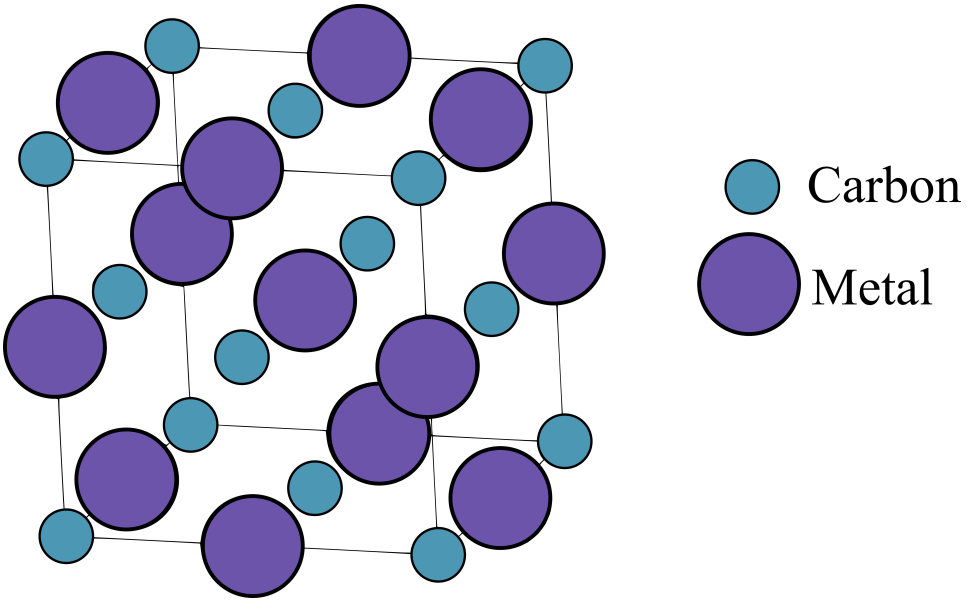

Figure 2.1: The B1 rocksalt (NaCl prototype) crystal structure conventional unit cell

The combination of covalent and metallic bonds in the transition metal carbides gives rise to B1 rocksalt crystal structure and other unique properties. Perhaps most important to this body of

work is the ability of the structure to support up to 50% carbon vacancies. This wide range of phase stability with respect to carbon content is demonstrated in Figure 2.2a which depicts the phase diagram of the Zr-C system and the stability of the ZrC_x phase between roughly 35 at% carbon and 50 at% carbon. This diagram is representative of the group IVB carbides and was constructed by using the Compound Energy Formalism (CEF) and the thermodynamic data of Guillermet *et al.* [1]. Figure 2.2b depicts the TaC phase diagram which is representative of the group VB carbides. It is apparent that in both diagrams the monocarbide phase, *i.e.* ZrC_x/ TaC_x, is stable across a wide range of stoichiometry, with the tolerance for carbon loss generally increasing with temperature [18]. Additionally, both phase diagrams display a feature common among the transition metal carbides: a substoichiometric peak in melting temperature, indicating there may be compound formation or ordering occurring [19].

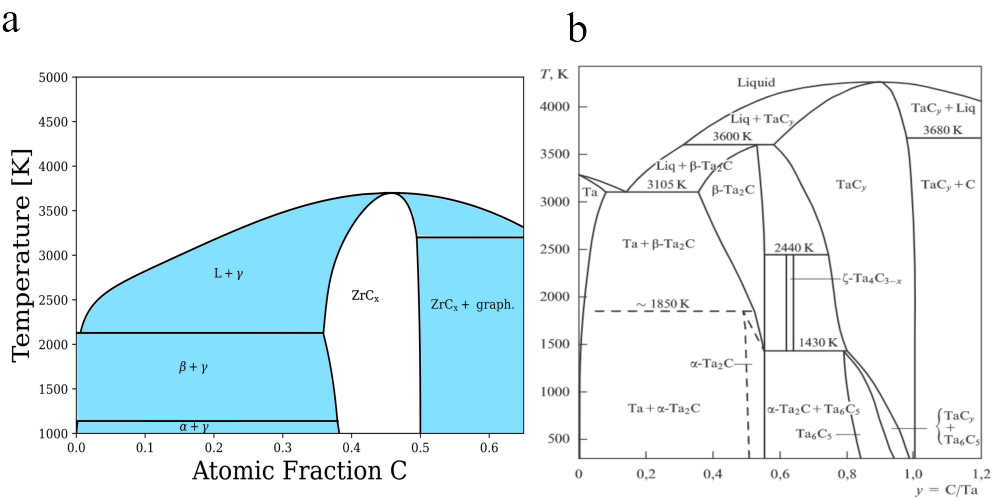

Figure 2.2: a) The Zr-C phase diagram constructed using the Compound Energy Formalism (CEF) and the thermodynamic data of Guillermet *et al.* [1]. b) The Ta-C phase diagram reported by Frisk *et al.* [2]

One major difference between the group IVB and VB carbides is that in the group VB carbides there is an additional phase that exists for intermediate carbon-to-metal ratios, for example from roughly $0.28 - 0.33$ for Ta_2C. The hemicarbide Me_2C phase consists of HCP arranged metal atoms with carbon atoms occupying only half of the octahedral interstices [18]. At sufficiently high temperatures each site on the carbon sublattice has an equal probability of being filled by a

carbon atom as seen, for example, in the L'3 structure. In contrast, at low temperatures vacancy-ordering takes place and the carbon atoms and vacancies separate into two octahedral interstitial planes such that no carbon atoms or vacancies are stacked on top of one another. This vacancy-ordered phase is known as the C6 structure. Additionally, in substoichiometric TaC, NbC, and VC with homogeneity ranges between the nominal 2:1 Me/C ratio of the hemicarbide and the 1:1 ratio of the stoichiometric monocarbide, a mixture of FCC and HCP metal stacking sequences can form, known as the zeta phase. In comparison to the other phases present in the transition metal carbide systems, we know relatively little about the zeta phase owing to it's relatively narrow homogeneity range as well as its low decomposition temperature and difficulty of synthesis [20]. In addition, the literature contains many contradictory claims about the zeta phase. For example, Zaplatynsky reported that the zeta phase formed via a diffusionless phase transformation from TaC and that it decomposed back into cubic $\mathrm{TaC_x}$ when compressive stresses were released; however, Brizes and Tobin reported the phase to be stable [21, 22].

In the group IVB carbides the metal atoms of the $\mathrm{Me_2C}$ phase remain in the FCC arrangement, though extensive vacancy-ordering on the interstitial carbon sublattice has been reported both computationally and experimentally. Vacancy-ordering in the $\mathrm{Me_2C}$ phases can take place in multiple ways. The first structure, which belongs to the $\mathrm{Fd\bar{3}m}$ space group, is most commonly reported and forms strings of structural vacancies along the $<110>$ directions. These strings are completely filled with either carbon atoms, or vacancies, or alternate between the two. The $\mathrm{Fd\bar{3}m}$ $\mathrm{Me_2C}$ structure is shown in Figure 2.3 along with the Ti-C phase diagram containing many of the vacancy-ordered structures.

In addition to the vacancy-ordered $\mathrm{Me_2C}$ structures, the convex hulls of the group IVB and VB transition metal carbides also contain several other vacancy-ordered structures, *e.g.* $\mathrm{Me_3C_2}$, $\mathrm{Me_4C_3}$, $\mathrm{Me_6C_5}$, $\mathrm{Me_7C_6}$ [3]. The convex hulls of the group IVB and VB transition metal carbides are shown in Figure 2.4.

In summary, the structures and phases present in the group IVB and VB transition metal carbide systems are complex, and due to the ability for these systems to undergo dramatic loss of carbon

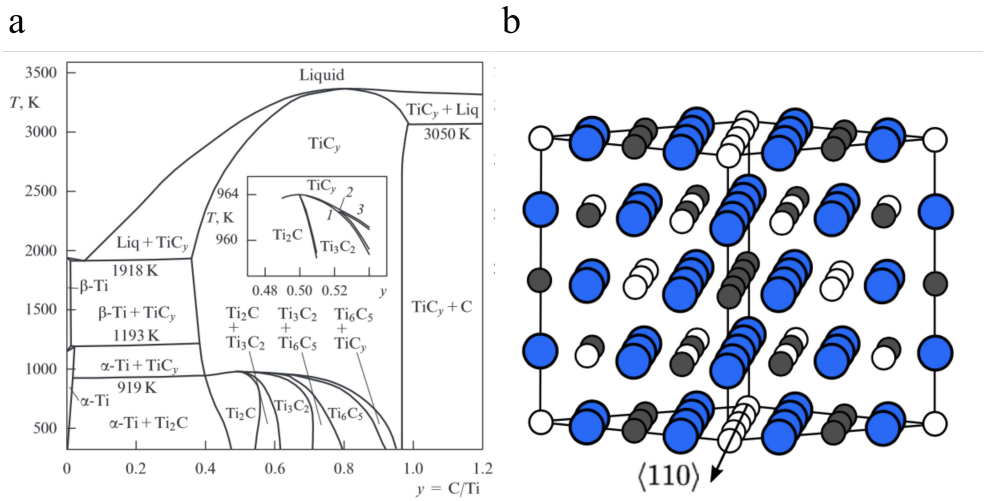

Figure 2.3: a) The Ti-C phase diagram reported by Weinberger & Thompson predicting the existence of several vacancy-ordered structures in substoichiometric TiC at low temperatures. b) The predicted vacancy-ordered Ti_2C structure belonging to the $Fd\bar{3}m$ space group.

on the interstitial sublattice, there are a variety of phases and structures present on the phase diagrams. In the group IVB carbides the metal atoms always arrange themselves in an FCC lattice; however, in the group VB carbides sufficient carbon loss can result in either FCC or HCP stacking of the metal atoms, or even a mixture of the two in the zeta phase. Additionally, the complex phases and the metallic covalent-ionic nature of their bonds produce many unique mechanical and thermodynamic properties.

2.3 Structure & Phases of Group IVB Transition Metal Nitrides

Like the transition metal carbides, the group IVB transition metal nitrides possess the B1 rock-salt crystal structure at near-stoichiometric nitrogen concentrations. Furthermore, they also possess the ability to promote substantial variation in composition due the presence of structural vacancies on the nitrogen sublattice [23]. As a result, the phase diagrams of the group IVB transition metal nitride systems are thought to contain many vacancy-ordered phases. Convex hull calculations, as shown in Figure 2.5 for the Zr-N system calculated by Yu *et al.*, support this suggestion; however, virtually no studies have produced low-temperature equilibrium phase diagrams of transition metal

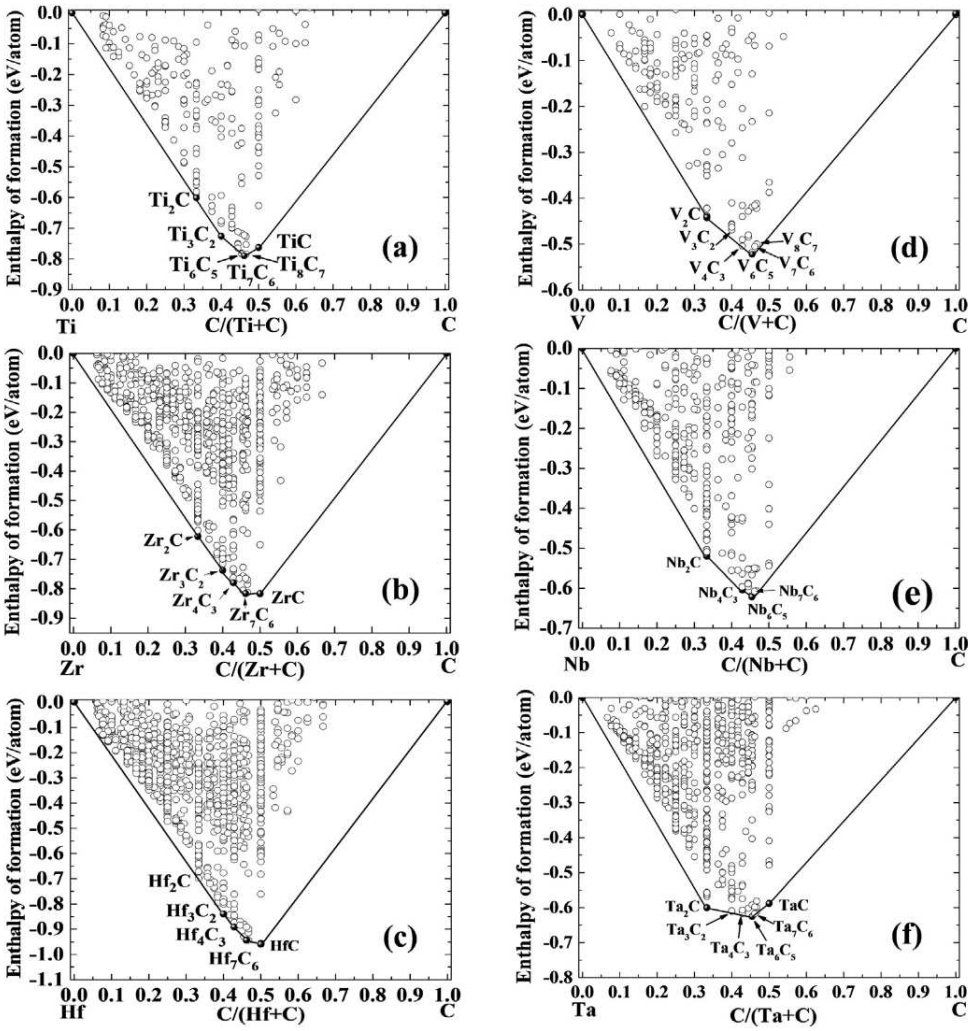

Figure 2.4: The convex hull constructions for the group IVB and VB transition metal carbides reported by Yu *et al.* [3]. (a) Ti-C (b) Zr-C (c) Hf-C (d) V-C (e) Nb-C (f) Ta-C.

nitride systems [4]. A representative phase diagram, calculated by [5] in the temperature range of roughly 1000-3500K, is shown in Figure 2.5b, but does not depict any of the vacancy-ordered phases.

One distinction between the carbides and the nitrides is that in general the transition metals have very low carbon solubilities, typically only able to support a few atomic percent at most before precipitating the carbide phase. In contrast, many of the transition metals are capable of supporting a significant atomic fraction of nitrogen, especially in the bcc phase. bcc-Zirconium, for example, reported supports nitrogen up to $\chi_N = 0.24$.

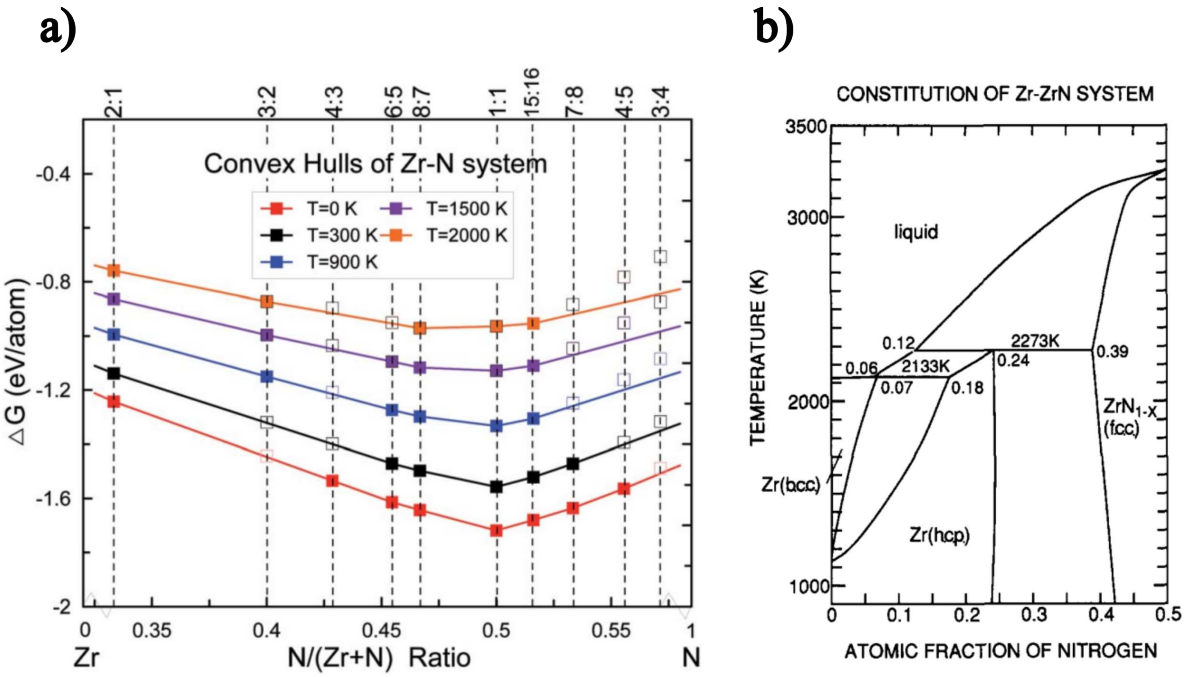

Figure 2.5: a) Convex hulls of the Zr–N system produced by Yu *et al.* in the temperature range of 0–2000K at ambient pressure. The solid squares represent stable structures, while open ones denote metastable structures. The solid P63/mmc phase of Zr, α-N2 (T = 0K) and N2 gas (T $\leq$ 300K) were adopted as reference states. Figure from Ref. [4] **b)** The Zr-N phase diagram calculated by Ogawa [5]

2.4 Mechanical Properties of Transition Metal Carbides & Nitrides

2.4.1 Fracture Toughness

The low fracture toughnesses of the transition metal carbides and nitrides is the primary reason for their failure to achieve widespread use as high-temperature structural materials. Fracture toughness is a measure of a material's ability to resist crack propagation and is generally reported in units of $\mathrm{MPa}\sqrt{\mathrm{m}}$. For materials with low fracture toughnesses, *i.e.*, materials that exhibit brittle behavior such as most ceramics, linear elastic fracture mechanics (LEFM) theory can be applied to model and solve problems related to crack propagation. There are two approaches to linear elastic fracture mechanics: the energy approach and the stress intensity approach. Using the energy approach fracture is thought to occur when the energy associated with crack growth overcomes the resistance of the material. Sources of material resistance to fracture could be surface energy,

plastic work, or other more complex mechanisms for energy dissipation that resist crack propagation [24]. In this approach, the strain energy release rate, $\mathcal{G}$, defined as the value of the rate of change of the total potential energy with respect to crack area, is used to define the criterion for fracture. Specifically, at the moment of fracture $\mathcal{G} = \mathcal{G}_c$, which is the critical energy release rate and is one measure of material's resistance to fracture. In the stress intensity approach the crack-tip conditions are characterized by the crack-tip stress intensity factor for mode I fracture, K_I. Using this approach the complete state of stress can be computed since each component of stress is proportional to K_I. If it is assumed that the material fails at some combination of stress and strain near the crack tip then the condition for fracture must be that the stress intensity factor reaches some critical value K_{IC}. Ultimately, the critical strain energy release rate and the critical stress intensity factor are related such that $G = \frac{K_I^2}{E}$ where E is the material's Young's Modulus, though we note that only K_{IC} is a direct measure of the material's fracture toughness.

Though fracture toughness is a material property, it is often difficult to determine. For ideally brittle materials, the fracture toughness can be measured by measurement of the energy R required for an increment of crack extension. In ideally brittle materials this curve, known as a resistance curve or R-curve is flat, indicating that the material's resistance to fracture does not change as a function of crack extension. Thus, in this unique circumstance the critical value G_c at which crack propagation becomes unstable can be uniquely identified. However, many materials, *e.g.* metals and ceramic composites, do not exhibit flat R-curves and therefore the fracture toughness cannot be uniquely determined. For non-ideal materials the R-curve can take on a variety of shapes. For example, in materials that exhibit ductile fracture the R-curve typically has a rising shape since the plastic zone surrounding the crack tip grows in size as the crack propagates. This has the effect of increasing the driving force required for further crack growth. In other materials, such as materials that fail by cleavage, the R-curve can have a falling shape since the initial resistance to fracture is greater than the resistance for further propagation. Furthermore, it is not only material characteristics that determine the shape of the R-curve, but size and geometry as well.

Experimental fracture toughnesses measurements have been gathered from the literature and are reported in Table 2.1. Fracture toughness data is very sparse in the literature and reported values vary due to differences in specimen dimension, grain size, porosity, carbon/nitrogen content, or other issues related to sample processing.

Carbide	Fracture Toughness [$\mathrm{MPa}\sqrt{\mathrm{m}}$]	Ref
TiC	1.55	[25]
TiN	1.66-2.16	[26]
ZrC	1.11	[25]
ZrN	1.33-1.83	[26]
HfC	3.39	[27]
HfN	1.29-1.91	[26]
VC	1.32	[25]
NbC	2.50	[28]
TaC	3.50	[29]

Table 2.1: Fracture Toughnesses of the group IVB and VB transition metal carbides and the group IVB transition metal nitrides

In general, the transition metal carbides and nitrides have poor fracture toughness with values typically below $5\mathrm{MPa}\sqrt{\mathrm{m}}$. In comparison, toughened ceramics typically have fracture toughness values greater than $10\mathrm{MPa}\sqrt{\mathrm{m}}$ with some, such as transformation toughened zirconia, having fracture toughnesses in excess of $20\mathrm{MPa}\sqrt{\mathrm{m}}$ [30]. Various toughening mechanisms exist and will be discussed in more detail in a subsequent section of this document. For now it will be sufficient to mention that despite the low fracture toughnesses of bulk transition metal carbides, the fracture toughnesses of ceramics can be improved through microstructural engineering.

One important example of the effects of microstructure on fracture toughness is zeta phase TaC, $\zeta - \mathrm{Ta_4C_{3-x}}$, which precipitates with a lath-like microstructure in substoichiometric TaC due to specific orientation relationships with the TaC and $\mathrm{Ta_2C}$ grains [31]. The lath-like structure is due to the precipitation of the zeta phase via a stacking-fault mechanism that results in the precipitation of laths on the $\{111\}$ planes of TaC. It has been reported that samples with high zeta phase volume fraction possess dramatically improved fracture toughnesses on the order of $15\mathrm{MPa}\sqrt{\mathrm{m}}$ [28].

2.4.2 Plastic Behavior and Creep

One important mechanical property for high-temperature structural applications is the post brittle-to-ductile transition critically resolved shear stress (CRSS) of these materials, which is related to the applied stress by a geometric factor, typically the Schmid factor [32]. The CRSS represents the critical value of the applied stress resolved onto a slip plane in the direction of slip for which yielding occurs and plastic deformation begins. The CRSS of the transition metal carbides is expected to decrease as a function of temperature for a variety of reasons. As an example, the temperature dependence of the CRSS on several slip systems reported by Katoh *et al.* [6] is shown in Figure 2.6. The slip system with the lowest CRSS is the $\{110\}\ <1\bar{1}0>$ for temperatures below 2200K, indicating that this is the preferred slip system at low temperatures.

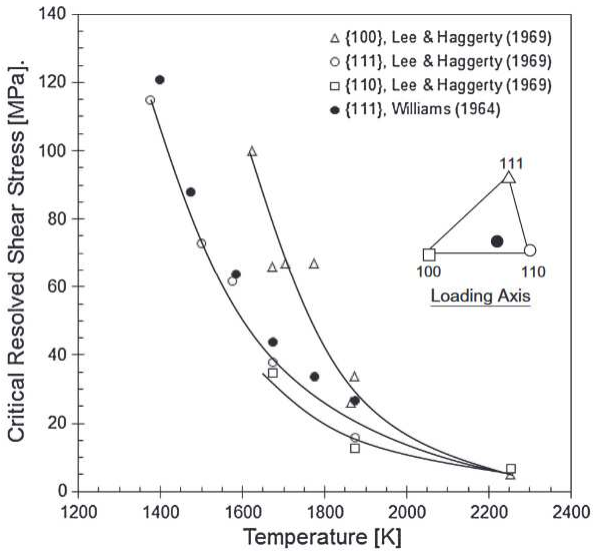

Figure 2.6: The variation of CRSS in $ZrC_{.96}$ on three slip systems as reported by Katoh *et al.* [6]

In general, the group IVB and VB transition metal carbides exhibit a brittle-to-ductile transition at around 30% of their melting temperature. This transition is most likely a result of the thermal activation of a sufficient number of slips planes such that the Von Mises criterion for plastic deformation is met [33]. At high temperatures all of the group IVB and VB transition metal carbides slip on the $\{111\}<1\bar{1}0>$ slip system, though at room temperature the active slip planes vary among

the carbides, with ZrC, TiC, and HfC predominantly slipping on the $\{110\}$ planes whereas VC and NbC are thought to slip on both $\{111\}$ and $\{110\}$ planes and TaC slips on $\{111\}$ planes [34].

To fully understand the high-temperature plastic deformation behavior of the transition metal carbides and nitrides we must also examine the thermal creep behaviors. Unfortunately, we know of no studies or experiments concerning creep in the group IV transition metal nitrides [35]. Most of the studies that have examined creep in the transition metal carbides have focused on understanding the creep mechanisms by determining the activation energy for creep and comparing it to the activation energies for diffusion of metal or carbon atoms [6, 36–40]. For a variety of reasons, including poor characterization of tested materials, there are conflicting claims about the nature of creep in the transition metal carbides. The relationship between creep rate and stress is given by equation 2.1:

$$\dot{\epsilon} = A\sigma^n \exp(\frac{-Q}{RT}) \tag{2.1}$$

where A is a constant, n is the stress exponent, Q is the activation energy for creep, R is the universal gas constant, and T is the temperature. This general empirical formula captures the behavior of nearly all diffusional creep mechanisms, where the stress exponent n corresponds to a specific mechanism, *e.g.*, $n = 1$ for Nabarro-Herring and Coble creep. The activation energy Q is most frequently associated with self-diffusion in the material. It is therefore possible to garner an understanding about the underlying creep mechanism in a material by determining the stress exponent and activation energy via experiment.

In a study on polycrystalline ZrC, Leipold and Neilsen determined the stress exponent to be $n = 3$, suggesting power law creep. Additionally, they found that below $2150^{\circ}\mathrm{C}$ the activation energy for creep was approximately 3.25eV and approximately 8.65eV above $2150^{\circ}\mathrm{C}$, suggesting that the creep was controlled by carbon self-diffusion at low temperatures since values reported for the activation energy for carbon self-diffusion in ZrC are between 1.4eV [41] and 4.9eV [42]. The 8.65eV activation energy was attributed to impurities at the grain boundaries – specifically free carbon [38]. It should be noted; however, that the reported values for zirconium self-diffusion

in ZrC are between 7.46eV as determined by experiment and 10.53eV if zirconium diffuses by a vacancy clustering mechanism [43]. Given this information, it is likely that the high-temperature creep is controlled by zirconium diffusion.

There is plenty of evidence that high-temperature creep is controlled by metal atom diffusion; for example, Sarian reported that the activation energy for titanium self-diffusion in TiC was 7.65eV whereas the carbon self-diffusion activation energy was reported to be only 4.14eV in $TiC_{.97}$ [44]. From a theoretical perspective this is logical due to the much larger size of titanium as compared to carbon and the fact that carbon diffuses by an interstitial mechanism and does not require additional energy for the formation of vacancies. Spivak *et al.* experimentally determined the activation energy for creep in TiC at 2973°C - 3173°C to be 5.65eV, concluding that the creep was controlled by titanium atom diffusion [45]. Smith *et al.* performed high-temperature creep tests on HfC (2500°C - 2700°C) and TaC (2100°C - 2300°C) and found the activation energies to be 7.1eV and 9.8eV respectively with the conclusion that creep operated via a Nabarro-Herring mechanism controlled by metal atom diffusion [46].

Lee and Haggerty measured creep in ZrC single crystals. These authors determined the stress exponent to be $n = 5$ with an activation energy of approximately 4.75eV for creep measured between $1400°\mathrm{C}$ and $2000°\mathrm{C}$. The authors therefore attributed the creep behavior of ZrC in this temperature range to be due to dislocation glide facilitated by carbon self-diffusion, which was reported to have an activation energy of 4.9eV by Sarian and Criscrione [42]. Additionally, the authors comment that this indicates that carbon is the lower-mobility species in ZrC, though this is almost certainly untrue, since the activation energy for metal diffusion is typically much greater than that of carbon diffusion in the transition metal carbides.

Darolia and Archbold measured the compressive yield stress of polycrystalline ZrC as a function of temperature. In their analysis they arrived at a value of 4.3eV for the activation energy carbon self-diffusion, though they arrived at this number by applying the Kelly-Rowcliffe model for slip to their compressive yield stress results. Surprisingly, this value is very similar to the activation energy for creep arrived at by Lee and Haggerty [36]. As a result, Darolia and Archbold

concluded that the high-temperature deformation of ZrC is controlled by the diffusion of carbon via carbon-diffusion assisted dislocation glide according to the Kelly-Rowcliffe model [37].

The Kelly-Rowcliffe model was originally constructed in order to conserve the octahedral coordination of carbon atoms and avoid metal upon metal atom stacking during $\{111\} <1\bar{1}0>$ slip in TiC. In summary, the model proposes that the dislocation associated with $<1\bar{1}0>$ slip dissociates according to Equation 2.2.

$$\frac{a}{2}[1\bar{1}0] \rightarrow \frac{a}{6}[2\bar{1}\bar{1}] + \frac{a}{6}[1\bar{2}1] \tag{2.2}$$

The authors note that if this dislocation occurs on a close-packed sheet of metal (Ti) atoms then tetrahedral coordination of carbon atoms is produced. If instead the dislocation occurs on a close-packed sheet of carbon atoms then metal atoms will be stacked directly above one another. According to Kelly and Rowcliffe, both of these situations can be avoided if each of the partial dislocations in the right hand side of Equation 2.2 themselves split into partial dislocations – one on the plane of carbon atoms and the other on the adjacent plane of metal atoms. These partial dislocations may be constituted according to Equation 2.3.

$$\frac{a}{6}[2\bar{1}\bar{1}] \rightarrow \frac{a}{6}[1\bar{2}1] + \frac{a}{6}[11\bar{2}] \tag{2.3}$$

This arrangement of partial dislocations produces a dislocation with its core extended normal to the slip plane, which the authors hypothesize would be difficult to move except at high temperatures [47, 48].

In summation, despite the intuitive conclusion that creep should be controlled by diffusion of the lower-mobility species in the transition metal carbides, in other words, by metal atom self-diffusion, many experimental studies have arrived at activation energies for creep that are much closer to the activation energy for carbon diffusion. This evidence, combined with the Kelly-Rowcliffe mechanism for slip/dislocation glide form a solid argument that carbon self-

diffusion is the rate-limiting factor for creep in these materials at low temperature whereas the high-temperature creep behavior is controlled, as expected, by metal atom diffusion.

2.4.3 Hardness & Elastic Properties

In addition to high melting temperatures, the transition metal carbides and nitrides are well known for their exceptional hardness - which arises as a result of the mixture of covalent, metallic, and ionic bonds present in this class of materials. Hardness is an important material property that indicates the material's resistance to localized deformation typically induced by indentation. The most popular method by far for measurement of indentation hardness is the Vickers hardness test, but it should be noted that other tip geometries exist and may be better suited to the indentation depending upon the material. In general, the indentation hardness is directly proportional to the tensile strength of the material and is fundamentally determined by the material's resistance to dislocation motion.

Hardness as well as many other mechanical properties scale with elastic constants. The elastic constants of the transition metal carbides as determined by Yu *et al.* using VASP simulations are shown in Table 2.2 [7]. Elastic constants for stoichiometric transition metal nitrides determined by Mei *et al.* are shown in Table 2.3 [26]. Yu *et al.* investigated the influence of carbon content on the elastic contents of the transition metal carbides and therefore the constants are reported at several different compositions. An estimate of the Vicker's hardness can be arrived at for polycrystalline hard materials using Equation 2.4 where G is the shear modulus and B is the bulk modulus [49]. This empirical relationship arises from the linear correlation between hardness and elasticity and is generally valid for brittle materials since it is a parametrization of hardness, shear modulus, and bulk modulus data from a variety of brittle compounds.

$$H_v = 2[\left(\frac{G}{B}\right)^2 G]^{0.585} - 3 \tag{2.4}$$

Table 2.2: The elastic constants of the transition metal carbides in GPa as reported by Yu *et al.*

Elastic Constant	TiC	ZrC	HfC	VC	NbC	TaC
$\chi = 0.75$						
C11	470	403	464	557	512	579
C12	113	105	101	164	150	172
C44	118	105	131	107	109	116
B	233	204	223	285	270	308
G	139	120	149	139	134	147
E	348	301	366	359	345	380
$\chi = 0.875$						
C11	520	460	508	640	608	684
C12	117	104	107	138	126	147
C44	154	139	162	170	153	157
B	252	223	223	305	287	337
G	171	153	176	199	181	195
E	419	374	425	490	452	488
$\chi = 0.96875$						
C11	541	484	535	663	628	709
C12	127	108	110	143	133	147
C44	162	146	170	184	162	169
B	265	234	252	317	287	337
G	179	161	184	211	192	207
E	438	394	445	518	474	515

Table 2.3: The elastic constants of the group IVB transition metal nitrides in GPa as reported by Mei *et al.*

Elastic Constant	TiN	ZrN	HfN
C11	585	521	580
C12	122	114	116
C44	163	110	114
B	275	250	271
G	188	141	152
E	460	357	385

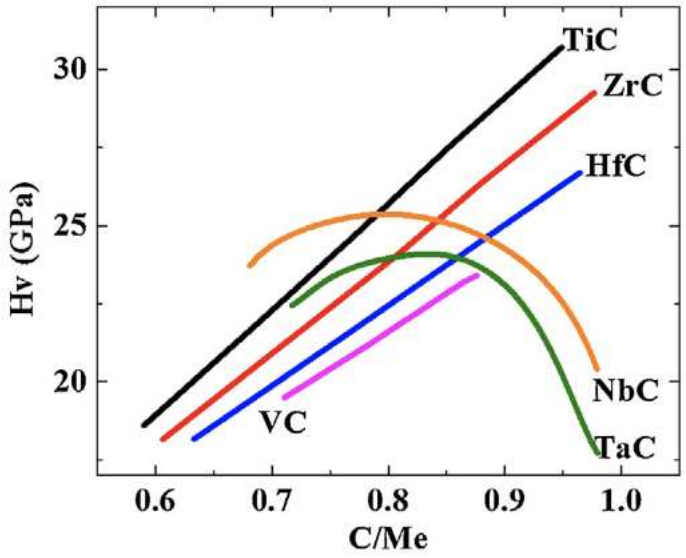

Figure 2.7: The vickers hardness of the transition metal carbides in GPa as reported by Yu *et al.* [7] The figure is reproduced from curves originally reported by Vinitskii [8].

2.4.4 Effects of Carbon-to-Metal Ratio

Hardness, in addition to many other material properties, has been shown to vary with carbon content in the transition metal carbides - likely as a result of changes in bonding due to the presence of vacancies on the carbon sublattice. The hardness trends are shown in Figure 2.7 for the group of IVB and VB carbides. In the group IVB carbides as well as VC the hardness increases with carbon content, whereas in TaC and NbC substoichiometric maxima are seen. The presence of these substoichiometric maxima is often referred to as anomalous hardness of the group VB transition metal carbides. Interestingly, vacancies are frequently attributed to hardening in crystal lattices [19], but in the transition metal carbides, or at least in the group IVB carbides, hardness appears to decrease as structural carbon vacancies are added to the lattice. This is likely due bonding between the carbon and metal atoms and thus when carbon is removed from the lattice the overall cohesion of the crystal is reduced. In the group VB carbides; however, there is likely a more complex mechanism at play.

Other material properties have also been found to vary with respect to the carbon content. Hollox also reports that the critically resolved shear stress and brittle-to-ductile transition temperature

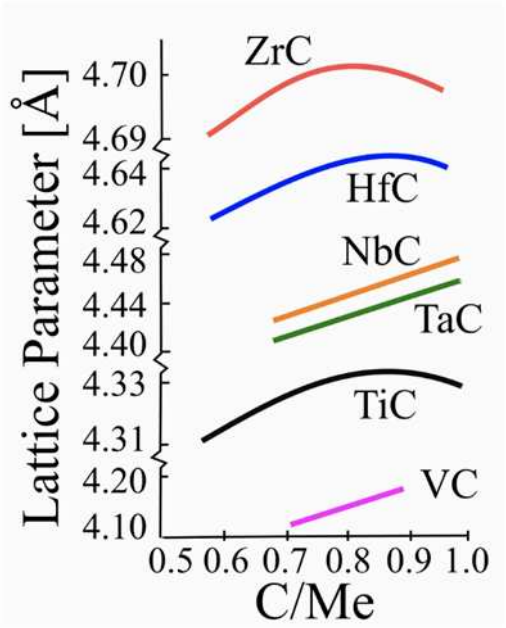

Figure 2.8: The variation in lattice parameter with respect to carbon content as reported by Vinitskii [8].

are composition dependent [19]. Most notably, Vinitskii has reported that the coefficient of thermal expansion, lattice parameter, electron work function, magnetic susceptibility, specific heat capacity, and superconductivity transition temperatures all vary with respect to the carbon content in these materials [8]. Shown in Figure 2.8 are the variations in lattice parameter with respect to carbon content reported by Vinitskii. The figure demonstrates different trends in the lattice parameter as carbon is removed. In the group IVB carbides there is a substoichiometric peak whereas the lattice parameter of the group VB carbides decreases monotonically. Together, these results indicate that the electronic configuration is changing as a function of carbon content and furthermore that the mechanism for these changes in electronic configuration is different between the group IVB and VB carbides despite their identical crystal structure. Vinitskii hypothesized that the differences seen between the two groups of carbides is due to differences in how the t_{2g} states are filled, with a larger degree of filling being achieved in the group VB carbides due to vacancy ordering reducing unfavorable overlapping of these orbitals [8].

In Sarian's radioactive tracer experiments, it was found that the diffusivity of carbon in TiC was dependent on the composition with the activation energy increasing by around 12% from $TiC_{.97}$ to

$TiC_{.89}$ [50]. Similar results were reported in ZrC by Spivak *et al.* [39]. The diffusivities reported by Sarian are shown in Equations 2.5 and 2.6.

$$D_{0.97} = (6.98 \pm 1.24 \mathrm{cm}^2/\mathrm{s}) \exp\left(-\frac{(95300 \pm 700 \mathrm{kcal/mol})}{RT}\right) \tag{2.5}$$

$$D_{0.89} = (45.44 \pm 5.12 \mathrm{cm}^2/\mathrm{s}) \exp\left(-\frac{(106800 \pm 400 \mathrm{kcal/mol})}{RT}\right) \tag{2.6}$$

These findings indicate that carbon diffusion is slower in substoichiometric $\mathrm{TiC_x}$ than in near-stoichiometric TiC. This finding is counter-intuitive as one would expect that the diffusion pre-factor would have increased as carbon was removed, due to a larger proportion of adjacent jump sites being occupied by vacancies on the carbon sublattice, but not that the activation energy would increase. Both Sarian and Spivak hypothesized that vacancy ordering was contributing to the compositional dependence of the carbon diffusivity. Despite this, the experiments were conducted at temperatures in excess of 1500K; whereas vacancy-ordered phases in TiC_x are thought to form below 1000K [18], though Sarian and Spivak would not have had access to these results at the time of their studies.

In contrast, Brizes reported that carbon diffusivity increased in TaC as carbon was removed from the lattice [51]. Brizes reported similar findings for NbC [52]. The behavior of carbon diffusion in TaC and NbC reported by Brizes is therefore in conflict with the report of carbon diffusion in TiC by Sarian and may be another example of a property with different behaviors with respect to carbon content in the group IVB versus the group VB carbides.

2.5 Nonmetal Atom Diffusion in Transition Metal Carbides and Nitrides

The most impactful material property on the phase transformation kinetics is the carbon/nitrogen diffusivity. In future chapters, we will endeavor to model the phase transformation process. To achieve this, our model must take as an input the carbon/nitrogen diffusivity in each phase present

Material/Phase	Diffusing Atom	D_0 [cm^2/s]	Q [eV]	Source
α-Zr	C	2.00×10^{-4}	1.57	[41]
β-Zr	C	8.90×10^{-2}	1.38	[41]
α-Zr	N	5.60×10^{-1}	2.50	[53]
ZrC	C	1.62×10^{2}	4.90	[42]
ZrN	N	2.90×10^{-9}	1.59	[23]
β-Ti	C	2.78×10^{1}	1.93	[54]
α-Ti	N	1.20×10^{-2}	1.96	[55]
β-Ti	N	3.50×10^{-2}	1.47	[55]
TiC	C	6.98	4.13	[56]
TiN	N	4.00×10^{-7}	2.26	[57]
α-Hf	C	5.00×10^{6}	3.90	[58]
α-Hf	N	2.40×10^{-2}	2.51	[53]
HfC	C	6.30×10^{1}	5.64	[59]
Hf_3N_2	N	2.00×10^{-2}	2.70	[60]
Hf_4N_3	N	1.40×10^{-1}	2.74	[60]
HfN	N	5.40×10^{-1}	2.73	[60]
Nb	C	4.00×10^{-3}	1.43	[61]
Nb_2C	C	3.00×10^{-1}	3.50	[52]
NbC	C	1.76×10^{1}	4.17	[52]
Ta	C	6.10×10^{-3}	1.67	[61]
Ta_2C	C	1.00×10^{3}	4.99	[51]
TaC	C	2.00	3.93	[51]

Table 2.4: Database of carbon/nitrogen diffusivities used as model inputs in this work

in the phase transformation. The carbon / nitrogen diffusivities in each of the phases considered are shown in Table 2.4.

Chapter 3

Methodologies

3.1 Finite Element Method Simulation of Diffusional Phase Transformations

The Finite Element Method (FEM) is a general method for numerically solving differential equations by minimizing approximation error associated with applying trial functions to the differential equation. We will consider diffusion on a one-dimensional domain, since this is the exact problem we will be concerned with in Chapter 1. The PDE describing diffusion is known as Fick's Second Law:

$$\frac{\partial c(x,t)}{\partial t} = D\frac{\partial^2 c(x,t)}{\partial x^2}. \tag{3.1}$$

To begin we, apply the Ritz-Galerkin method by first constructing the weak form of our PDE in the form of a weighted residual:

$$\int_\Omega \Big[V(x)[D\frac{\partial^2 c(x,t)}{\partial x^2} - \frac{\partial c(x,t)}{\partial t}]\Big]dx = 0 \tag{3.2}$$

where $V(x)$ is our weighting function and Ω is the simulation domain.

Using integration by parts:

$$V(x)D\frac{\partial c(x,t)}{\partial x}\Big|_\Omega - \int_\Omega \Big[D\frac{\partial c(x,t)}{\partial x}\frac{\partial V(x)}{\partial x} - V(x)\frac{\partial c(x,t)}{\partial t}\Big]dx = 0 \tag{3.3}$$

We will choose linear trial (hat) functions.

$$\Psi_1(x) = \frac{x_q - x}{h}, \Psi_2(x) = \frac{x - x_p}{h} \tag{3.4}$$

where h is the element length and therefore our composition profile can be written as

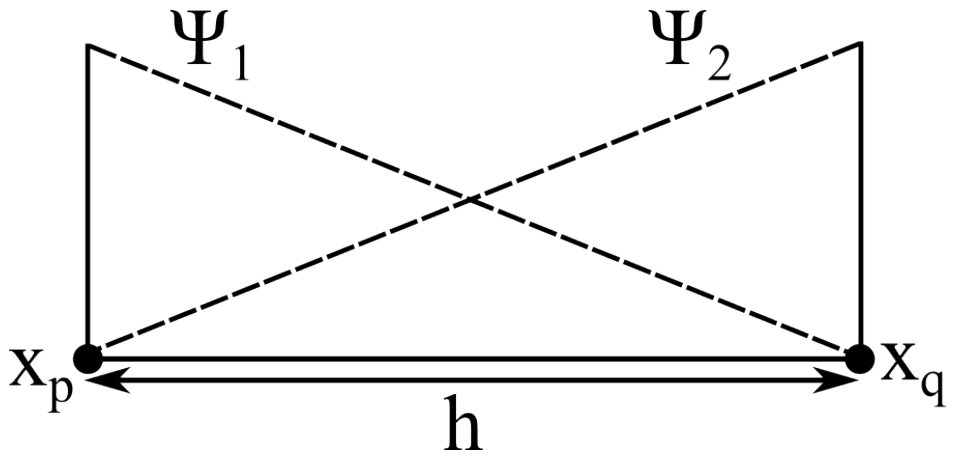

Figure 3.1: A schematic diagram illustrating the linear trial (hat) functions Ψ_1 and Ψ_2 over an element.

$$c(x,t) = \sum_{j=1}^{2} c_j(t)\Psi_j(x) \tag{3.5}$$

and our weighting function is

$$V(x) = \sum_i \Psi_i(x). \tag{3.6}$$

Using these relations, the weak form now becomes

$$\Psi_i(x) D \frac{\partial c(x,t)}{\partial x}\Big|_\Omega - \int_\Omega \Big[D \sum_{j=1}^{2} c_j(t) \frac{\partial \Psi_i(x)}{\partial x} \frac{\partial \Psi_j(x)}{\partial x} - \sum_{j=1}^{2} \Psi_i(x)\Psi_j(x) \frac{\partial c_j(t)}{\partial t} \Big] dx = 0. \tag{3.7}$$

We would like to write our global solution in the matrix form

$$K_{ij} c_j + M_{ij} \dot{c}_j = F_i \tag{3.8}$$

where the global matrices K, M, and F have a nesting property with single-element matrices k, m and f, as shown below for an example system containing a total of five nodes.

$$K = \begin{vmatrix} k_{11}^{(1)} & k_{12}^{(1)} & 0 & 0 & 0 \\ k_{21}^{(1)} & k_{22}^{(1)} + k_{11}^{(2)} & k_{12}^{(2)} & 0 & 0 \\ 0 & k_{21}^{(2)} & k_{22}^{(2)} + k_{11}^{(3)} & k_{12}^{(3)} & 0 \\ 0 & 0 & k_{21}^{(3)} & k_{22}^{(3)} + k_{11}^{(4)} & k_{12}^{(4)} \\ 0 & 0 & 0 & k_{21}^{(4)} & k_{22}^{(4)} \end{vmatrix} \tag{3.9}$$

$$M = \begin{vmatrix} m_{11}^{(1)} & m_{12}^{(1)} & 0 & 0 & 0 \\ m_{21}^{(1)} & m_{22}^{(1)} + m_{11}^{(2)} & m_{12}^{(2)} & 0 & 0 \\ 0 & m_{21}^{(2)} & m_{22}^{(2)} + m_{11}^{(3)} & m_{12}^{(3)} & 0 \\ 0 & 0 & m_{21}^{(3)} & m_{22}^{(3)} + m_{11}^{(4)} & m_{12}^{(4)} \\ 0 & 0 & 0 & m_{21}^{(4)} & m_{22}^{(4)} \end{vmatrix} \tag{3.10}$$

$$F = \begin{vmatrix} f_1^{(1)} \\ f_2^{(1)} + f_1^{(2)} \\ f_2^{(2)} + f_1^{(3)} \\ f_2^{(3)} + f_2^{(4)} \\ f_2^{(4)} \end{vmatrix} \tag{3.11}$$

where, for example, $k_{11}^{(1)}$ indicates the top left element of the 2x2 element stiffness matrix belonging to the first element in the domain.

By examination of the equations above it follows that the single-element stiffness and mass matrices are

$$k_{ij} = D \int_{x_p}^{x_q} \frac{\partial \Psi_i(x)}{\partial x} \frac{\partial \Psi_j(x)}{\partial x} dx = \frac{D}{h} \begin{vmatrix} -1 & 1 \\ 1 & -1 \end{vmatrix} \tag{3.12}$$

$$m_{ij} = \int_{x_p}^{x_q} \Psi_i(x) \Psi_j(x) dx = \frac{h}{6} \begin{vmatrix} 2 & 1 \\ 1 & 2 \end{vmatrix} \tag{3.13}$$

and the single-element force vector is

$$f_i = \left| \begin{array}{c} D\frac{\partial c(x)}{\partial x}|_{x_p} \\ D\frac{\partial c(x)}{\partial x}|_{x_q} \end{array} \right|. \tag{3.14}$$

When assembled into the global force vector F, all terms except for those associated with boundary conditions are zero due to the two terms summing to zero, e.g. $f_2^{(1)} + f_1^{(3)}$. The cancellation is due to the fact that when a single node is shared by two elements then the gradients associated with Ψ_2 for the first element are equal and opposite to the gradient associated with Ψ_1 for the second element.

In the following sections we will be concerned with modeling a diffusion-controlled phase transformation problem. The goal of this simulations is to determine the time required for metal layers of a metal-ceramic multilayer composite to disappear. Our approach is to model one half of a periodically repeating bilayer of the composite, where we define one bilayer to be the combination of a single ceramic and metal layer. At the center of each layer are planes with a mirror symmetry. By applying nuemann no-flux boundary conditions on these planes we effectively reproduce the periodic nature of the metal-ceramic multilayer composite.

To implement the boundary conditions the global matrices need slight modifications. For example, in our simulations we require no-flux Neumann boundary conditions on the left side of the ceramic phase and on the right side of the metal phase. These are implemented simply by setting the first and last value of the global force vector equal to zero. At the interface we apply Dirichlet boundary conditions to ensure chemical equilibrium. These are implemented by setting the element of the global force vector for these nodes, say the nth node, equal to the desired concentration, and then by setting the nth column and row of the global stiffness matrix equal to zero except for the i = n, j = n element, which should be set to 1. Similarly the nth column and row of the global mass matrix are set to zero.

As an example, shown below are the global matrices for a single phase consisting of five nodes with the aforementioned modifications to apply the boundary conditions.

$$K = \begin{vmatrix} k_{11}^{(1)} & k_{12}^{(1)} & 0 & 0 & 0 \\ k_{21}^{(1)} & k_{22}^{(1)} + k_{11}^{(2)} & k_{12}^{(2)} & 0 & 0 \\ 0 & k_{21}^{(2)} & k_{22}^{(2)} + k_{11}^{(3)} & k_{12}^{(3)} & 0 \\ 0 & 0 & k_{21}^{(3)} & k_{22}^{(3)} + k_{11}^{(4)} & 0 \\ 0 & 0 & 0 & 0 & 1 \end{vmatrix} \tag{3.15}$$

$$M = \begin{vmatrix} m_{11}^{(1)} & m_{12}^{(1)} & 0 & 0 & 0 \\ m_{21}^{(1)} & m_{22}^{(1)} + m_{11}^{(2)} & m_{12}^{(2)} & 0 & 0 \\ 0 & m_{21}^{(2)} & m_{22}^{(2)} + m_{11}^{(3)} & m_{12}^{(3)} & 0 \\ 0 & 0 & m_{21}^{(3)} & m_{22}^{(3)} + m_{11}^{(4)} & 0 \\ 0 & 0 & 0 & 0 & 0 \end{vmatrix} \tag{3.16}$$

$$F = \begin{vmatrix} 0 \\ 0 \\ 0 \\ 0 \\ C_e \end{vmatrix} \tag{3.17}$$

Where the value of the last element of the global force vector, C_e, is the equilibrium concentration to by enforced by the Dirichlet boundary condition.

Interface motion is incorporated by enforcing mass conservation as solute carbon atoms diffuse across the interface between phases. At each time step, the change in solute mass due to interfacial fluxes must be equal to the change in solute due to the movement of the interface. A schematic diagram of the concentration profile before and after movement is shown in Figure 3.2.

At either side of the interface are aforementioned Dirichlet boundary conditions which fix the concentration at the profile in order to ensure chemical equilibrium. Additionally, these boundary conditions act as sources/sinks for solute and therefore fluxes at the interface can cause the overall solute/mass to change by $\Delta J \Delta t$ from time-step to time-step. Movement of the interface by an

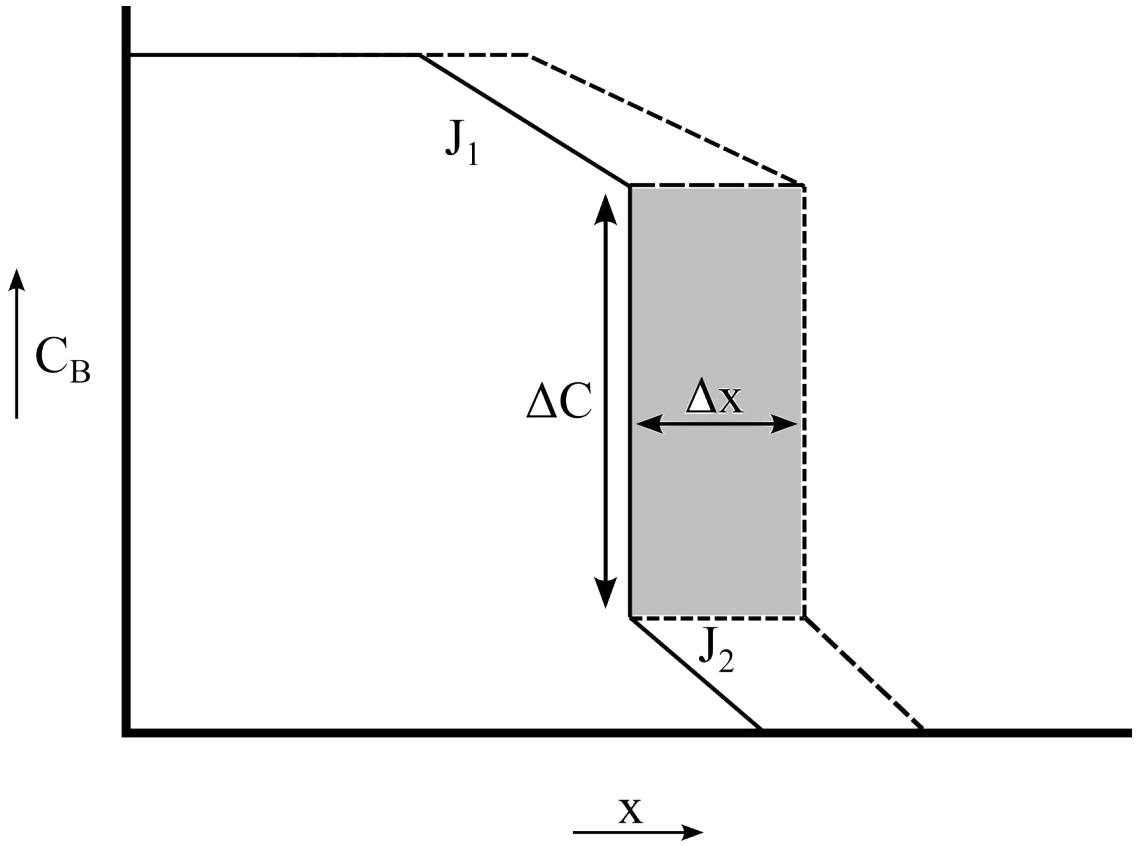

Figure 3.2: A schematic diagram depicting the interface motion due to mass conservation.

amount Δx also changes the mass by the amount $\Delta C \Delta x$, shown as the shaded area in Fiure 3.2. Thus, to ensure mass conservation these two quantities must be equal and the mass conservation law can be written as

$$\Delta J \Delta t = \Delta C \Delta x \tag{3.18}$$

where ΔJ is the difference between the fluxes in each direction across the interface, ΔC is the solute concentration difference at the interface (determined by enforcing chemical equilibrium at the interface assuming that the phase transformation is diffusion-controlled), and Δx is the distance that the interface has moved during time Δt. Therefore the interface motion at a single time step can be determined according to the following equation:

$$v = \frac{\Delta x}{\Delta t} = \frac{\Delta J}{\Delta C}. \tag{3.19}$$

To fully simulate both the evolution of the concentration profiles in each phase as well as the movement of the interface we need to further modify the global matrices shown previously. As before, we will consider an example with five nodes in each phase and we will incorporate an eleventh node associated with the location of the interface.

Thus, the matrices now become:

$$K = \begin{vmatrix} k_{11}^{(1)} & k_{12}^{(1)} & 0 & 0 & 0 & 0 & 0 & 0 & 0 & 0 & 0 \\ k_{21}^{(1)} & k_{22}^{(1)} + k_{11}^{(2)} & k_{12}^{(2)} & 0 & 0 & 0 & 0 & 0 & 0 & 0 & 0 \\ 0 & k_{21}^{(2)} & k_{22}^{(2)} + k_{11}^{(3)} & k_{12}^{(3)} & 0 & 0 & 0 & 0 & 0 & 0 & 0 \\ 0 & 0 & k_{21}^{(3)} & k_{22}^{(3)} + k_{11}^{(4)} & 0 & 0 & 0 & 0 & 0 & 0 & 0 \\ 0 & 0 & 0 & 0 & 1 & 0 & 0 & 0 & 0 & 0 & 0 \\ 0 & 0 & 0 & 0 & 0 & 0 & 0 & 0 & 0 & 0 & 0 \\ 0 & 0 & 0 & 0 & 0 & 0 & 1 & 0 & 0 & 0 & 0 \\ 0 & 0 & 0 & 0 & 0 & 0 & 0 & k_{22}^{(5)} + k_{11}^{(6)} & k_{12}^{(6)} & 0 & 0 \\ 0 & 0 & 0 & 0 & 0 & 0 & 0 & k_{21}^{(6)} & k_{22}^{(6)} + k_{11}^{(7)} & k_{12}^{(7)} & 0 \\ 0 & 0 & 0 & 0 & 0 & 0 & 0 & 0 & k_{21}^{(7)} & k_{22}^{(7)} + k_{11}^{(8)} & k_{12}^{(8)} \\ 0 & 0 & 0 & 0 & 0 & 0 & 0 & 0 & 0 & k_{21}^{(8)} & k_{22}^{(8)} \end{vmatrix} \tag{3.20}$$

$$M = \begin{vmatrix} m_{11}^{(1)} & m_{12}^{(1)} & 0 & 0 & 0 & 0 & 0 & 0 & 0 & 0 & 0 \\ m_{21}^{(1)} & m_{22}^{(1)} + m_{11}^{(2)} & m_{12}^{(2)} & 0 & 0 & 0 & 0 & 0 & 0 & 0 & 0 \\ 0 & m_{21}^{(2)} & m_{22}^{(2)} + m_{11}^{(3)} & m_{12}^{(3)} & 0 & 0 & 0 & 0 & 0 & 0 & 0 \\ 0 & 0 & m_{21}^{(3)} & m_{22}^{(3)} + m_{11}^{(4)} & 0 & 0 & 0 & 0 & 0 & 0 & 0 \\ 0 & 0 & 0 & 0 & 0 & 0 & 0 & 0 & 0 & 0 & 0 \\ 0 & 0 & 0 & 0 & 0 & 1 & 0 & 0 & 0 & 0 & 0 \\ 0 & 0 & 0 & 0 & 0 & 0 & 0 & 0 & 0 & 0 & 0 \\ 0 & 0 & 0 & 0 & 0 & 0 & 0 & m_{22}^{(5)} + m_{11}^{(6)} & m_{12}^{(6)} & 0 & 0 \\ 0 & 0 & 0 & 0 & 0 & 0 & 0 & m_{21}^{(6)} & m_{22}^{(6)} + m_{11}^{(7)} & m_{12}^{(7)} & 0 \\ 0 & 0 & 0 & 0 & 0 & 0 & 0 & 0 & m_{21}^{(7)} & m_{22}^{(7)} + m_{11}^{(8)} & m_{12}^{(8)} \\ 0 & 0 & 0 & 0 & 0 & 0 & 0 & 0 & 0 & m_{21}^{(8)} & m_{22}^{(8)} \end{vmatrix} \tag{3.21}$$

and the new global force vector is:

$$F = \begin{vmatrix} 0 \\ 0 \\ 0 \\ 0 \\ C_- \\ \frac{\Delta J}{\Delta C} \\ C_+ \\ 0 \\ 0 \\ 0 \\ 0 \end{vmatrix}, \tag{3.22}$$

where C_- and C_+ represent the equilibrium concentrations enforced as Dirichlet boundary conditions on the left and right sides of the interface respectively.

Finally, time evolution is incorporated using the Backwards Euler method for time integration. From this, the matrix form of the equation becomes:

$$(K + M/\Delta t)u_{new} = (M/\Delta t)u_{old} + F, \tag{3.23}$$

which can be solved using the standard linear algebra methods.

3.2 Density Functional Theory

Density functional theory (DFT) is a method developed in order to provide approximate solutions to many-body problems that are effectively impossible to solve using the Schrodinger equation. This computational method models the properties of many-electron systems by calculating the energy function as determined by spatially dependent electron densities. This is accomplished by solving the following equation, known as the Kohn-Sham Equation

$$\Big(-\frac{\hbar^2}{2m}\nabla^2 + v_{eff}(\mathbf{r})\Big)\phi_i(\mathbf{r}) = \epsilon_i\phi_i(\mathbf{r}) \tag{3.24}$$

where the first and second terms represent the kinetic and potential energies of the system, respectively. The Kohn-Sham Equation is an eigenvalue equation where ϵ_i is the orbital energy of the Kohn-Sham orbital ϕ_i and the charge density for a system of N non-interacting particles is $\rho(\mathbf{r}) = \sum_i^N |\phi_i(\mathbf{r})^2|$. The system energy, from which many properties can be derived, can then be written as a function of the charge density.

The effective single-particle potential $v_{eff}(\mathbf{r})$ is written as

$$v_{eff}(\mathbf{r}) = V(\mathbf{r}) + \int \frac{\rho(\mathbf{r'})}{|\mathbf{r} - \mathbf{r'}|}d^3r' + V_{XC}[\rho(\mathbf{r})] \tag{3.25}$$

where V(**r**) is the external potential generated by the atomic nucleus under the Born-Oppenheimer approximation, $\int \frac{\rho(\mathbf{r'})}{|\mathbf{r}-\mathbf{r'}|}d^3r'$ is the Hartree term describing the coulombic electron-electron interaction, and $V_{XC}[\rho(\mathbf{r})]$ is the exchange-correlation term that contains the quantum mechanical electron-electron effects. Since both the Hartree term and the exchange-correlation depend on the charge density $\rho(\mathbf{r})$, Equation 3.25 is nonlinear and typically solved using an iterative procedure during which an initial guess for $\rho(\mathbf{r})$ is made.

The exchange-correlation term $V_{XC}[\rho(\mathbf{r})]$ can be defined as a variational derivative of the exchange-correlation energy functional $E_{XC}(\mathbf{r})$ with respect to the electron density $\rho(\mathbf{r})$.

$$V_{XC}[\rho(\mathbf{r})] = \frac{\delta E_{XC}(\mathbf{r})}{\delta\rho(\mathbf{r})} \tag{3.26}$$

There are many methods for approximating the exchange-correlation terml; however, two primary methods stand out: the local density approximation (LDA) and the generalized gradient approximation (GGA). The LDA, first proposed by Kohn and Sham in 1965, assumes that the exchange-correlation energy can be written as a functional of the electron density. The exchange correlation energy for a homogeneous electron gas is known exactly, and therefore the

exchange-correlation term for an interacting inhomogeneous electron gas can be approximated by the exchange-correlation energy of a homogeneous electron gas by evaluating at the local density.

$$E_{XC}^{LDA}[\rho(\mathbf{r})] = \int \rho(\mathbf{r})\epsilon_{XC}^{HEG}(\rho(\mathbf{r}))d\mathbf{r} \tag{3.27}$$

As stated by the Kohn and Sham, the LDA is most appropriately used when the electron density slowly varies. Additionally, simulations conducted using LDA exchange-correlation functionals are known to frequently overbind the unit cell, thus predicting smaller lattice constants than are observed experimentally [62].

The GGA aims to improve upon LDA by including higher order terms in the approximation of the exchange-correlation energy functional, specifically by approximating it as not only a function of the local electron density but also by including the gradient. Perhaps most impactful is the GGA method developed by Perdew, Burke, and Erzehof in 1996 [63]. Their exchange-correlation functional is thought to provide greater accuracy in DFT calculations when compared to LDA exchange-correlation, especially when large gradients in the local electron density are present. The PBE GGA exchange-correlation functional is thought to underbind unit cells and therefore predicts lattice constants greater than are observed experimentally.

$$E_{XC}^{GGA}[\rho(\mathbf{r}), \nabla\rho(\mathbf{r})] = \int \rho(\mathbf{r})\epsilon_{XC}^{HEG}(\rho(\mathbf{r}), \nabla\rho(\mathbf{r}))d\mathbf{r} \tag{3.28}$$

Generally, DFT simulations reduce the number of electrons in the system by incorporating the shielding effect of all of the core electrons into so-called pseudopotentials by defining a fixed electron density near the ionic nucleus. Thus, using this method computational costs are dramatically reduced since only the valence electrons are directly simulated. Several different types of pseudopotentials exist; however, all of the simulations conducted in this work used projector augmented-wave (PAW) pseudopotentials.

The DFT simulations performed within this work were conducted using the Vienna Ab-Initio Simulation Package (VASP), which is a software package capable of iteratively solving the Kohn-

Sham Equations in order to determine the system energy. To accomplish this, the user inputs provides as an input files containing the ionic coordinates and unit cell parameters as well as a potential file containing the pseudopotential and exchange-correlation information.

3.2.1 Determining Structural Energies & Energy Barriers to Ionic Migration

In this work, we are primarily interested in using DFT simulations for two purposes: first, to determine structural energies which can later be used to fit a cluster expansion method model which will be used in Monte Carlo and kinetic Monte Carlo simulations, and secondly to determine the 'height' of saddle points along reaction paths of ionic migration, i.e., to determine the magnitude of the energy barrier for migration of atoms between lattice sites. In each case, VASP has built-in algorithms which will be briefly summarized here.

To determine the structural energy using VASP, the conjugate gradient method (CG) is employed. CG effectively minimizes the system energy with respect to the position of the ions, usually resulting in a 'relaxed' crystal structure where the individual ion positions have been moved in order to drive the system to a local energy minimum. The CG is an iterative method for minimizing the a system of equations until some convergence criterion is met. In practice, this is accomplished by repeatedly moving ions in system and recalculating the structural energy and its gradient.

In addition to being used in the fitting of a cluster expansion, structural energies will also be used in the calculation of energy barriers for ionic migration, which are instrumental to understanding the kinetics of diffusion. To calculate these energy barriers, the nudged-elastic band (NEB) method used and implemented automatically in VASP. For each NEB calculation an initial and final state is given as an input. To ensure accurate calculations of the energy barrier, these states must be 'relaxed' using CG prior to the NEB calculation. The NEB calculation works by interpolating image states along the reaction path between the initial and final reaction states. Imaginary 'spring' forces are applied to the images and act to maintain a equal distance between each image and its neighbors, effectively preventing image states from traversing their way down the potential

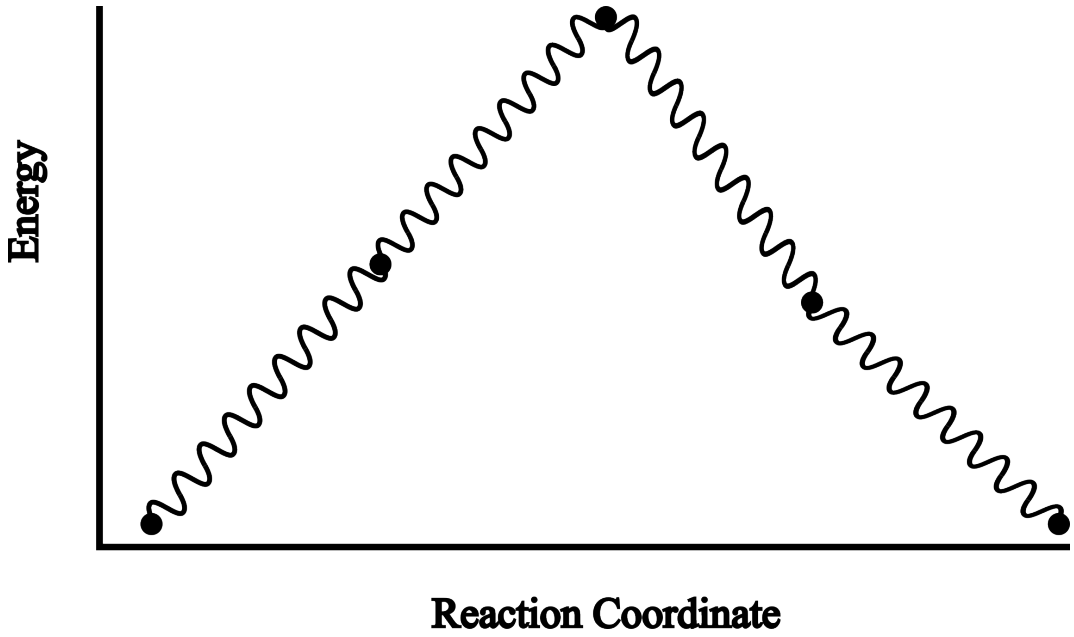

Figure 3.3: A diagram depicting several images between two endpoints of a reaction pathway. The images are connected by imaginary string forces that allows a saddle in the potential energy surface to be found.

energy gradient towards local energy minima. A representative schematic diagram depicting the energy of images along a reaction pathway is shown in Figure 3.3.

3.3 Monte Carlo Simulations

The Monte Carlo method is a statistical method the utilizes repeated random sampling and has applications across a wide variety of problems. In the context of computational materials science, the Monte Carlo method is most commonly used within the Metropolis-Hastings algorithm in order to drive a system to thermodynamic equilibrium by repetitive sampling of the Gibbs canonical ensemble wherein a state of energy E has the probability $P(E) = \frac{1}{Z} \exp \frac{-E}{k_B T}$. Here, Z is the partition function, k_B is Boltzmann's constant, and T is the simulation temperature.

A step-by-step description of the Metropolis-Hastings algorithm as implemented with Kawasaki Dynamics in the following work is shown below:

1. A simulation lattice is initialized into some initial state with a known, configuration-dependent total energy (calculated using either the CEM or an Ising Model)

2. For each iteration, a new state is proposed by swapping the spin variables S at two sites. The resulting change in energy ΔE is calculated

3. If $\Delta E < 0$ the swap is immediately implemented. If $\Delta E \geq 0$ then a random number u_1 is generated and compared to acceptance probability $\alpha = \exp \frac{-\Delta E}{k_B T}$. If $u_1 \leq \alpha$ then the swap is accepted and the configuration is updated whereas if $u_1 > \alpha$ the proposed swap is rejected

Built in to the Metropolis-Hastings algorithm is the assumption of ergodicity, that is to say that given enough iterations every possible microstate will be visited in a uniform and random sense, leading to the ability to determine average properties of the system using a sufficiently large number of samples. In this way, Monte Carlo simulations are able to effectively determine the equilibrium characteristics of simulated materials systems.

In the following work, Monte Carlo simulations were implemented in order to achieve several goals. First, to sample materials parameters, such as the short and long-range order parameters as a function of temperature. More generally, Monte Carlo simulations are frequently implemented in the literature in order to determine the limits of phase stability as part of the construction of phase diagrams. Secondly, for the diffusion studies conducted using kinetic Monte Carlo (kMC), the system was initialized into a state of thermal equilibrium via the Monte Carlo method prior to the kMC simulation.

3.4 Kinetic Monte Carlo Simulations

The kinetic Monte Carlo (kMC) method is statistical method for simulating the time evolution of processes with known transition rates between discrete states. Individually, these transitions are Poisson processes wherein the average time of an event is known (*e.g.* according to the transition rates); however, the exact timing of each event is unknown. For poisson processes, the probability of k occurrences during an interval of time is given by probability mass function of Poisson's distribution as shown below

$$P(x = k) = \frac{\lambda^k}{k!} \exp(-\lambda) \tag{3.29}$$

where λ is the expected number of occurrences during the time interval.

In kMC simulations; however, generally it is the inter-arrival time that we wish to model. For Poisson processes, the inter-arrival time is given by the exponential distribution as shown below

$$PMF = r\exp(-rt) \tag{3.30}$$

where r is the average arrival rate and t is the amount of time. Suppose now that we want to find the average arrival time $\overline{T}$. This can be accomplished by integration of the inter-arrival time PMF:

$$\int_0^\infty r\exp(-rt)dt = \frac{1}{r} \tag{3.31}$$

Similarly, the residence-time algorithm is used in order to implement time evolution in kMC simulations according to the following equation

$$\Delta t = -\frac{\ln u}{r} \tag{3.32}$$

where the Δt is the time increment between the current event and the last, and u is a random number between 0 and 1 generated from the uniform distribution. The residence-time algorithm has the same long-time average time scale as the average obtained from the inter-arrival time PMF. The advantage, then, of the residence-time algorithm is that it is able to draw the inter-arrival time for each simulation step from the Poisson distribution rather than always being the mean of the distribution.

The primary difficulty in performing kMC simulations is with determining the rates. The kMC method itself is unable to determine the rates and they therefore must be either experimentally determined, *e.g.* using diffusion experiments, or determine from first-principles calculations. Furthermore, at each step of the simulation, the rates for every possible transition out of the current state must be determined and used in the construction of a rate catalogue. This rate catalogue is

then used in the determination of which transition to carry out and in the determination of the time increment.

The algorithm for rejection-free kMC is shown below

1. Set the time $t = 0$
2. Choose and initial state (The simulations in this work use the final state of a Monte Carlo run)
3. Construct the list containing all possible transitions out of the current state k into the arbitrary state i
4. Construct the rate catalogue $R_{ki} = \sum_j r_{kj}$
5. Generate a uniform random number u_1
6. Determine which event to carry out by finding i for which $R_{k,i-1} < u_1 R_{k,N_k} \leq R_{ki}$
7. Carry out the transition from current state k to the new state i
8. Generate a new random number u_2
9. Update the time $t = \Delta t$ where Δt is calculated according to the residence-time algorithm shown above
10. Return to step 3

3.5 Cluster Expansion Method

The Cluster Expansion Method (CEM) is a statistical method for calculating configuration-dependent scalar properties of a crystal. It is formulated rigorously as a power-series expansion of the partition function [9, 64]. In computational materials science, it is often used as a method for connecting first-principles calculations, which are typically restricted to containing a few hundred atoms, to larger scale simulations containing thousands or millions of atoms, commonly using

Monte Carlo (MC) or kinetic Monte Carlo (kMC) methods. Using the CEM, any configuration dependent scalar quantity $P(\sigma)$ can be expanded as a linear combination of the correlation functions $\overline{\Phi}_\alpha$:

$$P(\sigma) = \sum_\alpha m_\alpha J_\alpha \overline{\Phi}_\alpha \tag{3.33}$$

where m_α is the multiplicity of orbit α, defined to be the number of clusters contained in an orbit, J_α is the ECI of orbit α, and $\overline{\Phi}_\alpha$ is the average cluster correlation function, which is defined to be the product of spins S within each cluster averaged over all of the clusters in orbit α.

Utilizing the CEM typically requires the first-principles calculation of a number of ground-state configurations of the materials system. From these ground states, a set of structures containing variable-composition atoms, known as clusters, are selected and used to fit effective cluster interactions (ECIs). In general, a cluster can be defined simply as a group of sites on the lattice, *e.g.* any nearest-neighbor pair of sites. Clusters equivalent by a space-group operation of the host lattice are grouped together as 'orbits' wherein each element of an orbit is a distinct cluster; however, all clusters in a given orbit possess the same ECI. Each orbit is therefore a set of clusters that all contain the same number of sites and cluster diameter, but having different orientations and containing different sites. The cluster size is defined as the number of sites contained in the cluster and can vary from zero, *i.e.*, the empty cluster all the way to the cluster containing all of the sites on the simulation lattice. The cluster diameter is defined as the largest distance between two sites in the cluster. Figure 3.4, from Ref. [9], shows examples of clusters of varying size and diameter.

Figure 3.5 depicts examples of different cluster orbits for two and three site clusters on a square lattice. In the left figure the green, purple, red, and yellow orbits correspond to nearest, second nearest, third nearest, and fourth nearest orbits of pair clusters respectively. On the right two sets of three-site orbits are shown.

Furthermore, sites may be shared by clusters; however, all clusters in an orbit must be distinct from one another. As an example, each site on a square lattice is shared by four nearest-neighbor pair clusters, shown in purple in Figure 3.5. Each of these clusters is an element of the orbit

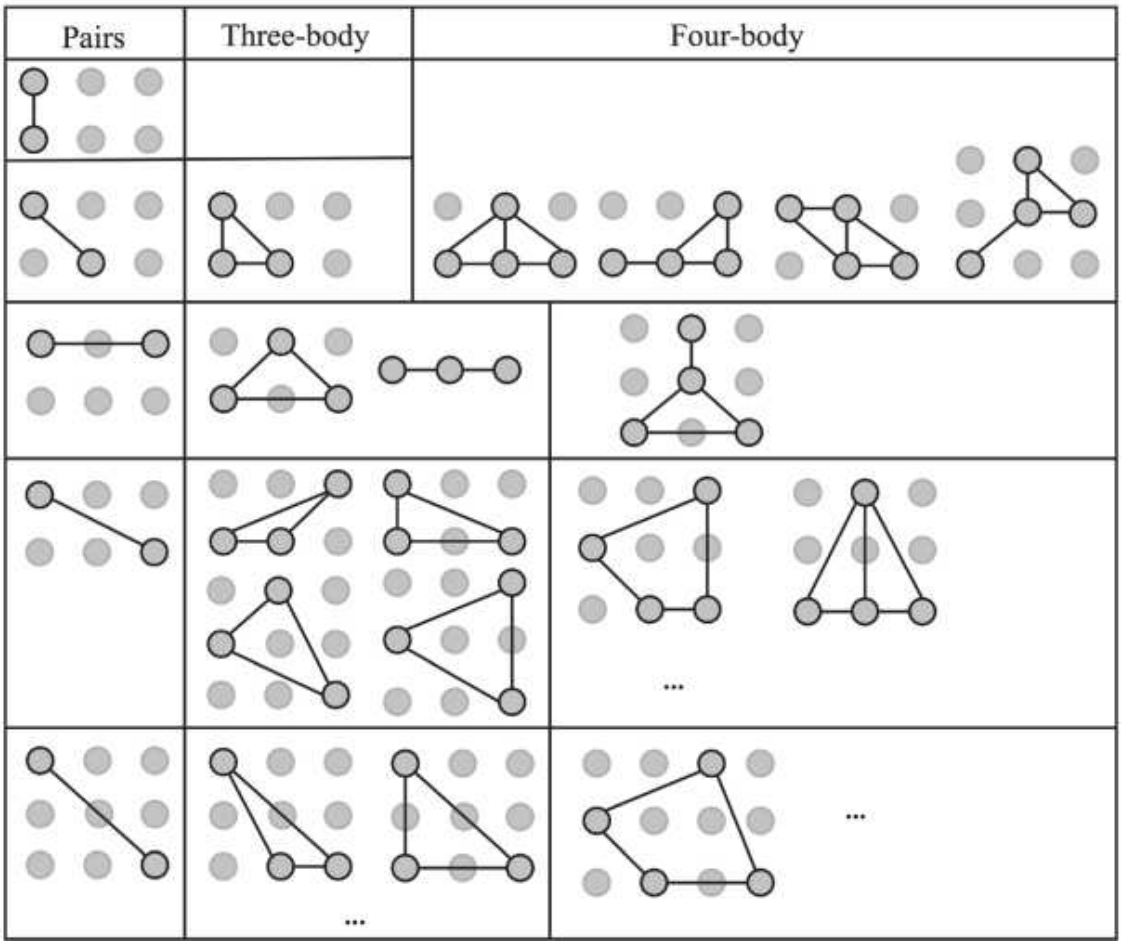

Figure 3.4: Clusters in a prototype square lattice, ranked in importance according to heuristic cluster selection rules. Cluster diameter, *i.e.*, the maximum distance between any two sites in the cluster, increases along the vertical axis from top to bottom. Cluster size, *i.e.*, the number of sites in the cluster, increases horizontally from left to right. Figure from Ref. [9].

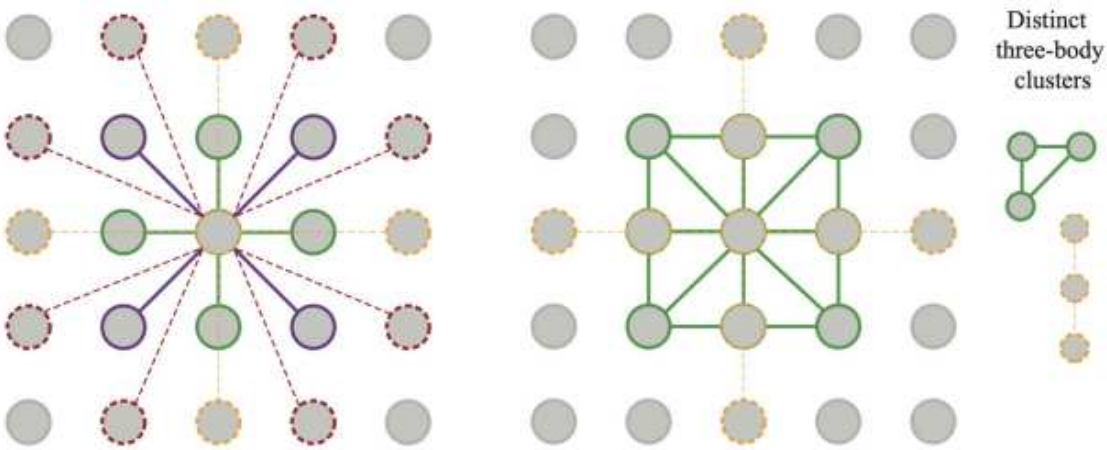

Figure 3.5: (Left) Four distinct sets (or orbits) of pair clusters highlighted in a prototype square lattice. Symmetrically equivalent pair clusters belong to the same orbit and are marked with the same color. Green, purple, red, and yellow correspond to nearest, second nearest, third nearest, and fourth nearest orbits of pair clusters. The multiplicity of a cluster m_α is defined as the number of clusters in the same orbit, e.g., four for the nearest and second nearest orbits in the square lattice. (Right) Two distinct set of three-body clusters highlighted in a prototype square lattice. Symmetrically equivalent three-body clusters are marked in the same color. Note that in all cases the pair or three-body cluster includes the central site. Figure from Ref. [9].

containing all of the nearest-neighbor pair clusters within the simulated domain, since all of the nearest-neighbor pairs are equivalent by space group operations, *e.g.* four-fold rotations or translations along the lattice vectors. Thus, the multiplicity for the nearest-neighbor pair orbit is equal to $m_{NN} = 4N_s$ where N_s is the number of sites in the simulated domain.

Each site on the lattice must be assigned a spin variable depending on the species present at the site. For example, in a substitutional solid solution containing A and B atoms of variable composition, a site containing an A atom may be assigned $S = 1$ whereas a site containing a B atom may be assigned $S = -1$. Then, the average correlation function for an orbit α can be calculated by averaging the product of the product of the spin variables S_j for each cluster i in the orbit α

$$\overline{\Phi}_\alpha = 1/N_\alpha \sum_i \Big(\prod_j S_j \Big) \tag{3.34}$$

In the following work, the Alloy Theoretical Automated Toolkit (ATAT) [65] was used in order to generate ground state structures and determine their total energies as well as to perform the cluster expansion fitting.

Chapter 4

Composite Initial Conditions & Transformation Time

4.1 Introduction & Background

The primary novelty of the type of metal-ceramic multilayer composites described in this dissertation is that these materials are able to undergo phase transformations that result in the disappearance of the metal composite layers. This phase transformation occurs due to the fact that the microsctructure of the as-deposited composites is 'frozen in'. In other words, the as-deposited composites are not in chemical equilibrium except at the interface between layers. Therefore, as the temperature rises and becomes sufficient for the diffusion of carbon/nitrogen, the interfaces between composite layers begin to migrate. Eventually, the interfaces defining each end of a single metal phase meet and result in the total disappearance of the metal layer.

Phase transformations in the transition metal carbides were studied experimentally in the 60's by Sarian [42, 50, 56] in the TiC and ZrC as well as Brizes [21, 51, 52] in NbC and TaC. These authors carried out layer growth studies from which they were able to estimate the diffusivity of carbon in the monocarbide and hemicarbide phases. Besides being some of the only available experimental measurements of the diffusivity of carbon in these materials, they also concluded that the kinetics of carbide formation and layer growth is controlled by carbon diffusion and not by diffusion of the metal atoms nor the interface. This latter point is important because it determines the boundary conditions applicable to the moving interfaces. In diffusion-controlled phase transformations the interface is considered to be in chemical equilibrium, which means that the carbon concentrations on the boundary between phases are Dirichlet boundary conditions wherein the carbon concentrations are fixed to the solubility limits available from phase diagrams.

The Finite Element Method was used to directly solve for the evolution of the carbon/nitrogen concentration profiles in each phase according to Fick's Second Law. Simultaneously, the interface migration was solved according to a derived mass-conservation law. From these simulations the time required for the composite to completely transform was determined. In the group IV carbides this time corresponded to the time required for the metal layers to disappear; however, an intermediate phase - the hemicarbide/nitride phase, is present in the group V carbides and group IV nitrides. In the latter simulations the transformation time measured corresponded to the time required for the disappearance of both the metal and hemicarbide/nitride phases. In either case, after the transformation time corresponded to the first time step for which the only phase present in the simulation was the monocarbide/nitride.

Perhaps the first people to investigate transforming transition metal carbide multilayers was Dahan *et al.* who experimentally explored the interdiffusion kinetics and structural evolution of Ti/TiC multilayers [66, 67]. From these experiments they determined the activation energy for carbon diffusion in TiC to be 1.37eV, significantly lower than previous reports. In these studies; however, Dahan *et al.* only investigated thin films and coatings and not bulk composites and they attributed the low activation energy to a large defect content due to low-temperature sputtering.

Several attempts to model diffusion controlled phase transformation problems have been made. For example, Carette *et al.* modeled the evolution of the group VB TaC/Ta_2C interface during carburization with subsequent annealing using a Newton-Raphson approach to fit an analytical solution to Fick's second law whereupon they calculated layer thicknesses based on layer growth coefficients obtained from the literature [68]. During annealing, Carette *et al.* described the shrinking of layers using an iterative procedure based on the conservation of mass (carbon solute). Unfortunately, this approach assumed a nonphysical immediate homogenization of the TaC layer after carburization stopped and a similar homogenization of the Ta_2C layer after the disappearance of the TaC layer. The assumption of immediate homogenization resulted in a clearly nonphysical discontinuity in the predicted layer thicknesses.

Similarly, Keddam *et al.* developed a model for simulating nitride layer growth in pure iron [69]. In their simulation, a more physical method for modeling interfaces between layers was achieved by using a Newton-Raphson routine to solve for the layer growth coefficients rather than obtaining them from literature. The major drawback for this approach was that the direct simulation of diffusion was missing and was assumed to be an error function solution to Fick's second law. Note that the error function solution is only valid in semi-infinite domains and cannot be used to simulate diffusion in periodic domains, such as our multilayer composites where simulation to the annihilation of one of the phases is desired.

The most physically meaningful method for modeling diffusion-controlled phase transformations requires directly simulating both bulk diffusion in all phases involved and the movement of the interface. In these cases, the solution involves the use of a partial differential equation in multiple domains separated by an interface that moves according to a conservation law. Problems of this sort are known as Stefan problems [70]. The literature on solving Stefan problems generally uses numerical methods such as finite difference [71–75], finite element [76–81], or phase field methods [82–85]. Numerical solutions to these problems often fail to conserve mass because of the imbalances between bulk diffusion and interface diffusion. In these cases, the loss of mass during the simulation results in changes in driving forces, caused by the mass imbalance, and thus contribute to inaccuracies in the final composition as well as the simulated times. Despite the difficulty associated with mass conservation, there are many methods for solving Stefan problems described in the literature. In one approach, Illingworth and Golosnoy [76] solved the Stefan problem using a rigorous mathematics approach. They used a finite difference method that included a Landau transform resulting in stationary interfaces in the new coordinate system. The resulting system of nonlinear partial differential equations was then solved by first decoupling the equations using a method known as coefficient freezing, and then solving the resultant tridiagonal matrix. Notably, this method results in error that is first order accurate with time step size and spatial discretization size. Illingworth and Golosnoy correctly identified that the difficulty in solving Stefan problems using numerical schemes is that the approximations used to calculate interfacial carbon fluxes are

different from those used to solve the diffusion equation in the bulk phases. The solution gains or loses mass depending upon the extent to which these approximations are imbalanced. Stefan problems arise in a variety of different scientific and industrial applications that include phase changes such as solid-state phase transformations [68, 69, 79], solidification [73, 77, 83, 84], liquid phase bonding [86] and second-phase precipitation or dissolution [78, 87, 88].

4.2 Methodology

4.2.1 Phase Transformation Simulations

As described above, Stefan problems are a class of problems composed of systems of partial differential equations with free boundaries that move according to a conservation law. These problems arise in a variety of different scientific and industrial applications that include phase changes such as solid-state phase transformations [68,69,79], solidification [73,77,83,84,89], liquid phase bonding [86] and second-phase precipitation or dissolution [78, 87, 88]. An excellent mathematical description of the phase field method is given in [82]. Due to the complexity of describing diffusion-controlled phase changes, many of the existing models are limited to planar geometries, though Schuh [74] extended the fixed-grid finite difference method to include planar, cylindrical, and spherical geometries.

Figure 4.1a illustrates the geometry of a two-phase multilayer transition metal and transition metal carbide composite under consideration in this work. Upon reaching temperatures sufficient for appreciable carbon diffusion, the multilayer composite undergoes a solid-state phase transformation controlled by the diffusion of carbon from the ceramic phase to the metal phase. The periodic nature of the lamella can be taken advantage of when simulating the phase transformation process since the behavior in a single bilayer is representative of the whole construction if periodic boundary conditions are applied. Furthermore, these periodic boundary conditions can be further simplified by taking advantage of the mirror symmetry of the lamellar bilayers and imposing zero flux Neumann boundary conditions upon the planes of reflection, *i.e.*, the midplanes of the ceramic and metal phases.

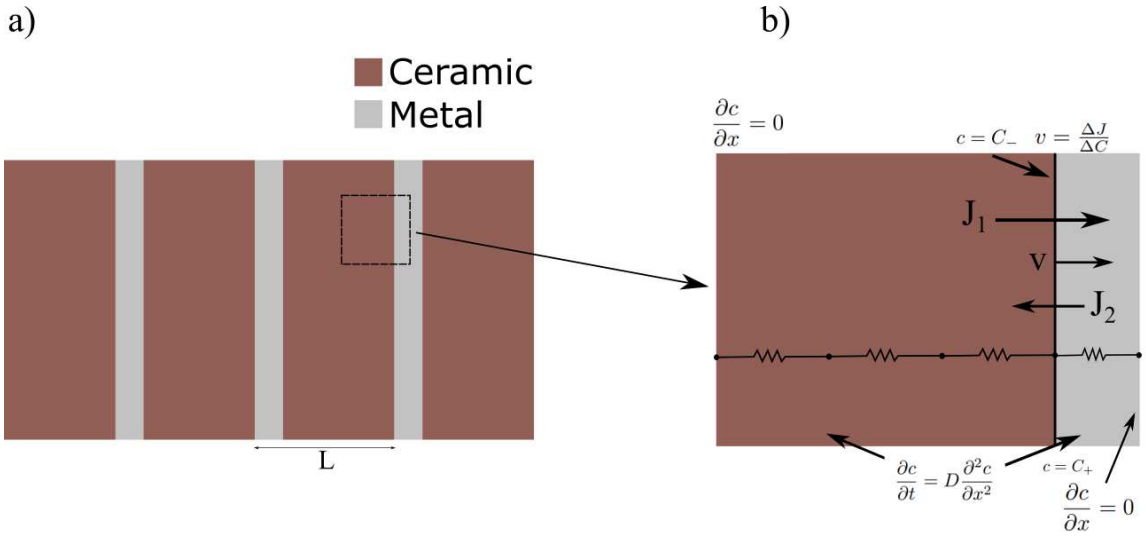

Figure 4.1: The lamellar microstructure of a two-phase transition metal and transition metal carbide multilayer composite. b) A schematic of the numerical model for the two-phase composite. The carbon concentrations at the interface, C and C+, were enforced as Dirichlet boundary conditions. The simulation domain was bounded on either end by no-flux Neumann boundary conditions. For group V composites (not shown) a third hemicarbide phase was simulated with small initial width. It was bounded on one side by an MeC/Me_2C interface and by an Me_2C/Me interface on the other

The reduced simulation domain that includes periodicity and mirror symmetry is shown in Figure 4.1b. No-flux Neumann boundary conditions were imposed upon the mirror reflection planes located at the left and right ends of the domain and mimic the periodicity of the lamellar composite. The two phases were separated by an interface whose position was allowed to vary continuously. The two-phase equilibrium carbon concentrations, which are denoted C_- and C_+, were imposed as Dirichlet boundary conditions on either side of the interface. The interfacial carbon fluxes, J_1 and J_2, were calculated using Fick's first law on either end of the interface. The interface movement, which occurs to conserve mass, depends upon the difference in interfacial carbon atom fluxes and carbon concentrations according to equation 4.1.

$$v = \frac{\Delta x}{\Delta t} = \frac{\Delta J}{\Delta C} \tag{4.1}$$

For three-phase composites, *i.e.*, group VB TMCs, a transient (assuming a complete phase transformation) third phase (the hemicarbide phase) was located in between the metal and mono-

carbide phases. The hemicarbide phase was bounded on either side by an interface with Dirichlet boundary conditions imposing equilibrium carbon concentrations across each interface. Simulations containing three phases also contained two interfaces, *i.e.*, an MeC/Me_2C interface and an Me_2C/Me interface.

As derived in Chapter 3, the diffusion-controlled phase transformations in the group IVB and VB TMCs, assuming Fickian diffusion and composition independent diffusivities, is modeled by the following system of partial differential equations:

$$\frac{\partial c_i(x,t)}{\partial t} = D_i \frac{\partial^2 c_i(x,t)}{\partial x^2}, x \in \Omega_i \tag{4.2}$$

$$v_j = \frac{\Delta J_j}{\Delta C_j}, x = \Gamma_j \tag{4.3}$$

where $c_i(x,t)$ is the carbon concentration field in phase Ω_i, D_i is the carbon diffusivity in phase Ω_i, v_j is the velocity of interface Γ_j, ΔJ_j is the difference in carbon atom fluxes across interface Γ_j, and ΔC_j is the difference in equilibrium carbon concentrations between the phases that meet at interface Γ_j. Since the phase transformation is diffusion-controlled, the interface between two phases is assumed to be in chemical equilibrium such that the concentrations on the boundaries are determined from equilibrium phase diagrams. In addition, we have assumed that the diffusivity is independent of carbon composition in each phase and that Fick's first law is followed. The latter two are assumptions that may not be strictly correct but should be sufficiently accurate to obtain reasonable predictions.

Past efforts to track moving interfaces have used both finite difference and finite element schemes to approximate solutions to the diffusion and interface movement coupled with partial differential equations. In this work, Equations 4.2 and 4.3 were solved by discretizing each phase into an equal number of linear elements (*e.g.*, $N_A = N_B = 20$) with equal lengths in each domain (see Chapter 3). Linear elements were chosen because their use results in a piecewise linear solution, which is convenient for linear interpolation after each solution and they are simple to implement. Using higher order elements is possible, but it is unclear if the approximation will

increase convergence rates due to the source of the mass loss error, which is a result of interface motion that will also be discussed in detail later. The mass and stiffness matrices were constructed based on the length of each element and the carbon diffusion coefficient for the phase in which the element was located consistent with the finite element approximation. There are two finite element nodes at the interface corresponding to the concentration of the two phases at equilibrium, but these are Dirichlet boundary conditions and thus are included in the force vector, providing no additional degrees of freedom. One additional degree of freedom was added to the unknowns that represents the physical position of the interface, which evolves according to Equation 4.2.

In some previous works, the interface movement was incorporated by uniformly stretching or compressing (affine deformation) the elements in each phase to meet the desired phase thicknesses. Affine deformation of the linear elements will give rise to significant mass errors unless the diffusion equations are altered to correctly account for the changing domains. In addition, this treatment for interface motion is inconsistent with Equation 4.2 as it has the form of a local balance law and therefore only the elements closest to the interface can have their length altered. Other forms of Equation 4.2 exist that appropriately describe the flux/mass conservation for uniformly changing domains, but this would result in the matrices losing their sparse nature, increasing computational expense.

Instead of using a mesh that changes length everywhere, the simulations conducted here only allow the interface node to move, changing the lengths of only the elements next to the interface during each timestep. However, after interface movement the spatial discretization scheme is left nonuniform. If left unchecked, the elements nearest to the nodes may become too short relative to their neighbors, producing large concentration gradients that give rise to significant error during the approximation of interfacial fluxes. Ultimately, this causes the simulation solution to diverge. To mitigate this issue, we choose to re-discretize the nodes to be equally spaced with equal lengths in each domain, *i.e.*, remesh. The concentration profile after interface motion is then interpolated onto the new nodes, which is consistent with the finite element solution prior to re-discretization. Since the remesh and interpolation are consistent with the original solution, this preserves the

convergence properties of the finite element solution. Explicit time integrators cannot be used to simulate the anticipated phase annihilation since, as the metal phase shrinks prior to annihilation, the elements become arbitrarily small. The small element sizes will eventually violate the stability condition of the explicit integrator, thus making the solution unstable. For this reason, time integration was done using a backwards Euler time integrator and simulations were allowed to continue until the metal phase was annihilated.

The mass error generated during the simulation can be easily quantified by integration of the concentration field before and after a complete phase transformation, or any time in between. The mass error is then the relative difference between the current mass and the initial mass. The mass error in our simulations is plotted in Figure 4.2, demonstrating that our finite element method combined with remesh behaves first order in terms of the spatial discretization, and thus clearly conserves mass to the first order. Since the current mass determines the rate of diffusion, mass loss results in incorrect predictions of the phase transformation times. Additionally, Figure 4.2 demonstrates that this error can be decreased by increasing spatial discretization. Since the initial mass is always known, this can be used to estimate errors in the simulations, a point we will discuss shortly.

The shape of the initial concentration profile is generally unknown and therefore it was necessary to make an assumption. We chose to initialize the concentration profile as a having a uniform stoichiometric composition in the half of the monocarbide phase that was furthest from the ceramic-metal interface and a quadratic decline in concentration towards the phase boundary concentration at the interface in the half of nearest to the interface. Similarly, there was a quadratic decline in concentration moving away from the interface in the metal layers and zero carbon concentration in the half farthest away from the interface. This profile is shown in Figure 4.3.

Although we chose our initial carbon concentration profile to be quadratic, we recognize that it is important to see how our assumption affected the phase transformation kinetics. Therefore, we also examined how changing the shape of the initial concentration profile affected the diffusivity prefactor extracted from the simulations. To accomplish this, we examined a total of five profile

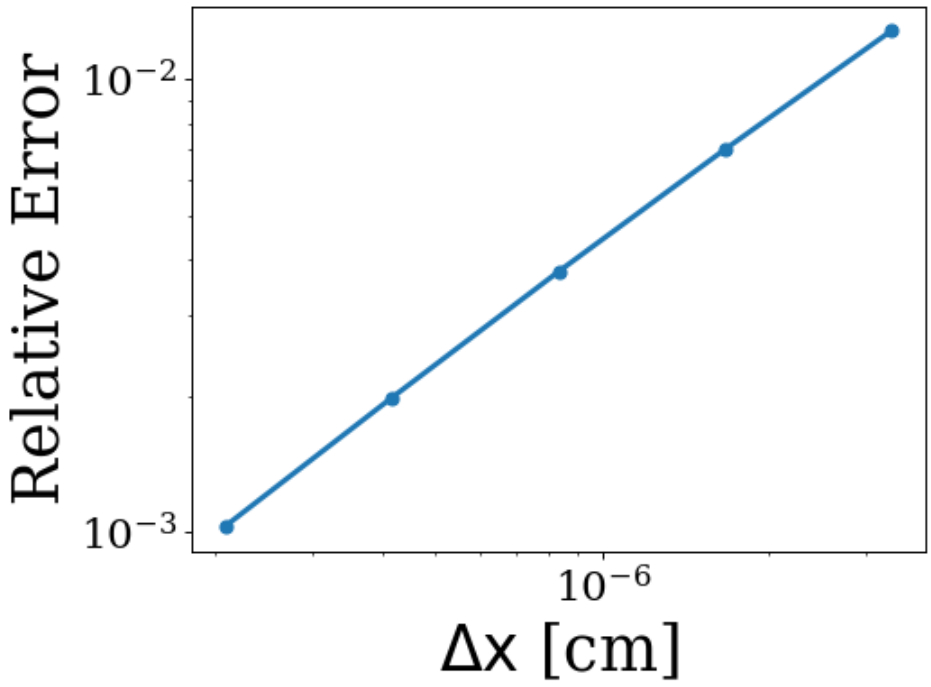

Figure 4.2: A log-log plot of the relative mass error vs. the initial spatial Discretization Size. The linear relationship between the relative mass error and initial spatial discretization size indicates that the method is first order in space.

shapes, including the quadratic profile shown above. The other four profiles examined are shown in Figure 4.4 and their affect on the apparent diffusivity prefactor are tabulated in Table 4.1.

Table 4.1: The apparent diffusivity prefactors determined from our simulations for multiple initial concentration profile shapes.

Concentration Profile	$D_0^{\text{app}}[\text{cm}^2/\text{s}]$
Quadratic	227
Bilinear	200
Tanh	234
Sawtooth	301
Sinusoid	302

The results in Table 4.1 show that, in general, the composition profiles with a greater concentration of carbon near the interface results in larger apparent diffusivities. We chose a quadratic shape for our initial carbon concentration profile where the profile has a uniform concentration

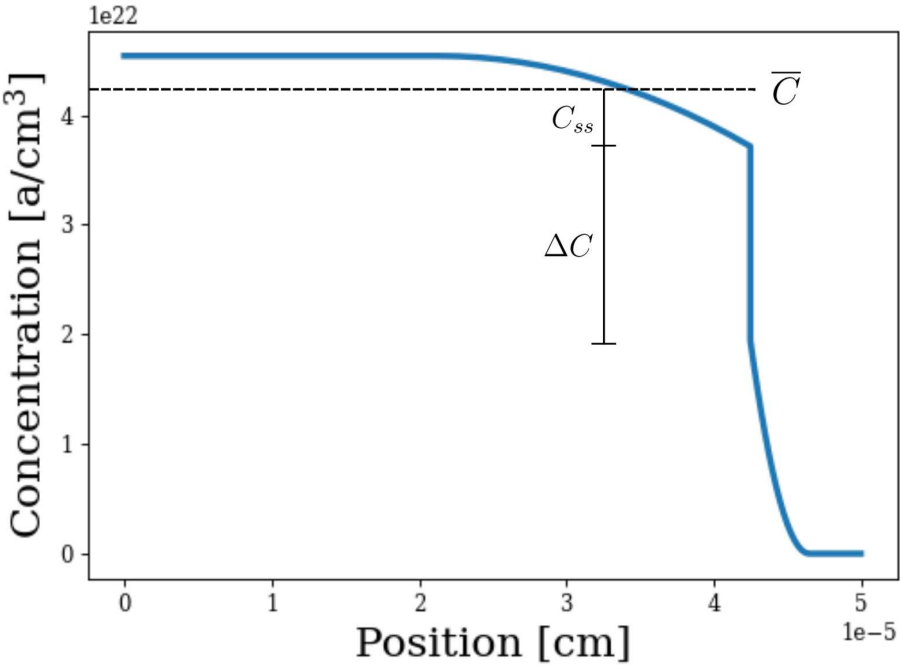

Figure 4.3: The initial concentration profile used for simulations done in this work. The profile is initially uniform and then goes to the phase equilibrium value quadratically.

far from the interface and then goes to the interface concentration quadratically. This shape was chosen since it seemed to be the most realistic compared to the other profile shapes investigated.

4.2.2 Apparent Diffusivity Calculations

For diffusion-controlled phase transformations there is a relationship between time and length. Therefore, we expect that for our phase transformations there should be some effective relationship between the time required for the completion of the phase transformation and the length of the composite bilayer. As such, we computed an apparent diffusivity as shown below:

$$D_{\text{app}} = \frac{l^2}{\tau} \tag{4.4}$$

where l is the composite bilayer length and τ is the transformation time, which we defined as the time required for the monocarbide/nitride phase to constitute 99.9% of the simulated domain. Furthermore, since diffusivity is an Arrhenius quantity we should expect that the calculated apparent

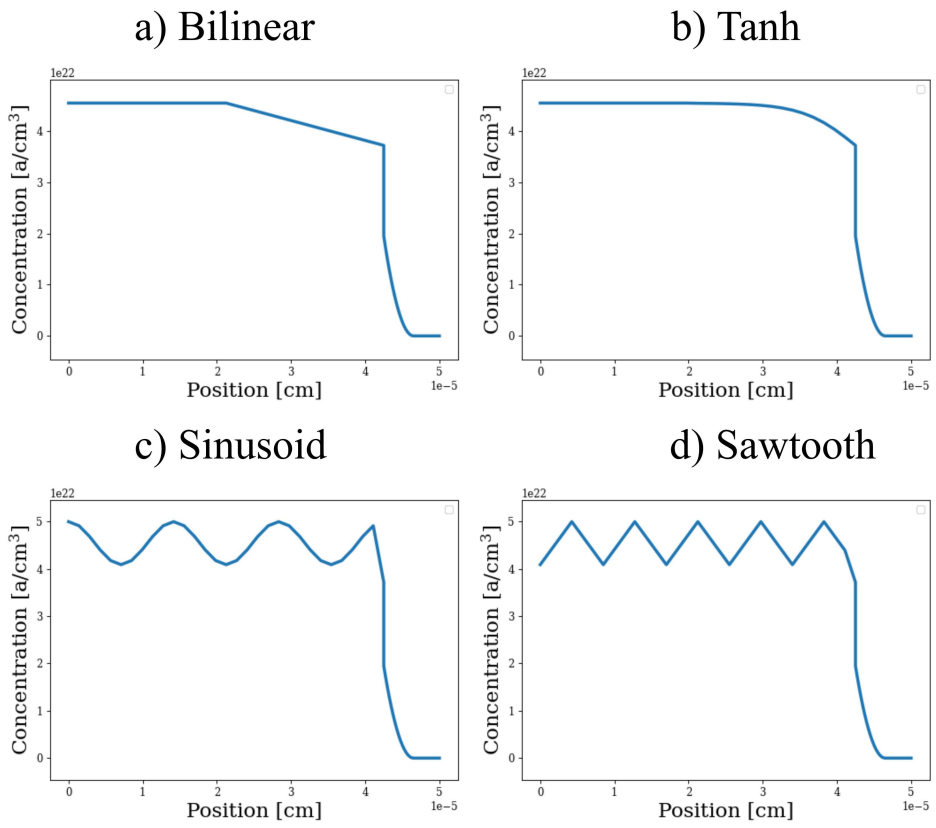

Figure 4.4: Examples of four of the initial concentration profiles used to investigate the effect of concentration profile shape on the apparent diffusivity that characterizes the phase transformation.

diffusivity should be as well. Figure 4.5 demonstrates that this is indeed the case, as the apparent diffusivity is shown to have a linear semi-log relationship with respect to inverse temperature.

As noted in the previous section, the mass error of the simulation is always known. Furthermore, the calculated diffusivity is a function of mass error since the amount of solute (carbon/nitrogen) is related to the driving force for the phase transformation. As a result, it should be possible to estimate the zero-error apparent diffusivity by extrapolation. Figure 4.6 demonstrates that the apparent diffusivity is a linear function of mass error and therefore the zero-error diffusivity can be easily determined by a small number of low computational cost simulations.

The extrapolation was carried out by first calculating the apparent diffusivity at multiple temperatures for a given number of finite element mesh nodes. Then, the process was repeated with a finer discretization, i.e. an increased number of nodes. The resulting diffusivity and average

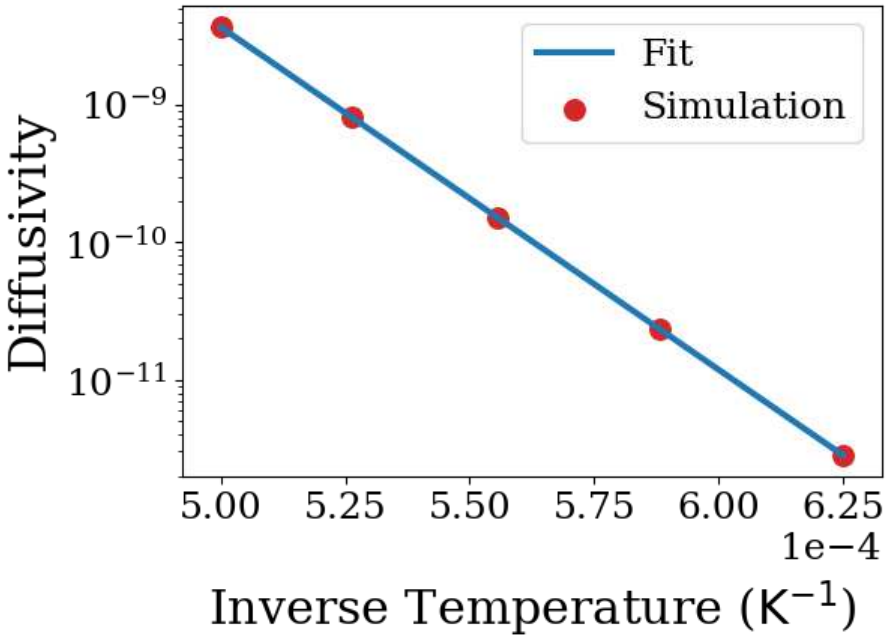

Figure 4.5: Semi-Log plot of the effective diffusivity vs inverse temperature of a ZrC/Zr lamellar composite. The linear fit indicates Arrhenius behavior.

mass error for each set of simulations was then used to construct a linear fit of the diffusivity as a function of mass error. The intercept of this fit was taken to be the zero-error diffusivity.

Finally, the Arrhenius behavior of the apparent activation energy can be exploited in order to calculate an apparent activation energy and diffusivity prefactor that characterize the kinetics of the phase transformation via Equation 4.5.

$$D^{app} = D_0^{\text{app}} \exp \frac{-Q^{\text{app}}}{k_b T} \tag{4.5}$$

Using this equation, we constructed plots depicting the relationship between the diffusivity prefactors and activation energies for carbon diffusion in the monocarbide phases and the apparent prefactor and activation energy determined by fitting the phase transformation. These plots are shown in Figures 4.7 and 4.8 and indicate that the apparent activation energy is approximately equal to the activation energy for carbon diffusion and that there is a linear relationship between the carbon diffusivity prefactor and the apparent diffusivity prefactor. Thus, if it is possible to

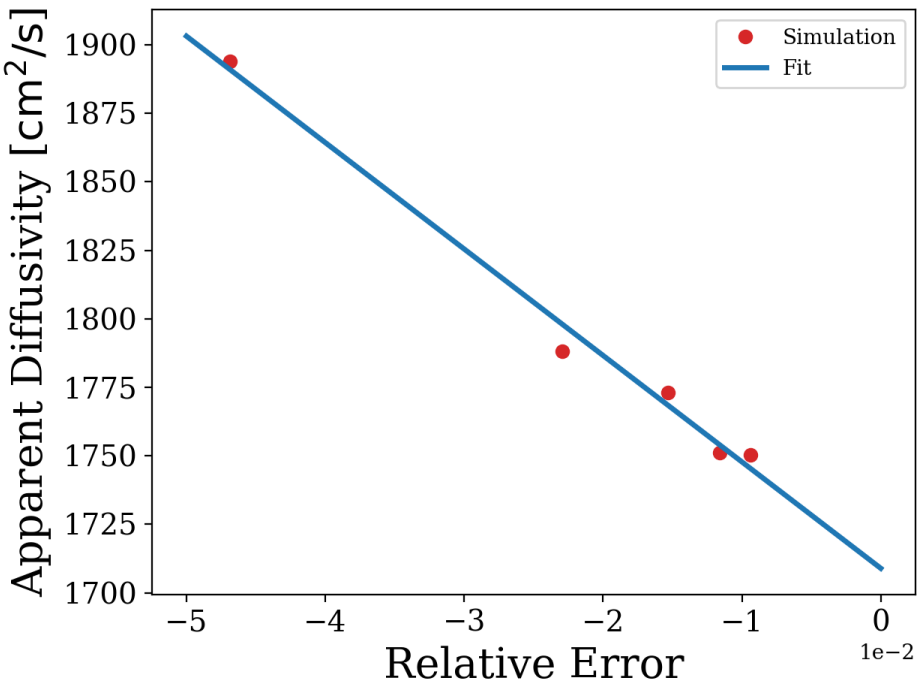

Figure 4.6: The apparent diffusivity plotted as a function of relative mass error. The figure demonstrates that there is a linear relationship between apparent diffusivity and mass error and therefore the zero-error diffusivity can be determined by extrapolation of data from low computational cost simulations.

establish the relationship between the apparent diffusivity prefactor and the diffusivity prefactor for carbon diffusion for a given composite geometry then the apparent diffusivity for the phase transformation and transformation time can hypothetically be determined without the need for direct simulation.

4.3 Results & Discussion

4.3.1 Zener Model

Before discussing the results of our FEM simulations, we will first derive an analytical expression for the evolution of the interface position as a function of time. This expression cannot be derived for the exact situation described previously; however, if we apply Dirichlet boundary conditions on either side of the ceramic phase (instead of the no-flux Neumann boundary conditions previously applied to the left side of the ceramic phase as shown in Figure 4.1) then the deriva-

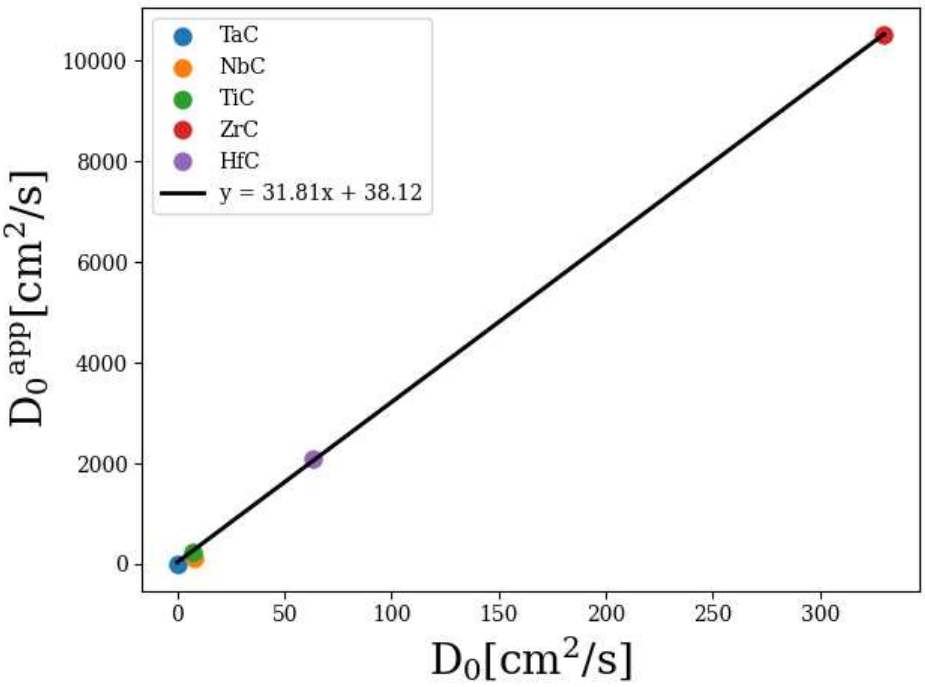

Figure 4.7: The apparent diffusivity prefactors plotted versus the diffusivity prefactor for carbon diffusion in the monocarbide phase. In contrast to the activation energies shown in Figure 4.8, the effective diffusivity prefactors are quite different from those for carbon diffusion but are linearly related.

tion (originally by Zener [90]), now representing the solution on a semi-infinite domain, is fairly straightforward.

Shown in Figure 4.9 is the schematic diagram of the layer growth. Our goal is to determine how the interface position x_i changes as a function of time in order to gain intuition on the factors that contribute to the rate of layer growth. Here, we have assumed that the metal phase is initially saturated with carbon/nitrogen in order to simplify the derivation by removing the carbon/nitrogen flux on the metal side of interface. The interface is assumed to be in chemical equilibrium with concentrations of C_γ and C_α on the ceramic and metal sides of the interface respectively. As mentioned previously, these equilibrium concentrations are enforced by Dirichlet boundary conditions in our FEM simulations. Far from the interface in the ceramic layer, shown on the left side of the diagram, the concentration is assumed to be fixed at a concentration of C_0. This assumption is the primary difference between the situation described here for the purposes of this derivation and of

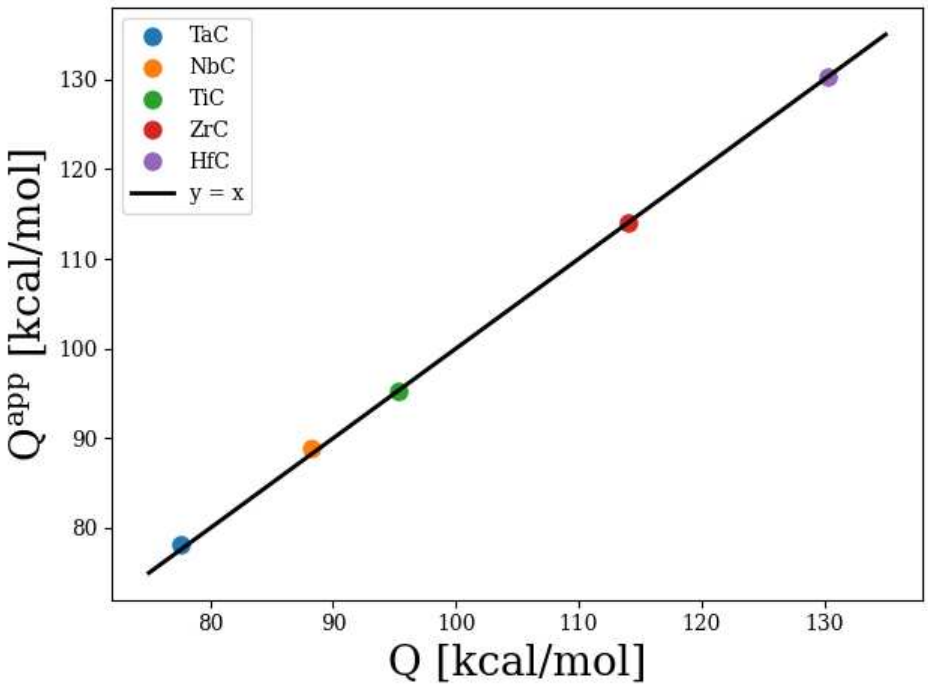

Figure 4.8: The calculated apparent activation energy for the composite phase transformation plotted against the activation energy for carbon diffusion in the monocarbide phase. The group IV composites have effective activation energies that match the carbon diffusion in the monocarbide. The group V composites have effective activation energies that are 0.79% (NbC) and 0.64% (TaC) larger than that for carbon diffusion in the monocarbide.

that in the FEM simulations, since in the FEM simulations the left side of the simulation domain contains a no-flux Neumann boundary condition.

To start, we will consider the condition of conservation of mass as the interface moves a distance dx_i in time dt. For mass to be conserved, the mass lost due to flux of carbon/nitrogen into the interface, which acts as a source/sink for carbon/nitrogen, must be equal to the mass gained by movement of the interface.

$$-D\frac{\partial c(x)}{\partial x}|_{x_i}dt = \Delta C dx_i \tag{4.6}$$

Rearranging for the interface velocity gives the following equation

$$\frac{dx_i}{dt} = v = -D\frac{1}{\Delta C}\frac{\partial c(x)}{\partial x}|_{x_i} \tag{4.7}$$

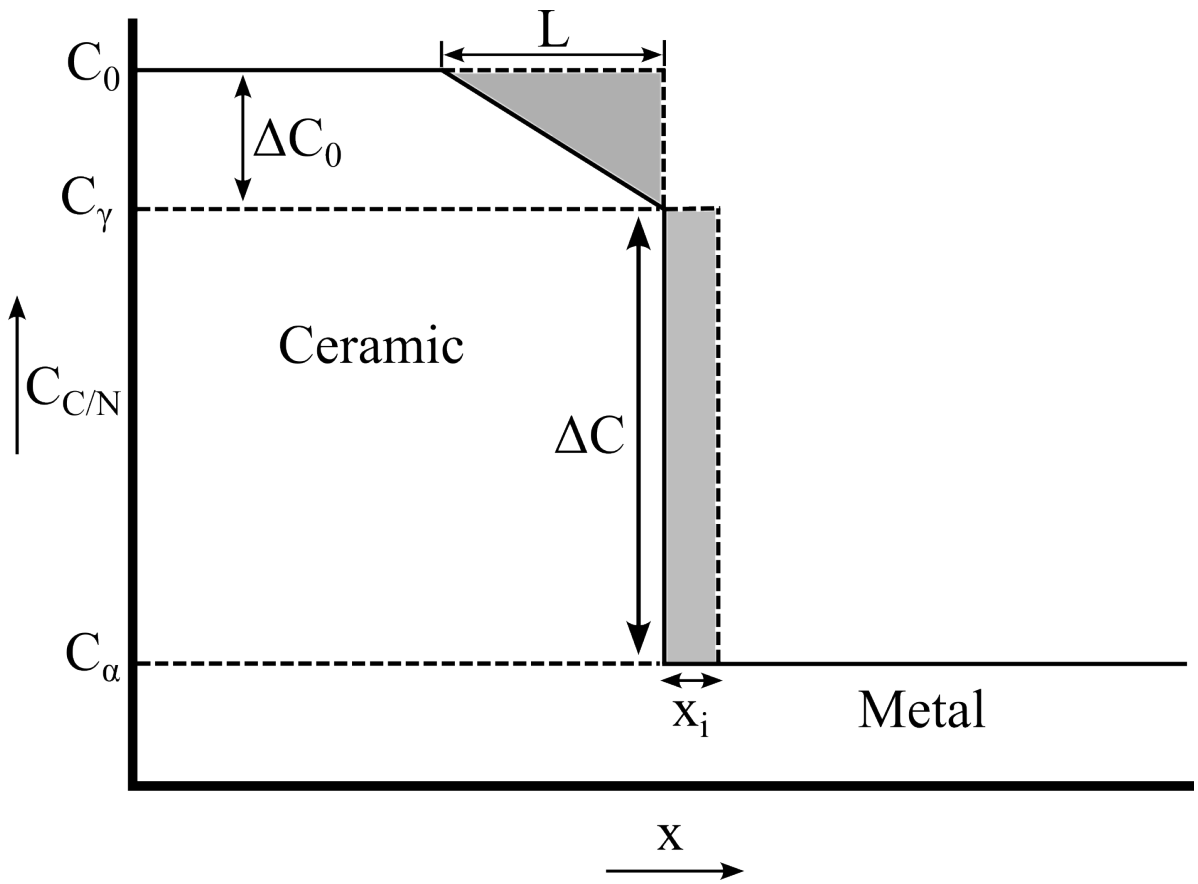

Figure 4.9: A schematic diagram of layer-growth on a semi-infinite domain.

The concentration gradient can be written $\frac{\partial c(x)}{\partial x}|_{x_i} = -\Delta C_0/L$, and L can be written as a function of the interface position by considering that the mass contained in the two shaded areas must be equal

$$\frac{L\Delta C_0}{2} = \Delta C x_i \tag{4.8}$$

and therefore $L = \frac{2\Delta C x_i}{\Delta C_0}$. Substituting this back into our velocity equation, we get

$$v = D\frac{\Delta C_0^2}{2\Delta C^2 x_i} \tag{4.9}$$

Rearranging, we can separate our variables for integration as follows

$$\int 2x_i dx_i = \int D\frac{\Delta C_0^2}{\Delta C^2} dt \tag{4.10}$$

and therefore the interface location as a function of time can be written as shown in Equation 4.11.

$$x_i(t) = \frac{\Delta C_0}{\Delta C}\sqrt{Dt} \tag{4.11}$$

There a several important things to note about this solution. First, and as previously mentioned, this solution represents the evolution of the interface on a semi-infinite domain with a fixed concentration far from the interface in the ceramic phase. Thus, the magnitude of the supersaturation ΔC_0 does not change as a function of time. As a result, it is expected that the interface velocity would be much greater in the semi-infinite case than in the periodic case described by our FEM simulations, since in the latter case the supersaturation term decreases as the phase transformation progresses. Secondly, we point out that this solution is entirely consistent with the existing knowledge about diffusion-controlled phase transformations. In other words, and as previously pointed out, for diffusion-controlled interface migration there is a parabolic relationship between length and time that is proportional to the diffusivity. Third, we point out that this exercise has revealed three primary factors that contribute to the kinetics of interface motion in our composites. First, the diffusivity in the ceramic phase. Second, the initial supersaturation ΔC_0 of the ceramic phase, and third, the magnitude of the concentration discontinuity at the interface ΔC. Finally, Figure 4.10 shows the interface position as calculated using the analytical expression shown in Equation 4.11 compared to that of an equivalent FEM simulation. The figure clearly shows, as expected, that the analytical expression over-estimates the interface velocity, and thus underestimates the annihilation time when compared to the simulation results.

We can gain further understanding of the kinetics by considering how long it would take to annihilate the metal phase in our semi-infinite example. We first consider that the distance the interface must move for the annihilation of the interface is equal to $\frac{\lambda(1-f)}{2}$ where f is the initial

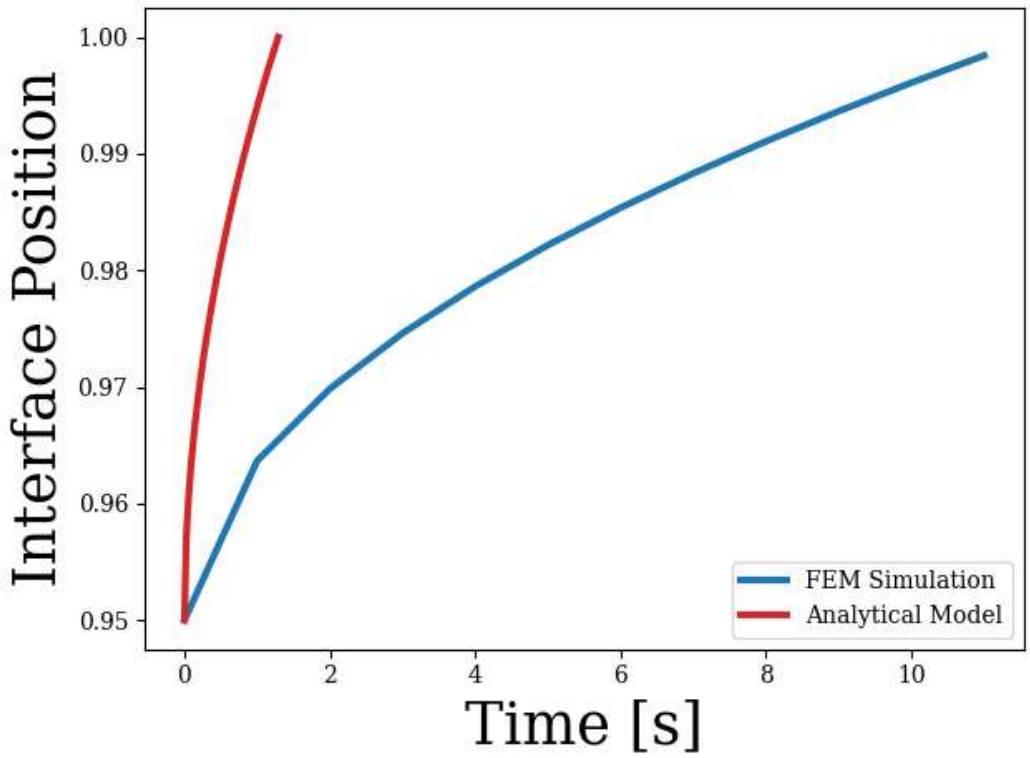

Figure 4.10: A comparison between the fractional interface position as a function time determined by Equation 4.11 (red) and the fractional interface position results determined by an FEM simulation (blue).

volume fraction of the ceramic phase and λ is the bilayer length of the composite. Thus, the time to annihilation τ can be determined by the following equation.

$$\frac{\lambda(1-f)}{2} = \frac{\Delta C_0}{\Delta C}\sqrt{D\tau} \tag{4.12}$$

Rearranging for τ, we find an analytical expression for the time required for the annihilation of the metal layer in the semi-infinite case, which reveals the form of the annihilation time of the composite with respect to its initial conditions.

$$\tau = \frac{(\lambda(1-f))^2\Delta C^2}{4D\Delta C_0^2} \tag{4.13}$$

4.3.2 FEM Simulation Results & Empirical Transformation Model

The simulations of the group IVB carbides naturally show the evolution of the two phases. An example profile from these simulations at different times is plotted in Figure 4.11. The simulations show that the metal phase quickly equilibrates, reaching a nearly uniform carbon concentration. In this sequence of profiles one can track how the carbide phase maintains a carbon concentration gradient that moves the interface until annihilation of the metal phase, shown in Figure 4.11d, and that the carbon concentration equilibrates in the single carbide phase after some time, as shown in Figure 4.11e.

In the simulations of the group VB carbides, the nucleation of a hemicarbide phase is provided, with that phase formation occurring immediately during the dynamics illustrated in Figure 4.12. What is interesting is that as the hemicarbide phase grows, both its interfaces move into the metal and monocarbide phases, meaning the monocarbide phase initially shrinks by as much as ten percent, as shown by Figure 4.12a. Eventually, the hemicarbide phase consumes the metal phase, Figure 4.12d. The monocarbide phase then consumes the hemicarbide phase, as shown in Figure 4.12e, and then equilibrates.

As previously mentioned, the apparent activation energy for the phase transformation is approximately equal to the activation energy for carbon/nitrogen tracer diffusion. Additionally, there is a

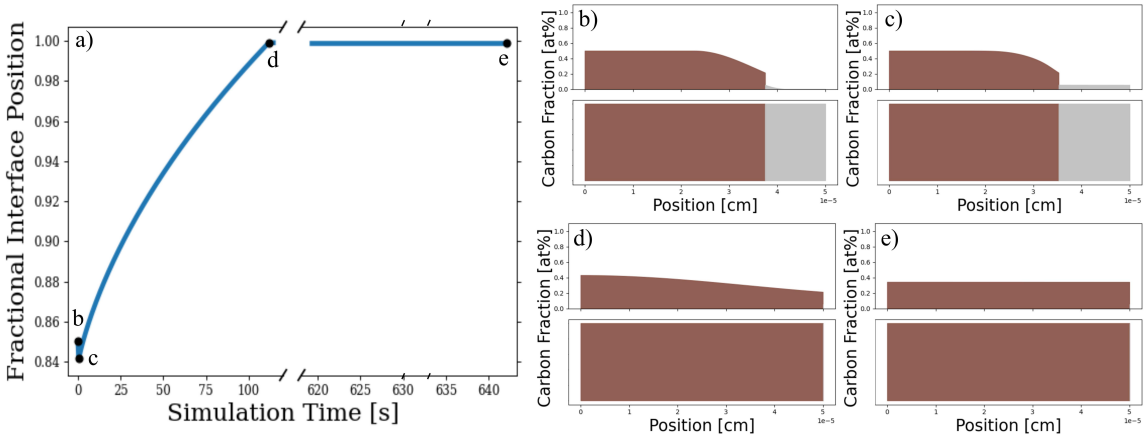

Figure 4.11: **a)** The fractional coordinate of the MeC/Me_2C interface over time. The points in time corresponding to the subplots b-e are marked. **b)** The initial carbon concentration profile for group IV phase transformations where the brown color represents the monocarbide phase and the grey color is the metal. The top illustrates the carbon concentration while the bottom simply shows the phase fractions. **c)** Shortly after the phase transformation begins the carbon concentration in the metal phase (silver) becomes nearly uniform **d)** annihilation of the metal phase, and **e)** after annihilation of the metal phase the carbon concentration in the monocarbide phase (brown) reaches equilibrium

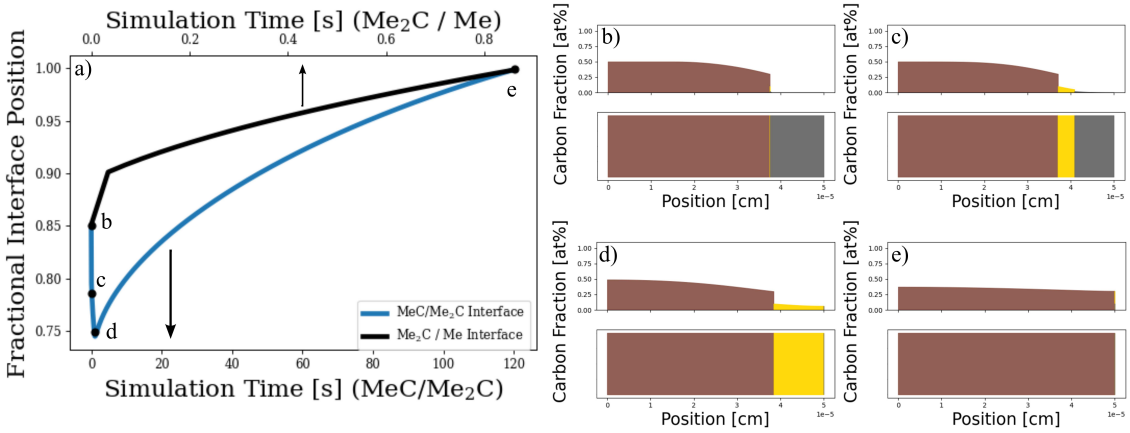

Figure 4.12: **a)** The fractional coordinate of the Me_2C/Me interface (black/top axis) and the MeC/Me_2C interface (blue/bottom axis) as a function of time. The points corresponding to the subplots b-e are marked. **b)** The initial carbon concentration profile for group V phase transformations, **c)** the hemicarbide phase (gold) nucleates at the interface between the monocarbide (brown) and metal (grey) phases and begins growing, **d)** the growth of the hemicarbide phase annihilates the metal phase ,and **e)** the monocarbide phase annihilates the hemicarbide phase

linear relationship between the prefactor for tracer diffusion and the apparent diffusivity prefactor that describes the phase transformation. This linear relationship can be written as shown in Equa-

tion 4.14 where $F(\chi_{\mathrm{TMC/N}}, f)$ represents a function of the initial conditions of the carbon/nitrogen composition profile in the monocarbide/nitride phase.

$$D_0^{app} = D_0^C F(\chi_{\mathrm{TMC/N}}, f) \tag{4.14}$$

Thus, if $F(\chi_{\mathrm{TMC/N}}, f)$ were known it would be possible to approximate the apparent diffusivity for an arbitrary MCM composite. This is the basis for the formulation of the following empirical transformation model. To begin, we postulate an approximate form for Equation 4.14 by noting that the apparent diffusivity must be related to the phase fraction of the monocarbide/nitride phase since as the initial phase fraction of the ceramic approaches unity the apparent diffusivity must diverge due to its relationship to the transformation time in Equation 4.5. Furthermore, it is reasonable to assume that the apparent diffusivity must depend on the size of the concentration discontinuity at the interface between layers, since this term appears in the denominator of Equation 3.19, which is used to determine the interface velocity in the FEM simulations. However, $\Delta\chi = \chi_{\mathrm{TMC/N}} - \chi_{\mathrm{Me}}$, and the $\chi_{\mathrm{TMC/N}}$ also appears in the determination of $f_{\min}$, so we choose to write $F(\chi_{\mathrm{TMC/N}}, f)$ instead of $F(\Delta\chi, f)$. Finally, we expect the 'supersaturation', χ_{ss} of the monocarbide/nitride phase to appear as well; however, this term can be considered effectively constant assuming that the composites initially contain a stoichiometric ceramic phase, which is most favorable.

To fit $F(\chi_{\mathrm{TMC/N}}, f)$ we conducted 489 FEM phase transformation simulations using the methodology described above with $0.55 < f \leq 0.95$, $0.25 < \chi_{\mathrm{TMC/N}} \leq 0.43$, and $0.21 \leq \chi_{\mathrm{TMC/N}} \leq 0.35$. For all simulations $\Delta\chi \geq 0.05$ and $f > f_{\min}$. For each combination of initial conditions three simulations were run and the apparent diffusivity prefactor and activation energy for the simulation were fit. Figure 4.13a shows a subset of the prefactor results of these simulations plotted with respect to f for three different values of $\chi_{\mathrm{TMC/N}}$. Similarly, Figure 4.13b shows a subset of the prefactor results plotted as a function of $\chi_{\mathrm{TMC/N}}$ for three different values of f.

Analysis of Figure 4.13a reveals the following trends in the behavior of the diffusivity prefactor: first, for each $\chi_{\mathrm{TMC/N}}$ the diffusivity appears to diverge towards infinity as $f \to 1$. This is an expected results, since as $f \to 1$ the composite's phase transformation essentially occurs infinitely

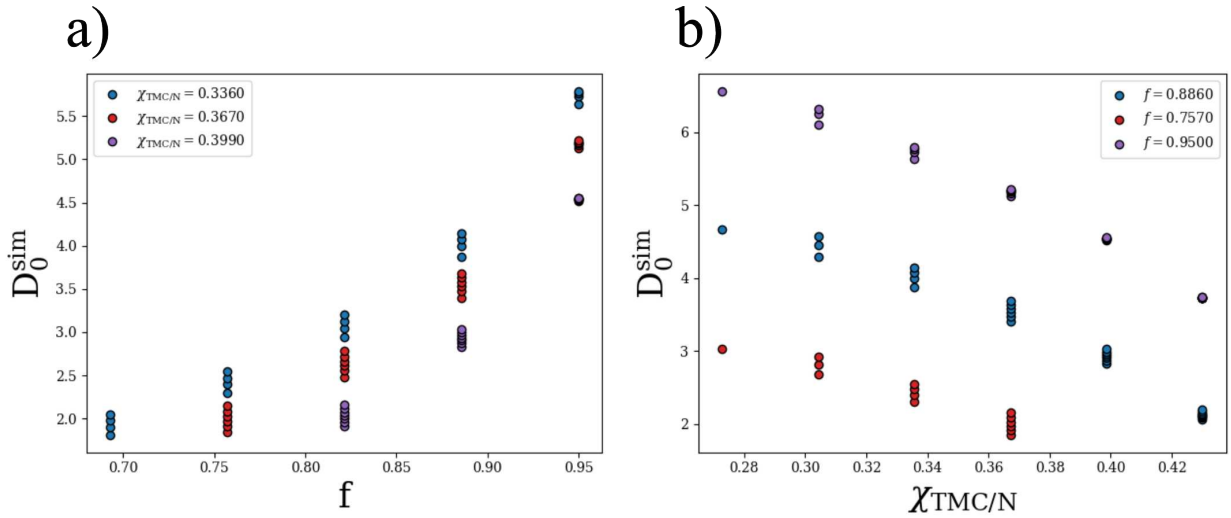

Figure 4.13: a) A subset of diffusivity prefactor results plotted as a function of the ceramic layer volume fraction f for $\chi_{\mathrm{TMC/N}} = 0.336(\mathrm{blue}), 0.367(\mathrm{red})$, and $0.399(\mathrm{purple})$. The data suggests that the diffusivity asymptotes as $f \to 1$ and goes to zero at some minimum value of f. **b)** A subset of diffusivity prefactor results plotted as a function of $\chi_{\mathrm{TMC/N}}$ for $f = 0.757(\mathrm{red}), 0.886(\mathrm{blue})$, and $0.950(\mathrm{purple})$. The data suggests that the diffusivity prefactor decreases linearly with increasing $\chi_{\mathrm{TMC/N}}$.

fast, since there is an infinitesimal metal layer volume fraction. Second, and in the other limit, we see that the diffusivity prefactor trends towards 0 at some value of f that appears to depend on $\chi_{\mathrm{TMC/N}}$. Using the priciple of mass conservation before and after the phase transformation, we identified that there is a minimum value $f_{\min} = \frac{\chi_{\mathrm{TMC/N}}}{1-\chi_{\mathrm{TMC/N}}}$ below which it is impossible for the phase transformation to complete. Thus, it is logical that we would see the diffusivity prefactor trend towards zero at this value.

Figure 4.13b suggests that the diffusivity prefactor decreases linearly as $\chi_{\mathrm{TMC/N}}$ increases. This result is somewhat surprising, since the interfacial velocity is inversely related to the size of the concentration discontinuity at the interface. However, the interfacial concentration discontinuity is not the only place where $\chi_{\mathrm{TMC/N}}$ appears in the kinetics. As discussed above, the minimum volume fraction $f_{\min} = \frac{\chi_{\mathrm{TMC/N}}}{1-\chi_{\mathrm{TMC/N}}}$ is solely dependent on $\chi_{\mathrm{TMC/N}}$ and heavily influences the driving force for the phase transformation, which appears to dominate over the contribution of ΔC to the kinetics.

From the trends identified in Figure 4.13, we can postulate a functional form of $F(\chi_{\mathrm{TMC/N}}, f)$ as shown in Equation 4.15 where the first term, $\left(\frac{f-f_{\min}}{1-f}\right)$ captures both limits of the behavior

shown in Figure 4.13a and the second term captures the behavior shown in Figure 4.13b. This functional form is essentially a pascals triangle constructed from the sums of powers of these two terms. To fit Equation 4.15, the exponents were allowed between 0 and 2, resulting in 9 total terms and a coefficient of determination $R^2 = 0.994$.

$$F(\chi_{\mathrm{TMC/N}}, f) = \sum_{i=0}^{2}\sum_{j=0}^{2} \alpha_{ij} \Big(\frac{f - f_{\min}}{1 - f}\Big)^{i} \chi_{\mathrm{TMC/N}}^{j} \tag{4.15}$$

To validate this empirical model, we compared its predicted diffusivity prefactors and transformation times to those determined from fits to simulation results. These comparisons are shown in Figures 4.14a and 4.14b respectively. The data in Figure 4.14a lies along the dashed line $y = x$, illustratrating the good fit between the model and simulation prefactor results. On the other hand, the transformation times shown in Figure 4.14b mostly lie below the dashed line, indicating that the model slightly underpredicts the transformation time, with a greater discrepancy for larger transformation times. This discrepancy is expected and understandable due to the fact that the model is fit to prefactor results and not the transformation times themselves. Additionally, the transformation time is a product of the diffusivity prefactor and an exponential factor containing the apparent activation energy. As a result, small difference between fit and simulation diffusivity prefactor results appear larger when transformed into transformation times. Regardless of these differences, the purpose of the empirical model is to generate order-of-magnitude estimates of the transformation time, which the model successfully accomplishes.

To further understand the sources of error in our model, Figure 4.15a and b shows the ratio $\frac{t_{\mathrm{fit}}}{t_{\mathrm{sim}}}$ as a function f and $\chi_{\mathrm{TMC/N}}$ respectively. In each case, there appears the ratio $\frac{t_{\mathrm{fit}}}{t_{\mathrm{sim}}}$ appears essentially constant at a value slightly less than unity, indicating that the size of the discrepancy between fit and simulation results is relatively independent of the initial conditions.

4.4 Summary & Conclusions

In this chapter of the dissertation, we have introduced a method for simulating the diffusion-controlled phase transformations of periodically arranged bilayers in a metal-ceramic multilayer

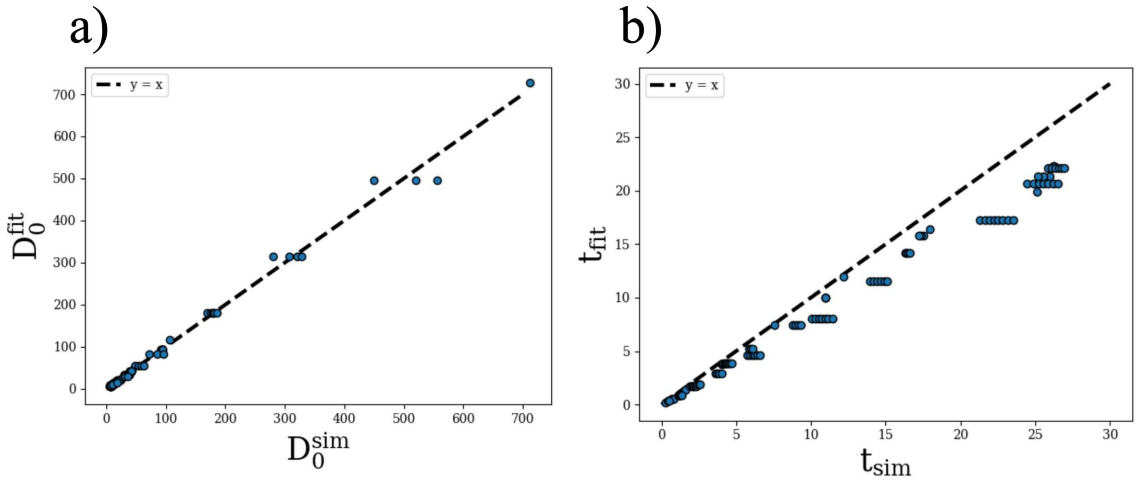

Figure 4.14: a) Comparison of diffusivity prefactors predicted from the fit to Equation 4.15 to the diffusivity prefactors determined by FEM simulations. **b)** Comparison of transformation times calculated using the diffusivity prefactors predicted by the fit to Equation 4.15 to those determined directly by FEM simulations.

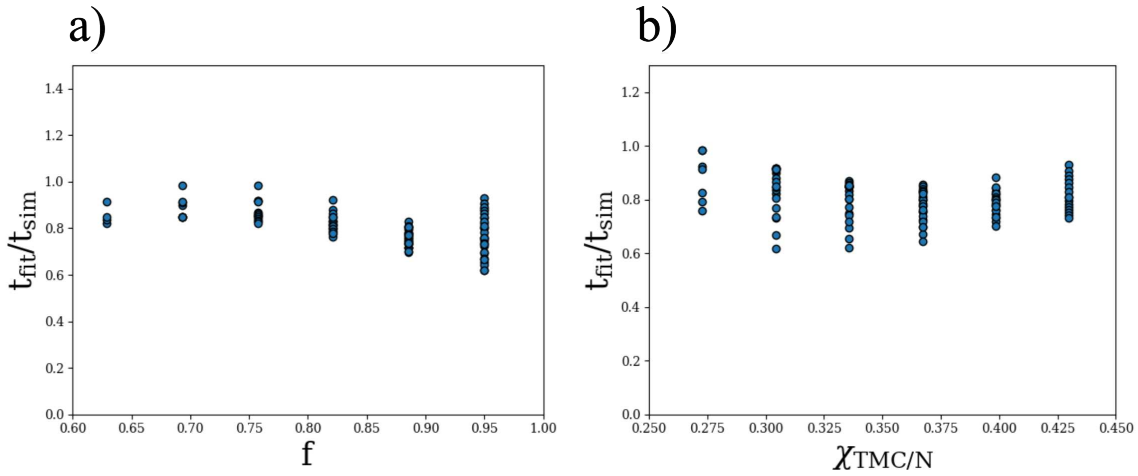

Figure 4.15: a) The ratio $\frac{t_{\text{fit}}}{t_{\text{sim}}}$ as a function of f. **b)** The ratio $\frac{t_{\text{fit}}}{t_{\text{sim}}}$ as a function of $\chi_{\text{TMC/N}}$

composite. To accomplish this, we used FEM simulations to simultaneously solve partial differential equations describing interstitial diffusion in each phase as well as the movement of interphase boundaries. One distinction from previous attempts to model similar phase transformations is the additional of a linear interpolation at each time step which has the effect of returning the finite element mesh to uniformity. In this approach, the accumulation of mass error is limited by preventing large concentration gradients from appearing near the interphase boundaries. Mass error

was further reduced using an extrapolation scheme which allowed the approximation of zero-error transformations.

From these simulations we observed the phenomenological behavior of the phase transformations in both the group IV and V transition metal carbides as well as the group IV nitrides. We observed that in the group V carbides and group IV nitrides there can be substantial backwards motion of the $\mathrm{MeC}/\mathrm{Me_2C}$ (or nitride) interface.

Furthermore, we used transformation time results from FEM simulations to parameterize an empirical model capable of predicting the apparent diffusivity prefactor as a function of the initial conditions of the carbon/nitrogen concentration profile. This empirical model takes as an input the carbon/nitrogen diffusivity in the ceramic phase as well as the initial phase fraction of the ceramic phase and the lower concentration phase boundary of the ceramic phase. Thus, using this model the apparent diffusivity for an arbitrary composite can be determined simply from thermodynamic and kinetic properties of the ceramic that are obtainable from the literature.

Chapter 5

Composition Dependence & Phase Transformations During Heating

5.1 Introduction & Background

In this chapter we will examine how the results of the finite element simulations presented in Chapter 4 are affected by slight modifications. First, we examine the results of simulations run with a non-constant temperature. In these simulations, the temperature changes with a constant rate. Second, we relax the assumption of a composition independent diffusivity.

In the first case, we perform phase transformations with a time-dependent temperature with the primary goal of determining how a constantly changing temperature affects the relationship between transformation time and bilayer length. We have seen from the literature [21, 23, 42, 44, 50–52, 56, 57, 91, 92] and the results presented in Chapter 4 that for phase transformations performed at a constant temperature there is a parabolic relationship between transformation time and bilayer length, which we have used to define and calculate an apparent diffusivity for the phase transformations. Here, with a time-dependent temperature, we are unable to use the same relationship, since increasing the temperature over time results in exponentially faster diffusion as the phase transformation progresses.

The purpose of this investigation is to model how these UHTC metal-ceramic multilayer composites will transform in an environment closer to that which might be seen in a real application. For example, it is proposed that these materials may be used as leading-edge coatings or structural components in hypersonic aircraft [11]. Within this application, it may be expected that the multilayers would undergo their phase transformation during flight, in which case they would experience an increasing temperature as aircraft speeds are increased. As another example, we might consider a component which, for reliability purposes, has been manufactured using the UHTC

metal-ceramic multilayer composite microstructure, but will be phase transformed in a furnace or using a torch prior to use. In some cases, the component may be placed in a furnace at ambient temperatures and allowed to heat up with the furnace. Here too, it may be useful to understand how changing temperature during the phase transformation process affects the transformation kinetics.

In the second case, we will modify the previous finite element approximation in order to relax the assumption of composition-independent diffusivities. This relaxation thus allows each element to have its own diffusivity rather than a single diffusivity for each phase, as was previously the case. Allowing each element to have a different, composition dependent, diffusivity provides the opportunity to gather a deeper understanding of the phase transformation kinetics. Primarily, we are interested in understanding whether the phase transformation kinetics will be limited by diffusion of carbon/nitrogen close to or far away from the interfaces and if the answer to that question depends on the direction of the diffusivity gradient. To accomplish this, we will perform simulations across a variety of temperatures and extract and apparent activation energy, similar to the process outlined previously in Chapter 4. Previously, we saw that this apparent activation energy was approximately equal to that for carbon/nitrogen diffusion in the ceramic phase. Many authors have observed this and concluded that it is due to solute diffusion from the bulk ceramic to the interface being the rate-limiting step in the kinetics. Here, we will be to directly assess these claims by comparing the apparent activation energy for the phase transformation to the composition-dependent diffusion activation energy.

5.2 Phase Transformations During Heating

Modification of the methodology used in Chapter 4 to implement a constantly increasing temperature was relatively straightforward. Each simulation was initialized at 273K and given as an inputs the bilayer width, diffusion activation energy in the ceramic layers, and a heating rate. At each time step the temperature of the simulation was adjusted according to the input heating rate and the diffusivity in each phase was recalculated according to the new temperature. At each time

step during the simulation, the diffusivities were determined according to Equation 5.1 where t is the simulation time, r is the heating rate, and T_0 is the initial temperature of the simulation.

$$D(t) = D_0 \exp\Big(-\frac{Q}{k_b(T_0 + tr)}\Big) \tag{5.1}$$

Shown in Figure 5.1a and 5.1b are the temperatures as a function of simulation time for 0.001m bilayer composites with $Q = 100$kcal/mol and $Q = 125$kcal/mol activation energies respectively. In each case, five different heating rates are shown and the temperature increases linearly with time due to the constant heating rate.

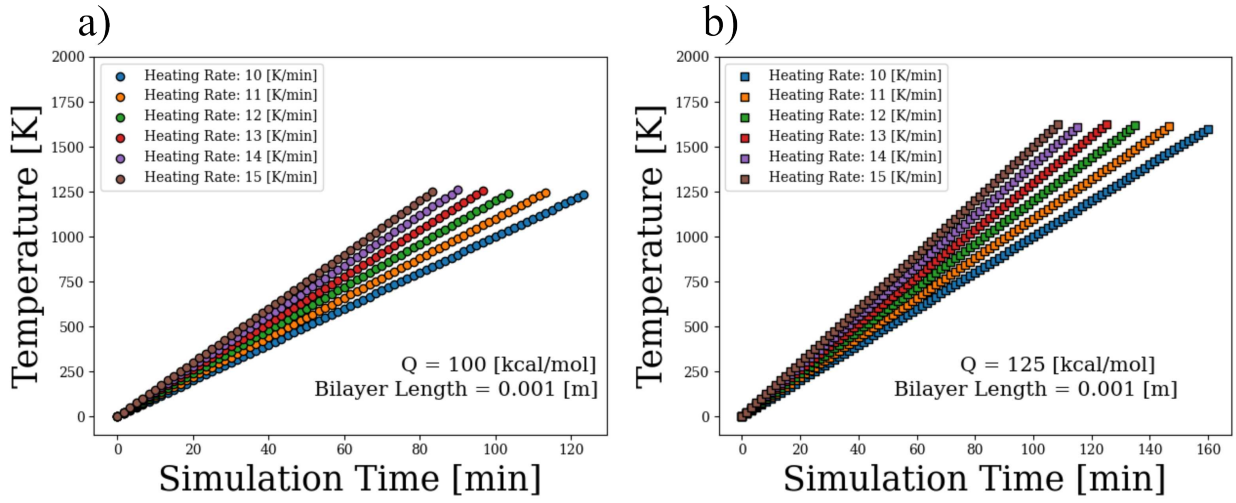

Figure 5.1: a) The simulation temperature versus time for 0.001m bilayer composites with an activation energy of $Q = 100$ kcal/mol **b)** The simulation temperature versus time for 0.001m bilayer composites with an activation energy of $Q = 125$ kcal/mol

Analysis of Figure 5.1 reveals an interesting feature of these simulations: for each heating rate the final temperature of the simulation is roughly equivalent. Additionally, we see that the final temperature is, at least in part, dependent upon the input activation energy for diffusion. The first result is somewhat surprising, since there is no intuitive reason to expect that the final temperature should all be the same. The dependence of this final temperature on the input activation energy; however, is unsurprising since we should expect that a greater temperature is required for the onset of the phase transformations with a larger diffusion activation energy.

Figure 5.2 shows the fractional interface positions over the course of the simulation for simulations with bilayer length $L = 5 \times 10^{-5}$m, and activation energy $Q = 100$ kcal/mol. Three simulations are shown with heating rates of $r = 5$ K/min (blue), $r = 10$ K/min (red) and $r = 15$K/min (purple). In each case, the simulation begins with a prolonged period wherein the interface motion is minimal. This initial period ends when the simulation temperature becomes sufficient for carbon/nitrogen diffusion, which we will refer to as the transformation onset temperature.

Figures 5.3a and 5.3b show the dependence of the transformation onset temperature as a function of diffusion activation energy in the ceramic phase and heating rate respectively. Figure 5.3a clearly demonstrates a direct linear relationship between the onset temperature and activation energy. This relationship makes intuitive sense, since we would expect that a greater activation energy would require a higher temperature before large-scale diffusion can take place. Figure 5.3b indicates a small dependence of the onset temperature on the heating rate as well, though the dependence is strongest for small heating rates and quickly goes to a constant value.

Recall that for simulations conducted at constant temperature there is a parabolic relationship between bilayer length, transformation time, and the apparent diffusivity that characterizes the phase transformation (Equation 4.4). In the case of a time-dependent temperature this relationship is no longer valid, since the diffusivity in each phase now contains a gradient in time. Despite this, it should still be possible to characterize the phase transformation using an apparent diffusivity prefactor D_0^{app} and activation energy Q^{app} as well as the initial temperature T_0 and the heating rate r.

To derive the new relationship we will modify our previous derivation of the composite layer growth. The composition profile for the derivation is the same as previously used in Chapter 4, Figure 4.9. We are interested in understanding how the position of the interface between the ceramic and the metal phase changes as a function of time. As before, we begin by considering mass conservation as the interface advances a distance dx_i in time dt. For mass to be conserved, the amount of mass lost due to flux into the interface is $-D\frac{\partial c(x)}{\partial x}|_{x_i}dt$ and the amount of mass

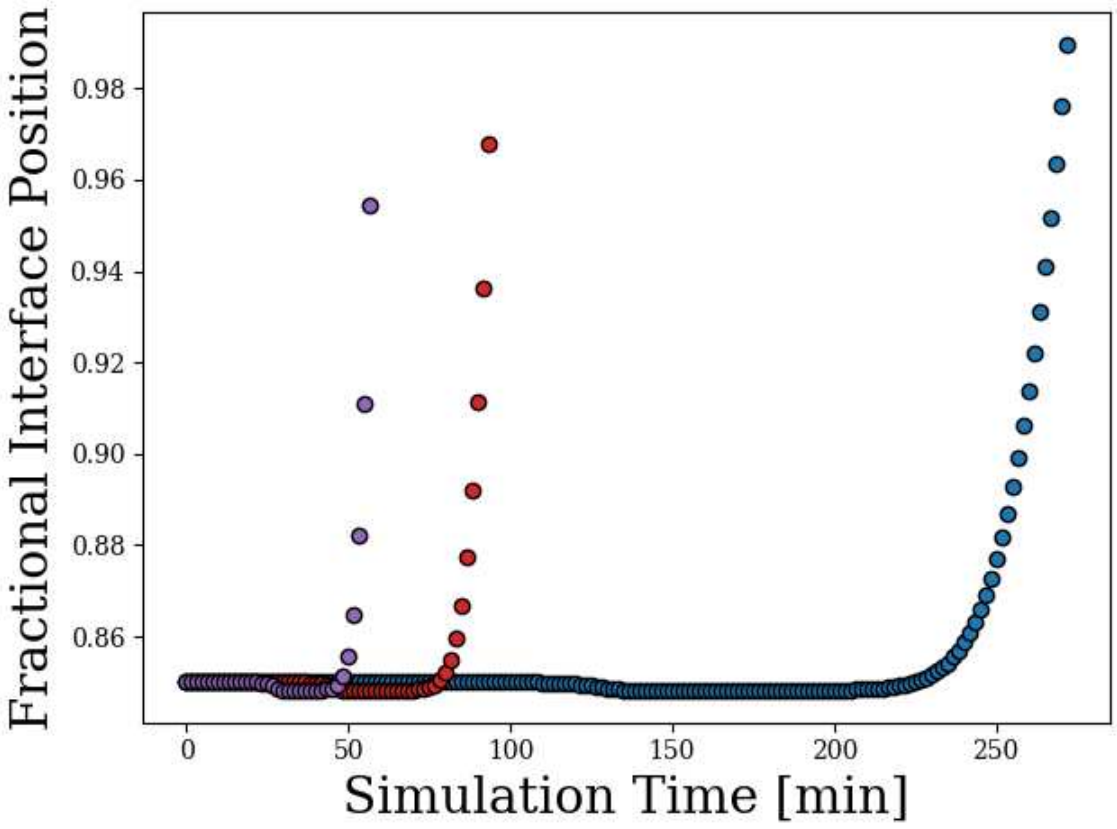

Figure 5.2: The interface positions for simulations run with bilayer length $L = 5 \times 10^{-5}$m, activation energy $Q = 100$ kcal/mol, and heating rates of 5 K/min (blue), 10 K/min (red) and 15 K/min (purple).

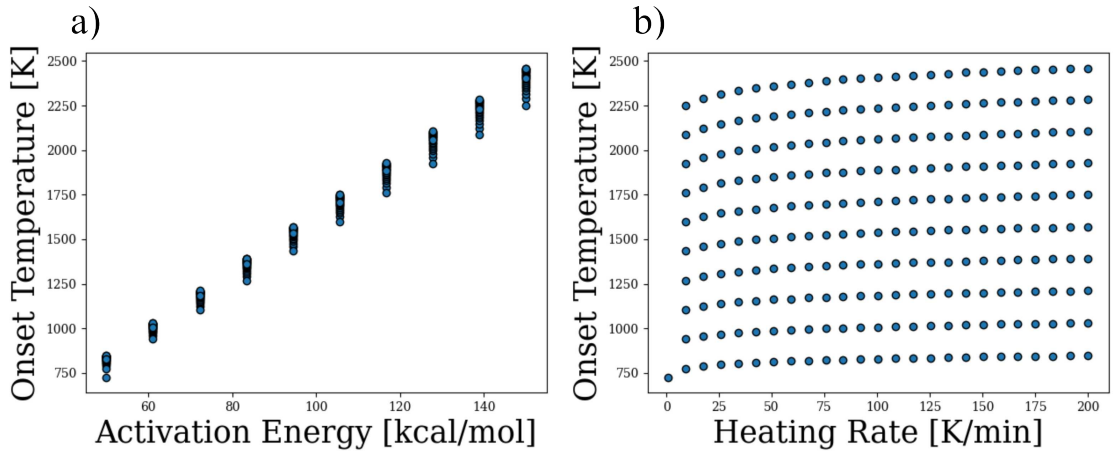

Figure 5.3: **a)** The onset temperature plotted as a function of the activation energy for carbon/nitrogen diffusion in the ceramic phase **b)** The onset temperature plotted as a function of the heating rate

gained due to interface motion is $\Delta C dx_i$. Thus, mass is conserved when these two quantities are equal as shown in Equation 5.13.

$$-D\frac{\partial c(x)}{\partial x}|_{x_i}dt = \Delta C dx_i \tag{5.2}$$

Rearranging Equation 5.13 for the interface velocity $v = \frac{dx}{dt}$, we arrive at the following equation

$$\frac{dx_i}{dt} = v = -D\frac{1}{\Delta C}\frac{\partial c(x)}{\partial x}|_{x_i} \tag{5.3}$$

which was previously shown to be equivalent to the following:

$$v = D\frac{\Delta C_0^2}{2\Delta C^2 x_i}. \tag{5.4}$$

Here, we implement our modification in order to consider a time-dependent temperature and, as a result, diffusivity $D(t) = D_0 \exp\Big(-\frac{Q}{k_b(T_0+tr)}\Big)$. Thus, the interface velocity can be written as

$$v = D_0 \exp\Big(-\frac{Q}{k_b(T_0+tr)}\Big)\frac{\Delta C_0^2}{2\Delta C^2 x_i}. \tag{5.5}$$

Integrating each side and rearranging for x_i, we arrive at an analytical form for the relationship between interface position and time as shown in Equation 5.6.

$$x_i = -\sqrt{D_0/2}\frac{\Delta C_0}{\Delta C}\sqrt{\int_0^\tau \exp\Big(-\frac{Q}{k_b(T_0+\tau r)}\Big)dt} \tag{5.6}$$

Combining the factors in front of the integral into a single fitting parameter D_0^{app} and carrying out integration we arrive at the relationship which will be used to characterize the phase transformations performed during heating with bilayer length λ, initial temperature T_0, and heating rate r. This relationship is shown in Equation 5.7 where Ei is the special function known as the exponential integral.

$$\lambda^2 = D_0^{\text{app}}\Big[\exp(-\frac{Q^{\text{app}}}{k_b(T_0+r\tau)})\frac{T_0+r\tau}{r} + \frac{Q^{\text{app}}}{k_b r}\text{Ei}(-\frac{Q^{\text{app}}}{k_b(T_0+r\tau)})\Big] \tag{5.7}$$

To further understand how this solution relates to the solution for a phase transformation at constant temperature we note that if the second term in Equation 5.7 is small and the $T_0 = 0$, then

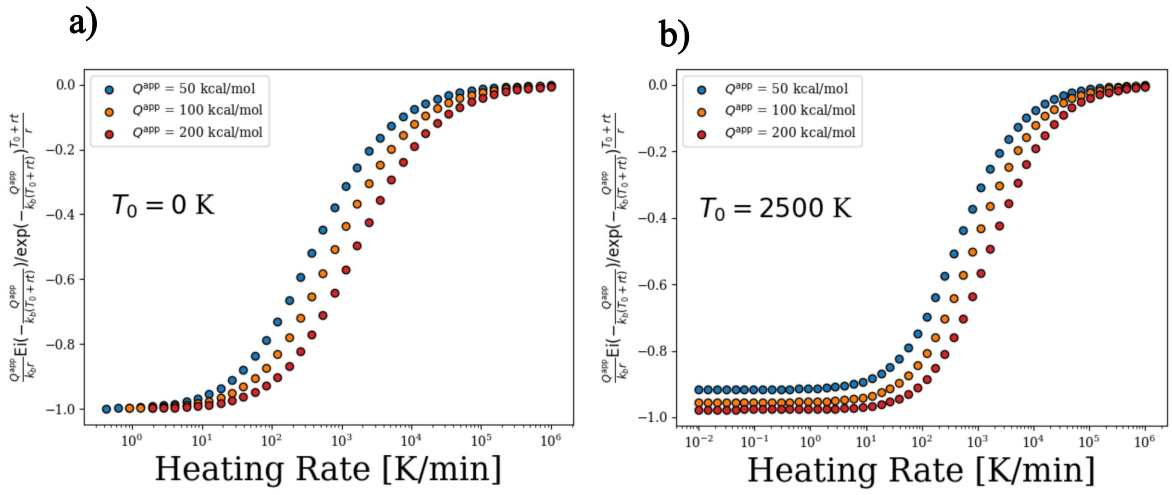

Figure 5.4: a) The ratio of the two terms in Equation 5.7 as a function of heating rate r with initial temperature $T_0 = 0$K. **b)** The ratio of the two terms in Equation 5.7 as a function of heating rate r with initial temperature $T_0 = 2500$K.

the solution is of the form as in the constant temperature case $\lambda^2 = D\tau$. Thus, it is important to know in which limits the second term is small compared to the first. To examine this, we plot the ratio of Ei term to the first term as a function of heating rate r across several orders of magnitude. These results, as shown in Figure 5.4a for an initial temperature of 0K and Figure 5.4b for an initial temperature of 2500K indicate that the ratio of these two terms is sigmoidal when viewed with a logarithmic scale on the heating rate. Thus, in the large heating rate limit we achieve kinetics that resemble a parabolic growth law once again, though we note that to achieve this effect heating rates exceed what is physically possible in any practical scenario.

Changing our attention now to the limit of low heating-rate r, we find that the ratio of these two terms goes to a constant value that appears to depend on the initial temperature T_0 as well as the apparent activation energy. To develop our understanding of this limit further we will consider the definition of the exponential integral $\mathrm{Ei}(u)$, shown in Equation 5.8 where u is the argument of the exponential integral.

$$\mathrm{Ei}(u) = \frac{e^u}{u}[1 + \frac{1!}{u} + \frac{2!}{u^2} + ...] \tag{5.8}$$

Inserting Equation 5.8 into Equation 5.7 with $u = -\frac{Q^{\text{app}}}{k_b(T_0+r\tau)}$ and leaving off the higher order terms we arrive at

$$\lambda^2 \approx D_0^{\text{app}}\Big[\exp(-\frac{Q^{\text{app}}}{k_b(T_0+r\tau)})\frac{T_0+r\tau}{r}+\frac{Q^{\text{app}}}{k_b r}\frac{k_b(T_0+r\tau)}{-Q}\exp(-\frac{Q^{\text{app}}}{k_b(T_0+r\tau)})[1-\frac{k_b(T_0+r\tau)}{Q}]\Big], \tag{5.9}$$

which can be simplified to Equation 5.10.

$$\lambda^2 = \frac{k_b(T_0+r\tau)^2}{Q^{\text{app}} r}D_0^{\text{app}}\exp(-\frac{Q^{\text{app}}}{k_b(T_0+r\tau)}) \tag{5.10}$$

When $T_0 = 0$ Equation 5.10 takes the form of Equation 5.11, where $T_f = r\tau$ is the temperature at which the phase transformation completes.

$$\lambda^2 \approx \frac{k_b T_f \tau}{Q^{\text{app}}}D_0^{\text{app}}\exp(-\frac{Q^{\text{app}}}{k_b T_f}) \approx \frac{k_b T_f}{Q^{\text{app}}}D^{\text{app}}\tau \tag{5.11}$$

Therefore, in the low heating rate limit too the functional form appears parabolic, though we note that additional temperature dependence is hidden in many of the parameters in Equation 5.11. Here, the diffusivity is calculated at temperature at which the phase transformation completes, but is modified by the unitless coefficient $\frac{k_b T_f}{Q^{\text{app}}}$ to account for the time spent at lower temperatures.

Examination of Equation 5.11 reveals another important quantity to consider: T_f, the final temperature of the simulation, in other words the temperature when the phase transformation completes. Table 5.1 shows the final temperatures for simulations conducted for each of the ceramics considered in this work. These temperatures were determined from simulations with an initial ceramic phase fraction $f = 0.85$, a heating rate $r = 10$ K/min, and diffusivities determined from Table 2.4.

Shown in Figure 5.5 are the transformation times of composites with activation energies $Q = 100$ kcal/mol as a function of bilayer length. The black lines indicate the fits of each piece of data to Equation 5.11. The r^2 scores from the fits were $r_5^2 = 0.999$, $r_{15}^2 = 0.989$, and $r_{25}^2 = 0.973$

Table 5.1: Final temperatures T_f for simulations conducted for each of the ceramics considered in this work. These temperatures were determined from simulations with an initial ceramic phase fraction $f = 0.85$, a heating rate $r = 10$ K/min, initial temperature $T_0 = 273$K, and diffusivities determined from Table 2.4.

Material	T_f [K]
TiC	1620
ZrC	1740
HfC	2060
TiN	1920
ZrN	2020
HfN	1170
NbC	1590
TaC	1610

for the 5 K/min, 15 K/min, and 25 K/min heating rate simulations respectively. It is interesting to note that the apparent activation energy determined by the fit is 99.27 kcal/mol and only 0.73 kcal/mol less than that of carbon/nitrogen diffusion in the ceramic phase. The difference is likely due to error in the fit, and probably indicates that the apparent activation energy for the case of a time-dependent temperature is approximately equal to that of carbon/nitrogen diffusion as we saw previously. Furthermore, when looking at the coefficients of determination we find that the quality of the fit appears to decrease as the heating rate r increases. This is consistent with the fact that Equation 5.11 was derived in the limit of a small heating rate and ignores the higher order terms.

Thus, in this section we have successfully developed simulations of the phase transformation process performed with a constant heating rate. Additionally, we applied kinetics theory to the case of layer growth on a semi-infinite domain in order to derive Equation 5.7, which related the bilayer length and transformation time using the idea of an apparent diffusivity characterized by a diffusivity prefactor D_0^{app} and apparent activation energy Q^{app}. By fitting our Equation 5.11 to the results of our FEM simulations we demonstrated that the derived equation correctly captures the kinetics present in our phase transformation. Furthermore, this equation reproduces parabolic growth, as is seen in constant temperature phase transformations in the limits of large and small heating rates.

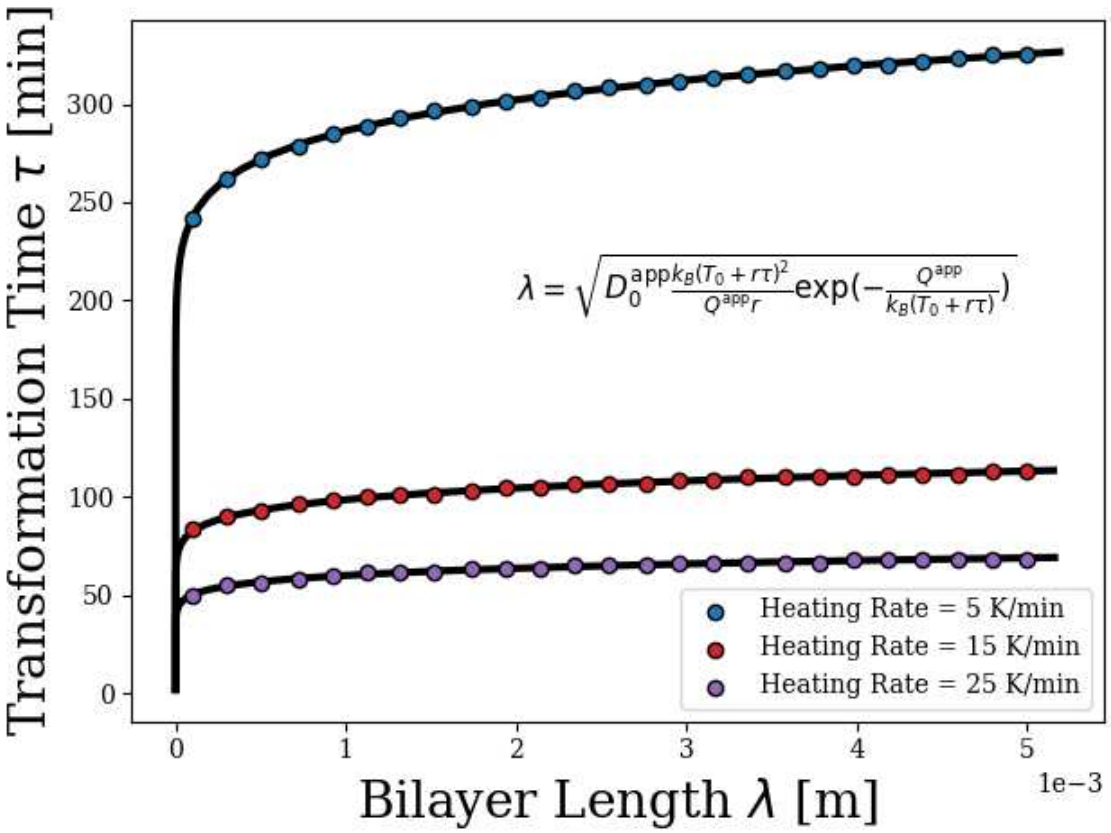

Figure 5.5: The transformation times of composites with activation energy $Q = 100$kcal/mol as a function of bilayer length. The black lines indicate the fits to each piece of data. The r^2 scores from the fits were $r_5^2 = 0.999$, $r_{15}^2 = 0.989$, and $r_{25}^2 = 0.973$ for the 5 K/min, 15 K/min, and 25 K/min heating rate simulations respectively.

5.3 Phase Transformations with Composition Dependent Diffusivities

In previous sections of this dissertation we have developed both analytical models and numerical simulations of the time evolution of the diffusion-controlled phase transformation that occurs in our novel MCM composites. In each case, we have shown that the apparent activation energy for the phase transformation is approximately equal to that of carbon/nitrogen diffusion in the ceramic phase. However, this is becomes complicated when we consider that in these ceramic materials the diffusivity is known to change as a function of carbon/nitrogen concentration. Thus, in some areas of the ceramic the diffusion activation energy may be larger. Classical kinetics theory would suggest that it is diffusion near the interface that controls the rate of the phase transformation; however, it is unclear if this remains true when there are large differences in the diffusivity within the ceramic phase.

To simulate a phase transformation where the diffusivity is not constant within each phase we must first derive the new governing equation, as the form of Fick's Second Law shown in Equation 4.2 assumes a constant diffusivity. To derive the new PDE governing diffusion in each phase, we will begin with the postulate that and therefore the diffusive flux of atoms moves down the concentration gradient with a rate proportional to its magnitude and therefore has the following form

$$J = -D(x)\frac{\partial c(x,t)}{\partial x} \tag{5.12}$$

From here, Fick's Second Law can be derived by considering the conservation of mass using the following continuity equation, which simply states that any change in mass must be due to the flux of atoms into or out of the surface.

$$\frac{\partial c(x,t)}{\partial t} = -\nabla \cdot J = \frac{\partial}{\partial x}\big(D(x)\frac{\partial c(x,t)}{\partial x}\big) \tag{5.13}$$

Now that we have derived the appropriate PDE, we can reconstruct our FEM model. To begin, we start by writing the weak form of Equation 5.13 over a single element.

$$\int_{\Omega} \Big[V(x)[\frac{\partial}{\partial x}\big(D(x)\frac{\partial c(x,t)}{\partial x}\big) - \frac{\partial c(x,t)}{\partial t}]\Big]dx = 0 \tag{5.14}$$

Using integration by parts this becomes

$$V(x)D(x)\frac{\partial c(x,t)}{\partial x}\Big|^{\Omega} - \int_{\Omega} D(x)\frac{\partial V(x)}{\partial x}\frac{\partial c(x,t)}{\partial x}dx - \int_{\Omega} V(x)\frac{\partial c(x,t)}{\partial t}dx = 0 \tag{5.15}$$

Again, we will choose linear trial (hat) functions:

$$\Psi_1(x) = \frac{x_q - x}{h}, \Psi_2(x) = \frac{x - x_p}{h} \tag{5.16}$$

where h is the element length and therefore our composition profile can be written as

$$c(x,t) = \sum_{j=1}^{2} c_j(t)\Psi_j(x) \tag{5.17}$$

and our weighting function is

$$V(x) = \Psi_i(x) \tag{5.18}$$

Using these relations, the weak form solution becomes

$$\Psi_i(x)D(x)\frac{\partial c(x,t)}{\partial x}\Big|_{\Omega} - \int_{\Omega} D(x)\sum_{j=1}^{2} c_j(t)\frac{\partial \Psi_i(x)}{\partial x}\frac{\partial \Psi_j(x)}{\partial x}dx - \int_{\Omega}\sum_{j=1}^{2}\Psi_i(x)\Psi_j(x)\frac{\partial c_j(t)}{\partial t}dx = 0 \tag{5.19}$$

As with before, we want our solution in the matrix form

$$K_{ij}c_j + M_{ij}\dot{c_j} = F_i \tag{5.20}$$

And with the non-constant diffusivity only the stiffness matrix K_{ij} is changed. The single-element stiffness matrix becomes

$$k_{ij} = \int_{x_p}^{x_q} D(x) \frac{\partial \Psi_i(x)}{\partial x} \frac{\partial \Psi_j(x)}{\partial x} dx, \tag{5.21}$$

and considering the case of $i = 1$ and $j = 1$

$$k_{11} = \int_{x_p}^{x_q} D(x)(-1/h)(-1/h)dx = \frac{1}{h^2} \int_{x_p}^{x_q} D(x)dx \tag{5.22}$$

Now, inserting the integral definition of the average of a function $\overline{f}(x) = \frac{1}{b-a} \int_a^b f(x)dx$ over the interval $[a, b]$

$$k_{11} = \frac{\overline{D}(x)}{h} \tag{5.23}$$

Repeating this for the other values of i and j we find the general equation for k_{ij}.

$$k_{ij} = \frac{\overline{D}(x)}{h} \begin{vmatrix} 1 & -1 \\ -1 & 1 \end{vmatrix} \tag{5.24}$$

Importantly, if we reintroduce our previous assumption of a constant diffusivity, then Equation 5.24 reduces back to Equation 3.12 which was derived previously. Moving on to the element mass matrix and force vector, we can see from Equation 5.19 that they are unchanged from those derived in Chapter 3. Thus,

$$m_{ij} = \int_{x_p}^{x_q} \Psi_i(x)\Psi_j(x)dx = \frac{h}{6} \begin{vmatrix} 2 & 1 \\ 1 & 2 \end{vmatrix} \tag{5.25}$$

and the global force vector is zero everywhere except where the boundary conditions are enforced.

In our previous FEM simulations, we demonstrated first-order scaling of the mass error accumulated during a simulation with the number of elements used in the discretization of the simula-

tion domain. Figure 5.6 demonstrates that this scaling remains after the changes to the governing PDE are introduced.

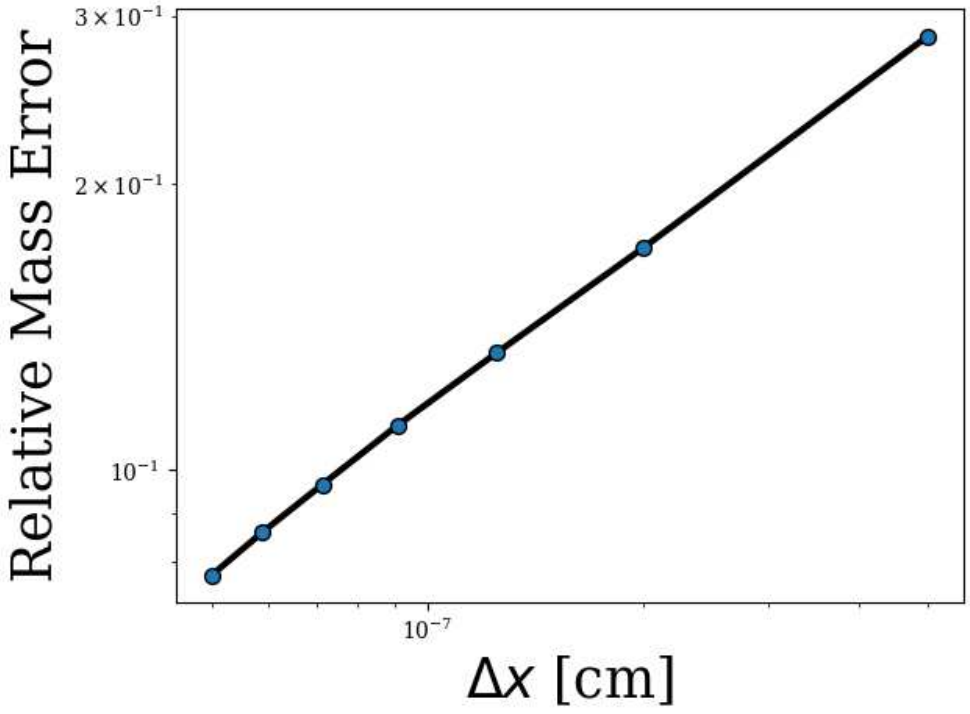

Figure 5.6: A log-log plot of simulation mass error versus the element length Δx used in the discretization of the simulation domain. The approximately linear relationship demonstrates first-order scaling of the mass error.

In order to implement the variable diffusivity each node in the ceramic phase was given a diffusivity. During each simulation time step the diffusivity of each node was recalculated according to its current carbon/nitrogen atomic fraction χ. We used two different models to calculate the diffusivity, one which resulted in a greater activation energy at low atomic fractions, and another which resulted in a greater diffusivity for larger atomic fractions. These diffusivity calculations were determined by Equations 5.26 and 5.27 respectively.

$$D(\chi) = D_0 \exp(-\frac{100 - 115(\chi - 0.37)}{k_B T}) \tag{5.26}$$

$$D(\chi) = D_0 \exp(-\frac{85 + 115(\chi - 0.37)}{k_B T}) \tag{5.27}$$

The purpose of these diffusivity models are to provide two different cases to inform our analysis of the physics of the phase transformation. In Equation 5.26 the largest activation energy occurs when $\chi = 0.37$, which was the value of χ at the lower phase boundary of the ceramic phase in these simulations. Thus, using Equation 5.26 to calculate the diffusivity resulted in fast diffusion far from the interface and the slowest diffusion at the interface. The opposite is true for the simulations conducted with diffusivity calculations done according to Equation 5.27, wherein the slowest diffusion happened far from the interface and the fastest diffusion was at the interface.

To determine whether it is diffusion near or far from the interface we first plot the apparent activation energy for each of our activation energy models. As shown in Figure 5.7, simulations run with diffusivities calculated according to Equation 5.26 (blue) resulted in an apparent activation energy of $Q_{5.26} = 93.48$ kcal/mol and simulations run with diffusivities calculated according to Equation 5.27 (red) resulted in an apparent activation energy of $Q_{5.27} = 88.89$ kcal/mol. These apparent activation energies correspond to $\chi \approx .444$ and $\chi \approx .465$ respectively.

In the case of Equation 5.27, it is simple to show that this apparent activation energy must arise due to diffusion near the interface. As shown, in Figure 5.8, the large activation energy for diffusion far from the interface, *i.e.*, on the left side of the simulation domain, results virtually no change in composition over the course of the simulation. Thus, the region where large changes in the composition profile are present is near the interface. This gives the concentration profile a much different shape than we are used to seeing in the case of a constant diffusivity. In this case, the composition profile has is convex, rather than concave.

Furthermore, by examining the time average of the left and right quarters of the simulation domain we can gain a better understanding of the kinetics. Shown in Figure 5.9 are the time averages of the left quarter of the domain (red) and right quarter of the domain (blue). It can be seen that the average composition in the left quarter remains virtually unchanged as a function of time. Taking the time average of the average composition in the left quarter and using it in

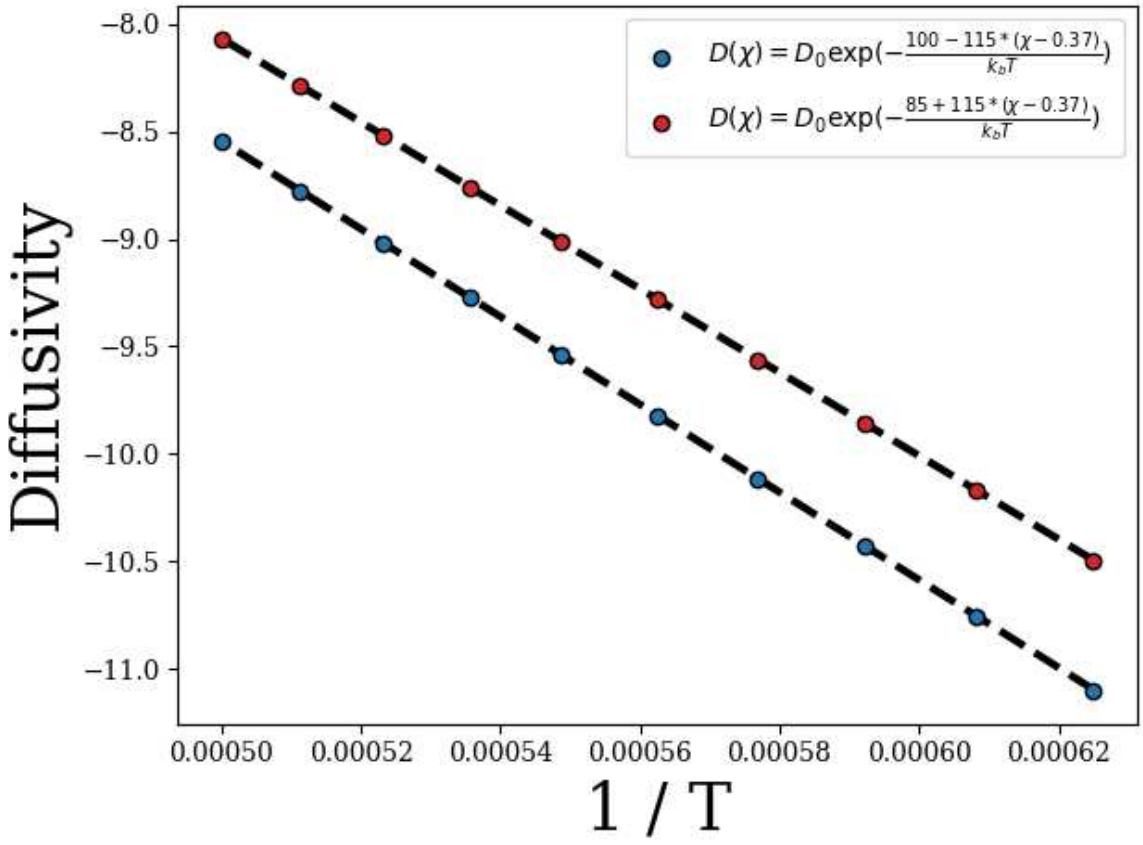

Figure 5.7: An Arrhenius plot depicting diffusivity versus inverse temperature for each of the activation energy models

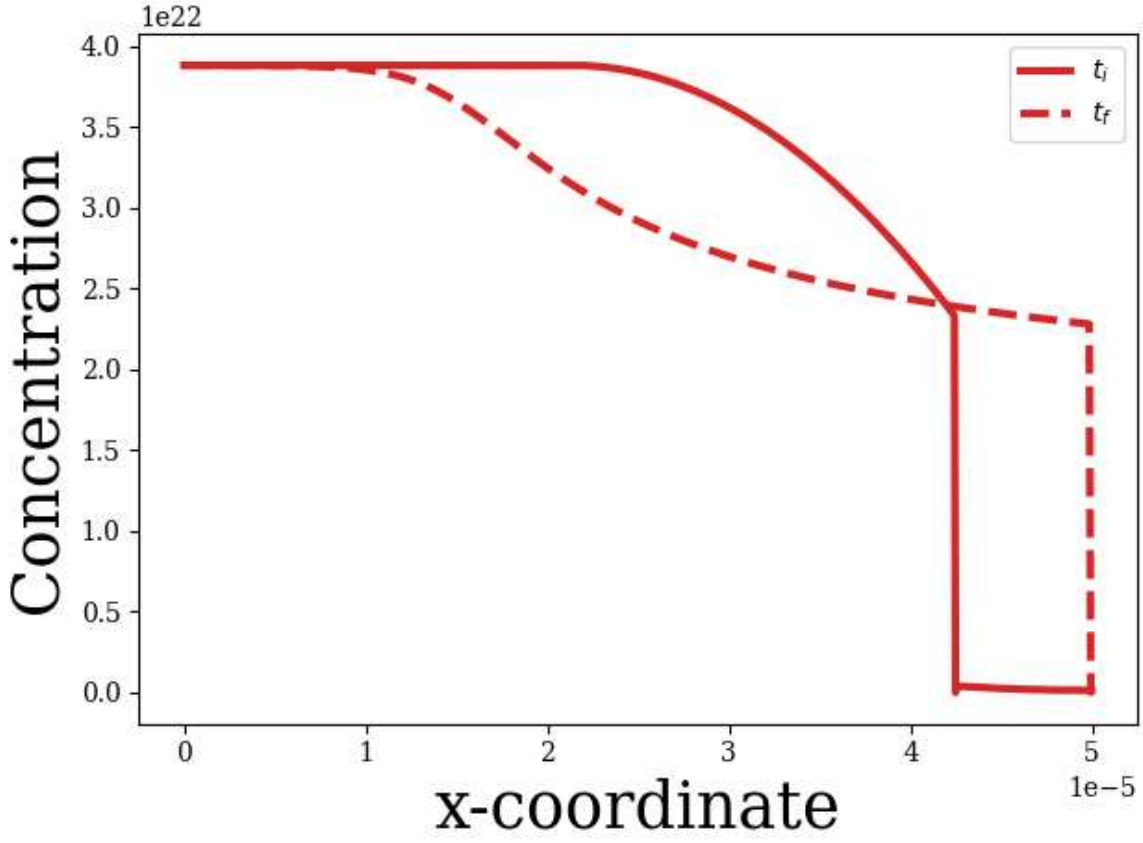

Figure 5.8: The initial and final composition profiles of the phase transformation performed using diffusivities calculated according to Equation 5.27. Unlike simulations run with a constant diffusivity, the final composition profile is convex as a result of the high activation energy for diffusion far from the interface.

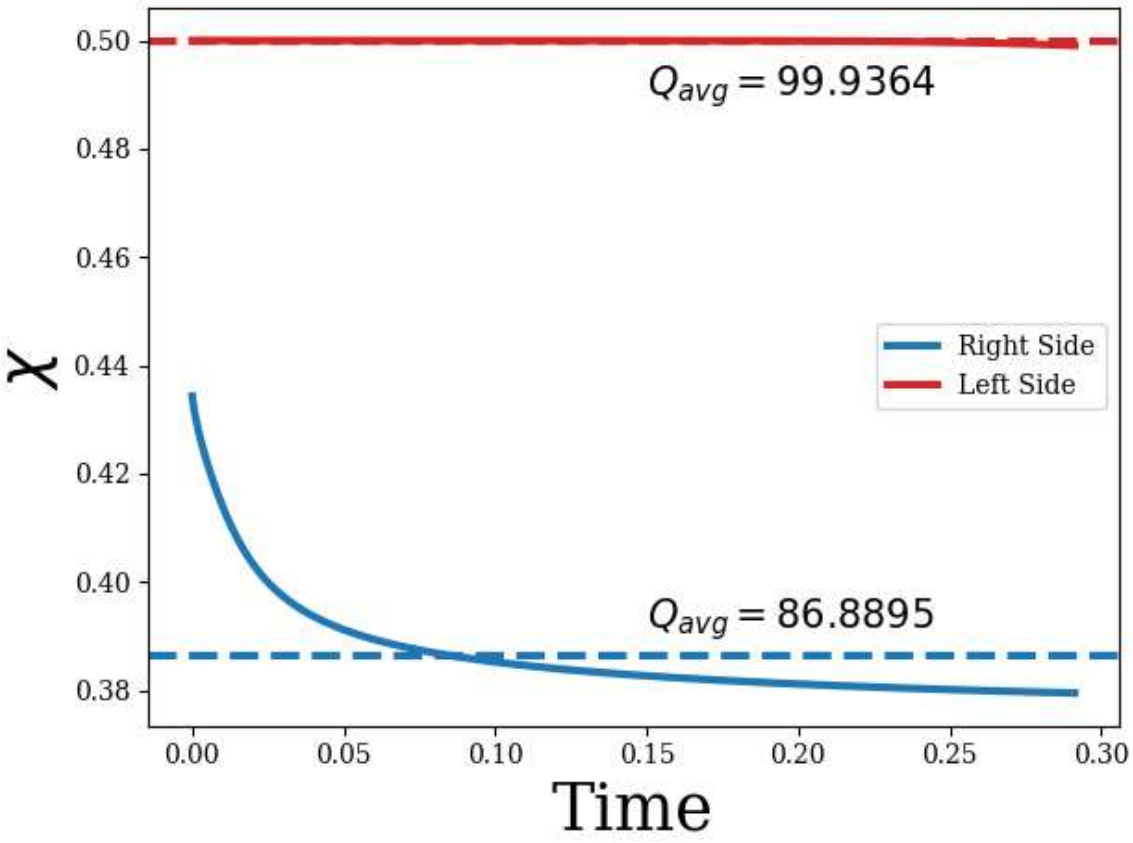

Figure 5.9: Average compositions in the left (red) and right (blue) quarters of the ceramic phase as a function of time for a representative simulation conducted with Equation 5.27.

Equation 5.27 indicates that if diffusion far from the interface, *i.e.*, in the bulk, were dominating then the apparent activation energy would be close to 100 kcal/mol. Applying the same analysis to the average composition of the right quarter of the domain indicates that if diffusion in this region were controlling the phase transformation then the apparent activation energy would be approximately 86.89 kcal/mol. Thus, from this we can conclude that when there is a larger activation energy for diffusion far from the interface it is diffusion near the interface that controls the phase transformation.

Now turning our attention back to simulations conducted with diffusivities calculated according to Equation 5.26, we can attempt to apply the same analysis. Shown in Figure 5.10 are the initial and final composition profiles of a representative simulation. Here, we can see that as in the case of a constant diffusivity, the final composition profile is concave. Additionally, we see that the

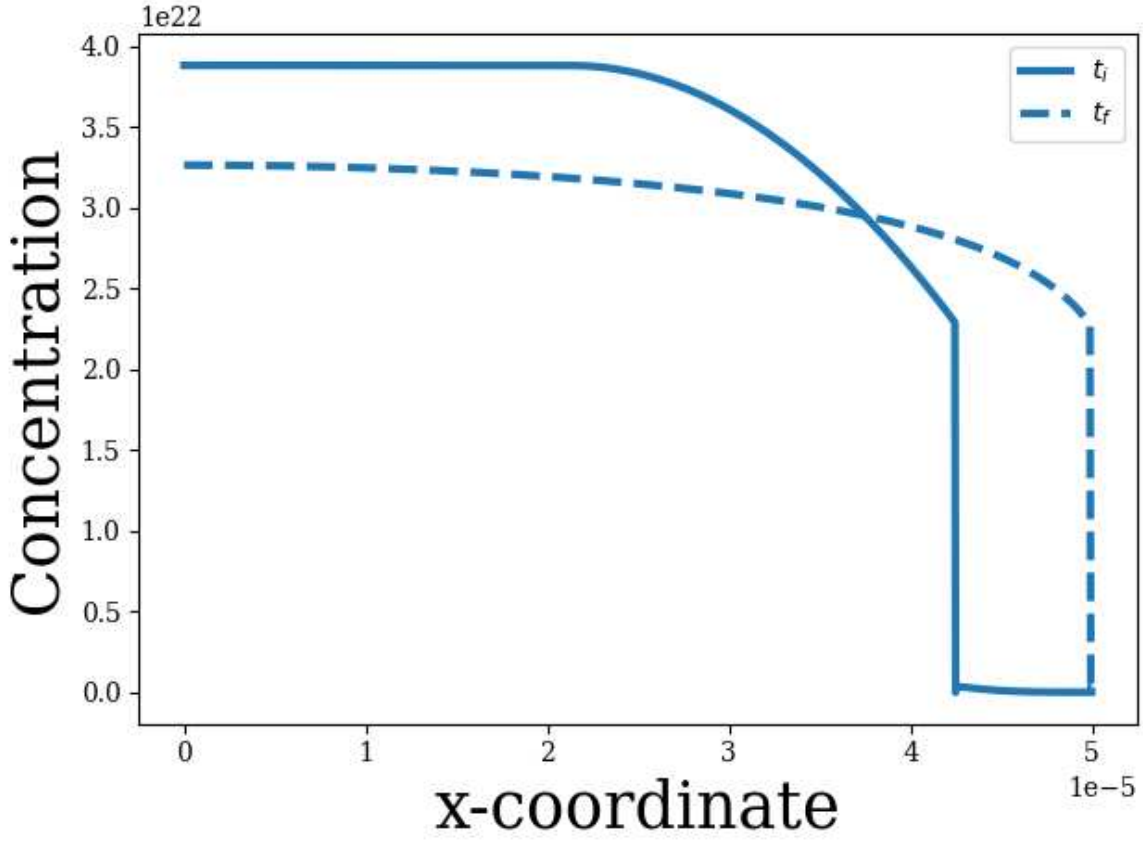

Figure 5.10: The initial and final composition profiles of the phase transformation performed using diffusivities calculated according to Equation 5.26. As with simulations run with a constant diffusivity, the final composition profile is concave.

composition far from the interface has dramatically changed over the course of the simulation. Thus, it is more difficult in this case to determine whether it is diffusion near or far from the interface that is controlling the phase transformation.

If we again examine the time averages of the average composition in the left (red) and right (blue) quarters of the ceramic phase, as shown in Figure 5.11, we find that if interface motion were controlled by diffusion far from the interface then the apparent diffusivity would be approximately 88.20 kcal/mol whereas if it were controlled by diffusion near the interface the apparent diffusivity would be approximately 93.73 kcal/mol. Thus, since the latter case agrees well with the value determined from the apparent activation energy calculation from Figure 5.7, there is substantial evidence that the interface motion is controlled by diffusion near the interface.

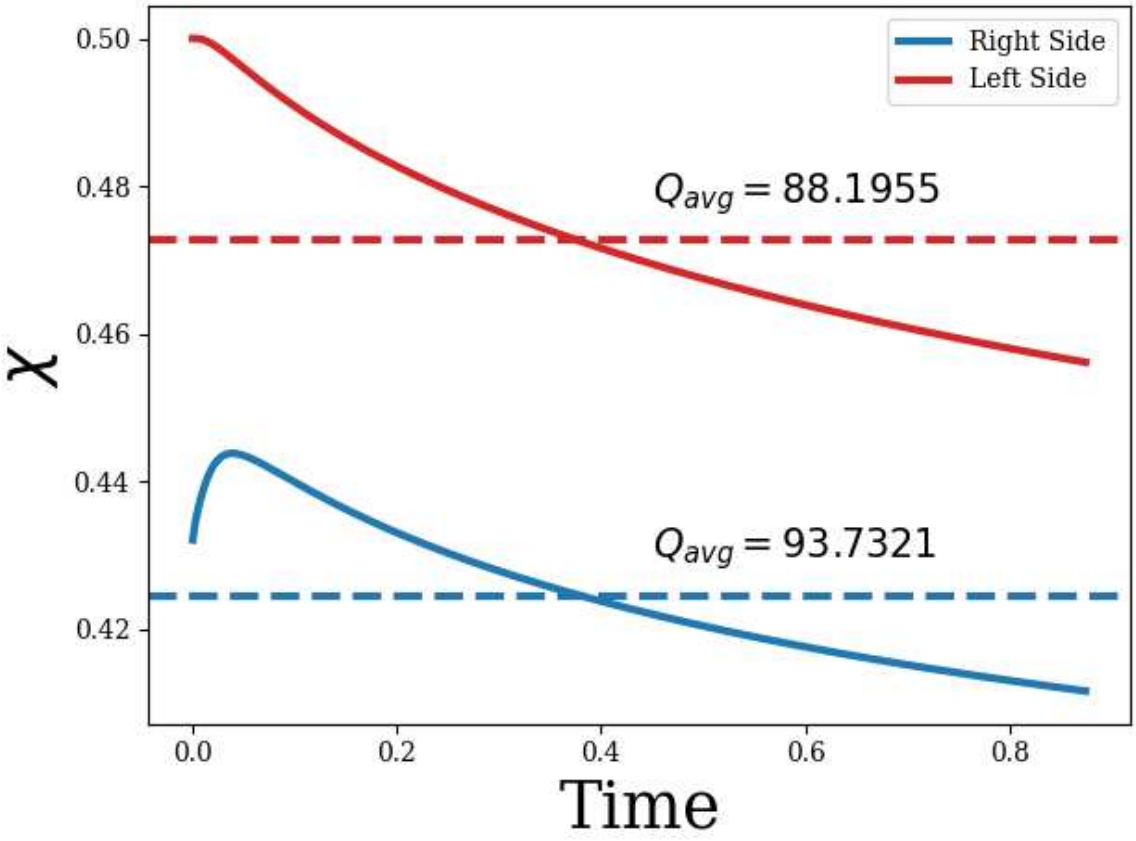

Figure 5.11: Average compositions in the left (red) and right (blue) quarters of the ceramic phase as a function of time for a representative simulation conducted with Equation 5.26.

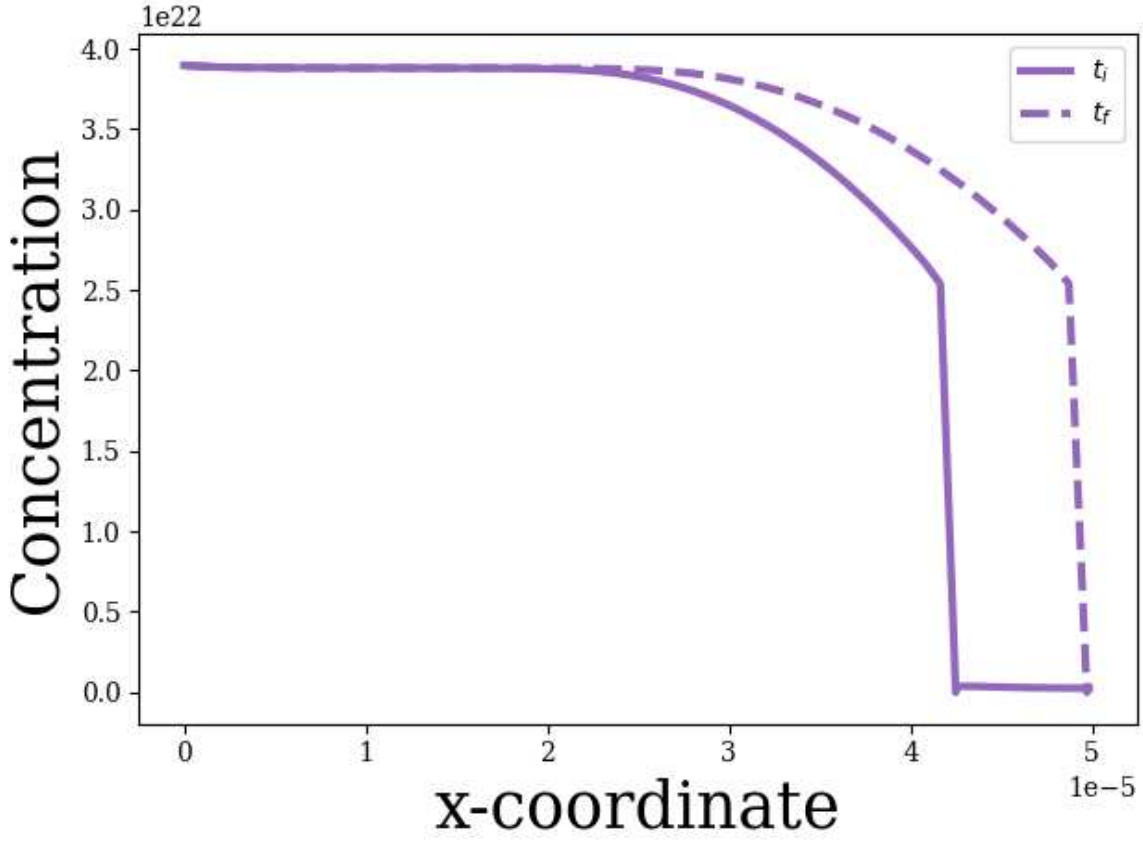

Figure 5.12: The initial and final composition profiles of the phase transformation performed using diffusivities calculated according to Equation 5.26 and with a constant composition boundary condition applied to the node on the left side of the simulation domain.

To make this claim more concrete we can change the boundary condition at the left side of simulation domain such that the concentration remains fixed far from the interface. Shown in Figure 5.12 are the initial and final concentration profiles of the ceramic phase in this case. Here, the problem represents a phase transformation on a semi-infinite domain where the concentration is fixed far from the interface and the diffusivities are calculated via Equation 5.26. Here, we can see with the constant concentration boundary condition applied the composition far from the interface no longer changes. Thus, we can conclude that in this case the apparent diffusivity must be due to diffusion near the interface. In this case, the apparent diffusivity for the phase transformation was calculated to be 92.43 kcal/mol.

To summarize, in this section we sought to determine whether interface motion was controlled by diffusion near or far from the interface. Classical kinetics theory suggests that all diffusion-controlled phase transformations are controlled by diffusion near the interface; however, it is unclear if this would remain true when the diffusivity changes as a function of composition, especially in the case where diffusion far from the interface has a high activation energy. In the latter case, one might argue that the phase transformation would be controlled by the region space which has the smallest average diffusivity, *i.e.*, the largest activation energy for diffusion.

Here, we examined two cases, one where there was a large activation energy near the interface, and another where the largest activation energy ocurred far from the interface. In each case we were able to show that the apparent activation energy for the phase transformation was approximately equal to that of diffusion near the interface, regardless of whether or not this region had the highest activation energy.

Chapter 6

Composite Design & Materials Selection

6.1 Introduction & Background

Ultra-high temperature ceramics are a class of materials with exceptionally high melting temperatures and impressive high-temperature properties such as strength, ductility, moderate oxidation resistance, and creep resistance. Despite this, the lack of fracture toughness near ambient temperatures makes manufacturing and assembly of UHTC components difficult.

Several strategies have been used to increase a ceramic's resistance to fracture, including transformation toughening, ductile phase toughening, and fiber reinforced composites. Unfortunately, many of these reinforcement methods are generally limited to relatively low temperatures around 1500K due to oxidation or are otherwise limited by difficulty in processing [93]. Historically, the UHTC industry has solved the issue of low temperature brittleness via the introduction of UHTC fibers/whiskers to the matrix, making UHTC ceramic matrix composites (UHTCMCs) [94]. In these composites, toughening and graceful failure are provided by the introduction of the fibers; however, fabrication of UHTCMCs can be challenging, leaving room for alternative solutions.

One solution to the latter problem is to construct metal ceramic multilayer composites which can be processed more easily than ceramic matrix composites. These composites are constructed from alternating layers of metal and ceramic, *e.g.* Me/MeC, and toughening is provided by the addition of the ductile metal phase, *i.e.*, ductile phase toughening. Here, the ductile phase absorbs energy as the crack propagates as well as providing crack bridging due to the presence of in tact ligaments within the crack wake. Engineered multilayer systems including Al/Al_2O_3 [30, 95–97], Nb/Nb_3Al [98], Co/WC [99] and others [100–105].

Additionally, toughening in layered materials has been the subject of numerous studies. For example, He *et al.* studied the mechanics of crack growth in layered materials and found that there are two primary factors responsible for toughening: interface debonding and metal layer

width [95]. In the first case, they found that interface decohesion elevates both the crack initiation resistance K_N, which is the initial fracture resistance on the resistance curve, as well as the steady-state fracture resistance K_{ss} achieved after sufficient crack extension. In cases of a well-bonded interface the primary source of toughening came from bridging due to the metal layers with K_{ss} increasing as a function of metal layer width.

Shaw *et al.* narrowed their focus in on the renucleation of cracks across metal layers and found that the cracking behavior was dominantly dependent upon the metal layer phase fraction and thickness [96]. They performed crack-growth experiments on notched Al/Al_2O_3 composites with no signs of interfacial debonding. Both K_N and K_{ss} were seen to increase as a function of metal layer width. In addition, substantial plastic deformation of metal layers were observed and crack renucleation appeared to occur on the same plane as the notch in the specimen.

Flinn *et al.* performed fracture experiments on Al/Al_2O_3 with emphasis on the mechanics of bridging of ductile ligaments as well as controlled interfacial debonding. They found that the primary source of toughening in bridged composites came from energy dissipation due to plastic deformation of the bridging ligaments between the cracked surfaces. Additionally, they developed a theoretical model for crack bridging assuming that the tractions imposed upon the crack surfaces obeyed a linear softening law of the form $\sigma_b = \sigma_c(1 - u/u_c)$ where σ_b is the bridging traction, σ_c and u_c are constants to be determined by experiment, and u is the crack tip opening displacement (CTOD). Comparison of this model with measurements of work of rupture indicated that σ_c and u_c were key material parameters.

Evans and Meeking investigated crack bridging in ceramics reinforced by bridging of well-bonding particles and whiskers [99]. Though this investigation did not directly study layered materials, the bridging mechanism for layered materials is similar to that of whiskers. The primary findings of this investigation were that it is vital for reinforcements to avoid fracture at the crack tip in order to provide toughening. Fracture of bridging ligaments can be avoided via two mechanisms. First, debonding between the bridging ligament and the matrix can occur such that stresses are alleviated within the bridging ligament and it remains intact. Second, the bridging ligament

must have a sufficiently high modulus compared to the matrix such that the stress intensity is reduced below the critical threshold. One or both of these conditions are sufficient for successful reinforcement by bridging.

Tomaszewski *et al.* [106] investigated interfacial slip and debonding in Al_2O_3/$LaPO_4$ composites and found that the work of rupture in these composites was extremely high as a result of crack deflection at weak Al_2O_3/$LaPO_4$ interfaces. Work of rupture was reported to be 36.2J/m^2 and 4.7J/m^2 for monolithic Al_2O_3 and $LaPO_4$ respectively whereas the work of rupture was reported to be 11700J/m^2 for the Al_2O_3/$LaPO_4$ composite. Crack propagation was deflected perpendicularly to the laminate plane leading to energy dissipation associated with the creation of free surfaces as the interface delaminates. Interestingly, the work of fracture was reported to increase with decreasing layer thickness.

Other authors have conducted similar investigations as well, such as Bloyer *et al.* who examined the fracture toughness and resistance-curve behavior of $\mathrm{Nb}/\mathrm{Nb_3Al}$ layered composites as a function of layer width and layer orientation with respect to the direction of crack-growth and found that they were able to model the resistance curve behavior by assuming a uniform traction across the bridging zone [98]. Similarly, Chen *et al.* measured the mechanical properties such as strength and hardness of $\mathrm{Ni}/\mathrm{Al_2O_3}$ composites at different metal and ceramic layer thicknesses and found that the steady-state fracture toughness increased with reinforcement layer thickness [107]. Kruzic *et al.* investigated the effects of plastic constraint on the fatigue behavior of metal ceramic multilayer composites and found that for monotonically increasing loads the fracture toughness increased with metal layer thickness; however, for cyclic loads the driving force for crack growth decreased with metal layer thickness [100]. In more modern studies, layer widths have been reduced to the nanoscale in order to achieve codeformation of ceramic layers, as demonstrated in the Al/TiN system [108, 109].

Fracture resistance is heavily dependent upon the specimen geometry and is therefore not an intrinsic material property. As a result, if specimen dimensions are too small then effects due to

large-scale bridging can be present. This increases the fracture resistance and often prevents the onset of steady-state fracture [110].

In the present chapter, we outline several design strategies for UHTC metal-ceramic multilayer composites with the ability to phase transform. Of primary concern are the limitations to ceramic phase fractions, the relationship between the observed toughening, transformation time, and composite geometry, as well as the effects of material selection. To accomplish this, we consider composites composed of the group IV transiton metal carbides and nitrides as well as group V carbides and their associated metals for the metal layers. As deposited, the multilayer structure is not in equilibrium and carbon/nitrogen will flow from the ceramic phase to the metal phase, transforming at least part of the metal into a ceramic when sufficiently heated, as has been demonstrated experimentally in Ti/TiC films by Dahan *et al.* [66,67] and by Brizes in TaC and NbC layer growth experiments [21,51,52].

Additionally, our collaborators Michael Large and Dr. Gregory Thompson at University of Alabama have recently demonstrated the ability to phase transform in Zr/ZrC films [111]. The results of their study are shown in Figure 6.1. Figures 6.1a and 6.1b show the as deposited Zr/ZrC film in secondary and back scattered electron microscopy respectively. Figure 6.1b shows the clear chemical distinction between the thin Zr and thick ZrC layers of the film. Figures 6.1a and 6.1b show the same sample after annealing, wherein the Zr layers are no longer visible.

To confirm that the Zr layers had completely disappeared, Large *et al.* also performed XRD prior to and after annealing of the composite. As shown in Figure 6.2, in the as deposited composite peaks associated with Zr are present, but in the annealed composite only peaks associated with the substoichiometric $ZrC_{0.64}$ phase are present.

6.2 Thermodynamic Considerations

To begin, we will use as an example a composite composed initially of Zr/ZrC to create our MCM. To illustrate the design concept, consider the ZrC phase diagram shown in Figure 6.3, which was reconstructed from the thermodynamic data of Guillermet *et al.* [1]. We will assume that the

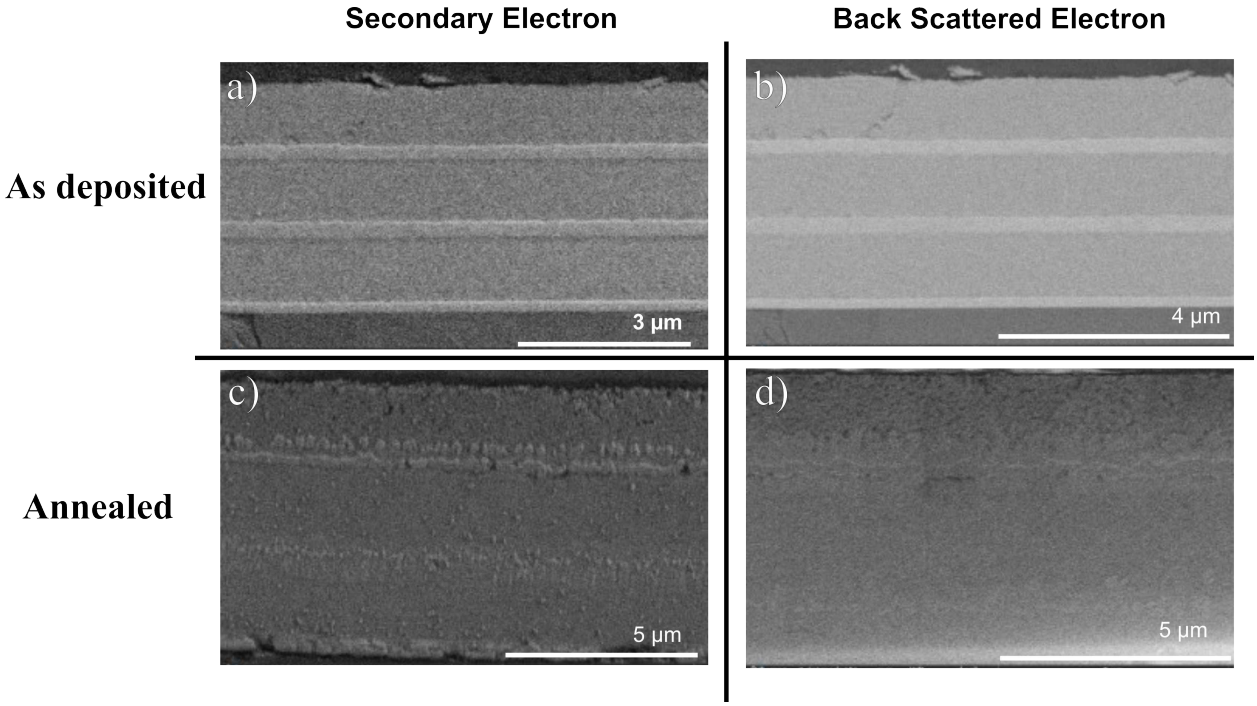

Figure 6.1: a) The as deposited Zr/ZrC film imaged using Secondary Electron STEM **b)** The as deposited Zr/ZrC film imaged using Back Scattered Electron STEM **c)** The annealed film imaged using Secondary Electron STEM **d)** The annealed film imaged using Back Scattered Electron STEM

composite's ceramic layers contain stoichiometric ZrC, i.e. there is a 1:1 carbon-to-metal ratio and the overall composition lies on the phase boundary at $\chi_C = 0.50$. We will further assume that the Zr layers are completely void of any carbon. The volume fractions are f and $1 - f$ for the ceramic and metal layers respectively.

Upon fabrication, the composite is not in chemical equilibrium anywhere except at the interphase between layers. As a result, upon reaching temperatures sufficient for carbon diffusion, the phase transformation of metal layers will begin. The extent to which this phase transformation completes depends upon the initial volume fractions of the composite, since for any geometry with an initial ceramic volume fraction less than some minimum value f_{min} there will not be enough carbon available to completely transform all metal layers.

Thus, to achieve a composite with the ability to completely phase transform the volume fractions must be selected such that the overall carbon content lies within the single phase ZrC_x region

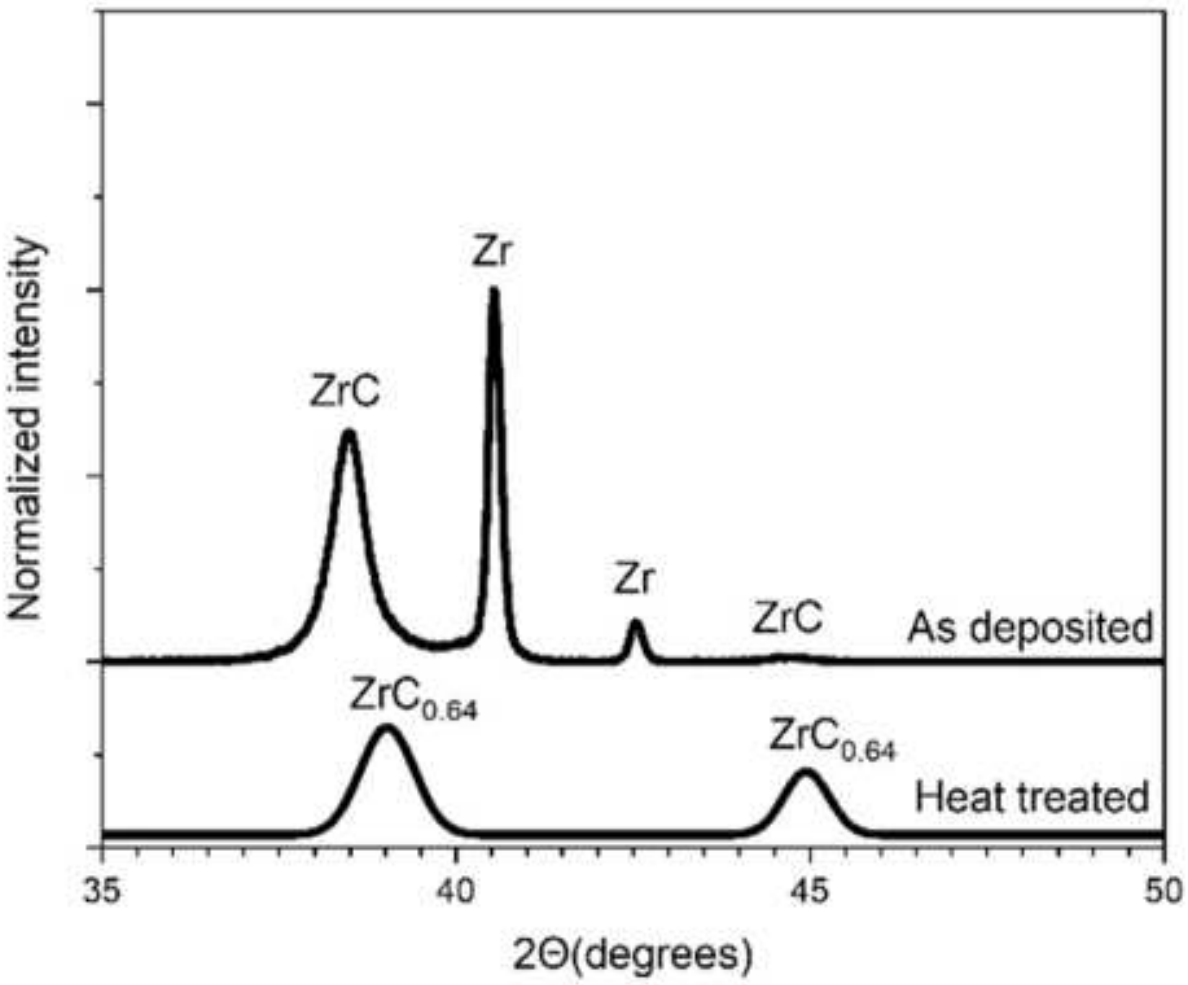

Figure 6.2: XRD of the as deposited and annealed Zr/ZrC film

of the phase diagram. Thus, the minimum volume fraction can be calculated according to mass conservation before and after the phase transformation.

For any physical process mass must be conserved, as such the total number of carbon atoms must remain constant before and after the phase transformation.

$$f_i \frac{0.5}{1-0.5} \Omega_{\mathrm{ZrC}}^{-1} = \frac{\chi_f}{1-\chi_f} \Omega_{\mathrm{ZrC}}^{-1}$$

Cancelling out terms and inputting the minimum ZrC_x carbon content $\chi_{min}(T)$ for χ_f gives the minimum ceramic volume fraction required for metal layers of the composite to fully transform.

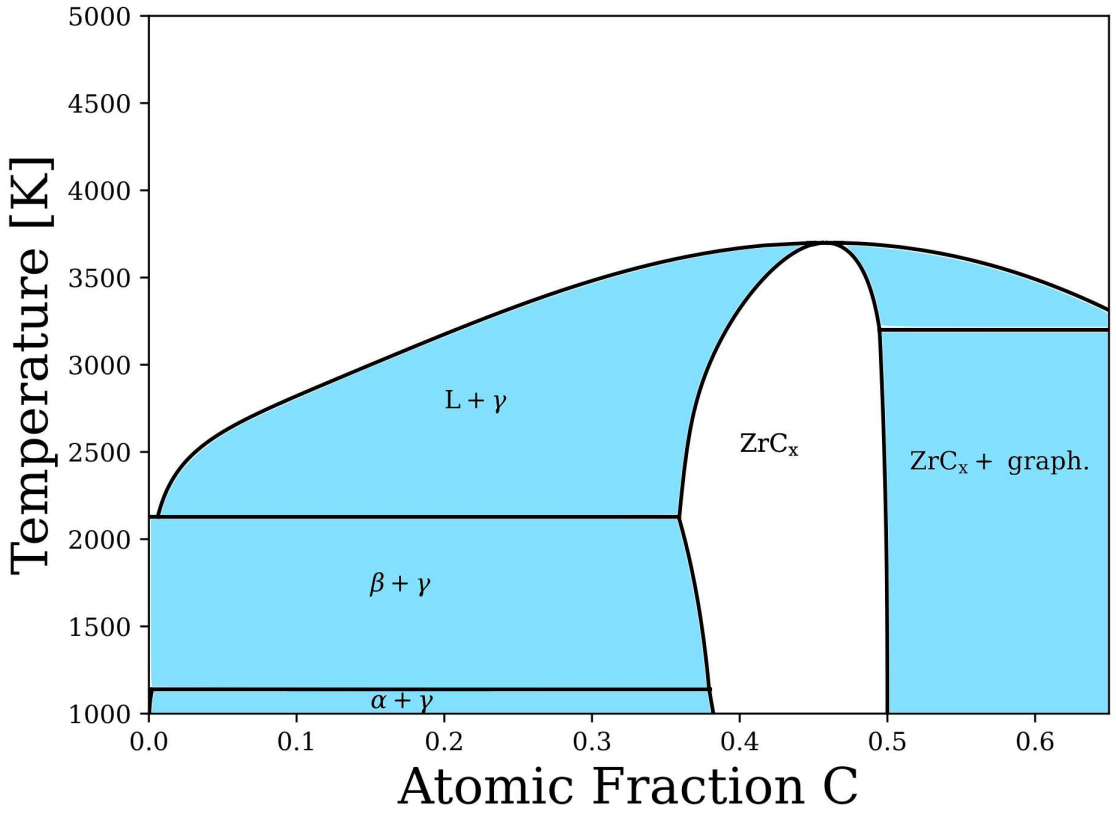

Figure 6.3: Zr-C Phase Diagram constructed from the thermodynamic data of Guillermet *et al.* Of particular importance to the construction of UHTC MCM composites with the ability to phase transform is the ability of the ZrC_x phase to remain stable over a large region of carbon concentration.

$$f_{\min}(T) = \frac{\chi_{\min}(T)}{1 - \chi_{\min}(T)} \tag{6.1}$$

As reported in the previous chapter, the minimum initial ceramic volume fraction has considerable effect on composite's phase transformation properties. It not only determines the thermodynamic constraints on the composites ability to transform, but also affects the kinetics of the phase transformation, since composites with an initial volume fraction close to the minimum will have sluggish kinetics due to a flatter carbon concentration profile, *i.e.* smaller concentration gradients that reduce atomic fluxes. Additionally, experimental literature suggests that the toughening achieved by a composite is proportional to the initial volume fraction of the metal layers [98]. As a result, one method for maximizing toughening is to maximize the metal volume fraction (in other

words, minimize the initial ceramic volume fraction). Thus, the minimum initial ceramic volume fraction directly contributes to the maximum achievable toughening for a given composite material selection.

The other thermodynamic consideration is the melting temperature of the post-transformation ceramic. Using Figure 6.3 again as an example, all of the materials considered in this document exhibit composition-dependent melting temperatures that may be important factors to consider in composite design, especially given that many applications for these materials involve extreme high-temperature environments. One unique quality of these composites is that the post-transformation melting temperature can be directly controlled though the initial ceramic phase fraction of the composite. These melting temperatures are depicted as a function of atomic fraction carbon/nitrogen for all of the considered materials in Figure 6.4. Since the melting temperature is simply a function of overall carbon/nitrogen content, the initial ceramic phase fraction corresponding to the desired melting temperature can be easily determined using the phase lever rule as shown in Equation 6.2 where the overall carbon atomic fraction is χ_c, the initial volume fraction of the ceramic is f_i, and the initial atomic fraction of carbon in the ceramic phase is χ_i. Typically, $\chi_i = 0.50$ since it is most logical to start with a stoichiometric ceramic phase. We note that generally the composition of nonmetal atoms in the metal phase would have to be considered as well; however, since we have assumed that there is zero carbon/nitrogen contained in the metal layers initially, the entirety of the nonmetal atom content is contained within the ceramic layers.

$$\chi_c = f_i \chi_i = 0.50 f_i \tag{6.2}$$

For material selection and design, we have examined the thermodynamics for the group IVB and VB transition metal carbides as well as the group IVB nitrides. Shown in Table 6.1 are the minimum ceramic volume fractions, volume fraction at $3000^{\circ}C$, volume fraction at the maximum melting temperature, and source for the thermodynamic data for each material considered.

Previously, we called attention to the fact that the initial volume fraction can be chosen in order to optimize transformation rates, toughening, and post-transformation melting temperature;

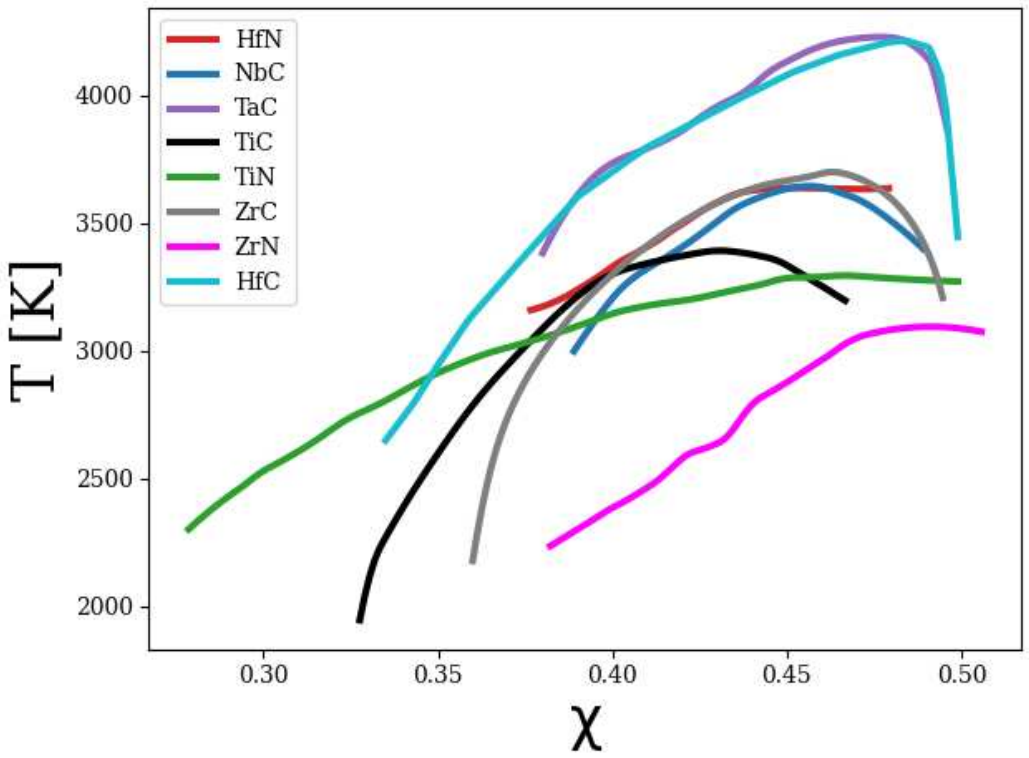

Figure 6.4: Melting temperatures as a function of carbon/nitrogen atomic fraction χ for each of the materials considered.

Table 6.1: Metal layer volume fractions calculated via Equations 6.1 and 6.2. Column two contains the maximum metal phase volume fractions that results in a complete phase transformation. Columns three and four contain the metal phase volume fractions required to achieve a 3000°C and maximum carbide melting temperature post-transformation.

Material	Maximum Me Volume Fraction	Me Volume Fraction at 3000°C Melting Temperature	Me Volume Fraction at Maximum Melting Temperature	Thermodynamic Data Source
Zr/ZrC	0.46	0.35	0.18	[1]
Ti/TiC	0.51	0.36	0.30	[112]
Hf/HfC	0.48	0.42	0.08	[113]
Ta/TaC	0.39	0.37	0.11	[2]
Nb/NbC	0.53	0.35	0.18	[114]

however, it is also important to point out that for the transition metal carbides and nitrides many mechanical properties are concentration-dependent. These properties may include hardness, elastic constants, lattice parameter, CRSS, and others. Furthermore, as pointed out by Large *et al.*, considerations must be made for the effects of transformation strain on the post-transformation ceramic grains. In films deposited with low initial ceramic volume fraction, significant grain boundary decohesion was observed in the as deposited columnar ZrC grains. As shown in Figure 6.5a, these grains lose a significant amount of carbon during the phase transformation, causing a reduction in lattice parameter and associated stress-free linear strains, *i.e.*, eigenstrains, as shown in Figure 6.5b [111]. The elastic strains can be determined from compatibility and force equilibrium. Force equilibrium can be written as shown in Equation 6.3

$$f_1 t E \epsilon_1^e + f_2 t E \epsilon_2^e \tag{6.3}$$

The compatibility is written as shown in Equation 6.4

$$\epsilon_1^* + \epsilon_1^e = \epsilon_2^* + \epsilon_2^e \tag{6.4}$$

By treating Equations 6.3 and 6.4 as a system of equations and solving for the elastic strain ϵ_1^e we get Equation 6.5.

$$\epsilon_1^e = \frac{\epsilon_2^* - \epsilon_1^*}{1 + \frac{f_1}{f_2}} \tag{6.5}$$

Finally, using Hooke's law we can calculate the stress associated with the elastic strain in the post-transformation ZrC layers.

$$\sigma_1 = E\epsilon_1^e = E\frac{\epsilon_2^* - \epsilon_1^*}{1 + \frac{f_1}{f_2}} \tag{6.6}$$

Thus, the stresses and strains in the annealed composite are a function of the volume fractions of the ceramic and metal layers. This effect is demonstrated in Figures 6.5c and 6.5d where the

eigenstrains, elastic strains and stresses in each layer are plotted as a function of the initial ZrC volume fraction of the composite.

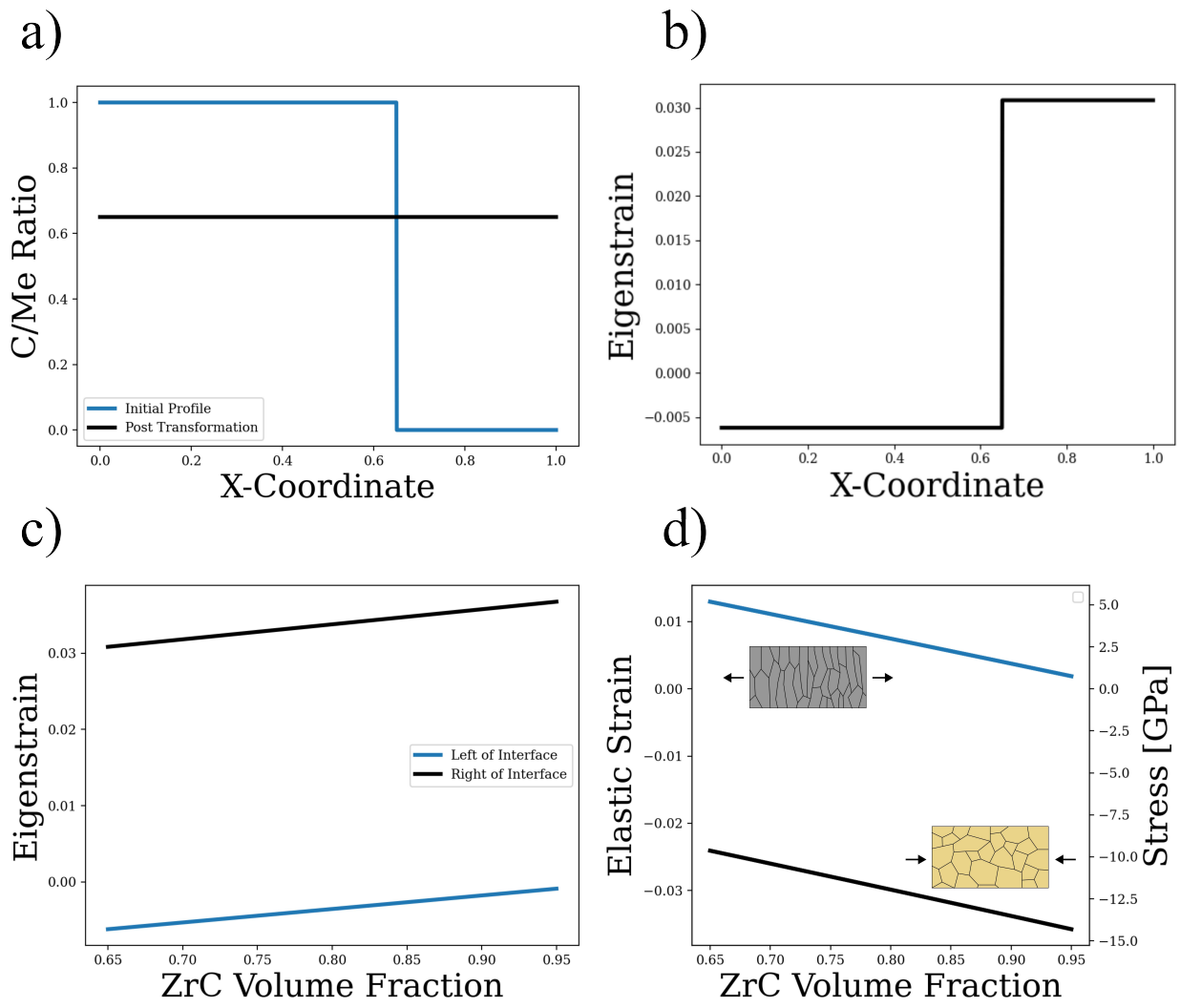

Figure 6.5: a) The carbon composition profiles before (blue) and after (black) annealing. **b)** The eigenstrain profile after annealing. A compressive eigenstrain is present in the locations where the ZrC has lost carbon to the phase transformation (left) and a tensile eigenstrain is present where Zr layers have been transformed in to ZrC_x (right). **c)** The eigenstrains on the left (blue) and right (black) sides of the interface as a function of ZrC volume fraction. **d)** The elastic strains on the left (blue) and right (black) sides of the interface as a function of ZrC volume fraction. Tensile strains in the columnar ZrC grains lead to grain boundary decohesion whereas compressive strains are present in the equiaxed ZrC grains that formed as a result of the phase transformation.

Altogether, we have discussed how a variety of thermodynamic, kinetic, and mechanical properties that are tied to the initial ceramic/metal layer volume fractions. As a result, composite design

must careful balance the trade offs associated with these effects in order to determine the combinations of geometries and materials that optimize these properties.

6.3 Toughening

Previously we reviewed some of the literature concerning toughening in metal-ceramic multilayer composites. Here, we apply ideas from the literature in order to estimate toughening in these UHTC MCM composites. To begin, we will assume that the toughening in these composites is primarily due to the bridging of the crack by intact metal layers of the composite and all other sources of toughening can be ignored. Thus, other factors that may contribute to toughening, such as toughening related to interfacial factors or plasticity mechanisms surrounding the crack-tip are neglected. We note that these mechanisms are likely to positively contribute to toughening in these composites, but are difficult to explicitly model and are likely to be secondary to the effects of crack-bridging. As a results, our toughening estimates are likely to somewhat under-predict actual observed toughening and are therefore a conservative estimate.

Following the work of Bloyer *et al.* [98], the toughening due to crack-bridging can be calculated by determination of the reduction of the near-tip (crack tip) stress intensity factor. In general, the toughening is dependent upon the traction distribution function, crack length, and composite geometry. To simplify our model, we assume that the traction distributions are uniform everywhere in the bridging zone (where metal bridging layers are intact); therefore, the effective tractions can be taken to be $(1-f)\sigma_c$, which is the product of the constrained flow stress σ_c and the volume fraction of the ductile reinforcement $(1-f)$. In many cases, the yield stress of the ductile reinforcement is used as an approximation for the constrained flow stress. Using these approximations, the toughening, ΔK, can be modeled via Equation 6.7 where $h(x,a,W)$ is a weight function that depends on the crack length a and the specimen width W. The integration is carried out over the bridging zone of length L, which is the length from the crack tip to the last intact bridging ligament in the crack wake as shown in the schematic diagram of the bridging zone in Figure 6.6a.

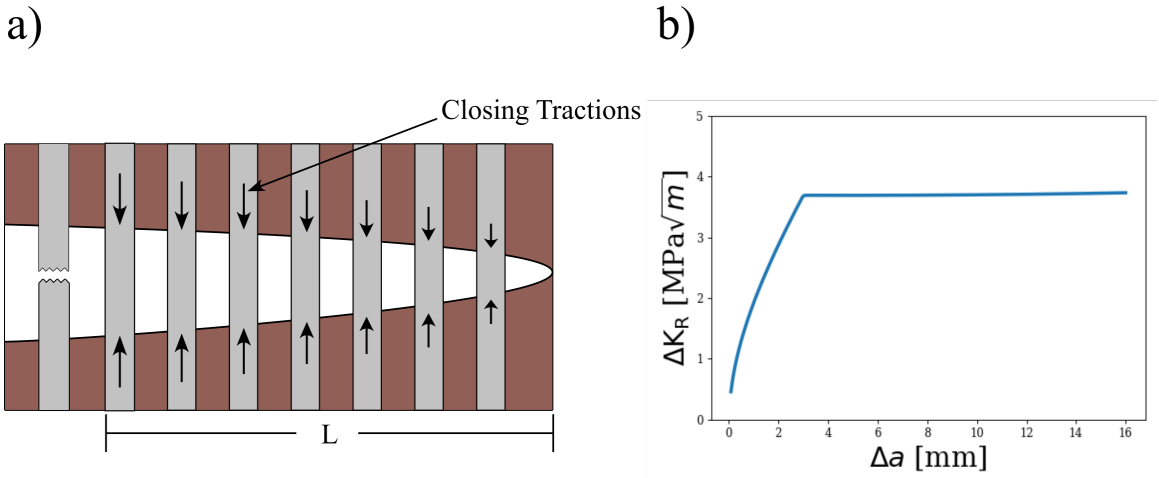

Figure 6.6: a) A schematic diagram of the bridging zone within the crack wake. Ductile ligaments (dark gray) impart closing tractions on the crack wake resulting in improved fracture toughness. At some distance $L + \lambda$ behind the crack tip the ductile reinforcement strain reaches some critical value and experiences failure. The bridging zone length L, then, is the distance behind the crack tip to the last intact bridging ligament. **b)** An example resistance curve demonstrating the rising behavior of the fracture resistance with respect to crack extension as modeled using Equation 6.7. At $\Delta a = L$ the fracture resistance reaches steady-state due to failure of bridging ligaments in the crack-wake occurring at the same rate as crack renucleation across bridging ligaments in front of the crack tip.

$$\Delta K = f\sigma_c \int_L h(a, x, W)dx \tag{6.7}$$

An example of the resulting resistance curve generated using Equation 6.7 is plotted in Figure 6.6b. The resistance curve depicts two distinct regions. First, there is a regime of increasing fracture resistance wherein the bridging zone length is growing as the crack extends. The second regime is the steady-state fracture from crack bridging in the limit of small-scale yielding. This steady-state fracture resistance is reached when the bridging zone length reaches its steady-state value from the rupture of bridging ligaments in the crack wake occurring at the same rate as re-nucleation of the crack across new ligaments at the crack tip.

Unfortunately, the bridging zone length is typically unknown and difficult to calculate from first principles. In practice the bridging zone length is often determined by experiment, but following the derivation by Evans *et al.* [99] it can be shown that Equation 6.7 can be reduced to Equation 6.8 in the limit of small-scale yielding (SSY) thereby eliminating the need to calculate the bridging

zone length. Several new variables are introduced including μ and ν – the shear modulus and Poisson's ratio of the composite - which we have assumed to be equal to that of the brittle matrix as well as u_c, the critical displacement of the bridging ligament associated with rupture.

$$\Delta K = 2\left[\frac{f\sigma_c\mu u_c}{1-v}\right]^{1/2} \tag{6.8}$$

To improve our estimates, we endeavored to model the constrained flow stress using a Hall-Petch-type relationship with the ductile layer width as shown in Equation 6.9 to include the known length scale effects on the toughness. This relationship should be a reasonable model for the increase in constrained flow stress as ductile layer width decreases since the arresting force felt by a crack as it approaches a ductile ligament is directly analogous to the pileup of dislocations at grain boundaries.

$$\sigma_c = \sigma_0 + \frac{k_{hp}}{\sqrt{r}} \tag{6.9}$$

Here, σ_c is the constrained yield stress, σ_0 is the flow stress in the limit of large layer widths, k_{hp} is the Hall-Petch coefficient, and r is the width of the metal layers. Bloyer *et al.* suggested that the constrained flow stress is often taken to be the yield stress of the ductile reinforcement; however, comparison of their reported constrained yield stresses to the uniaxial yield stress indicates that the constrained flow stress may be larger by around a factor of two in their layer width regime. Plotting the constrained flow stress results from Bloyer *et al.* versus their reported ductile layer widths, as shown in Fig. 6.7a, indicates that the Hall-Petch model for constrained flow stress matches the experimental behavior well. The solid line plotted alongside the data of Bloyer *et al.* in Figure 6.7a is the Hall-Petch relationship that is produced if one uses the uniaxial yield stress (120MPa) and Hall-Petch coefficient (340MPaμm$^{1/2}$) for grain boundary hardening in niobium reported by Cordero *et al.* [115]. In contrast, fitting the experimental data of Bloyer *et al.* produces an intercept stress value of 270MPa and a Hall-Petch coefficient of 2000MPaμm$^{1/2}$ – approximately an order of magnitude larger.

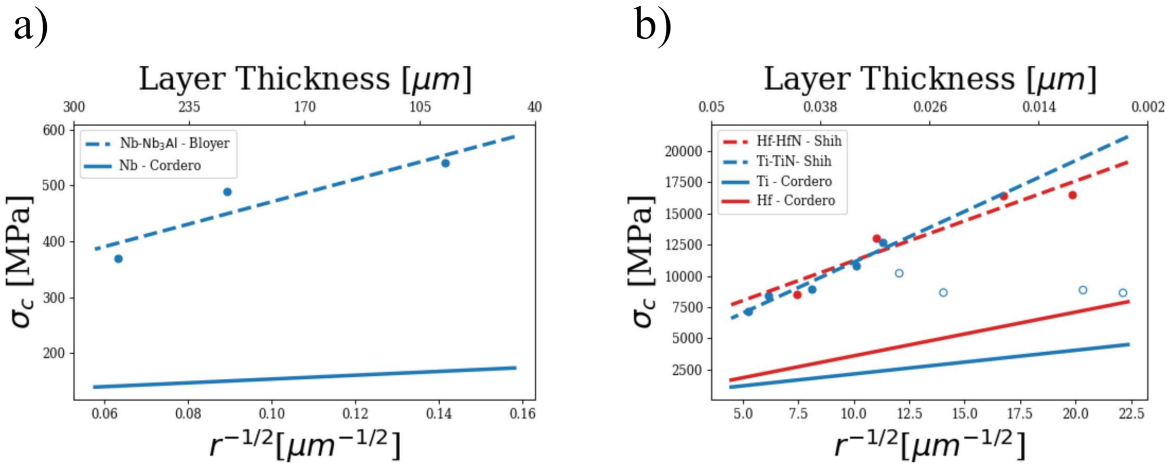

Figure 6.7: a) The constrained yield stress estimated using the Hall-Petch data for niobium reported by Cordero *et al.* is plotted alongside the fit of the experimental data of Bloyer *et al.* for Nb/Nb3Al multilayers. **b)** The constrained yield stress estimated using the Hall-Petch data for titanium and hafnium reported by Cordero *et al.* is plotted alongside the experimental data of Ti/TiN and Hf/TiN multilayers reported by Shih and Dove.

To further demonstrate the Hall-Petch type relationship, we compared hardness data in Hf/HfN and Ti/TiN MCMs from a study of the effects of metal layer width on composite hardness [116] This data was compared to our predicted constrained flow stresses using the Hall-Petch relationship and the uniaxial yield stress along with the Hall-Petch coefficient data of Cordero *et al.* The composite layer widths in Shih and Dove's study were much thinner and thus are representative of a very different layer width regime than the data of Bloyer *et al.* Despite this difference, a Hall-Petch type relationship with layer width is still observed. Using the data available from Shih and Dove, we estimate the uniaxial yield stress via the approximate relationship between Vickers hardness and yield strength shown in Equation 6.10:

$$\sigma_y = 3H_v \tag{6.10}$$

Figure 6.7b plots the constrained flow stress predicted by our Hall-Petch relationship, which underpredicts that for the prior reports for Hf/HfN and Ti/TiN composites, indicating that the use of the Hall-Petch coefficient and uniaxial yield strength in our model will consistently produce conservative estimates. The Ti/TiN reported data has a Hall-Petch breakdown at sufficiently thin

layers and as such only the data recorded before breakdown was used in our fit. (Note that the data recorded after Hall-Petch breakdown is shown with open blue data points to indicate that it was not used in our fit.) The fit results show that the Hall- Petch slope for the constrained flow stress as a function of layer width is similar to that reported by Cordero *et al.*, but the intercept is much larger than the reported uniaxial yield strength.

These results clearly indicate, as expected, that the Hall-Petch coefficient for the constrained flow stress is not the same as the Hall- Petch coefficient for grain boundary hardening and, moreover, that the constrained flow stresses are underpredicted by Hall-Petch coefficient for grain boundary hardening. These points are important because Hall-Petch coefficients for the constrained flow stress with respect to ductile layer width are not readily available in the literature; however, the uniaxial yield stress and Hall-Petch coefficient for grain boundary hardening are available for most materials and can be used in their place with the understanding that the toughening and constrained flow stress will be underestimated by using these as inputs in Equations 6.8 and 6.9.

Returning now to our discussion to modeling the toughening of our composites due to crack-bridging, substitution of Equation 6.9 into Equation 6.8 results in the following equation for toughening:

$$\Delta K = 2\left[\frac{f(\sigma_0 + \frac{k_{hp}}{\sqrt{r}})\mu u_c}{1-v}\right]^{1/2} \tag{6.11}$$

where again f is the volume fraction of the ductile reinforcement, r is the layer width of the ductile reinforcement, σ_0 is the uniaxial yield strength of the ductile reinforcement, ν is the Poisson's ratio, μ is the shear modulus, and u_c is the critical displacement where rupture of the bridging ligaments occurs. To carry out computation of ΔK, we have assumed that ligament rupture occurs at some critical strain ϵ_c which is related to the thickness of the bridging ligaments such that $u_c = \epsilon_c r$. Therefore, by making a further assumption about the failure strain of the bridging ligament, the toughening calculation can be carried out. To arrive at a reasonable assumption, we examined the micrograph images of bridging ligaments reported by Flinn *et al.* [97] and measured

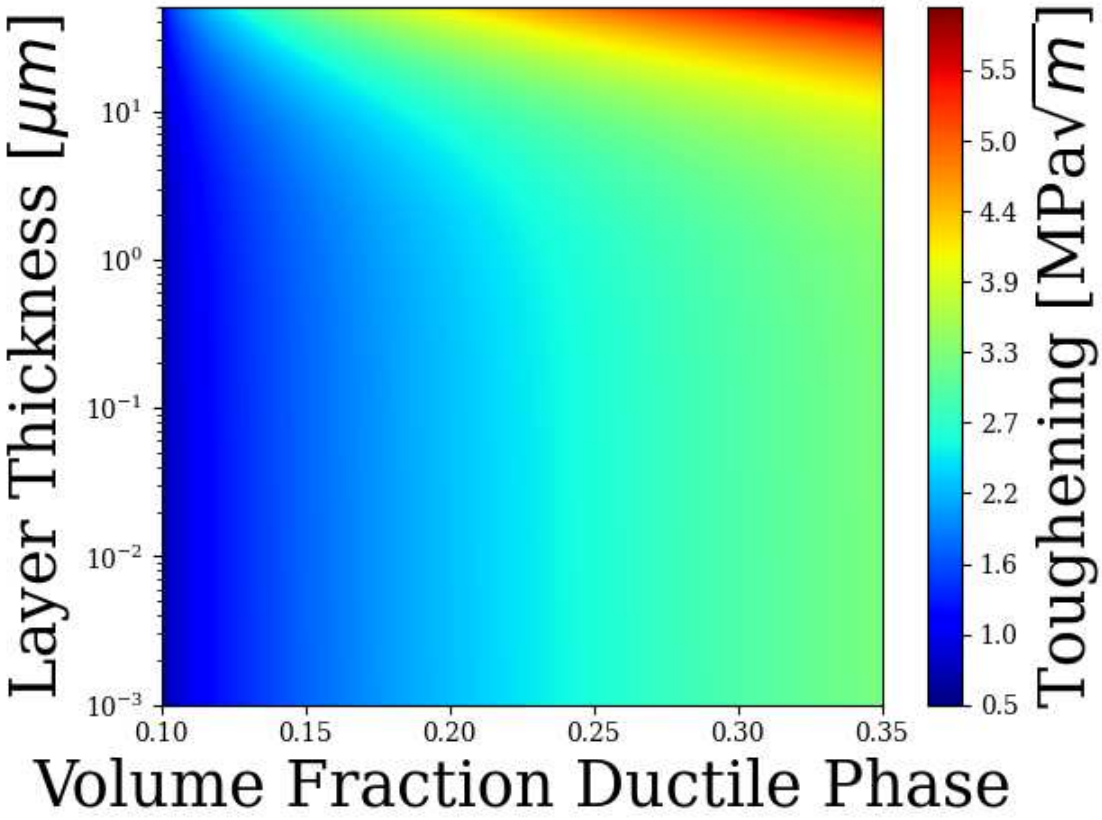

Figure 6.8: A contour plot depicting the predicted toughening for a Zr/ZrC composite as a function of volume fraction of ductile reinforcement and ductile layer thickness. Layer thicknesses were plotted between 0.001μm and 50μm. These limits were chosen because larger layer thicknesses are unlikely to result in small-scale yielding and smaller layer thicknesses provide little to no toughening.

the crack opening displacement in relation to the bridging ligament width just before rupture of the bridging ligament. The strain calculated from these measurements was approximately $\epsilon_c = 0.30$.

Figure 6.8 displays the steady-state stress intensity as a function of metal phase volume fraction and layer width for a Zr/ZrC MCM composite. The toughening, as can be seen in Equation 6.11, is directly related to the ductile layer volume fraction and layer thickness. Importantly, this model only reflects toughening due to crack bridging and does not include contribution from other mechanisms such as slip or debonding at the interface between layers or process zone toughening in the plastic region surrounding the crack tip. As was previously mentioned, our estimate of the constrained flow stress using the uniaxial yield strength and Hall-Petch coefficient for grain-boundary hardening of the metal underpredicts the actual constrained yield stress. Due to these factors, the

predicted magnitude of toughening is expected to be smaller than experimentally observed values will be and therefore represents a conservative estimate of toughening. Despite this, our results indicate that fracture toughness in the proposed MCMs could be up to five or six times greater than those of a monolithic ceramic, representing an excellent solution to the reliability of UHTC structural components.

6.4 Figure of Merit & Design Space

Characterization of composite performance requires consideration of its important properties including the transformation time, improvement in fracture toughness, and the melting temperature of the monolithic ceramic produced by the phase transformation. To simplify the characterization, we propose the construction of the parameter κ, defined in Equation 6.12, to act as a figure of merit that describes the performance of the composite, though this is only one example of many possible choices.

$$\kappa = \frac{\Delta K}{\log_{10} \tau} \frac{T_m}{3000} \tag{6.12}$$

where ΔK is the steady-state toughening, τ is the phase transformation time in seconds, and T_m is the post-transformation melting temperature in Kelvin of the ceramic. The idea of this figure of merit is to characterize the performance of the composite as the amount of toughening weighted by the phase transformation time and the post-transformation melting temperature. Shown in Figure 6.9 is the figure of merit κ as a function of ductile layer volume fraction and layer thickness for a Zr/ZrC composite.

Figure 6.9 illustrates that κ is greatest for large ductile layer widths and either small or large ductile layer volume fractions. The figure of merit appears to be optimized for large layer widths at the volume fraction boundaries, suggesting that design constraints are needed to point towards an optimum design. For example, one design strategy would be to maximize the steady-state toughening subject to constraints on the post-transformation melting temperature and transformation time. Here, we will choose these constraints to be the ability to completely phase transform in under 15

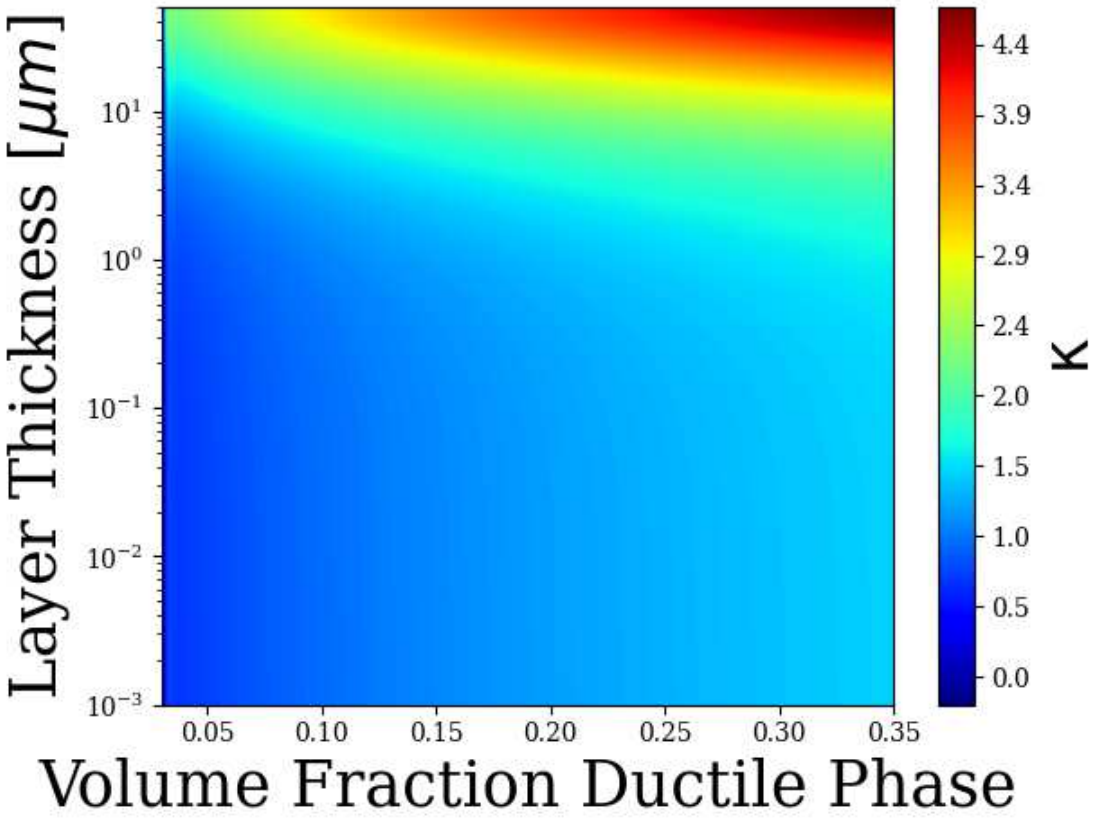

Figure 6.9: A contour plot of the figure of merit κ with respect to ductile layer volume fraction and thickness of a Zr/ZrC composite.

Table 6.2: A comparison of constrained composite performance for the group IVB and VB transition metal carbides. The imposed constraints are a maximum phase transformation time of 15min and a minimum post-transformation melting temperature of 3000K. Listed in the table are the ductile layer thickness r and volume fraction f that result in the greatest steady-state fracture resistance given the constraints.

Material	r [μm]	f	τ [min]	T_m [K]	ΔK [MPa$\sqrt{m}$]	κ
Zr/ZrC	1.84	0.39	15.0	3015	6.37	2.17
Zr/ZrN	2.12	0.17	15.0	3000	4.40	1.50
Ti/TiC	2.81	0.41	15.0	3205	7.32	2.64
Ti/TiN	3.70	0.45	15.0	3000	8.62	2.92
Hf/HfC	0.11	0.41	15.0	3325	2.50	0.94
Hf/HfN	1.01	0.15	15.0	3640	2.89	1.19
Nb/NbC	1.20	0.20	15.0	3645	3.71	1.53
Ta/TaC	4.48	0.39	15.0	3620	9.91	4.05

Table 6.3: A comparison of constrained composite performance for the group IVB and VB transition metal carbides. The imposed constraints are a minimum steady-state toughening of 5MPa$\sqrt{m}$ and a minimum post-transformation melting temperature of 3300K. Listed in the table are the ductile layer thickness r and volume fraction f that result in the quickest transformation time given the constraints.

Material	r [μm]	f	τ [min]	T_m [K]	ΔK [MPa$\sqrt{m}$]	κ
Zr/ZrC	1.17	0.34	5.54	3305	5.0	2.19
Zr/ZrN	-	-	-	-	-	-
Ti/TiC	1.23	0.38	2.70	3305	5.0	2.50
Ti/TiN	-	-	-	-	-	-
Hf/HfC	1.17	0.41	1855	3305	5.0	1.09
Hf/HfN	5.50	0.14	424.3	3640	5.0	1.38
Nb/NbC	3.0	0.20	90.3	3645	5.0	1.63
Ta/TaC	0.38	0.39	0.11	3620	5.0	7.38

min. at 2000 K and a post-transformation melting temperature greater than 3000 K. Using these constraints, the optimal design for each material can be found. Results of this comparison are shown in Table 6.2.

A second design strategy would be to minimize the transformation time subject to constraints on the degree of toughening as well as the post-transformation melting temperature. Here, we will minimize transformation time subject to the constraints of a minimum steady-state toughening of $5\text{MPa}\sqrt{m}$ and a minimum post-transformation melting temperature of 3300K. Design solutions under this set of constraints with the phase transformation carried out at 2000 K are tabulated in Table 6.3.

Analysis of Table 6.2 shows that Ti/TiN and Ta/TaC appear to be the most effective choices for overall toughening. In this design setting the Ta/TaC composites have a slight advantage in toughening and have a melting temperature more than 600K higher than the Ti/TiN composites. Table 6.3 shows a similar trend, with the fastest phase transformation occurring in the Ta/TaC composites; however, the Zr/ZrN and Ti/TiN composites are not represented in this table due to the fact that they can never achieve a melting temperature of 3300K. Additionally, in each case the value of κ coincides with the order of performance according to the optimized parameter. This may indicate that the figure of merit is an appropriate measure of composite performance. Interestingly, composite performance as indicated by Tables 6.2 and 6.3 generally relate to carbon/nitrogen diffusion activation energy as reported in Chapter 4. Collectively, the higher carbon/nitrogen diffusion activation energy results in lower composite performance. This appears to be the most important differentiating factor between the composites likely because other input parameters for our model are very similar among the transition metal carbides/nitrides and carbon/nitrogen diffusivity directly affects optimum layer width for a given constraint.

It is worth noting that Hf/HfC composites represent outliers in both design scenarios outlined due to the exceptionally low diffusivity of carbon in HfC [59]. Additionally, this result is consistent with the carbon vacancy migration energies reported by Yu *et al.* [7] from density functional theory. As a result of slow diffusion, constraints on transformation time in the first case study led to very small layer widths and a small amount of toughening.

It is important to consider that this comparison only accounts for the composite performance as defined by the figure of merit, toughening, and transformation time – whereas real design choices may account for costs associated with raw materials as well as composite manufacturing that may change as a function of ductile layer thickness and volume fraction. In addition, material properties such as creep and oxidation resistance may skew design towards one material or another.

6.5 Summary & Conclusions

In this work we have introduced a new method for the creation of damage resilient UHTCs. The fracture toughness can be increased by the construction of an MCM in which ductile metal layers contribute to toughening through several mechanisms including crack bridging and slip/debonding of interfaces. In contrast to the behavior of standard MCMs, the high-temperature properties of the TMCs are not sacrificed due to a phase transformation that occurs as the material reaches high temperatures. During this phase transformation the ductile metal layers disappear and are replaced by a single monolithic ceramic, *e.g.*, ZrC_x. To completely describe the design space for these composites, we first considered the thermodynamic limits of the transition metal carbides. We outlined how a proper choice of metal volume fraction or, equivalently, ratio of metal and carbide/nitride composite layer thicknesses affects the overall carbon/nitrogen content and thereby the melting temperature post-transformation and the driving force for the phase transformation.

In a previous publication, we built a coarse-grained model capable of predicting the phase transformation kinetics of these composites based on the initial concentration profile, metal-to-ceramic layer ratios, and the carbon/nitrogen diffusivities available in the literature. Here, we used this model to predict the time required for a complete phase transformation to occur and extended its use to the group VB carbide and IVB nitride composites under the assumption that the metal layer disappears quickly and that the coarse-grain model remains valid when the secondary phase is the hemicarbide/heminitride instead of the metal. This assumption is likely valid given that the activation energies for carbon/nitride diffusion are lower in the hemicarbide/heminitride than the monocarbide/mononitride [51, 52].

Additionally, we predicted the steady-state toughening of the multilayer composites under the assumption of small-scale yielding. The toughening, a result of crack-bridging due to closing tractions imposed on the crack wake by the ductile metal layers of the composite and falls within a very reasonable range when comparing it to the literature on toughened ceramics. Additionally, we noted that these predictions are likely to be conservative estimates because of our use of the uniaxial yield stress and Hall-Petch coefficients of the metal when calculating the constrained flow stress of

the bridging ligaments. We suggest that this, combined with the fact that toughening effects from large scale bridging and slip/debonding of interfaces (or other toughening mechanisms) are likely to be present in real composites, means that real components are likely to exhibit significantly higher fracture resistances than those predicted herein.

Hence, it follows that our method for constructing high-toughness ceramics without sacrificing high-temperature mechanical and thermodynamic properties has an advantage over other methods for toughening UHTCs. Our composites facilitate improved fracture toughness at low temperatures while allowing for the high temperature post-transformation properties to be controlled by the choice of layer thicknesses. An additional advantage over CMCs may be that the transforming MCMs can be constructed using a variety of processing techniques including sputtering, cold spray, and plasma spray and are therefore amenable to use as protective coatings.

Finally, we examined two design scenarios: one where the degree of toughening is maximized given constraints on transformation time and post-transformation melting temperature and another where transformation time was minimized given constraints on the amount of toughening and final melting temperature. The results indicated that all the transition metal carbides performed similarly with ideal ductile layer widths in the range of microns to tens of microns. Ti/TiN and Ta/TaC composites seem to have slight advantages in performance because of fast carbon/nitrogen diffusion, and, in the case of Ta/TaC composites, high melting temperatures even among these UHTCs. In both design scenarios we examined, the order of performance was essentially equivalent to the order of ascending carbon/nitrogen diffusion. In both scenarios the Hf/HfC composite's performance was an outlier due to its high activation energy for carbon diffusion in HfC. In this paper we have outlined how designers can make use of thermodynamic phase diagrams as well as carbon/nitrogen diffusivity coefficients and mechanical properties, all available in the literature, to arrive at conservative estimates for the toughening (in the limit of small-scale yielding), phase transformation rates, and melting temperature achieved by a specific composite design as a function of layer thickness and metal volume fraction. When all is considered, the transforming transition metal carbide/nitride metal ceramic multilayer composites outlined herein represent a

solution to the need for high-toughness UHTCs with a wide design space that makes them suitable to a variety of applications where a low-temperature reliability needs to be balanced with favorable high-temperature thermodynamic and mechanical properties.

Chapter 7

Vacancy-Ordering & Diffusion

In the experimental literature on carbon diffusion in substoichiometric $TiC_{0.67}$ there remains an open question. In Sarian's manuscript *Anomalous Diffusion of 14C in TiC0.67* [50], an unusual change in activation energy for carbon-14 tracer diffusion at $2080°C$ is reported. The activation energy is reported to be 4.82eV at low temperature but only 2.22eV at high temperature. Recognizing this strange behavior, Sarian hypothesized that the anomalous change in activation energy is due to an order-disorder phase transformation on the carbon sublattice of the B1 rocksalt structure. Despite having been an open question in the literature for more than half a century, there have been very few investigations concerning the intersection of vacancy-ordered phase transitions and their effects on interstitial diffusion.

To gather a general understanding of these effects, we first used a combination of Monte Carlo and kinetic Monte Carlo simulations on square lattices with two different toy-model Hamiltonians. The purpose of each Hamiltonian was to generate a different type of ordered structure. One structure, which we referred to as the 'checkerboard' structure, contained isolated vacancies which we predicted would inhibit interstitial diffusion due to the lack of interconnected pathways for diffusion. The other structure, which we referred to as the 'labyrinthine' structure, ordered in a manner which would produce long strings of vacancies. We predicted that due to these long interconnected pathways diffusion would be enhanced in the ordered 'labyrinthine' structure when compared to disordered configurations.

Finally, in an attempt to clearly determine the cause of Sarian's anomaly, we used Density Functional Theory calculations implemented in VASP in combination with the cluster expansion method to recreate the energetics of TiC_x. Then, we conducted Monte Carlo and kinetic Monte Carlo simulations with energetics calculated according to our cluster expansion in order to examine the relationship between short and long-range order, hop correlation factor, and tracer diffusivity.

7.1 Vacancy Ordering & Diffusion on a Square Lattice

7.1.1 Introduction

Some crystallographic systems contain a lattice or sublattice composed of a binary mixture of atoms and structural vacancies. At high temperatures, the arrangement of atoms and vacancies in these structures is completely random; however, at low temperatures ordered superlattices of structural vacancies are formed, similar to the ordered superlattices formed by ordered substitutional alloys. Studies on the effects of ordering on diffusion in ordered substitutional alloys have shown that ordered phases generally exhibit greater activation energies for diffusion compared to unordered phases, *e.g.* α_2-TiAl versus α-Ti [117–122]. Similarly, vacancy ordering is likely to affect diffusion in vacancy-ordered lattices.

Despite the obvious similarity between diffusion in ordered substitutional alloys and vacancy-ordered structures, there are two important differences. First, vacancies, the carriers of diffusion, are themselves ordering in addition to atoms. Second, the diffusion occurs by a mechanism involving structural vacancies rather than thermal vacancies and thus vacancy formation energy does not contribute to the thermally activated behavior of the diffusion. The fact that the structural vacancies themselves are forming ordered structures may have important implications on the diffusion since there is an energetic predilection for vacancies to remain in low-energy ordered configurations. This preference for order is likely to inhibit diffusion. On the other hand, some ordered structures possess networks of vacancies with low energy barriers that may act as high-diffusivity pathways in a manner similar to dislocation pipe diffusion for vacancies [123, 124]. Under these circumstances, it is conceivable that vacancy-ordered structures could demonstrate an increase in diffusivity.

Perhaps the most important materials demonstrating vacancy ordering effects on diffusion are the intercalated lithium metal oxides. The lithium metal oxides have become ubiquitous in portable energy storage systems and as a result lithium diffusion in the metal oxides has been the topic of many studies [125–130]. Despite this, the effects of vacancy ordering on diffusion have not been studied. This is likely because the effects of vacancy ordering are often difficult to separate

from other concentration-dependent mechanisms such as divacancy diffusion, tri-vacancy diffusion, and metal ion valency [131–133]. Nevertheless, there is evidence that the lithium diffusivity in $LiCoO_2$ has a minimum with respect to lithium concentration at the concentrations coinciding with the vacancy ordered phase boundaries, i.e., the minimum and maximum Li concentrations of the vacancy-ordered Li_x CoO_2 phase [134, 135].

In another group of materials, the transition metal carbides and nitrides, the effects of vacancy ordering on hardness and magnetic susceptibility have been documented, with the former increasing as a function of ordering and the latter decreasing [136–139]. The effect of vacancy ordering on vacancy self-diffusion; however, has not been the subject of any studies. The best evidence for order effects on diffusion in these materials comes from a study on the effects of carbon concentration on carbon diffusion in substoichiometric titanium carbide. In his study, Sarian found that the apparent activation energy for carbon diffusion nearly doubled at a temperature of 2080°C in $TiC_{0.67}$ [50]. Sarian attributed this observed change in apparent activation energy to a vacancy order-disorder transition occurring on the carbon sublattice of the B1 rocksalt (NaCl-type) structure; though more recent thermodynamic studies conducted by Gusev *et al.* have indicated that the long range order-disorder transition occurs at a much lower temperature [18, 140–142]. If Sarian's anomaly is indeed a consequence of ordering, it raises the question of how ordering actually affects diffusion and if it is related to short-range ordering or long-range ordering.

There is speculation that short-range order may influence many material behaviors. Multicomponent solid solutions, especially high entropy materials such as High Entropy Alloys (HEAs) and High Entropy Ceramics (HECs) [143–147] have grown in popularity over the past two decades [148]. These materials systems involve equimolar mixtures containing five or more alloying elements with the intention of improving phase stability by driving up the configurational entropy of the mixture [149–151]. High entropy materials are often reported to have exceptional mechanical, thermodynamic, and functional properties [152–154]. Several mechanisms are proposed to contribute to the improved properties, including short-range order effects due to preferential pair-bonding of alloying elements [155]. It is especially likely that short-range ordering can dra-

matically affect kinetic processes in these high entropy materials, whose improved properties are often attributed in part to 'slow diffusion' [156–158].

In studies on two-dimensional lattice-gas adsorption systems 'memory effects' have been shown to have profound effects on tracer and collective diffusivities within two-dimension ordered phases as well as near phase transition boundaries [159, 160]. In particular, the hop correlation factor has been shown to be heavily dependent on composition/coverage in these systems as well as having a profound effect on the apparent activation energy. Previous authors have described these effects by writing the tracer diffusivity as a rate equation containing separate terms for each type of hop and accounting for hop multiplicity [161, 162]. Using this formulation, the apparent activation energy can be understood as a weighted average of hops having different energy barriers. Importantly, this framework highlights how the apparent activation energy can change as a function of temperature and composition due to the corresponding changes in hop multiplicity [161, 163].

From this brief review of the literature, it is evident that diffusion on vacancy-ordered sublattices represents an interesting and understudied intersection between two fundamental physical phenomena: vacancy order-disorder transformations and tracer diffusion. The effects of vacancy ordering on the tracer diffusivity and its apparent activation energy are generally not known. Furthermore, it is unclear if long range order (LRO) or short-range order (SRO) is responsible for observed changes in hop correlation factor. In this work, we conduct Monte Carlo (MC) and kinetic Monte Carlo (kMC) simulations on a square lattice consisting of A atoms and structural vacancies in order to garner insight into the effects of vacancy ordering on tracer diffusion.

7.1.2 Methodology

Monte Carlo Simulation

To capture ordering effects, we used two different model Hamiltonians with repulsive interactions. The first was a classical antiferromagnetic nearest neighbor Ising model [164–166] as shown in Equation 7.1 resulting in a 'checkerboard' type ordered structure. The second Hamiltonian, shown in Equation 7.2, was constructed in order to create an energetic preference for second

nearest neighbors to be of like type and third nearest neighbors to be of unlike type, i.e. a Hamiltonian with competing second-nearest and third-nearest neighbor mechanisms [167, 168], resulting in a 'labyrinthine' structure consisting of rows or columns having the same type of sites. These rows or columns of vacancies hypothetically act as high-diffusivity pathways which may influence diffusion. Here, $J_1 = -1c$ is the interaction coefficient which we have chosen in the first case and $J_2 = -0.25c$ in the second, where we have defined the constant $c = k_B \times 1K$ in order to give our interaction coefficients the correct units. The second interaction coefficient was chosen to be smaller in order to make the energies more comparable between the structures. The spin variables σ take on values of 1 or -1 depending on if the site is occupied by an atom or a vacancy. σ_i is the spin variable of the ith site and σ_j, σ_k and σ_l are the spin variables of sites in the first, second, and third neighbor shells respectively. Thus, the 'checkerboard' structure is constructed by creating a repulsive force between nearest neighbors of the same spin and the 'labyrinthine' structure is constructed by creating an attractive force between second nearest neighbors of same spin and a repulsive force between third nearest neighbors of the same spin.

$$\mathcal{H} = -\frac{1}{2} J_1 \sum_{ij} \sigma_i \sigma_j \tag{7.1}$$

$$\mathcal{H} = \frac{1}{2} J_2 \Big(\sum_{ik} \sigma_i \sigma_k - \sum_{il} \sigma_i \sigma_l \Big) \tag{7.2}$$

The canonical ensemble was then sampled to generate structures and determine equilibrium properties using Kawasaki Dynamics [169], *i.e.*, for each transition the system's total spin (vacancy concentration) was conserved by proposing to swap the spins of any two sites. In essence, for any swap to be meaningful it must occur between sites with unlike spin, since swapping sites with the same spin has no effect on the energetics or configuration of the system. This process was carried out for 1000 Monte Carlo steps on a 30×30 square lattice, where each Monte Carlo step consisted of a single sweep of the lattice wherein the spin variables at two sites were proposed to be swapped. In other words, a single Monte Carlo step was considered to have completed after

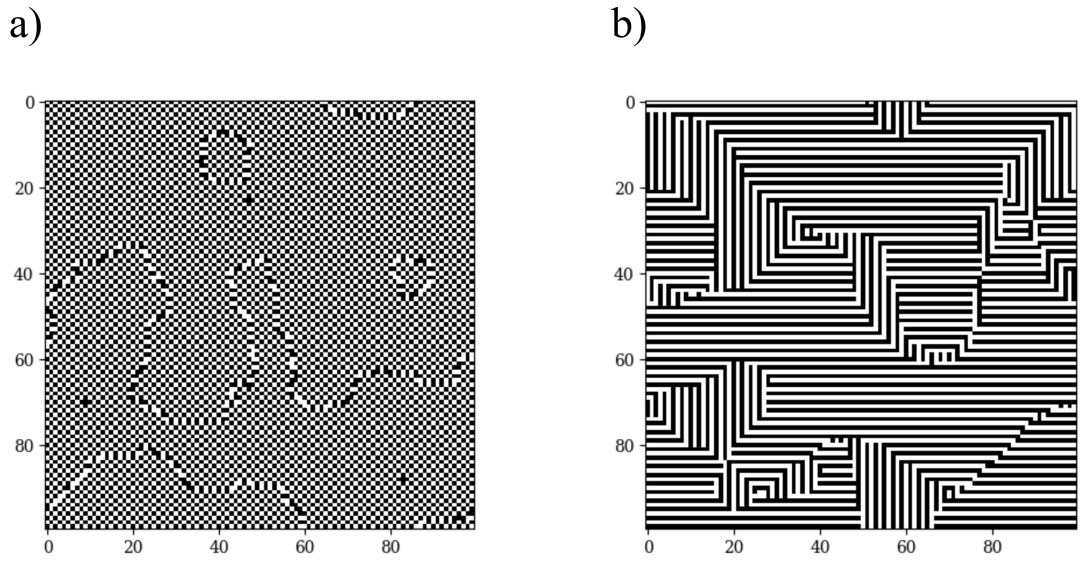

Figure 7.1: a) The 'checkerboard' structure produced by the Hamiltonian shown in Equation 7.1. b) The 'labyrinthine' structure produced by the Hamiltonian shown in Equation 7.2.

the number of proposed swaps was equal to the number of sites on the lattice. The change in energy was calculated for each proposed swap and swaps resulting in a reduction in energy were automatically accepted whereas swaps resulting in an increase in energy were accepted according to Boltzmann's distribution, Equation 7.3, where ΔH is the change in energy, k_b is the Boltzmann constant, and T is the simulation temperature. For swaps resulting in an energy increase, a random number $u_1(0,1)$ was generated and the swap was accepted if $u_1 < P(\Delta H, T)$, *i.e.*, with the probability determined by Equation 7.3.

$$P(\Delta H, T) = \exp\left(-\frac{\Delta H}{k_b T}\right) \tag{7.3}$$

Sample equilibrium structures are shown in Figure 7.1 for the a) checkerboard structure and b) labyrinthine structure at very low temperatures, illustrating the nature of low temperature order. Shown in Figure 7.2 is the energy per site versus MC step for the 'checkerboard' (blue triangles) and 'labyrinthine' (red squares) simulations at $k_b T = 1.0$. After 300 MC steps, represented by the dashed vertical line, the system was considered to be in equilibrium.

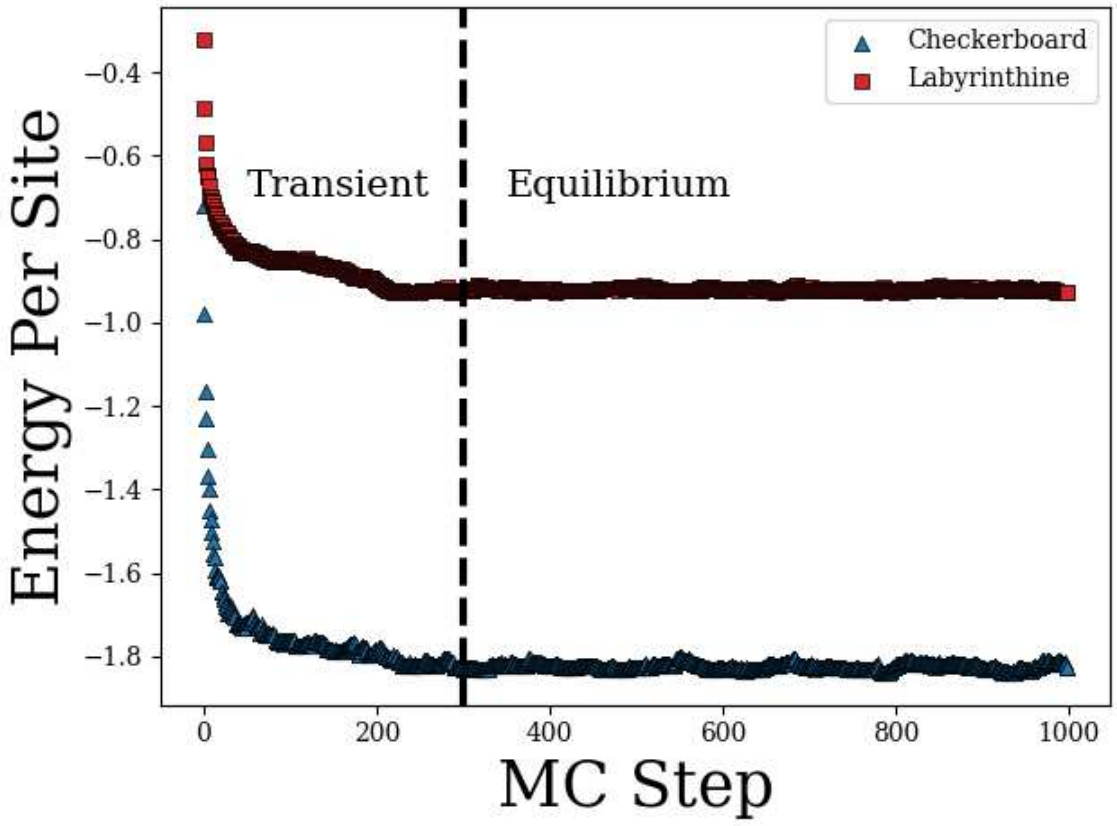

Figure 7.2: The energy per site as a function of MC step for representative 'checkerboard' (blue triangles) and 'labyrinthine' (red squares) simulations at $k_bT = 1.0$. After 300 MC steps, represented by the dashed vertical line, the system was considered to be in equilibrium.

Kinetic Monte Carlo Simulation

The rejection free kinetic Monte Carlo method was employed in order to model atomic migration. The energy barrier ΔH^* for each event was then calculated via Equation 7.4 where $\Delta\mathcal{H}$ is a direction-independent kinetically resolved activation energy (KRA), in other words, an energy barrier formulated using the Brønsted–Evans–Polanyi principle [132, 170]. Here, we have made the assumption that all of the diffusion transition states occur at the same energy level, chosen as $15c$ arbitrarily in order to prevent negative, and therefore physically meaningless, activation energies. ΔH is the difference in energy between the final and initial configurations of the selected event. During the simulation, before an event was selected to be carried out, a rate catalogue was constructed by determining the energy barrier associated with all of the possible jumps that could be made by each vacancy. The possible jumps were restricted to nearest-neighbor sites with opposite spin. For each vacancy-atom pair the system energy was determined from Equation 7.1 for the 'checkerboard' structure and Equation 7.2 for the 'labyrinthine' structure.

$$\Delta H^* = \Delta\mathcal{H} + \frac{\Delta H}{2} \tag{7.4}$$

The rate associated with a hop from configuration C_i to configuration C_j was then determined according to Equation 7.5 where r_{ij} is the rate, ν is the attempt frequency which we have chosen as 10^{12} Hz, ΔH^* is the energy barrier for the transition, and T is the simulation temperature.

$$r_{ij} = \nu \exp\Big(-\frac{\Delta H_i^*}{k_B T}\Big) \tag{7.5}$$

The rate catalogue was then constructed according to Equation 7.6 where R_j is the jth element of the rate catalogue. Selection of an event is carried out by taking the product of a random number $u_2(0,1)$ and the total rate R_N and then performing a binary search to find the element R_n of the rate catalogue such that $R_{(n-1)} < u_2 R_N < R_n$. Afterwards, the configuration is updated to C_n and the simulation time is increased according to Equation 7.7 where $u_3(0,1)$ is a random number uncorrelated with u_2. Using this approach, each element of the rate catalogue has a probability of

being selected that is proportional to the rate at which the event occurs.

$$R_j = \sum_{j=1}^{N} r_{ij} \tag{7.6}$$

$$\Delta t = R_N^{-1} \ln \frac{1}{u_3} \tag{7.7}$$

For each kMC simulation a MC simulation was first conducted using the methodology described above. The final configuration of the MC simulation was used as the initial state of the kMC simulation. Each kMC simulation was allowed 1000 kMC steps where a single kMC step would be comprised of N diffusion events, i.e. time steps, where $N = 900$ is the number of sites in the simulation.

Diffusivity Calculations

The tracer diffusivity, D_T can be calculated from the mean squared displacement (MSD) of atoms over the course of the simulation according to Equation 7.8 where D_T is the tracer diffusivity, n is the number of spatial dimensions, and t is the simulation time [132].

$$D_T = \lim_{t \to \infty} \frac{MSD}{2nt} \tag{7.8}$$

The temperature and composition dependence of the tracer diffusivity can then be further described as shown in Equation 7.9

$$D_T(\chi, T) = \frac{a^2}{n} \Gamma(\chi, T) f_T(\chi, T) \tag{7.9}$$

where $f_T(\chi, T)$ is the hop correlation factor, a is the nearest-neighbor hop distance, and $\Gamma(\chi, T)$ is the average single-particle jump rate [161]. The correlation factor, $f_T(\chi, T)$ contains the so-called 'memory effects' that arise as a result of correlated hops. The correlation factor can be determined from simulations by considering the relationship the average number of hops as shown

in Equation 7.10 [161].

$$f_T = \frac{MSD}{a^2 \langle N_h \rangle} \tag{7.10}$$

Frequently, the diffusivity can be described by an Arrhenius relationship defined by Equation 7.11, where D_0 is the diffusivity prefactor and Q is the apparent activation energy. When diffusivity is plotted against inverse temperature on a semi-log plot, these quantities are related to the intercept and slope respectively. Over the course of our kMC simulations, the MSD and time were stored and used to fit the diffusivity using the least-squares method and compute the correlation factor.

$$D_T = D_0 \exp\Big(- \frac{Q}{k_B T} \Big) \tag{7.11}$$

Order Parameters

To quantify the degree of ordering in our simulations, we have elected to use the Warren-Cowley [171, 172] short-range order parameters $\alpha^{(n)}$ defined according to Equation 7.12 where n corresponds to the neighbor shell. For example, $\alpha^{(1)}$ would correspond to an SRO defined by nearest-neighbor bonds. Here, $p_{ij}^{(n)}$ is the average fraction of unlike bonds in the nth shell of an atom and χ_A and χ_{Va} are the atomic fraction of atoms and vacancies respectively.

$$\alpha^{(n)} = 1 - \frac{p_{ij}^{(n)}}{2 \chi_A \chi_{Va}} \tag{7.12}$$

Long-range order was described using the parameter ζ [173] defined according to Equation 7.13 where r_A is the fraction of sites that are correctly occupied by atoms when compared to the ground state, *i.e.*, the ordered 'checkerboard' structure that the simulation is initialized in.

$$\zeta = \frac{r_A - \chi_A}{1 - \chi_A} \tag{7.13}$$

7.1.3 Results & Discussion

'Checkerboard' Structure

The simulation structures after 1000 Monte Carlo steps using the 'checkerboard' Hamiltonian are shown as a function of temperature and composition in Figure 7.3. Here, vacancies are shown as black and atoms as white. At the lowest temperature, ordered domains are seen at all compositions except $\chi_A = 0.15$ and $\chi_A = 0.85$. At the $\chi_A = 0.50$ composition the whole simulation domain has ordered with the exception of single site. At the intermediate temperature, the degree of ordering is much lower, though some small ordered domains remain for the $\chi_A = 0.35$, $\chi_A = 0.50$, and $\chi_A = 0.65$ compositions. Unsurprisingly, the most substantial ordering remains present at the $\chi_A = 0.50$ composition. At high temperatures virtually no ordered domains are present.

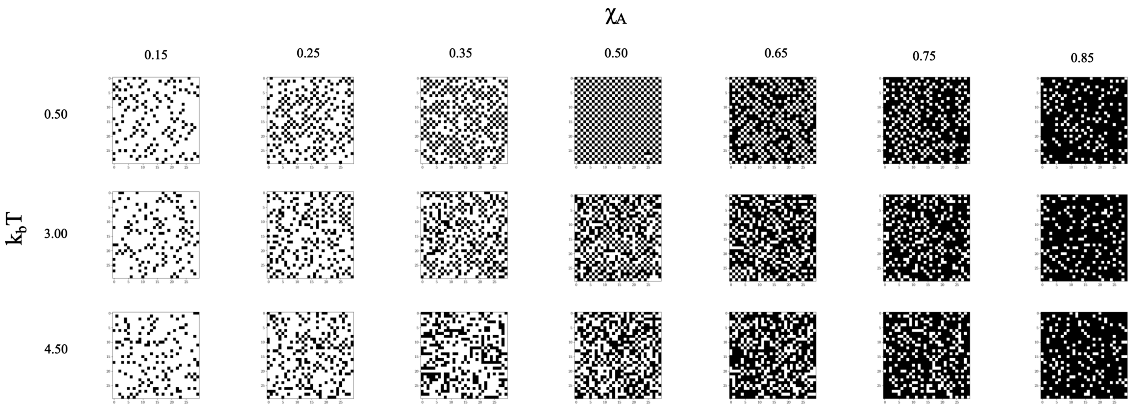

Figure 7.3: The simulation structure generated by a Monte Carlo simulation of 1000 steps with energetics calculated according to Equation 7.1. At low temperature there are substantial ordered domains of the 'checkerboard' structure are present, especially at $\chi_A = 0.50$ wherein the entire simulation has ordered except for a single site. At the intermediate temperature much of the short-range order is lost except for some small ordered domains present at $\chi_A = 0.35$, $\chi_A = 0.50$, $\chi_A = 0.65$. At high temperatures the ordering has disappeared.

To better understand the effects of temperature and composition on short range order in this system, we have plotted the Warren-Crowley parameters for the first, second, and third nearest neighbors as a function of temperature for several different compositions. Figure 7.4 shows that in the low temperature limit for the $\chi_A = 0.50$ composition $\alpha^{(1)} \rightarrow -1$, indicating the presence of

unlike spins in the nearest neighbor shell whereas $\alpha^{(2)} \rightarrow 1$ and $\alpha^{(3)} \rightarrow 1$ indicating the presence of alike spins in the second and third neighbor shells respectively. Of course, these are expected results since the Hamiltonian was chosen in order to construct the 'checkerboard' structure by penalizing same type nearest neighbor bonds. In the high temperature limit, all of the Warren-Crowley parameters trend towards zero as expected for a random solution.

The diffusivity and first nearest neighbor SRO parameter $\alpha^{(1)}$ in the kMC simulations are plotted in Figure 7.5a as a function of temperature for compositions ranging from $\chi_A = 0.15$ to $\chi_A = 0.85$. At high temperatures, the alloy is disordered and the slope of the diffusivity, *i.e.* the apparent activation energy, appears to be roughly the same for all compositions. However, in the low temperature limit, several compositions exhibit changes in apparent activation energy, with the most dramatic change at the $\chi = 0.50$ composition where there is a significant increase. Interestingly, this composition also possesses the greatest degree of short-range order as $^{(1)} \rightarrow -1$.

Figure 7.5b shows the diffusivity and SRO results obtained as a function of composition at temperatures ranging from $k_bT = 1.5$ to $k_bT = 3.0$. Examination of the trends in $\alpha^{(1)}$ reveal that for all of the temperatures sampled there is a peak in the SRO corresponding to the $\chi = 0.50$ composition. Furthermore, this peak is associated with local minima in the diffusivity at the same composition for $k_BT = 1.5$ and $k_BT = 2.0$, but no minima are present at the higher temperatures sampled. Additionally, we see that $\alpha^{(1)} > 0.80$ at the $\chi = 0.50$ composition for the two curves that display local diffusivity minima, whereas $\alpha^{(1)} < 0.5$ for the curves that do not. Furthermore, we note that the asymmetry of the tracer diffusivity about $\chi_A = 0.50$ is due to the availability of adjacent vacancies for atoms to hop to changing as a function of vacancy concentration.

Figure 7.6a shows the diffusivity (blue circles), SRO (red squares), LRO (green diamonds), and correlation factor (purple triangles) data at the $\chi_A = 0.50$ composition as a function of temperature. The black dashed lines indicate a bilinear fit to the diffusivity data. The range of the two linear fits and their intersection was determined by plotting the sum of the residuals for both fits as points were added from one linear fit and removed from the other, and then selecting the partition that minimized the sum of the square of the residuals. The intersection of these two lines then

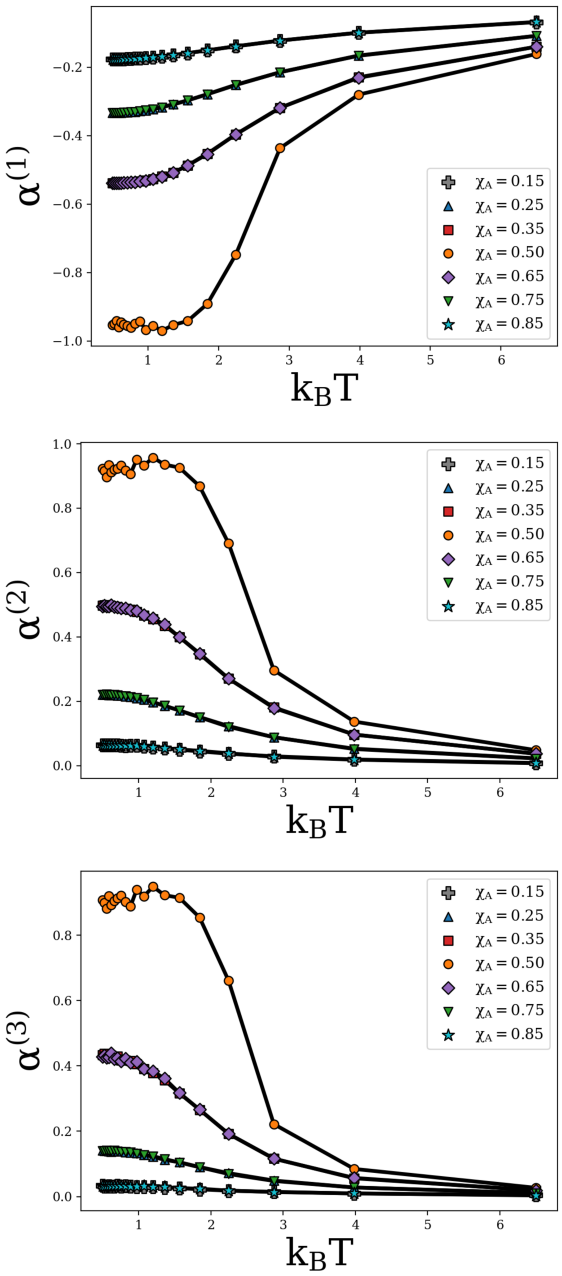

Figure 7.4: The SRO parameters determined by averaging the SRO parameters from the last 100 Monte Carlo steps of each simulation for simulations conducted with the Hamiltonian shown in Equation 7.1 Here, we can see that at low temperatures $\alpha^{(1)} \rightarrow -1$ indicating the presence of unlike spins in the nearest neighbor shell whereas $\alpha^{(2)} \rightarrow 1$ and $\alpha^{(3)} \rightarrow 1$ indicating the presence of alike spins in the second and third neighbor shells respectively.

determines the temperature where the diffusivity transitions from a high to low apparent activation energy. Using this method, the transition temperature was determined to be $k_b T_{trans} = 2.89$ and is shown as a dashed vertical line in Figure 7.6a.

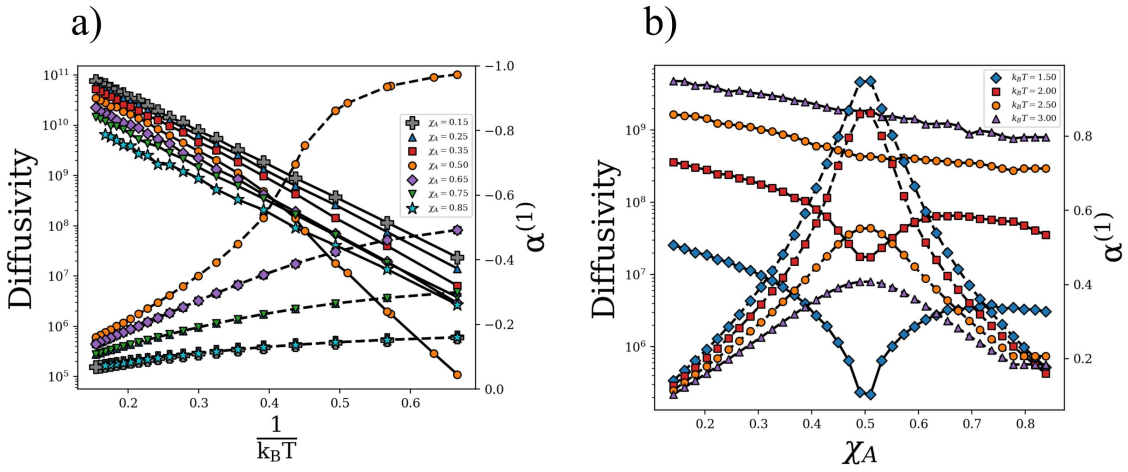

Figure 7.5: a) The tracer diffusivity (solid) and short-range order (dashed) results from kMC simulations conducted using the Hamiltonian in Equation 7.1 and SRO parameter in Equation 7.12 as a function of temperature. The plot demonstrates that at the $\chi_a = 0.50$ composition a rapid increase in short-range order is associated with a decline in diffusivity. **b)** The tracer diffusivity (solid) and short-range order (dashed) results from kMC simulations conducted using the Hamiltonian in Equation 7.1 and SRO parameter in Equation 7.12 as a function of composition. It can be seen that diffusivity minima correspond to SRO maxima at the $\chi_A = 0.50$ composition.

Examination of Figure 7.6 reveals several interesting insights. First, the transition from low to high apparent activation energy was determined to be $k_bT = 2.89$, whereas the LRO transition temperature appears to be $k_bT \approx 2.26$, which is consistent with Onsager's solution for the order-disorder transition of the two-dimensional Ising model [174]. Second, the correlation factor f_T is shown to smoothly decrease as the magnitude of SRO increases, even in the temperature regime where $\zeta = 0$, suggesting that hop correlation factor is more closely related to SRO than LRO. Figure 7.6b plots the correlation factor as a function of the magnitude of SRO and reveals a power-law relationship between the quantities with an exponent of roughly 2.30. Finally, Figure 7.6a also shows that the change in apparent activation energy is substantial, with the low temperature apparent activation energy being nearly twice that of the high temperature. At first, this seems surprising, especially considering that the low temperature apparent activation energy is greater than the energy barrier for any single hop present in the kMC simulation. However, this can all be rationalized by a detailed understanding of the energetics of diffusion and the contribution of memory effects.

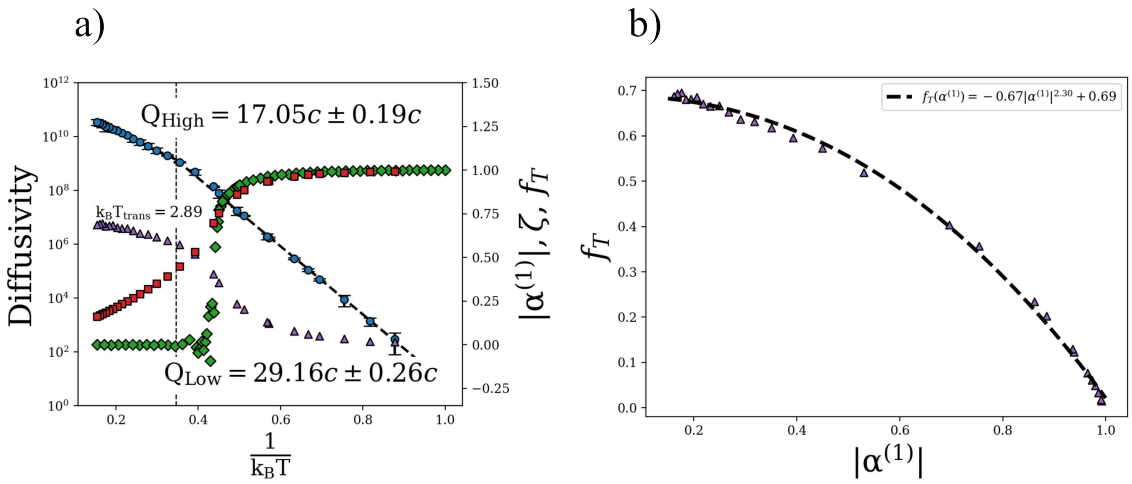

Figure 7.6: a) The tracer diffusivity (blue circles), SRO, $\alpha^{(1)}$, (red squares), LRO, ζ, (green diamonds) and correlation factor, f_T (purple triangles), of the $\chi_A = 0.50$ composition as a function of temperature as determined from kMC simulations. The black dashed lines indicate the linear fits to each section of data. A dashed vertical line indicates the transition temperature $k_b T_{trans} = 2.89$ at which the apparent activation energy is seen to increase. The apparent activation energies obtained from these fits are $Q_{High} = 17.05c \pm 0.19c$ and $Q_{Low} = 29.16c \pm 0.26c$ for the high temperature and low temperature respectively. **b)** The calculated correlation factor, f_T, plotted with respect to the absolute value of SRO, $\alpha^{(1)}$. The dashed line indicates a power-law fit to the relationship between f_T and $|\alpha^{(1)}|$.

The Four-Step Diffusion Mechanism and Memory Effects

To determine the mechanism causing the high apparent activation energy, we first looked at the distribution of energy barriers associated with successful jumps from our kMC simulations. Examples of such distributions for temperatures above and below the change in slope are shown in Figure 7.7a and 7.7b respectively. These distributions were generated by creating histogram of energy barriers found in the simulation, sampled at the end of each kMC step and normalized such that the distribution sums to unity. For simulations run at temperatures above the change in slope, the energy barriers are approximately normally distributed about $\Delta H = 15c$, which the reader may recall was the direction-independent energy barrier that we selected. Of course, this result is to be expected since in disordered configurations a single diffusion event should be equally likely to result in an increase or decrease in energy. In the low temperature case, the distribution is seen to be effectively bimodal with the most common barriers being the smallest and the largest present in the simulation. This suggests that, in the ordered state, the majority of diffusion events consist of an atom hopping out of the ordered state – an event that would have the greatest activation energy

– and then immediately hopping back into the ordered state due to the energetic preference and low activation barrier associated with a transition into the low energy ordered state.

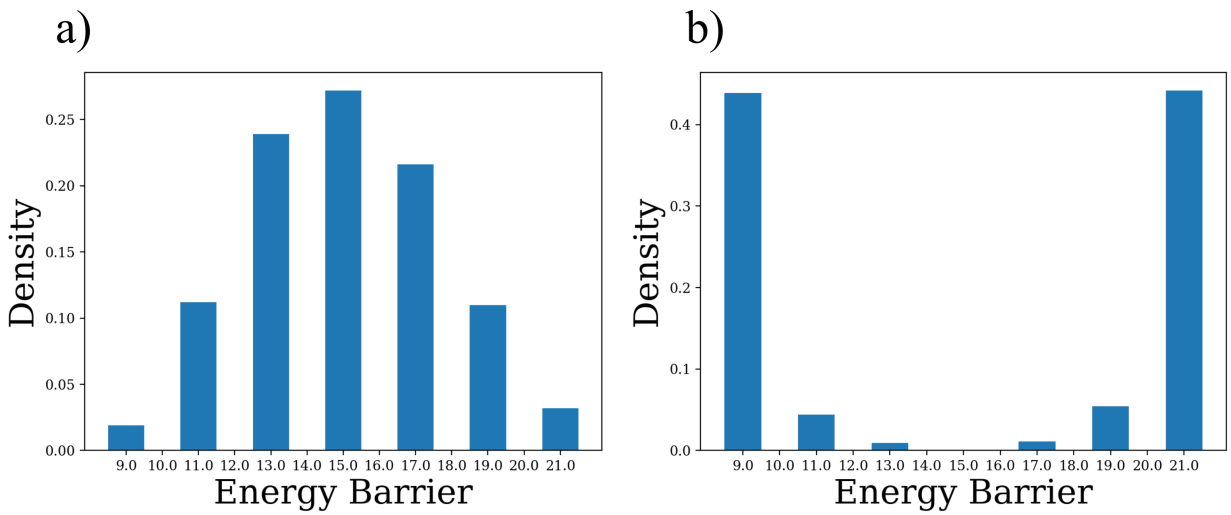

Figure 7.7: **a)**The distribution of energy barriers generated by kMC simulations at a temperature of $k_BT = 6.5$ using the Hamiltonian defined in Equation 7.1. The barriers were sampled at each 'kMC step' as previously defined for a total of 1000 samples per simulation. The energy barriers appear to be approximately normally distributed around $15c$. **b)** The distribution of energy barriers generated at a temperature of $k_BT = 1.5$ using the Hamiltonian defined in Equation 7.1. The distribution is approximately bimodal with the most common energy barriers being the smallest and largest possible in the simulation.

To completely understand the large apparent activation energy shown at low temperatures in Figure 7.6a, we first need to understand how diffusion occurs in the ordered 'checkerboard' structure. That is to say, when there is no intercalating network of vacancies for the atom to diffuse through, what is the simplest way to achieve net diffusion? Figure 7.8 depicts the simplest mechanism that results in two second nearest neighbor atoms switching places and thereby producing net diffusion via a four-step mechanism.

To determine the apparent activation energy of this mechanism, we performed a constrained kMC simulation on a 4×4 square lattice with an initial state as shown in the first step of Figure 7.8. The sites on the perimeter of the simulation cell were constrained such that no atoms on the perimeter were allowed to move. In other words, the only diffusion events available were those that occurred within the center four sites. The tracer 'diffusivity' of our four-step mechanism was then

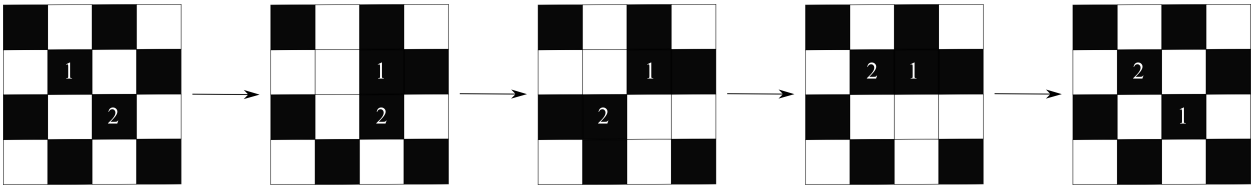

Figure 7.8: A schematic representing one mechanism by which net diffusion can occur in the ordered 'checkerboard' structure. The mechanism requires at least four hops after which two second nearest neighbor atoms swap places. The black squares represent atoms, and the white squares represent structural vacancies.

determined by counting the number of times that the atoms in this center square swapped places over the course of the simulation. We note that here the number of swaps refers to the number of times that the two atoms within these constrained kMC simulations swap places and is not the same as the number of times that an atom and vacancy swap places. Following the standard procedure, we were then able to extract the apparent activation energy associated with this mechanism by fitting the slope of the Arrhenius plot. This plot as well as the distribution of energy barriers over the course of the constrained simulation are shown in Figures 7.9a and 7.9b, respectively. These results provide two interesting insights into the low-temperature behavior presented in Figures 7.5 and 7.6. First, the apparent activation energy of the four-step mechanism was found to be $Q = 28.74c$, which is larger than any individual energy barrier present in the simulation, just as was found in the low-temperature behavior of the larger scale kMC simulations shown in Figure 7.6a. This result is encouraging because it provides support that the mechanism for net diffusion in our larger scale kMC simulations is indeed comprised of a multi-step process involving correlated hops.

The energy barrier distributions shown in Figure 7.9b are also quite similar to the low temperature distributions shown in Figure 7.7b. The most significant feature of both distributions is the fact that the most common events are the lowest and highest energy barriers present in the system. The prevalence of these energy barriers suggests that at low temperatures the atoms spend most of their time hopping the states shown in steps 1 and 2 in Figure 7.8. Hopping from step 1 to 2 requires the atom to go from a state in which all four of its nearest neighbors are vacancies, which is the most favorable state, into a state in which three of the four of its nearest neighbors are atoms,

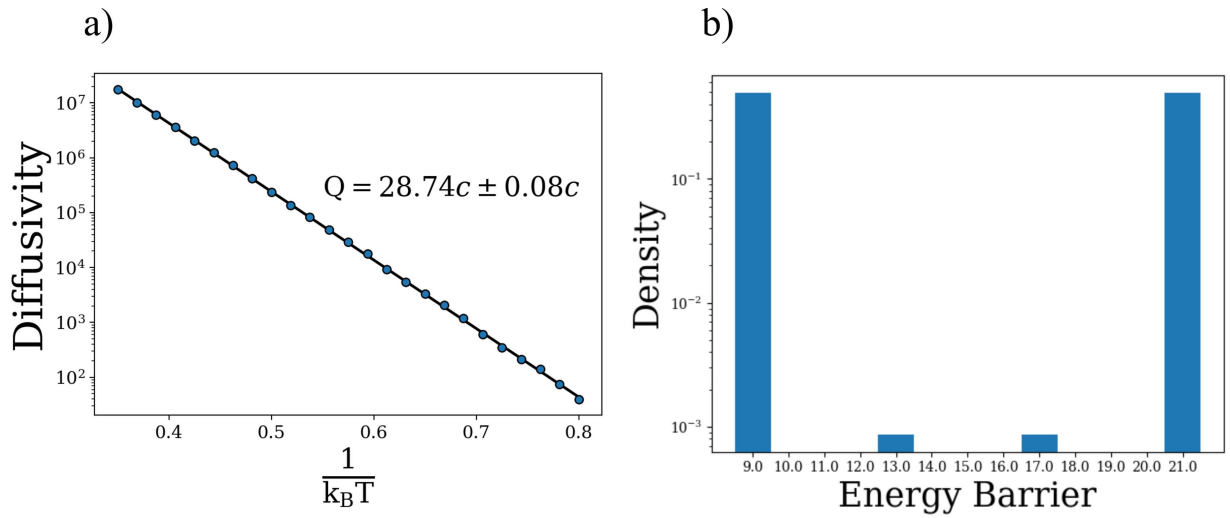

Figure 7.9: a) The Arrhenius plot constructed from the constrained kMC simulation representing the four-step mechanism. The apparent activation energy determined from fitting the slop was found to be $Q = 28.74c \pm 0.08c$, which is higher than any of the individual energy barriers present in the simulation. **b)** The distribution of energy barriers present in the constrained four-hop simulation. The most common energy barriers are the smallest and largest present in the system.

which is an energetically unfavorable state due to same-type neighbors. Though the least energetically favorable state would be for an atom to have four same-type nearest neighbors, the situation described here actually represents the largest and smallest energy barriers when determined according to Equation 7.4. This is because it is not possible for an atom to go from the lowest energy state to the highest energy state in a single jump due to the necessity for an atom to swap places with a neighboring vacancy in order for diffusion to occur. Thus, any diffusion event must result in the diffusing atom having at least one neighboring vacancy before and after the hop.

The kMC results demonstrate that indeed the apparent activation energy for diffusion is higher than any individual event at low temperatures, which must be a result of correlated events. As noted in [161–163], the apparent activation energy can be split into contributions from the total hop rate and the correlational effects: $Q = Q_{corr} + Q_{hop}$. At low temperatures, the total Q_{hop} is the largest barrier, here $21c$, and so the Q_{corr} is approximately $8c$. While this approach provides an understanding of the additional energy barrier and its origins, it is unable to concretely quantify the activation energies without direct simulations.

Here, we take an alternative approach (developed by Xiaochuan Tang) by considering a five-state random walk as illustrated in Figure 7.10a, an atom must hop across four energy barriers successfully and each in succession. The probability of the atom in state n at time t is $P(n,t)$ and the initial condition is $P(n,0) = \delta_{n_1}$. Because the transition rates between consecutive states are known and the new walk depends on previous walks, the evolution of $P(n,t)$ can be expressed in a Markov chain where the transition matrix is as follows:

$$\frac{dP(n,t)}{dt} = r_{n-1\to n}P(n-1,t) + r_{n+1\to n}P(n+1,t) - (r_{n\to n-1} + r_{n\to n+1})P(n,t) \tag{7.14}$$

The physical meaning of Equation 7.14 is the probability rate of change equals the net flux, where $r_{n-1\to n} = \nu \exp\left(-\Delta H_{n-1\to n}/k_B T\right)$ is the rate for walking from the state $n-1$ to n. After obtaining $P(n,t)$ from Equation 7.14, the net rate to reach state 5 can be computed as $r_{4\to 5}P(4,t)$. Though the analytic solution of $P(n,t)$ does not exist, we can approximate the arrival time by the exponential distribution (Poisson's process) and obtain the apparent activation energy at low-temperature and high-temperature limits. In Dr. Tang's approximate model, the net jump time from state 1 to 5 is the sum of the time for all possible net jumps from the state $n-1$ to n where $n \leq 5$. At high temperatures, the apparent activation energy is

$$\Delta H = \frac{4\Delta H^*_{12} - 3\Delta H^*_{21} + 6\Delta H^*_{23} - 4\Delta H^*_{32} + 6\Delta H^*_{34} - 3\Delta H^*_{43} + 4\Delta H^*_{45}}{10} \tag{7.15}$$

And at low temperatures, the apparent activation energy in our example is

$$\Delta H = \Delta H^*_{12} + \Delta H^*_{23} - \Delta H^*_{21} \tag{7.16}$$

which makes intuitive sense since it is simply the energy level of the highest transition state in the sequence of hops shown in Figure 7.10a.

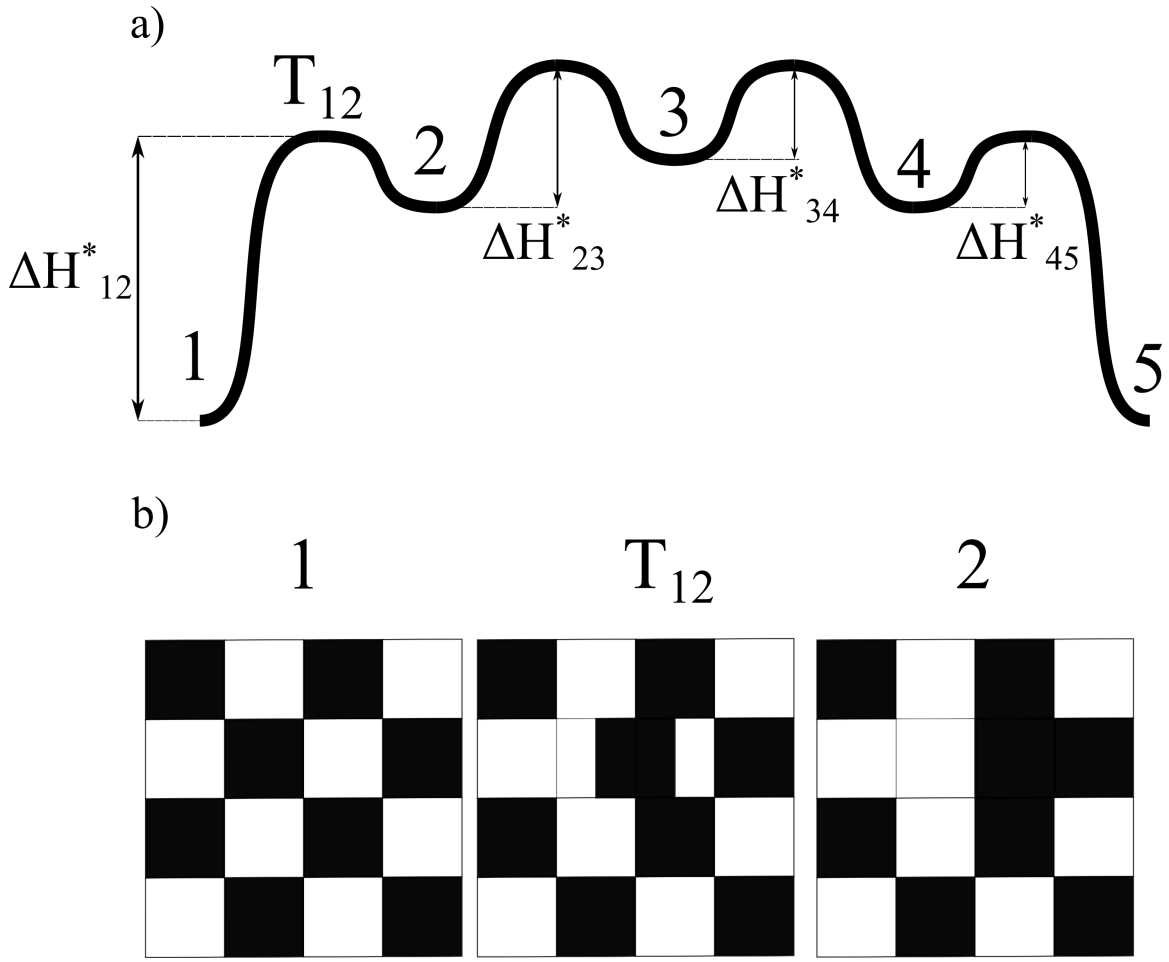

Figure 7.10: a) A schematic representation of the potential energy landscape throughout the four-step process. Each equilibrium position is labelled 1-5 corresponding to the configurations in Figure 7.8. The label T_{12} indicates the transition state between configurations 1 and 2. We note that using the Brønsted–Evans–Polanyi principle, all of the transition states have the same energy; however, under our analytical model this assumption is relaxed. The energy barriers between each position are labelled and correspond to the four energy barriers present in the distribution in Figure 7.9b. **b)** The configuration of atoms at at the equilibrium and transition positions during the hop from 1 to 2.

Inserting the values from the energy barrier distribution in Figure 7.9b, $\Delta H^*_{12} = \Delta H^*_{54} = 21c$, $\Delta H^*_{23} = \Delta H^*_{43} = 17c$, $\Delta H^*_{34} = \Delta H^*_{32} = 13c$, and $\Delta H^*_{45} = \Delta H^*_{21} = 9c$, we find that the apparent activation energy is $29.0c$ in the low-temperature limit and $17.0c$ in the high-temperature limit. The analytical value at low temperatures compares well with the results of the constrained kMC simulation shown in Figure 7.9a, indicating a match between Dr. Tang's analytical theory and the constrained kMC. Additionally, the apparent activation energies from our four-step mechanism are within one standard deviation of error of the result determined from the large-scale kMC in

both low temperatures and high temperatures shown in Figure 7.6. Due to the agreement of the apparent activation energies across our low temperature large-scale kMC, constrained kMC, and approximate model, we conclude that the mechanism for net diffusion present in the low temperature large-scale kMC is the proposed four-step mechanism. This, in turn, provides a reasonable explanation for the relationship between the increase in SRO and the increase in activation energy, since the four-step mechanism assumes that the diffusion is constrained by a preference to retain SRO which leads to additional correlational effects on the tracer diffusivity.

'Labyrinthine' Structure

The simulation structures after 1000 Monte Carlo steps with energetics calculated according to Equation 7.2 are shown as a function of temperature and composition in Figure 7.11. As with the structures generated by the Hamiltonian in Equation 7.1, the structures become disordered as the simulation temperature is increased with only small ordered regions present at $k_bT = 3.00$ and virtually random arrangements at $k_bT = 4.50$. At the lowest temperature, two distinct types of ordering are present. The first and most obvious is shown at the $\chi_A = 0.50$ composition in which the entire simulation domain has ordered into stripes along the x-axis. This structure is what we have called the 'Labyrinthine' structure in Figure 7.1 because of the appearance of the structure being reminiscent of a labyrinth when many ordered domains of different orientation are present. The second structure is the 'hatch' structure which is most prominent at the $\chi_A = 0.25$ and $\chi_A = 0.75$ compositions, though small domains are present at all compositions with the exception of $\chi_A = 0.50$.

The SRO parameters are shown in Figure 7.12. In contrast to the results from the 'checkerboard' simulations, we see very little ordering of the first-nearest neighbors, with the exception of the $\chi_A = 0.25$ and $\chi_A = 0.75$ compositions for which $\alpha^{(1)} \rightarrow -0.25$ at low temperatures, corresponding to ordering in the 'hatch' structure. Of course, the lack of strong nearest neighbor interactions is expected since the Hamiltonian in Equation 7.2 is only written in terms of second and third nearest neighbor interactions. As a consequence, Figure 7.12 shows $\alpha^{(2)} \rightarrow -1.0$ and $\alpha^{(3)} \rightarrow 1.0$ for the $\chi_A = 0.50$ composition at low temperatures. $\alpha^{(3)}$ indicates low-temperature

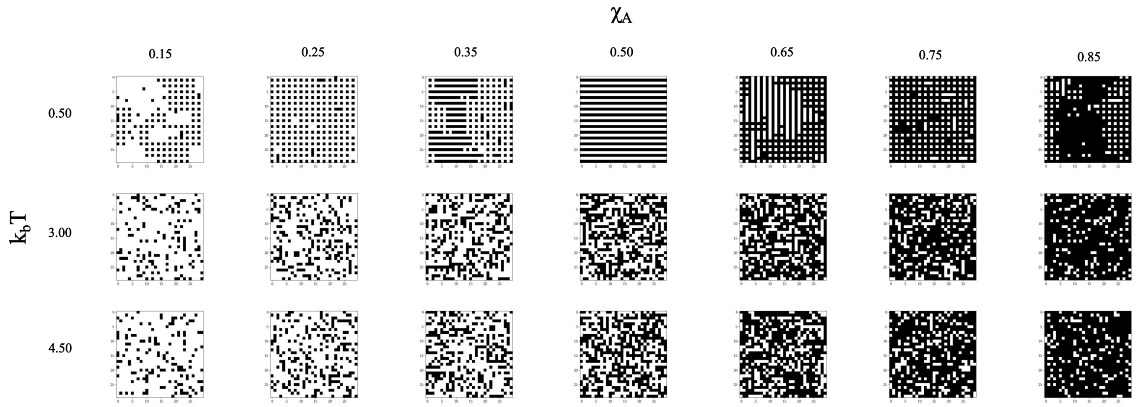

Figure 7.11: The simulation structures generated by Monte Carlo simulations of 1000 steps with energetics calculated according to Equation 7.2. At low temperature there are substantial ordered domains of the 'labyrinthine' structure are present, especially at $\chi_A = 0.50$ wherein the entire simulation has ordered in a single direction along the x-axis. The other compositions depict a 'hatch' type of structure. At the intermediate and high temperatures most of the short-range order is lost.

attraction between same-type third nearest neighbors for all of the compositions sampled. This suggests that the third nearest neighbor interactions may dominate in forming the 'hatch' structure whereas the 'labyrinthine' structure requires both repulsion of second nearest neighbors and attraction of third nearest neighbors. In fact, $\alpha^{(3)} \rightarrow 1$ at low temperature for all of the compositions sampled. This is because at low temperatures all compositions show some degree of ordering.

Figure 7.13 plots the diffusivities and SRO results obtained from kMC simulations as a function of temperature and composition for simulations run with Hamiltonian 7.2. As before, we see that there is an increase in apparent activation energy (slope) associated with the rising SRO. Most apparently, the $\chi_A = 0.50$ composition appears have the largest increase in its activation energy as well as the most SRO. At low temperatures, Figure 7.13b indicates that there are multiple minima in diffusivity with respect to composition. These minima also appear to correspond to peaks in the SRO at the $\chi_A = 0.25$, $\chi_A = 0.50$, and $\chi_A = 0.75$ compositions and thus correspond to the ordered low energy 'labyrinthine' and 'hatch' structures.

Figure 7.14a shows the tracer diffusivity, SRO, and correlation factor as a function of inverse temperature for the $\chi_A = 0.50$ composition as this state has the largest change in diffusivity. There is a notable change in the diffusivity slope on the semilog plot at $k_b T_{trans} = 2.27$. The value of the SRO parameter $\alpha^{(3)}$ at this temperature was roughly 0.16. In contrast to the 'checkerboard'

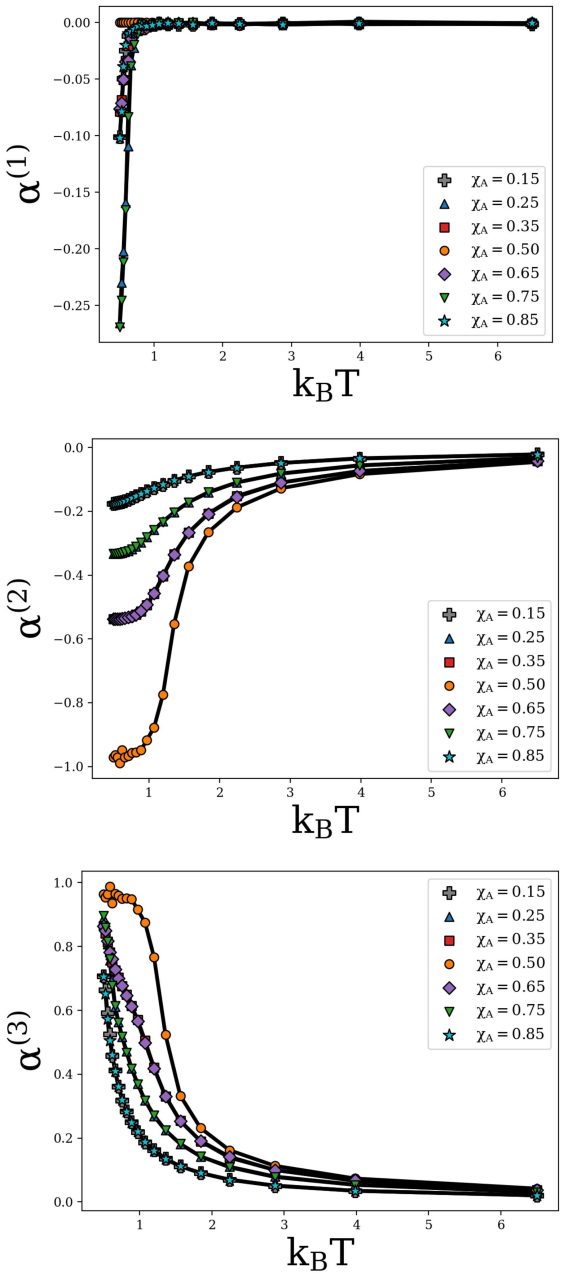

Figure 7.12: The SRO parameters determined by averaging the SRO parameters from the last 100 Monte Carlo steps of each simulation for simulations conducted with the Hamiltonian shown in Equation 7.2.

structure, the magnitude of the change in slope is lower and there is a lesser degree of SRO at the transition temperature.

Figure 7.14b depicts the correlation factor as a function of $\alpha^{(3)}$. The figure shows that for the 'labyrinthine' structure, as was also seen in the 'checkerboard' structure, there is a power-low type

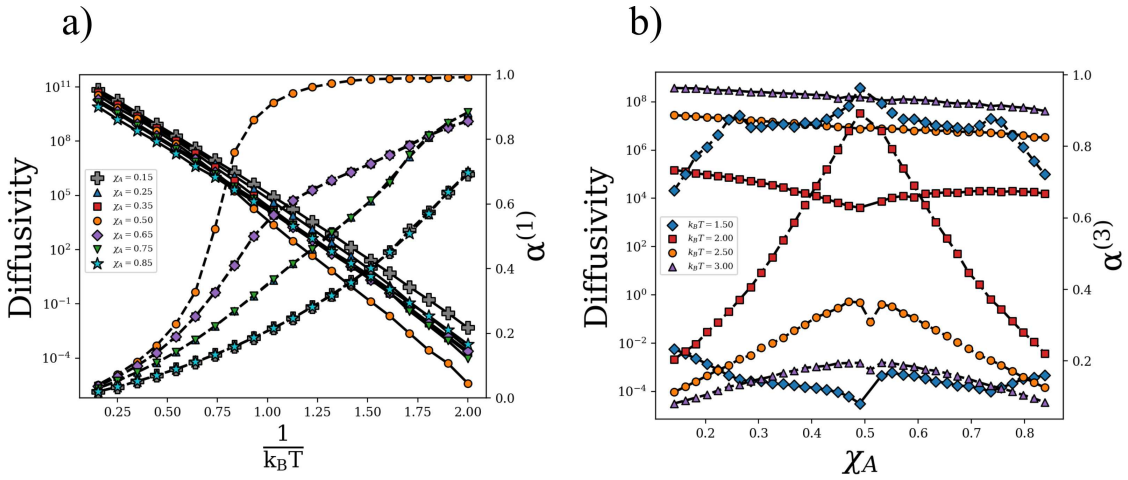

Figure 7.13: a) The tracer diffusivity (solid) and short-range order (dashed) results obtained from kMC simulations conducted using the Hamiltonian in Equation 7.2 and SRO parameter in Equation 7.12 as a function of temperature. The results demonstrate the correlation between SRO and a change in diffusion activation energy as the slope of the semi-log plot increases at temperatures below the order-disorder transition. This effect is most apparent for the $\chi_A = 0.50$ composition in which the ordering is strongest and corresponds to the lowest diffusivity at temperatures below the order-disorder transition. **b)** The tracer diffusivity and SRO as a function of composition. Here, we can see that for the $k_B T = 1.50$ curve there are three maxima in SRO corresponding to the onset of the 'hatch' structures at $\chi_A = 0.25$ and $\chi_A = 0.75$ compositions as well as the 'labyrinthine' structure at $\chi_A = 0.50$. Here, we can see that this corresponds to minima in diffusivity at $\chi_A = 0.50$ and $\chi_A = 0.75$. As the temperature increases, less ordering was evident as the diffusivity curves become essentially linear because of the compositional dependence of the diffusivity prefactor.

relationship between the correlation factor and SRO with an exponent of roughly 2.30. In the case of the 'labyrinthine' structure; however, the power-law fit contains a smaller leading coefficient which may be due to the fact that the ordering of the 'labyrinthine' structure contains a larger network of connected diffusion when compared to the 'checkerboard' structure that has very few connected vacancies.

The energy barrier distributions for the simulations conducted above and below the transition temperature, at $k_b T = 6.50$ and $k_b T = 0.71$, are plotted in 7.15a and 7.15b respectively. The energy barrier distribution shown in Figure 7.15a strongly resembles that of Figure 7.7a, wherein the energy barriers are normally distributed around $15c$. However, we note a major difference in the low-temperature distribution, shown in Figure 7.15b, between the ordered 'labyrinthine' structure and the 'checkerboard' structure. As opposed to the bimodal distribution observed for the 'checkerboard,' the distribution for the 'labyrinthine' structure is trimodal with the most common

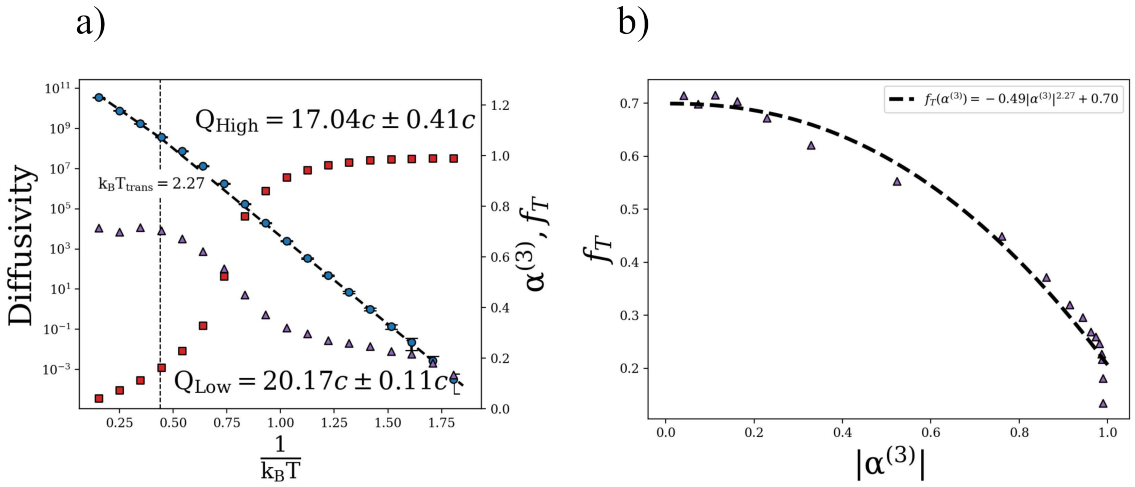

Figure 7.14: **a)**The tracer diffusivity (blue circles), SRO, $\alpha^{(3)}$, (red squares), and correlation factor, f_T (purple triangle), for the kMC simulations run with the Hamiltonian in Equation 7.2 at $\chi_A = 0.50$. As was seen before with the first Hamiltonian, there is a slight change in apparent activation energy (slope) at $k_bT = 2.27$. In contrast with the 'checkerboard' structure, the 'labyrinthine' structure has a much less significant change in slope. The value of $\alpha^{(3)}$ at the transition was roughly 0.16. **b)** The calculated correlation factor, f_T, plotted with respect to the absolute value of SRO, $|\alpha^{(3)}|$. The dashed line indicates a power-law fit to the relationship between f_T and $|\alpha^{(3)}|$.

energy barrier being $15c$. In the 'labyrinthine' structure, this energy barrier is also associated with diffusion down a row of vacancies, since the local environment is constant for an atom diffusing anywhere along a vacant row. According to our earlier idea that these vacant rows would act as high-diffusivity pathways, this energy barrier would be most common. The other two peaks are associated with the largest changes in energy available for a single jump given that the energetics are determined by Equation 7.2. As we saw in the 'checkerboard' structure, the high frequency of occurrence of these barriers is likely due to an atom jumping into and out of the ordered structure repeatedly before any net diffusion occurs. Thus, in the 'labyrinthine' structure, diffusion likely occurs by an atom jumping into and out of the low energy ordered structure repeatedly until it escapes its initial local environment. Once the atom has distanced itself from the initial local environment, a net displacement is achieved via diffusion along a string of vacancies acting as a high-diffusivity pathway.

Finally, we can use these energy barrier distributions as inputs in our approximate solution shown in Equations 7.15 and 7.16 to estimate the apparent activation energy for a four-step diffu-

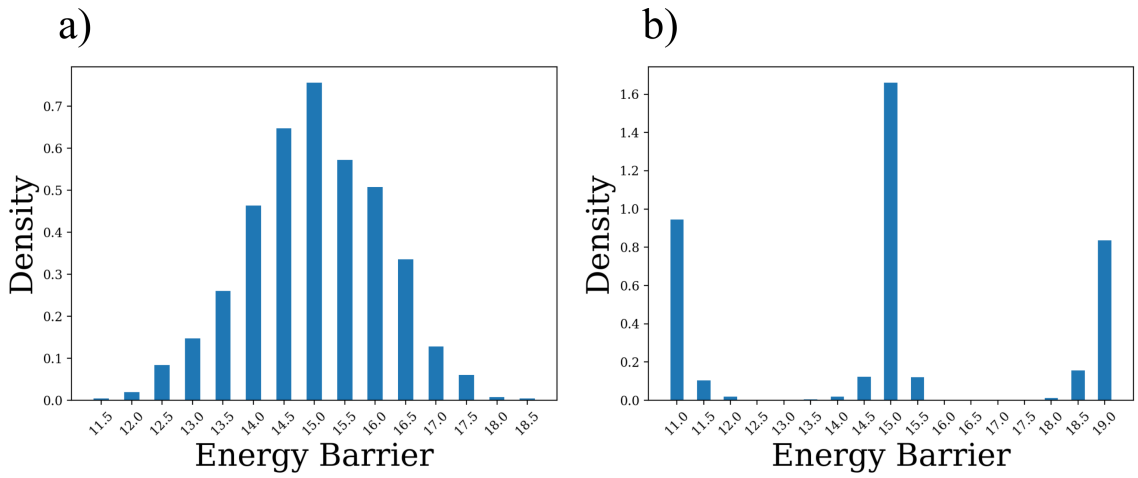

Figure 7.15: a) The distribution of single-hop energy barriers present in a kMC simulation conducted at $k_bT = 6.5$ with energetics according to Equation 7.2. The energy barriers are approximately normally distributed around $15c$, which is associated with a hop with no net change in energy. **b)** The distribution of single-hop energy barriers present in a kMC simulation conducted at $k_bT = 0.71$. The energy barriers are distributed approximately trimodally, with the most frequent jumps being those with no net energy change as well as the jumps associated with the greatest changes in energy.

sion event as we did with the 'checkerboard' structure. A schematic of this diffusion process is shown in Figure 7.16. Although the approximate model was constructed in order to represent the four-step mechanism described previously, it can be applied here to describe a scenario in which an atom jumps out of the ordered 'labyrinthine' structure and into a row of vacancies. The atom then completes two jumps within the row of vacancies before it is able to jump back into the ordered structure, though in the larger scale simulations it is likely that the diffusing atom jumps along the row of vacancies many times before it is able to jump back into the ordered structure.

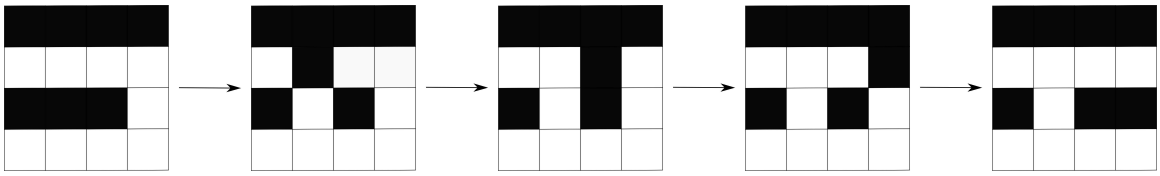

Figure 7.16: A schematic representing the configurations described by the application of our approximate model to diffusion along a row of vacancies in the ordered 'Labyrinthine' structure. The atom (black) begins by jumping into a row of vacancies (white) followed by two hops along the row and then a final jump back into the row of atoms, though it should be noted here that the ordered structure is imperfect due to the presence of an additional vacancy in the row of atoms. In a large-scale simulation, it is likely that many more jumps along the row of vacancies would occur before the atom is able to jump back into thow of atoms.

To describe this situation, we use $\Delta H_{12}^* = 19c$, $\Delta H_{23}^* = \Delta H_{34}^* = 15c$, and $\Delta H_{45}^* = 11c$, as inputs to the model, since, within the row of vacancies, the energy barrier is $15c$. Given these inputs, the apparent activation energy at high temperature is $16.2c$ which is close to kMC results. However, the apparent activation energy at low temperatures from Equation 7.16 gives Q=23c, which is somewhat larger than the apparent activation energy determined from our fit of the kMC data. According to Dr. Tang's approximate model, the apparent activation energy at low-temperature limit can be written in Equation 7.16 only when the activation energy for the net jump $\Delta H_{12}^* + \Delta H_{23}^* - \Delta H_{21}^*$ is much larger than the activation energy for other net jumps. In this case, there are two net jumps with the activation energy $23c$ ($\Delta H_{12}^* + \Delta H_{23}^* - \Delta H_{21}^*$,$\Delta H_{12}^* + \Delta H_{23}^* + \Delta H_{34}^* - \Delta H_{32}^* - \Delta H_{21}^*$). This would then explain the large modes of energy barriers $11k_B$,$15k_B$, and $19k_B$ in Figure 7.15b, which are associated with the back-and-forth jumps (ΔH_{12}^*, ΔH_{21}^*) and ($\Delta H_{23}^*, \Delta H_{32}^*$). We also notice that the activation energy of the net jump $\Delta H_{12}^* = 19c$ which is much less than $23c$ and therefore the approximate model has less accuracy, presumably because the actual diffusion process here contains more than four jumps. In this case, it would be more accurate to use the rigorous solution from Equation 7.14 to obtain the apparent activation energy at low temperatures. While the approximate model was developed based on a simplified physical process, it is shown to still provide reasonable estimates.

7.1.4 Summary & Conclusions

In this work, we have used Monte Carlo and Kinetic Monte Carlo simulations on a square lattice in order to investigate the influence of vacancy ordering on diffusion. We examined two different energetic scenarios that produced three different ordered structures. In the first case, the ordered 'checkerboard' phase formed near $\chi_a = 0.50$ because of the energetic penalty for like-type nearest neighbors in Equation 7.1. In the second case, two ordered structures formed: the 'hatch' structure at the $\chi_a = 0.25$ and $\chi_a = 0.75$ compositions and the 'labyrinthine' structure at $\chi_a = 0.50$. These structures developed as a result of repulsive interactions between like second nearest neighbor sites and attraction between like third nearest neighbor sites.

The degree of short-range order was quantified using the Warren-Cowley ordering parameters for the first, second, and third nearest neighbors. We found that for each case the apparent activation energy for tracer diffusion was larger in structures that had a high degree of SRO when compared to the disordered structures. This was then concretely demonstrated by analysis of the correlation factor, which was determined to have a power-law relationship with SRO in both the 'checkerboard' and 'labyrinthine' structures. In each case, the power-law exponent was roughly 2.30 whereas the leading coefficient's magnitude was greater for the 'checkerboard' structure, suggesting that the strength of the relationship between hop correlation factor and SRO depends on the extent of vacancy networks available in the ordered structure. This is supported by the fact that the 'labyrinthine' structure, which contains strings of vacancies that may act as high diffusivity pathways, possesses a weaker relationship between hop correlation factor and SRO than the 'checkerboard' structure that has no interconnected vacancies.

In our examination of the effects of concentration on diffusivity, we found that minima in diffusivity corresponded to maxima in SRO parameters. This again suggests that as SRO increases diffusivity is hindered due to memory effects contained within the hop correlation factor. To explain the mechanism for orderings effect on tracer diffusion, we constructed an analytical model based on kinetics theory. Our results suggest ordering inhibits diffusion, even when 'high diffusivity pathways' are present, because the rate-limiting step in the kinetic process becomes escaping the local environment of an energetic minima. This step consists of a diffusing atom or vacancy jumping in and out of a low-energy local configuration repeatedly. This process occurs because of a strong energetic bias for the atom to remain in the ordered configuration. In effect, the ordering acts as 'traps', keeping diffusing atoms stuck in the vicinity of the ordered configuration. We found that this process could result in an apparent activation energy for tracer diffusion that surpasses any individual energy barrier in the diffusive process. We note that the diffusion of dilute species, such as light elements, is likely to be enhanced by the presence of strings of structural vacancies in cases where the diffusing species does not form ordered sublattices. A similar inhibition of diffu-

sion may be achieved in these cases if defects are present to act as low-energy 'traps'; for example, when diffusing hydrogen encounters TiC precipitates in α-iron [175].

Turning our attention to the work of Sarian, whose carbon diffusion anomaly in substoichiometric titanium carbide partially motivated this study, we can make several comments. First, Sarian hypothesized that the change in carbon tracer diffusion activation energy was the result of a vacancy order-disorder transition; though we pointed out that the work of Gusev indicates that the order-disorder transition in titanium carbide occurs at significantly lower temperature than Sarian's anomaly. However, Gusev reports the phase boundaries for LRO, but here we have shown that diffusion is likely more strongly affected by SRO, which typically persists to higher temperatures than LRO. Therefore, the results presented here support Sarian's hypothesis and suggest that the reported change in activation energy was likely a result of a short-range order-disorder transition on the carbon sublattice of titanium carbide. This suggests that it is SRO, not LRO, that affects the properties of diffusion and implies that diffusivity can be directly impacted by local SRO in vacancy-ordered structures with the greatest impact in structures that have a stronger tendency to form SRO.

7.2 Understanding the Anomalous Carbon Diffusion in Ti_3C_2

7.2.1 Introduction

In the late 1960's Sarian performed tracer diffusion experiments in various refractory carbides [42, 50, 56]. Of particular interest is Sarian's tracer diffusion experiments of carbon-14 in TiC_x where the tracer diffusivity was reported to depend on concentration. Surprisingly, for some temperature ranges the carbon-14 tracer diffusivity was seen to decrease as carbon was removed from the lattice. This overall decrease was attributed to an increase in carbon diffusion activation energy as the carbon vacancy content increased. At the same time, the carbon tracer diffusion prefactor was seen to linearly increase with increasing carbon vacancy content. Thus, a reduction in overall carbon content simultaneously increased the diffusivity prefactor and activation energy with the overall effect of reducing the carbon-14 tracer diffusivity.

In his manuscript, Sarian reports a discontinuity in the diffusivity of $\mathrm{TiC}_{0.67}$ at 2353K, which he hypothesized was due to an order-disorder transition, though he was unable to conclusively establish the presence of long-range order using XRD or analysis of a Weissenberg photograph of a sample annealed for 8 hours at 2018K. From these results, he concluded that if ordering were present in their sample, it could only be short-range. Decades later, Gusev and Rempel calculated the phase boundaries of the vacancy-ordered phases in the Ti-C system using the order-parameter functional method. They reported an order-disorder transition temperature in $\mathrm{Ti_3C_2}$ of roughly 964K [140]. These phase boundaries were corroborated by specific heat measurements conducted by Lipatnikov and Gusev [176]. Thus, Sarian's lack of long-range order is supported both by theoretical and experimental evidence.

In the previous section, we used kinetic Monte Carlo simulations to examine the effects of vacancy ordering on diffusion on a 2D square lattice and achieved results that were phenomenologically similar to those reported by Sarian, suggesting that a vacancy order-disorder transition could hypothetically explain Sarian's anomaly. Specifically, we demonstrated that in 2D simulations of diffusion using simple Ising models that there is a change in activation energy for diffusion that is correlated with changes in short range order, not long-range order in those structures. However, those results are based on an Ising model and are carried out in two dimensions and thus are not conclusive. In the current work, we use a combination of density functional theory simulations implemented in VASP, the cluster expansion method implemented using the alloy theoretical automated toolkit (ATAT) [65], and an in-house Monte Carlo and kinetic Monte Carlo code in order to attempt to understand how long-range order, short-range order, and jump correlation effects contribute to the apparent diffusivity as a function of temperature in $\mathrm{TiC_0}.67$. Thus, this work will provide a definitive test of Sarian's hypothesis and determine if the change of activation energy through changes in short range order can explain his observations.

7.2.2 Methodology

Diffusion Coefficients

To model the process of carbon diffusion on the carbon-vacancy sublattice of the B1 rocksalt $\mathrm{TiC_0}.67$ structure, we consider an interstitial diffusion process with the assumption that carbon atoms must exchange their position with nearest-neighbor vacancies in order to facilitate motion. The tracer diffusivity D_T for carbon atoms can then be written in terms of the squared displacement of the carbon atoms, as shown in Equation 7.17 [132].

$$D_T = \lim_{t\to\infty}\Big[\frac{1}{2nt}\big(\frac{1}{N_A}\sum_{i=1}^{N_A}\langle\vec{r_i}(t)\rangle^2\big)\Big] \tag{7.17}$$

In most cases, the apparent diffusivity can also be expressed as an Arrhenius quantity, as shown in Equation 7.18. Here, the apparent diffusivity can be separated into apparent prefactor and activation energy components D_0^{app} and Q_{app} which can be determined by fits from the tracer diffusivity data.

$$D_{\mathrm{app}} = D_0^{\mathrm{app}}\exp\big(-\frac{Q_{\mathrm{app}}}{k_bT}\big) \tag{7.18}$$

We note that here the apparent activation energy Q_{app} may be different from the energy barrier encountered by a diffusing atom during an individual hop. During such an event the energy barrier ΔE_a associated with the hop is equal to the difference between the energy associated with an atom at the saddle point of the hop, E_{saddle}, and the energy when the atom is at the initial position before the hop E_{initial}.

Thus, for any given hop, the energy barrier E_a depends on the shape of the potential energy surface around the hop. In contrast, Q_{app} represents the slope of the natural log of the tracer diffusivity when plotted with respect to the inverse temperature. As a result, the apparent diffusivity factor contains collective effects of all hops associated with atomic diffusion.

Cluster Expansion Method

To model diffusion in Ti_3C_2 we must first consider the configurational dependence of the total energy of the system. Using the cluster expansion method, any scalar quantity can be written as an expansion of effective cluster interactions (ECIs) and cluster orbits that act as descriptors for the crystal structure [64]. When all possible cluster interactions are included the cluster expansion is exact. In practice, a small set of cluster orbits (typically on the order of 25-50 different orbits) must be selected. Each cluster (except for the empty cluster) contains a combination of variable-composition species in the structure. For example, the simplest clusters contain individual carbon atoms or vacancies. As the cluster size, *i.e.* the number of sites within a cluster, increases, each cluster may contain a pair of nearest-neighbor sites, each being occupied by either a carbon atom or vacancy, or sets of three sites, four sites, and so on. In addition to cluster size, clusters are also described by the cluster diameter, which is defined as the maximum distance between two sites in the cluster. Each cluster belongs to a set of clusters, known as an orbit, which are equivalent via symmetry operations of the crystal as defined by its space group, *e.g.* translation by lattice vectors, rotations, inversions, etc. All clusters contained in an orbit possess the same ECI. The number of clusters contained within an orbit is known as the cluster multiplicity.

Using the cluster expansion method the energy of the crystal in configuration σ can be determined via Equation 7.19, where α denotes the cluster orbit (*e.g.* nearest neighbor pairs), m_α is cluster multiplicity, J_α is the ECI coefficient for orbit α, and $\overline{\Phi}_\alpha$ is the average of the cluster correlation functions. The average cluster correlation functions are defined as $\overline{\Phi}_\alpha = 1/N_\alpha \sum_i \left(\prod_j S_j \right)$ where S_j is the spin variable of the jth site in cluster i. Typically in binary systems the spin variable takes a value of either 1 or -1 depending on the species present at the site. The configuration σ then needs only to be a vector containing the spin variables S_j for each site.

$$E(\sigma) = \sum_\alpha m_\alpha J_\alpha \overline{\Phi}_\alpha \tag{7.19}$$

Thus, in order to determine the energy of an arbitrary configuration three things are needed: first, a set of cluster orbits. Second, the ECI coefficients, and third, the vector σ that contains the spin variable for each site.

In practice, the cluster expansion is carried out by fitting the ECIs in Equation 7.19 to a set of first-principles electronic structure calculations. To carry out our cluster expansion, we used the maps code, a constituent program of the ATAT that is capable of generating cluster expansions. Using maps we generated candidate structures of varying composition in the Ti-C system and determined their energies using the Vienna ab-initio Simulation Package (VASP). Following the VASP simulations, maps automatically generated cluster expansions and selected the set of orbits and ECIs that minimized the cross-validation score.

$$CV = \Big(\frac{1}{n}\big(\sum_{1}^{n}(E_i^{\mathrm{VASP}} - E_i^{\mathrm{CEM}})\Big)^{\frac{1}{2}} \tag{7.20}$$

Monte Carlo & Kinetic Monte Carlo Simulations

We employed the kinetic Monte Carlo (kMC) method to simulate the migration of carbon atoms on the carbon-vacancy sublattice of $\mathrm{Ti_3C_2}$ and numerically determine the apparent diffusivity as a function of temperature. To achieve this, each simulation was initialized at a constant carbon composition and temperature. The initial configuration of each kMC simulation representing thermal equilibrium was obtained using standard canonical Monte Carlo simulations. For each temperature the configuration after 500 Monte Carlo steps, *i.e.* 500 sweeps through the lattice, was used as the initial state for the kMC simulations. Each sweep through the lattice consisted of N_A swaps, equal to the number of carbon atoms in the simulation. To minimize the system energy and drive the system to equilibrium while keeping the carbon concentration constant Kawasaki Dynamics were used [165, 169]. For each swap, a single carbon atom and vacancy were selected and proposed to have their positions exchanged. If the exchange resulted in a decrease in energy, then the swap was immediately accepted and implemented. If the exchange resulted in an increase in energy, then the swap was accepted and implemented with a probability $P = \exp(-\frac{\Delta E}{k_b T})$ where ΔE is the change in energy associated with the exchange.

The general algorithm for the kMC simulations began by initializing the simulation time to $t = 0$ and implementing the initial state from the Monte Carlo simulations. Then, a rate catalogue was constructed according to Equation 7.21, where r_{ki} is the rate from state k into state i and the sum is over all possible transitions out of the current state.

$$R = \sum_i r_{ki} \tag{7.21}$$

After construction of the rate catalogue, a transition to carry out was selected by finding the jth element of R for which $R_{j-1} < u_1 R \leq R_j$ using binary search, where u_1 is a uniform random number on the interval (0,1]. The configuration is updated to the state j and the simulation time is updated by Δt according to Equation 7.22, where u_2 is a new uniform random number on the interval (0,1]. kMC simulations were considered to be finished after $500N_A$ repetitions of this process.

$$\Delta t = \frac{-\ln u_2}{R_{ki}} \tag{7.22}$$

Determination of the rates r_{ki} was carried out according to transition state theory and Equation 7.23, where ν is the attempt frequency, which we assumed to be 0.15×10^{12}Hz for all transitions, ΔE_a is the energy barrier associated with the transition from state k to state i, and T is the simulation temperature.

$$r_{ki} = \nu \exp(-\frac{\Delta E_a}{k_b T}) \tag{7.23}$$

Each energy barrier was calculated using the difference between the energies of the initial and final configurations of the hop ΔE_σ as well as a kinetically resolved activation energy ΔE_{KRA}. The kinetically resolved activation energy is a direction-independent energy barrier formulated according to the Brønsted–Evans–Polanyi principle [170]. Thus, when the energies of the initial and final configurations are equal $\Delta E_a = \Delta E_{\mathrm{KRA}}$.

$$\Delta E_a = \Delta E_{\mathrm{KRA}} + \frac{\Delta E_\sigma}{2} \tag{7.24}$$

To determine the value of ΔE_{KRA} we used the nudged elastic band (NEB) method implemented in VASP. The NEB method effectively finds the minimum energy pathway along the migration pathway, in this case of a carbon atom, between two energetically stable end points [177]. The saddle point is determined by creating images of the migrating atom along at discrete locations along the migration pathway. Next, energy minimization is conducted whereby the atom locations are connected to their neighboring images with an imaginary spring force. The result is analogous to the tightening of an elastic band across the potential energy landscape.

The primary difficulty comes in choosing an appropriate transition to perform the NEB calculations on. To accomplish this, we begin by recognizing, as previously mentioned, that $\Delta E_a = \Delta E_{\mathrm{KRA}}$ when there is no change in energy due to the hop. Therefore, if we are able to find a transition within the ordered $\mathrm{Ti_3C_2}$ with this characteristic, then it would be suitable for use as ΔE_{KRA}. In the previous chapter, we examined the effects of vacancy ordering on diffusion using kMC simulations on a square lattice. From this investigation we found that transitions within strings of interconnected vacancies typically possess this characteristic. These strings of vacancies are present in the $\mathrm{Ti_3C_2}$ structure, as shown in Figure 7.17a where titanium atoms are shown in blue, carbon atoms in brown, and vacancies in black. Examination of the structure suggests that the primary mechanism for carbon diffusion is through these pathways. This can occur when carbon atoms located in the carbon-depleted planes exchange with in-plane nearest neighbor vacancies, as shown in the transitions denoted Q_2 in Figure 7.17. The other type of migration occurs when carbon atoms hop from carbon-full planes to the carbon-depleted planes – denoted as Q_1 in Figure 7.17. The inverse, hops from carbon-depleted planes to an empty site in carbon-full planes, are denoted Q_3. NEB calculations of these transitions are shown in Figure 7.17b. As expected, the transitions along the strings of vacancies with activation energy Q_2 have $\Delta E_\sigma \approx 0$, which can be seen by comparing the energy of images 6 and 12 in Figure 7.17b. This result seems to justify the

use of a KRA in the first place and, as a result, we choose $\Delta E_{\mathrm{KRA}} = Q_2 = 3.25\mathrm{eV}$ in our kMC simulations.

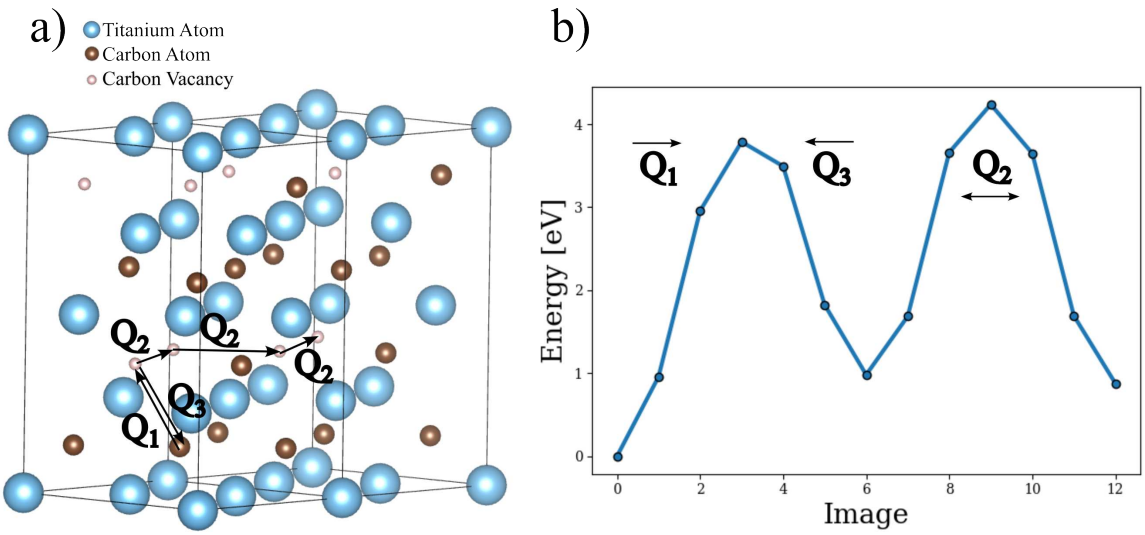

Figure 7.17: a) The crystal structure of the vacancy-ordered $\mathrm{Ti_3C_2}$ phase. Arrows indicate possible transitions with activation energies denoted Q_1, Q_2, and Q_3. **b)** The results of NEB calculations for the transitions shown. Analysis of the figure indicates that $Q_1 = 3.80\mathrm{eV}$, $Q_2 = 3.25\mathrm{eV}$, and $Q_3 = 2.83\mathrm{eV}$.

We would like to use our simulations to understand how short-range order (SRO) and long-range order (LRO) are related to diffusion kinetics. To accomplish this, we use the Warren-Cowley short range order parameters $\alpha^{(n)}$ [171, 172], defined in Equation 7.25 where n corresponds to the neighbor shell, and the LRO parameter ζ [173], defined in Equation 7.26, to quantitatively define the degree of order present in our simulations. In Equation 7.25 the quantity $p_{ij}^{(n)}$ is the average fraction of unlike bonds, *i.e.* bonds between an atom and vacancy, in the nth shell of an atom. In Equation 7.26, r_A is the fraction of sites that are correctly occupied by atoms when compared to the ordered $\mathrm{Ti_3C_2}$ structure.

$$\alpha^{(n)} = 1 - \frac{p_{ij}^{(n)}}{2\chi_A\chi_{Va}} \tag{7.25}$$

$$\zeta = \frac{r_A - \chi_A}{1 - \chi_A} \tag{7.26}$$

Finally, to determine the character of any observed phase transformations we will use the heat capacity. The heat capacity is defined according to Equation 7.27, where E is the energy per atom determined from our Monte Carlo simulations.

$$C = \frac{\langle E^2 \rangle - \langle E \rangle^2}{k_b T^2} \tag{7.27}$$

Density Functional Theory Calculations

Density Functional Theory calculations were carried out in VASP in order to determine the structural energies used to fit our cluster expansion. Additionally, VASP was used to perform energy barrier calculations of several carbon transitions within the ordered $\mathrm{Ti_3C_2}$ structure. The structural energy calculations were carried out using both GGA and LDA cross-correlation functionals. All ground states up to 26 atoms per unit cell were calculated using the *pollmach* and *ezvasp* functions of the ATAT. ATAT INCAR tags used to perform these VASP calculations were PREC = high, ISMEAR = 1, SIGMA = 0.1, IBRION = 2, ISIF = 3, and KPPRA = 1000.

7.2.3 Results & Discussion

We begin our discussion with the results of our Monte Carlo simulations. For each cluster expansion we calculated LRO and SRO parameters as well as the heat capacity as a function of temperature, as shown in Figure 7.18. Beginning with the GGA cluster expansion results, shown as blue squares and circles respectively in Figure 7.18a, we observe clear discontinuities in both LRO and SRO at a temperature of roughly 1665K. These discontinuities in the order parameters correspond exactly to the divergence in the heat capacity for the GGA cluster expansion, shown in blue in Figure 7.18b. Altogether, these results strongly suggest a first-order phase transformation at approximately 1665K. Turning our attention now to the LDA cluster expansion results, we note several interesting features. First, there is a discontinuity in the LRO parameter, shown as red triangles in Figure 7.18a. In contrast, the SRO, shown as red diamonds, appears to smoothly increase as a function of temperature. The heat capacity for the LDA cluster expansion, shown in red in Figure 7.18b, displays a peak at roughly 1115K and, importantly, does not appear to

diverge. Thus, we conclude that the phase transformation present in our LDA cluster expansion results is second order. We note that previous studies have argued that the $\mathrm{Ti_3C_2} \rightarrow \mathrm{TiC_x}$ order-disorder transition must be first-order based on the symmetry of $C222_1$ space group; however, examination of the experimental data, such as the specific heat measurements of the $\mathrm{Ti_3C_2} \rightarrow \mathrm{TiC_{0.62}}$ transformation conducted by Lipatnikov and Gusev, show a symmetric peak that does not rule out the possibility of a second-order transformation. Furthermore, it is unclear whether the preferred $\mathrm{Ti_3C_2}$ structure belongs to the $C222_1$ space group, as reported by Lipatnikov and Gusev, or the $C2/m$ space group as is predicted by DFT.

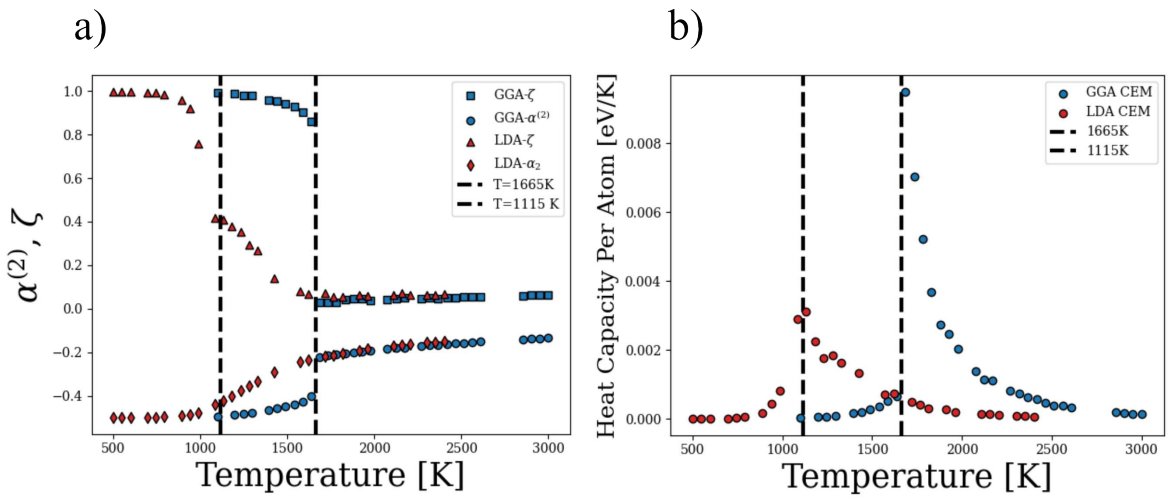

Figure 7.18: a) SRO and LRO data collected from Monte Carlo simulations using our GGA and LDA cluster expansions. LRO and SRO parameters are plotted for the GGA as blue squares and circles respectively. LRO and SRO parameters are plotted for the LDA as red triangles and diamonds respectively. **b)** The heat capacity per atom determined by Equation 7.27 for Monte Carlo simulations conducted with LDA (red) and GGA (blue) cluster expansions. Dashed lines correspond to the phase transformation temperatures. For the LDA, this appears to be a second-order phase transformation at roughly 1115K, as demonstrated by the peak in the heat capacity. For the GGA simulations the phase transformation appears to be first order, as demonstrated by the divergence in the heat capacity at roughly 1665K.

Shown as blue circles in Figure 7.19 is the diffusivity data collected from our kMC simulations, conducted with energetics according to our GGA cluster expansion and using $\Delta E_{\mathrm{KRA}} = 3.25$eV. At temperatures above roughly 1615K the apparent activation energy determined by fit to Equation 7.18 is approximately 3.51eV and at temperatures below 1615K the apparent activation energy is

approximately 4.61eV. Sarian's tracer diffusivity data is shown as red squares, with an apparent activation energy of approximately 2.22eV above 2353K and an apparent activation energy of approximately 4.83eV below 2353K. When we examine how the short-range and long-range order change as a function of temperature, as depicted in Figure 7.18a, we find see that a first-order phase transition occurs at roughly 1665K, suggesting that the order-disorder transition is a primary factor in causing the change in activation energy seen in our data in Figure 7.19. It is worth noting that the transition temperature depicted in Figure 7.18a occurs nearly 700K above the transition temperature of 964K reported by Gusev and Rempel. Similarly, Sarian's anomaly occurs at 2353K, nearly 1400K above the transition temperature of Gusev and Rempel.

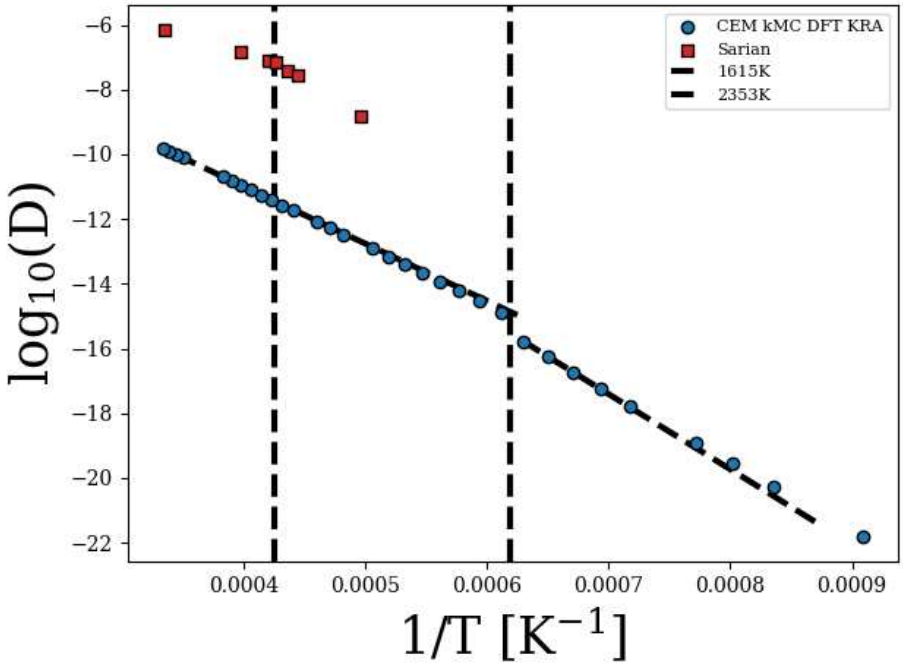

Figure 7.19: Diffusivity data plotted on a semi-log plot versus inverse temperature. Data collected from kMC simulations in the present work is shown as blue circles. Sarian's tracer diffusivity data is shown as red squares.

When comparing our kMC data to that of Sarian, the low temperature apparent activation energies appear to agree, except for that Sarian reports this apparent activation energy persisting to higher temperatures. At high temperatures, however, our apparent activation energies disagree.

In fact, compared to other measurements of carbon diffusion, Sarian's high-temperature apparent activation energy of 2.22eV is very low, even approaching the apparent activation energy for carbon diffusion in β-Ti of 1.93eV reported by Bucur and Wagner [54]. In contrast, Van Loo *et al.*, measured carbon diffusion in $\mathrm{TiC_x}$ across it's homogeneity range at temperatures in the range 1573-2023K using carbide layer growth measurements [178]. Their results indicated that the apparent activation energy for carbon diffusion in this temperature range was roughly 3.42 ± 0.21eV and did not vary with carbon content. At these temperatures we expect disorder on the carbon-vacancy sublattice, which is corroborated by the fact that if ordering were present then there would likely have been a composition dependence of the apparent activation energy due to order-order transitions. We note that the apparent activation energy measured by Van Loo *et al.* is in good agreement with our high-temperature apparent activation energy of 3.52eV.

Additionally, it is obvious that the transition temperature that we report here, the transition temperature reported by Lipatnikov and Gusev, and the temperature at which Sarian reported a change in activation energy for carbon diffusion are all in disagreement. Leaving aside Sarian's data for a moment, we can briefly discuss the discrepancy between the data in this work and that of Lipatnikov and Gusev. Lipatnikov and Gusev report a first-order transition at roughly 964K, though we note that they did not conclusively rule out a second-order transformation. Furthermore, the transition temperature they reported does not correspond to the peak in the specific heat and instead is reported at an earlier point in the rise of the specific heat. Their reported peak in specific heat occurs at roughly 1070K. Our LDA Monte Carlo results indicate a second-order transformation with a peak in heat capacity at roughly 1115K while our GGA Monte Carlo results indicate a first-order phase transformation at 1615K. Thus, there is good agreement between the peak in specific heat reported by Lipatnikov and Gusev and the peak in heat capacity in our LDA results. The transition temperature determined from the peak in heat capacity from our GGA results is significantly higher, most likely due to over-binding of the crystal structure, which is a common occurrence when using GGA cross-correlation. Thus, the combined evidence leads to the conclusion that the $\mathrm{Ti_3C_2} \rightarrow \mathrm{TiC_x}$ order-disorder transformation temperature lies somewhere in

the region 1000-1600K and is very likely to be close to 1100K based on experiment and our LDA results. In light of this, Sarian's reported transition temperature of 2353K becomes even more confounding.

To reiterate, Sarian hypothesized that the anomalous change in apparent activation energy for carbon diffusion was a result of an order-disorder phase transition occurring on the carbon-vacancy sublattice of $\mathrm{TiC}_{0.67}$. In theory, it is possible that correlated jumps within the vacancy-ordered structure could cause a substantial increase in apparent activation energy at temperatures where vacancy ordering is present. Furthermore, migration pathways with large energy barriers may be present and common in the ordered structure and not in disordered structures, as is demonstrated by the energy barrier histograms shown in Figure 7.20a. Examination of Figure 7.20a reveals a considerable difference in the shape of the histograms, with the high-temperature distribution being approximately normally distributed around $\Delta E_{\mathrm{KRA}} = 3.25\mathrm{eV}$ and the low-temperature distribution being effectively trimodal with distinct peaks around approximately 2.8eV, 3.25eV, and 3.75eV. In the previous section, we observed a similar trimodal distribution in 2D lattices with long strings of vacancies, thus the reappearance here provides further evidence of the hypothetical diffusion pathway, *i.e.*, that carbon diffusion occurs primarily through strings of interconnected vacancies in $\mathrm{Ti}_3\mathrm{C}_2$ and with randomly occupied nearest-neighbor vacancies in the disordered $\mathrm{TiC}_{0.67}$.

Shown in Figure 7.20b is the hop correlation factor $f_T = \frac{MSD}{a^2\langle N_h \rangle}$ as a function of temperature, determined from our kMC simulations. Clearly demonstrated in the correlation factor is the effects of the first-order order-disorder transformation, with highly correlated hops ($f_T \to 0$) below the transition temperature, and uncorrelated hops ($f_T \to 1$) above the transition temperature. The discontinuity in the correlation factor is consistent with the discontinuities shown in the LRO and SRO and the divergence in the heat capacity shown in Figure 7.18. Altogether, these support the conclusion that there is a first-order phase transformation at 1615K in our GGA Monte Carlo and kinetic Monte Carlo simulations that coincide with the observed change in activation energy from our kMC simulations shown in Figure 7.19. From these we conclude that the discontinuity in the

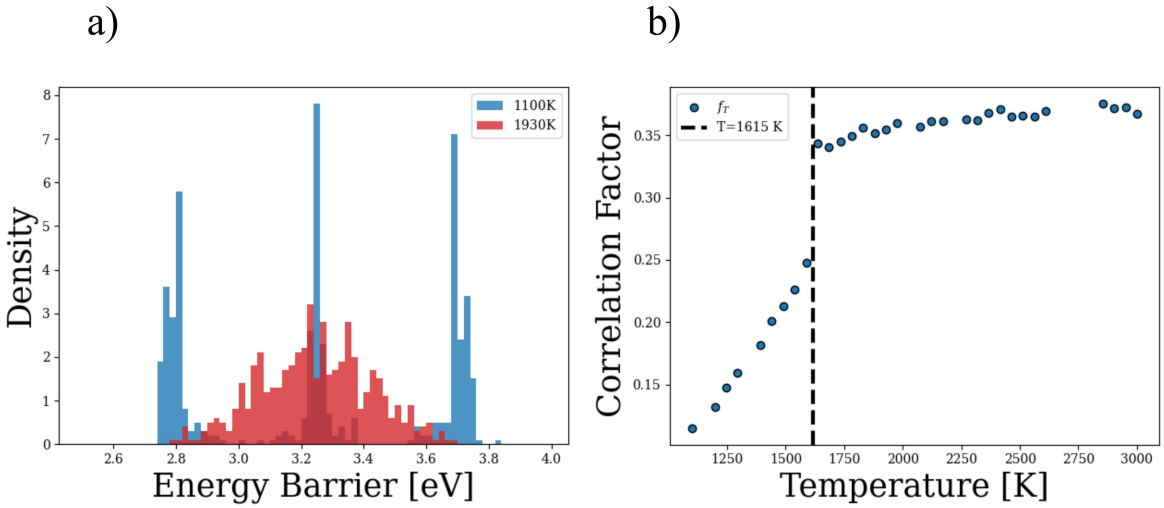

Figure 7.20: a) A histogram depicting the frequency of energy barriers encountered during the diffusion of carbon atoms at 1100K (blue) and 1930K (red). The low-temperature distribution appears tri-modal with peaks at approximately 2.8eV, 3.25eV, and 3.75eV. The high-temperature distribution is approximately normally distributed around the $\Delta E_{\mathrm{KRA}} = 3.25$eV. **b)** The hop correlation factor f_T plotted as a function of temperature. At 1615K a discontinuity is present, consistent with the discontinuity in the LRO and SRO and the divergence in the heat capacity shown in Figure 7.18.

diffusivity and the change in activation energy for carbon diffusion must be due to the first-order order-disorder transition and correlated hops in the ordered $\mathrm{Ti_3C_2}$ phase.

Despite the evidence supporting correlated hops in the ordered phase as the mechanism for the change in activation energy in our kMC simulations, we cannot conclude that the same mechanism explains Sarian's anomaly. We have shown that the effects of a vacancy order-disorder transition match Sarian's data phenomenologically, but all evidence suggests that ordering in the Ti-C system disappears above roughly 1600K. In all likelihood the disordering occurs near 1100K. It is difficult to identify any mechanisms for Sarian's anomaly that agree with all of the experimental facts. For example, the simplest explanation would be competing transport mechanisms; however, in the case of Sarian's anomaly the high activation energy mechanism dominates at low temperature and the low activation energy mechanism at high temperature, opposite to the observed behavior of systems with competing mechanisms. Another potential explanation is that substitutional impurities, such as oxygen or nitrogen, on the carbon-vacancy sublattice inhibit diffusion. It is likely that tightly bound vacancy-impurity complexes would result in increased energy barriers for carbon-vacancy

hops in the area surrounding vacancy-impurity complexes. This would likely lead to the observed behavior, but it is unlikely that this effect would persist to the 2353K temperature that Sarian reported. In addition, impurities cannot explain the extremely low apparent activation energy that Sarian reported above 2353K.

To our knowledge there remains only one mechanism that could hypothetically produce the observed behavior: diffusion through grain boundary phases [179–182]. Specifically, it has been reported that grain-boundary phases with an amorphous structure can appear as a disordered thin film partially or completely wetting the grain boundary, as shown schematically as thick lines in Figure 7.21a. These grain boundary phases can occur in single-phase solid regions near the solidus, shown hypothetically as a blue dashed line for the TiC_x phase in Figure 7.21b.

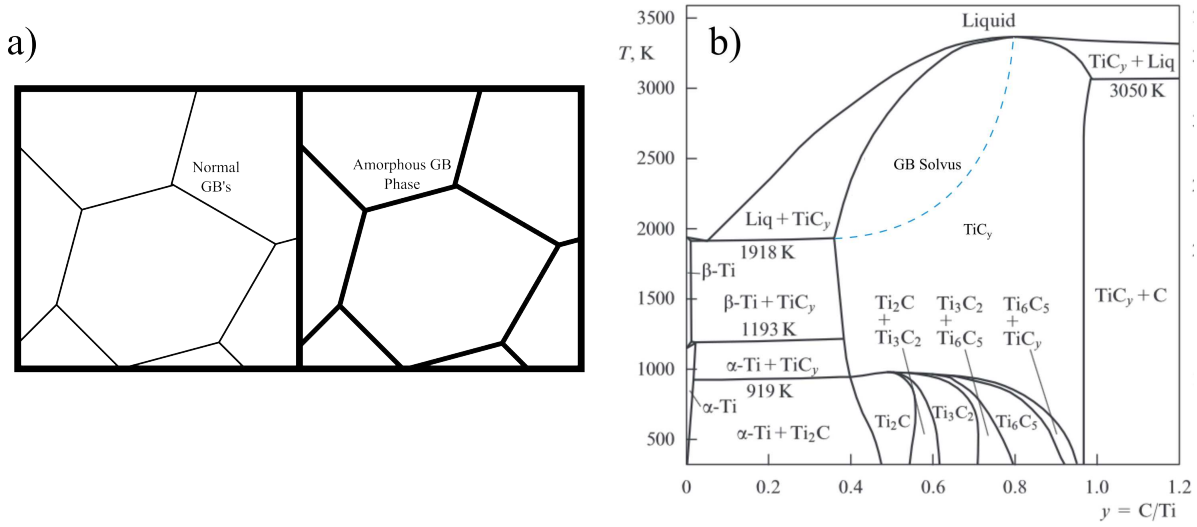

Figure 7.21: a) A schematic diagram depicting normal grain boundaries (left) and grain boundaries containing partially or completely wetted by a disordered amorphous phase (right). **b)** The Ti-C phase diagram of Gusev and Rempel. Shown as a blue dashed line is a hypothetical grain boundary phase solvus that could result in the anomalous behavior reported by Sarian.

Diffusion through an amorphous grain boundary phase appears as an attractive explanation for Sarian's anomaly for several reasons. First of all, we would not expect the grain boundary phase to appear until temperatures exceed the eutectic temperature. According to Gusev and Rempel, the eutectic temperature of the Ti-C system is approximately 1918K. Thus, at 2353K where Sarian

reported the anomalous change in apparent activation energy, it is possible that amorphous phase wetting of the grain boundaries begins. This would also explain why no other studies have observed this phenomenon, since most of the studies on carbon diffusion in the Ti-C system either did not exceed 2000K or studied the carbon-saturated region of the phase diagram where it is less likely for amorphous grain boundary phases to appear. We make this hypothesis by pointing out that there is very likely to be a carbon compositional dependence of the grain boundary energy. At the very least, Hossain *et al.* have reported a compositional dependence of the cleavage energy in the Ta-C system, which often behaves similarly. Furthermore, it is likely that carbon transport through an amorphous phase would have an extraordinarily low activation energy – similar to that reported by Sarian above 2353K. Therefore, the appearance of an amorphous grain boundary phase at approximately 2353K would potentially provide a low-activation energy pathway for mass transport which would not exist at more intermediate temperatures. It is likely that this mechanism would appear phenomenologically similar to the behavior reported by Sarian.

7.2.4 Summary and Conclusions

To summarize, in this investigation we sought to test Sarian's hypothesis regarding the cause of the sudden change in carbon diffusion activation energy that they reported at 2353K. Sarian hypothesized that this change in activation energy was due to an order-disorder transition occurring on the carbon-vacancy sublattice of the B1 rocksalt $\mathrm{TiC}_{0.67}$ crystal. According to this hypothesis, the large apparent activation energy of 4.83eV would correspond to the $\mathrm{Ti}_3\mathrm{C}_2$ vacancy-ordered phase and the lower apparent activation energy of 2.22eV would correspond to carbon diffusion through a disordered carbon-vacancy sublattice in $\mathrm{TiC}_{0.67}$.

To test the hypothesis, we used MC and kMC simulations conducted with energetics according to a cluster expansion method fit to first-principles energy calculations implemented in VASP. Our GGA Monte Carlo simulation results indicated a first-order phase transformation at roughly 1615K as evidenced by discontinuities in the LRO and SRO as well as a divergence in the heat capacity. Our LDA Monte Carlo results indicated smooth transitions in the LRO and SRO as well as a

peak in the heat capacity at 1115K, agreeing well with the 1070K peak in specific heat reported experimentally in $\mathrm{TiC}_{0.62}$ by Lipatnikov and Gusev. Diffusivity results from kMC simulations carried out with ΔE_{KRA}=3.25eV and our GGA cluster expansion were phenomenologically similar to Sarian's diffusivity data, with an activation energy of 4.61eV below 1615K and an activation energy of 3.52eV above 1615K. Additionally, we observed a discontinuity in the diffusivity at 1615K consistent with the evidence of a first-order phase transformation gathered from our Monte Carlo simulations. Despite the similar phenomenological behavior, our transition temperatures and activation energies disagreed with those reported by Sarian.

To attempt to explain Sarian's anomalous change in activation energy, we considered other potential mechanisms, such as competing mass transport mechanisms or impurity effects, but neither of these agree with all of the experimental facts. As a result, we make a new hypothesis for the cause of Sarian's anomalous carbon diffusion: amorphous grain boundary phases. Though these grain boundary phases have not been directly observed in the Ti-C system, this hypothesis fits Sarian's observations well. Few other mechanisms could reasonably explain the transition from large to small apparent activation energy at temperatures in excess of 2000K.

Chapter 8

Conclusions & Future Work

The work presented in this dissertation introduces a novel category of composites for using in ultra-high temperature environments. Though these composites begin as kinetically stabilized metal-ceramic multilayers with bolstered fracture resistance, they also possess the ability to phase transform into monolithic ceramics upon heating. Thus, this type of composite has improved low-temperature properties without sacrificing any high-temperature properties. Additionally, we have observed that engineering of the initial volume fractions of metal and ceramic layers of these composites provides the unique opportunity to control composition-dependent materials properties.

In this investigation we have introduced an innovative new method for modeling diffusion-controlled phase transformations using the Finite Element Method, achieving results that are first-order with respect to mass error without the need for complex mathematical transformations. Furthermore, we have produced a framework for designing composites based on our phase transformation model as well as modifications to existing models of crack-bridging and toughening in metal-ceramic multilayer composites.

Along the way, we were sidetracked by a mission to answer an question from literature dating back to 1968, and though were were not able to concretely reject the hypothesis presented all those years ago, we were able to advance the literature surrounding the anomalous diffusion of carbon in Ti_3C_2 as well as garner a better understanding of the intersection between vacancy-ordered phases and interstitial vacancy self-diffusion.

Finally, we developed our phase transformation model further by investigating the affects of concentration-dependence in the carbon/nitrogen diffusivity and time-evolving temperature on the phase transformation kinetics.

Over the course of this investigation, we have endeavored to answer many questions surrounding the development of these novel composites and the wider literature surrounding transition metal carbides/nitrides as a whole; however, as is often the case in science, new questions arose as we

progressed. The following sections describe some of these questions with the hope that future materials scientists may carry the torch.

8.1 Modeling of Non-Lamellar Composites

Perhaps the most straightforward extension to this work is to imagine a different composite geometry. In this work we have assumed a lamellar composite composed of alternating layers of metal and ceramic; however, it is certainly the case that other geometries could provide similar toughening and phase transformation properties. For example, one could easily imagine a composite with a three-dimensional geometry composed of spherical particles of ceramic separated by network of metal. This geometry might be achieved via sintering of a mixture of large ceramic and small metal particles such that metal particles fill the voids between ceramic particles. Additionally, allowing a partial phase-transformation could result in further removal of intergranular voids. Figure 8.1 depicts an idealized cross-section schematic of such a composite.

Interesting questions arise when you change the composite microstructure in this way. For example, the phase-transformation kinetics are certainly different from the lamellar case. Though it is very likely that the phase transformation apparent activation energy would still be equal to that of carbon/nitrogen diffusion in the ceramic phase, the geometry of the interface is likely to change the apparent diffusivity prefactor significantly.

Furthermore, the toughening characteristics would likely be somewhat different. In the lamellar composites we saw that the toughening was primarily due to crack-bridging provided by the strained metal layers. Here, we may see a similar mechanism due to grain-bridging, but it is also likely that the fracture mechanism will be more complicated than in the lamellar case. For example, the interfaces between metal and ceramic particles may be favorable for crack propagation, leading to a toughening mechanism dominated by intergranular crack deflection. On the other hand, transgranular fracture may dominate and the toughening mechanism may be bridging due to intact metal grains within the crack wake.

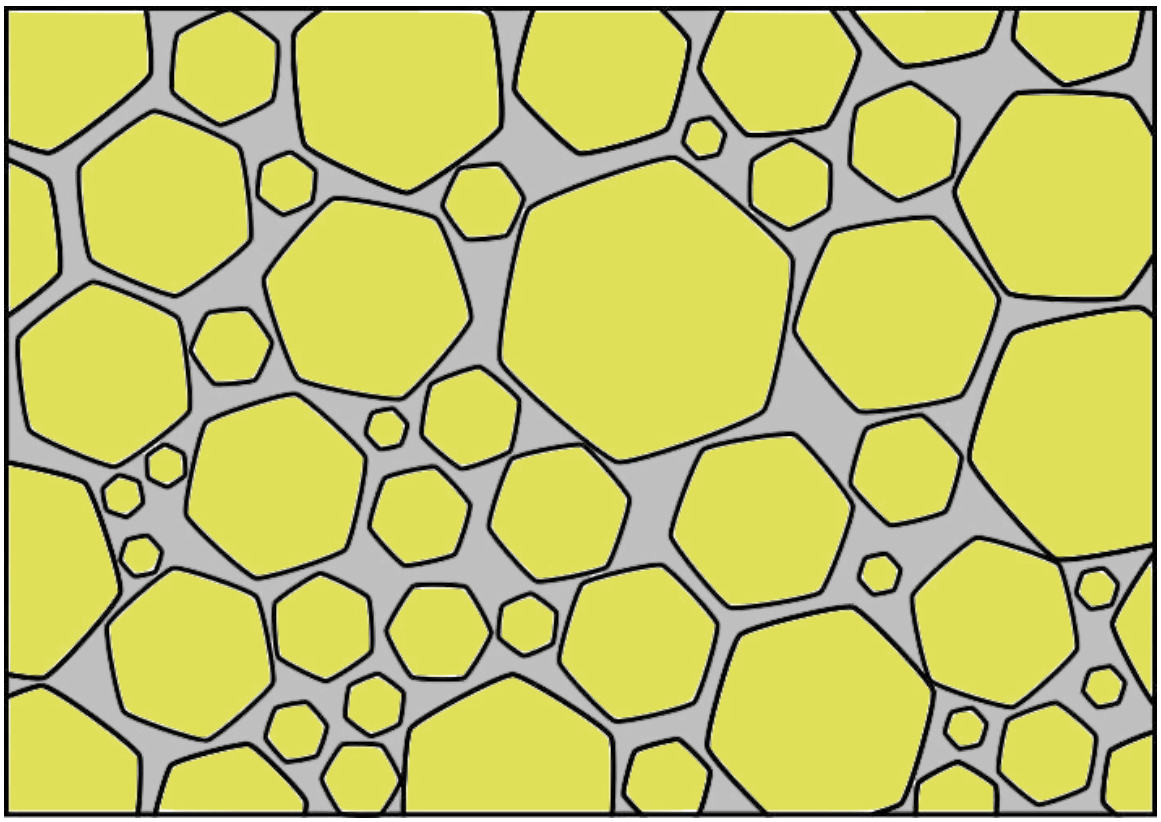

Figure 8.1: A schematic diagram of the two-dimensional cross-section of the proposed composite. Ceramic particles are shown in gold whereas the network of small metal particles is shown in silver.

For computational investigation of the phase transformation kinetics we recommend an extension of the Finite Element Method phase transformation simulations outlined in Chapter 3 into two or three dimensions. If it is determined that this sort of extension is too difficult, for example due to the lack of symmetry in the higher-dimensional case, phase field simulations may be a suitable alternative.

To model toughening, the existing literature on ceramic/metal matrix composites may be sufficient. In the case that it is not, simulations of intergranular and transgranular fracture as demonstrated in Ta_2C by Hossian *et al.* may be used to construct an empirical model of toughening based on composite geometry and material choice.

8.2 Phase Transformations with a Temperature Gradient

One apparent oversight of the phase transformation simulations described in Chapters 4 and 5 is that the simulations were conducted assuming a constant temperature everywhere within the composite; whereas real composites will be heated from the surface. Thus, depending on specific circumstances, there is a potential for large temperature gradients to be present within the composites. It is unclear what affect these temperature gradients may have on mechanical, thermodynamic, and especially kinetic properties of the composites.

Here, we suggest that the affects of these concentration gradients could be investigated using a simple extension of the Finite Element Method simulations described in Chapter 3. Simulations with temperature gradients within the composite could be constructed by adding a temperature field described by the same discretization as the concentration field. Then, it would be straightforward to solve for the temporal evolution of the temperature field and concentration field simultaneously, since they are described by the same partial differential equation. The only difference is that the evolution of the temperature field is dependent on the thermal diffusivity of each element whereas the concentration depends on the carbon/nitrogen diffusivity.

8.3 Deconvolution of Layer-Growth Studies

As mentioned previously, there are two primary experiments used to report carbon/nitrogen diffusivities in the literature. In the group IV carbides, the primary method reported in the literature is carbon tracer diffusion wherein the tracer diffusivity is directly determined using by using isotopes. In other experiments, the carbon/nitrogen diffusivity reported is determined by layer-growth experiments. As a result, these diffusivities are convoluted with the affects discussed in Chapter 4, such as the shape of the concentration profile and the concentration discontinuity between layers. Thus, these are not representative of the true kinetics of carbon/nitrogen diffusion. In fact, the diffusivities reported by these experiments are likely orders of magnitude different from that of carbon/nitrogen tracer diffusion, though the activation energies should be the same.

Here, we propose that the Finite Element Method simulation framework described in Chapters 3 and 4 could be modified to deconvolve the affects of the phase transformation kinetics and estimate tracer diffusivities. There are several materials, such as titanium carbide, for which both tracer diffusion and layer growth experiments are reported and these materials especially could prove useful in understanding specifically how the layer growth diffusivity and tracer diffusivity are related.

8.4 Vacancy-Ordered Domain Coarsening Kinetics

Another understudied topic adjacent to the research contained in this literature is the coarsening kinetics of ordered domains. These ordered domains can be hard to resolve, often requiring expensive techniques like neutron diffraction in order to identify ordered domain boundaries. As a result, very few studies have directly observed vacancy ordering and there is little known about the kinetics of domain growth.

Kinetic Monte Carlo simulations and Potts Models are two examples of methodologies which may independently or in combination be capable of modeling the domain growth kinetics in systems with ordering of structural vacancies. For example, using similar methods to those described in Chapter 7, one could develop a simple 2-dimensional system that exhibits vacancy-ordering using an Ising Model type Hamiltonian. Domain sizes could be identified using a tree-like algorithm that would identify all sites that belong to a certain domain. It would then be straightforward to study that statistics and kinetics of grain size as the simulation progressed.

A similar algorithm could be developed for identifying grain sizes in 3-dimensional lattices. Then using the cluster expansion method kinetics for real materials systems could be estimated. It is likely that these kinetics would be phenomenologically similar to grain growth kinetics.

Bibliography

[1] A. Fernández Guillermet. Analysis of thermochemical properties and phase stability in the zirconium-carbon system. *Journal of Alloys and Compounds*, 217(1):69–89.

[2] K. Frisk and A. Fernández Guillermet. Gibbs energy coupling of the phase diagram and thermochemistry in the tantalum-carbon system. *Journal of Alloys and Compounds*, 238(1):167–179.

[3] Xiao-Xiang Yu, Christopher R. Weinberger, and Gregory B. Thompson. Ab initio investigations of the phase stability in group IVB and VB transition metal carbides. *Computational Materials Science*, 112:318–326.

[4] Shuyin Yu, Qingfeng Zeng, Artem R. Oganov, Gilles Frapper, Bowen Huang, Haiyang Niu, and Litong Zhang. First-principles study of zr–n crystalline phases: phase stability, electronic and mechanical properties. *RSC Adv.*, 7(8):4697–4703.

[5] Toru Ogawa. Structural stability and thermodynamic properties of zrn alloys. *Journal of Alloys and Compounds*, 203:221–227.

[6] Yutai Katoh, Gokul Vasudevamurthy, Takashi Nozawa, and Lance L. Snead. Properties of zirconium carbide for nuclear fuel applications. *Journal of Nuclear Materials*, 441(1):718–742.

[7] Xiao-Xiang Yu, Gregory B. Thompson, and Christopher R. Weinberger. Influence of carbon vacancy formation on the elastic constants and hardening mechanisms in transition metal carbides. *Journal of the European Ceramic Society*, 35(1):95–103.

[8] I. M. Vinitskii. Relation between the properties of monocarbides of groups IV–v transition metals and their carbon content. *Powder Metall Met Ceram*, 11(6):488–493.

[9] Sara Kadkhodaei and Jorge A. Muñoz. Cluster expansion of alloy theory: A review of historical development and modern innovations. *JOM*, 73(11):3326–3346.

[10] A. T. Santhanam. Application of transition metal carbides and nitrides in industrial tools. In S. T. Oyama, editor, *The Chemistry of Transition Metal Carbides and Nitrides*, pages 28–52. Springer Netherlands.

[11] Anish Paul, Jon Binner, and Bala Vaidhyanathan. UHTC composites for hypersonic applications. In William G. Fahrenholtz, Eric J. Wuchina, William E. Lee, and Yanchun Zhou, editors, *Ultra-High Temperature Ceramics*, pages 144–166. John Wiley & Sons, Inc.

[12] H. Holleck. Material selection for hard coatings. *Journal of Vacuum Science & Technology A: Vacuum, Surfaces, and Films*, 4(6):2661–2669.

[13] Rishi Raj. Fundamental research in structural ceramics for service near 2000oc. *J American Ceramic Society*, 76(9):2147–2174.

[14] Lance L. Snead, Yutai Katoh, and Sosuke Kondo. Effects of fast neutron irradiation on zirconium carbide. *Journal of Nuclear Materials*, 399(2):200–207.

[15] Ian E. Porter, Travis W. Knight, Michael C. Dulude, Elwyn Roberts, and Jim Hobbs. Design and fabrication of an advanced TRISO fuel with ZrC coating. *Nuclear Engineering and Design*, 259:180–186.

[16] E. Wuchina, M. Opeka, S. Causey, K. Buesking, J. Spain, A. Cull, J. Routbort, and F. Guitierrez-Mora. Designing for ultrahigh-temperature applications: The mechanical and thermal properties of HfB_2, HfC_x, HfN_x and hf(n). *Journal of Materials Science*, 39(19):5939–5949.

[17] Alan Cottrell. *Chemical bonding in transition metal carbides*. Number 613 in Book / The Institute of Materials. Institute of Materials.

[18] Christopher R. Weinberger and Gregory B. Thompson. Review of phase stability in the group IVB and VB transition-metal carbides. *Journal of the American Ceramic Society*, 101(10):4401–4424. _eprint: https://onlinelibrary.wiley.com/doi/pdf/10.1111/jace.15768.

[19] Graham E. Hollox. Microstructure and mechanical behavior of carbides. *Materials Science and Engineering*, 3(3):121–137.

[20] Christopher R. Weinberger and Gregory B. Thompson. The crystal structure and phase stability of the zeta phase in the group VB transition metal carbides: a computational investigation. *Acta Crystallogr B Struct Sci Cryst Eng Mater*, 75(5):870–879.

[21] W. F. Brizes and J. M. Tobin. Isolation of the zeta phase in the system tantalum-carbon. *J American Ceramic Society*, 50(2):115–116.

[22] I. Zaplatynsky. Observations on zeta phase in the system ta-c. *J American Ceramic Society*, 49(2):109–109.

[23] J. G. Desmaison and W. W. Smeltzer. Nitrogen diffusion in zirconium nitride. *J. Electrochem. Soc.*, 124(1):152. Publisher: IOP Publishing.

[24] T. L. Anderson. *Fracture mechanics: fundamentals and applications*. CRC Press/Taylor & Francis, fourth edition edition.

[25] Richard Warren. Measurement of the fracture properties of brittle solids by hertzian indentation. *Acta Metallurgica*, 26(11):1759–1769.

[26] Zhi-Gang Mei, Sumit Bhattacharya, and Abdellatif M. Yacout. First-principles study of fracture toughness enhancement in transition metal nitrides. *Surface and Coatings Technology*, 357:903–909.

[27] Cheng Zhang, Ankur Gupta, Sudipta Seal, Benjamin Boesl, and Arvind Agarwal. Solid solution synthesis of tantalum carbide-hafnium carbide by spark plasma sintering. *J Am Ceram Soc*, 100(5):1853–1862.

[28] Xingyuan Zhao, Maanas Togaru, Qianying Guo, Christopher R. Weinberger, Leslie Lamberson, and Gregory B. Thompson. Carbon influence on fracture toughness of niobium carbides. *Journal of the European Ceramic Society*, 39(16):5167–5173.

[29] Xiaohong Zhang, Gregory E. Hilmas, and William G. Fahrenholtz. Densification and mechanical properties of TaC-based ceramics. *Materials Science and Engineering: A*, 501(1):37–43.

[30] A. G. Evans, M. Rühle, B. J. Dalgleish, and P. G. Charalambides. The fracture energy of bimaterial interfaces. *Materials Science and Engineering: A*, 126(1):53–64.

[31] Robert A. Morris, Billie Wang, Lawrence E. Matson, and Gregory B. Thompson. Microstructural formations and phase transformation pathways in hot isostatically pressed tantalum carbides. *Acta Materialia*, 60(1):139–148.

[32] E. Schmid and W. Boas. *Kristallplastizität: Mit Besonderer Berücksichtigung der Metalle*. Number 17 in Struktur und Eigenschaften der Materie, Eine Monographiensammlung. Springer Berlin Heidelberg.

[33] G. E. Hollox and R. E. Smallman. Plastic behavior of titanium carbide. *Journal of Applied Physics*, 37(2):818–823.

[34] Hang Yu, Mohammadreza Bahadori, Gregory B. Thompson, and Christopher R. Weinberger. Understanding dislocation slip in stoichiometric rocksalt transition metal carbides and nitrides. *J Mater Sci*, 52(11):6235–6248.

[35] Michele Pettinà, Robert W. Harrison, Luc J. Vandeperre, Farid R. Biglari, Peter Brown, William E. Lee, and Kamran Nikbin. Diffusion-based and creep continuum damage modelling of crack formation during high temperature oxidation of ZrN ceramics. *Journal of the European Ceramic Society*, 36(9):2341–2349.

[36] D. W. Lee and J. S. Haggerty. Plasticity and creep in single crystals of zirconium carbide. *J American Ceramic Society*, 52(12):641–647.

[37] R. Darolia and T. F. Archbold. Plastic deformation of polycrystalline zirconium carbide. *J Mater Sci*, 11(2):283–290.

[38] Martin H. Leipold and Thomas H. Nielsen. Mechanical properties of hot-pressed zirconium carbide tested to 2600oc. *J American Ceramic Society*, 47(9):419–424.

[39] I. I. Spivak, R. A. Andrievskii, and V. V. Klimenko. Diffusion-controlled processes in the homogeneity range of zirconium carbide. *Powder Metall Met Ceram*, 12(3):212–214.

[40] Yu. V. Miloserdin, K. V. Naboichenko, L. I. Laveikin, and A. G. Bortsov. The high-temperature creep of zirconium carbide. *Strength Mater*, 4(3):302–305.

[41] R. P Agarwala and A. R Paul. Diffusion of carbon in zirconium and some of its alloys. *Journal of Nuclear Materials*, 58(1):25–30.

[42] S. Sarian and J. M. Criscione. Diffusion of carbon through zirconium monocarbide. *Journal of Applied Physics*, 38(4):1794–1798.

[43] Vsevolod I. Razumovskiy, Andrei V. Ruban, Joakim Odqvist, and Pavel A. Korzhavyi. Vacancy-cluster mechanism of metal-atom diffusion in substoichiometric carbides. *Phys. Rev. B*, 87(5):054203.

[44] S. Sarian. Diffusion of 44ti in TiCx. *Journal of Applied Physics*, 40(9):3515–3520.

[45] I. I. Spivak, R. A. Andrievskii, V. N. Rystsov, and V. V. Klimenko. Creep of titanium monocarbide in its homogeneity range. *Powder Metall Met Ceram*, 13(7):574–578.

[46] Chase J. Smith, Morgan A. Ross, Nicholas De Leon, Christopher R. Weinberger, and Gregory B. Thompson. Ultra-high temperature deformation in TaC and HfC. *Journal of the European Ceramic Society*, 38(16):5319–5332.

[47] A. Kelly and D. J. Rowcliffe. Slip in titanium carbide. *phys. stat. sol. (b)*, 14(1):K29–K33.

[48] A. Kelly and D. J. Rowcliffe. Deformation of poly crystalline transition metal carbides. *J American Ceramic Society*, 50(5):253–256.

[49] Xing-Qiu Chen, Haiyang Niu, Dianzhong Li, and Yiyi Li. Modeling hardness of polycrystalline materials and bulk metallic glasses. *Intermetallics*, 19(9):1275–1281.

[50] S. Sarian. Anomalous diffusion of 14c in TiC0.67. *Journal of Applied Physics*, 39(11):5036–5041. Publisher: American Institute of Physics.

[51] W. F. Brizes. Diffusion of carbon in the carbides of tantalum. *Journal of Nuclear Materials*, 26(2):227–231.

[52] Wm.F. Brizes, L.H. Cadoff, and J.M. Tobin. Carbon diffusion in the carbides of niobium. *Journal of Nuclear Materials*, 20(1):57–67.

[53] A. Anttila, J. Räisänen, and J. Keinonen. Diffusion of nitrogen in -zr AND -hf. *Journal of the Less Common Metals*, 96:257–262.

[54] E. Bucur and F. C. Wagner. RATE OF DIFFUSION OF CARBON IN ALPHA AND IN BETA TITANIUM AS a FUNCTION OF THE TEMPERATURE AND CONCENTRATION. FINAL TECHNICAL REPORT FOR PERIOD DECEMBER 12, 1952-JULY 1, 1954.

[55] F. W. Wood and O. G. Paasche. Dubious details of nitrogen diffusion in nitrided titanium. *Thin Solid Films*, 40:131–137.

[56] S. Sarian. Diffusion of carbon in TiC. *Journal of Applied Physics*, 39(7):3305–3310. Publisher: American Institute of Physics.

[57] F Abautret and P Eveno. Diffusion of nitrogen implanted in titanium nitride (TiN1-x).

[58] J. Keinonen and J. Räisänen. Annealing behaviour of c-implanted -hf. *Appl. Phys. A*, 40(4):253–256.

[59] Mingqui Liu and John Cowley. Hafnium carbide growth behavior and its relationship to the dispersion hardening in tungsten at high temperatures. *Materials Science and Engineering: A*, 160(2):159–167.

[60] W Lengauer. The hafnium-nitrogen system: Phase equilibria and nitrogen diffusivities obtained from diffusion couples.

[61] R. W. Powers and Margaret V. Doyle. Diffusion of interstitial solutes in the group v transition metals. *Journal of Applied Physics*, 30(4):514–524. Publisher: American Institute of Physics.

[62] W. Kohn and L. J. Sham. Self-consistent equations including exchange and correlation effects. *Phys. Rev.*, 140(4):A1133–A1138.

[63] John P. Perdew, Kieron Burke, and Matthias Ernzerhof. Generalized gradient approximation made simple. *Phys. Rev. Lett.*, 77(18):3865–3868. Publisher: American Physical Society.

[64] Qu Wu, Bing He, Tao Song, Jian Gao, and Siqi Shi. Cluster expansion method and its application in computational materials science. *Computational Materials Science*, 125:243–254.

[65] A. van de Walle, M. Asta, and G. Ceder. The alloy theoretic automated toolkit: A user guide.

[66] I. Dahan, U. Admon, N. Frage, J. Sariel, and M.P. Dariel. Diffusion in ti/TiC multilayer coatings. *Thin Solid Films*, 377-378:687–693.

[67] I. Dahan, N. Frage, and M. P. Dariel. Structural evolution of ti/TiC multilayers. *Journal of Applied Physics*, 95(9):4662–4669.

[68] Laurent Carette, Philippe Jacquet, Dominique Cotton, Vincent Vignal, and Sébastien Faure. (TaC/ta2c) bilayer formed on carburized and annealed tantalum; development of a numerical growth model. *Applied Surface Science*, 467-468:84–88.

[69] M. Keddam, M. E. Djeghlal, L. Barrallier, and E. Salhi. Computer simulation of nitrided layers growth for pure iron. *Computational Materials Science*, 29(1):43–48.

[70] S. C. Gupta. Chapter 1 - the stefan problem and its classical formulation. In S. C. Gupta, editor, *The Classical Stefan Problem (Second Edition)*, pages 1–35. Elsevier.

[71] T. E. Lee, M. J. Baines, and S. Langdon. A finite difference moving mesh method based on conservation for moving boundary problems. *Journal of Computational and Applied Mathematics*, 288:1–17.

[72] C. F. Hsu, E. M. Sparrow, and S. V. Patankar. Numerical solution of moving boundary problems by boundary immobilization and a control-volume-based finite-difference scheme. *International Journal of Heat and Mass Transfer*, 24(8):1335–1343.

[73] Damir Juric and Grétar Tryggvason. A front-tracking method for dendritic solidification. *Journal of Computational Physics*, 123(1):127–148.

[74] Christopher Schuh. Modeling gas diffusion into metals with a moving-boundary phase transformation. *Metall Mater Trans A*, 31(10):2411–2421.

[75] J. I. Goldstein and R. E. Ogilvie. The growth of the widmanstätten pattern in metallic meteorites. *Geochimica et Cosmochimica Acta*, 29(8):893–920.

[76] T. C. Illingworth and I. O. Golosnoy. Numerical solutions of diffusion-controlled moving boundary problems which conserve solute. *Journal of Computational Physics*, 209(1):207–225.

[77] P Zhao and J. C Heinrich. Front-tracking finite element method for dendritic solidification. *Journal of Computational Physics*, 173(2):765–796.

[78] F. J. Vermolen and S. van der Zwaag. A numerical model for the dissolution of spherical particles in binary alloys under mixed mode control. *Materials Science and Engineering: A*, 220(1):140–146.

[79] G. D. Verros and N. A. Malamataris. Finite element analysis of ferrite–austenite diffusion controlled phase transformation. *Computational Materials Science*, 24(3):380–392.

[80] John M. Sullivan, Daniel R. Lynch, and Kevin O'Neill. Finite element simulation of planar instabilities during solidification of an undercooled melt. *Journal of Computational Physics*, 69(1):81–111.

[81] A. Jacot, M. Rappaz, and R. C. Reed. Modelling of reaustenitization from the pearlite structure in steel. *Acta Materialia*, 46(11):3949–3962.

[82] Gunduz Caginalp. An analysis of a phase field model of a free boundary. *Arch. Rational Mech. Anal.*, 92(3):205–245.

[83] A. A. Wheeler, B. T. Murray, and R. J. Schaefer. Computation of dendrites using a phase field model. *Physica D: Nonlinear Phenomena*, 66(1):243–262.

[84] Ryo Kobayashi. Modeling and numerical simulations of dendritic crystal growth. *Physica D: Nonlinear Phenomena*, 63(3):410–423.

[85] Lijun Zhang, Ingo Steinbach, and Yong Du. Phase-field simulation of diffusion couples in the ni–al system. *International Journal of Materials Research*, 102(4):371–380. Publisher: De Gruyter.

[86] W D MacDonald and T W Eagar. Transient liquid phase bonding. *Annual Review of Materials Science*, 22(1):23–46. _eprint: https://doi.org/10.1146/annurev.ms.22.080192.000323.

[87] M. Kajihara and M. Kikuchi. Numerical analysis of dissolution of phase in // diffusion couples of the fecrni system. *Acta Metallurgica et Materialia*, 41(7):2045–2059.

[88] Guus Segal, Kees Vuik, and Fred Vermolen. A conserving discretization for the free boundary in a two-dimensional stefan problem. *Journal of Computational Physics*, 141(1):1–21.

[89] Chijioke P. Egole, Henry E. Mgbemere, Gbeminiyi M. Sobamowo, and Ganiyu I. Lawal. Micro-macro modelling of thermal evolution during solidification of binary equiaxed alloys with experimental validation. *Results in Engineering*, 14:100444.

[90] Clarence Zener. Theory of growth of spherical precipitates from solid solution. *Journal of Applied Physics*, 20(10):950–953.

[91] Andrew O'Hara and Alex Demkov. Oxygen and nitrogen diffusion in -hafnium from first principles. *Applied Physics Letters*, 104:211909.

[92] C. J. Rosa and W. C. Hagel. A film-thickness determination of nitrogen diffusion in zirconium nitride. *J. Electrochem. Soc.*, 115(5):467. Publisher: IOP Publishing.

[93] Anthony G. Evans. Perspective on the development of high-toughness ceramics. *J American Ceramic Society*, 73(2):187–206.

[94] Luca Zoli, Antonio Vinci, Pietro Galizia, Cesare Melandri, and Diletta Sciti. On the thermal shock resistance and mechanical properties of novel unidirectional UHTCMCs for extreme environments. *Sci Rep*, 8(1):9148.

[95] M. Y. He, F. E. Heredia, D. J. Wissuchek, M. C. Shaw, and A. G. Evans. The mechanics of crack growth in layered materials. *Acta Metallurgica et Materialia*, 41(4):1223–1228.

[96] M. C. Shaw, D. B. Marshall, M. S. Dadkhah, and A. G. Evans. Cracking and damage mechanisms in ceramic/metal multilayers. *Acta Metallurgica et Materialia*, 41(11):3311–3322.

[97] Brian D. Flinn, Calvin S. Lo, Frank W. Zok, and Anthony G. Evans. Fracture resistance characteristics of a metal-toughened ceramic. *J American Ceramic Society*, 76(2):369–375.

[98] D. R. Bloyer, R. O. Ritchie, and K. T. Venkateswara Rao. Fracture toughness and r-curve behavior of laminated brittle-matrix composites. *Metall Mater Trans A*, 29(10):2483–2496.

[99] A.G. Evans and R.M. McMeeking. On the toughening of ceramics by strong reinforcements. *Acta Metallurgica*, 34(12):2435–2441.

[100] J. J Kruzic, J. M McNaney, R. M Cannon, and R. O Ritchie. Effects of plastic constraint on the cyclic and static fatigue behavior of metal/ceramic layered structures. *Mechanics of Materials*, 36(1):57–72.

[101] M. Ben Daia, P. Aubert, S. Labdi, C. Sant, F. A. Sadi, Ph. Houdy, and J. L. Bozet. Nanoindentation investigation of ti/TiN multilayers films. *Journal of Applied Physics*, 87(11):7753–7757.

[102] S.J. Bull and A.M. Jones. Multilayer coatings for improved performance. *Surface and Coatings Technology*, 78(1):173–184.

[103] D Chicot, Y Bénarioua, and J Lesage. Hardness measurements of ti and TiC multilayers: a model. *Thin Solid Films*, 359(2):228–235.

[104] C.H. Liu, Wen-Zhi Li, and Heng-De Li. Structure and hardness enhancement of fe/TiC multilayered films. *Nuclear Instruments and Methods in Physics Research Section B: Beam Interactions with Materials and Atoms*, 95(3):323–326.

[105] S. Kumar, D. Zhuo, D.E. Wolfe, J.A. Eades, and M.A. Haque. Length-scale effects on fracture of multilayers. *Scripta Materialia*, 63(2):196–199.

[106] Henryk Tomaszewski, Helena Węglarz, Anna Wajler, Marek Boniecki, and Dariusz Kalinski. Multilayer ceramic composites with high failure resistance. *Journal of the European Ceramic Society*, 27(2):1373–1377.

[107] Zheng Chen and John J. Mecholsky. Toughening by metallic lamina in nickel/alumina composites. *J American Ceramic Society*, 76(5):1258–1264.

[108] Hongfei Shang, Jian Li, and Tianmin Shao. Mechanical properties and thermal stability of TiAlN/ta multilayer film deposited by ion beam assisted deposition. *Applied Surface Science*, 310:317–320.

[109] N. Li, H. Wang, A. Misra, and J. Wang. In situ nanoindentation study of plastic co-deformation in al-TiN nanocomposites. *Sci Rep*, 4(1):6633.

[110] F. Zok and C.L. Hom. Large scale bridging in brittle matrix composites. *Acta Metallurgica et Materialia*, 38(10):1895–1904.

[111] Michael J. Large, J. Carter Stotts, Christopher Weinberger, and Gregory B. Thompson. Microstructural evolution in a one-directional phase transforming ultrahigh temperature ceramic laminate composite. *Journal of the European Ceramic Society*, 45(1):116814.

[112] Karin Frisk. A revised thermodynamic description of the ti–c system. *Calphad*, 27(4):367–373.

[113] H. Bittermann and P. Rogl. Critical assessment and thermodynamic calculation of the binary system hafnium-carbon (hf-c). *JPE*, 18(4):344–356.

[114] J. F. Smith, O. N. Carlson, and R. R. De Avillez. The niobium-carbon system. *Journal of Nuclear Materials*, 148(1):1–16.

[115] Z. C. Cordero, B. E. Knight, and C. A. Schuh. Six decades of the hall–petch effect – a survey of grain-size strengthening studies on pure metals. *International Materials Reviews*, 61(8):495–512.

[116] K. K. Shih and D. B. Dove. Ti/ti-n hf/hf-n and w/w-n multilayer films with high mechanical hardness. *Appl. Phys. Lett.*, 61(6):654–656.

[117] L. A. Girifalco. Vacancy concentration and diffusion in order-disorder alloys. *Journal of Physics and Chemistry of Solids*, 25(3):323–333.

[118] Y. Mishin and Chr. Herzig. Diffusion in the ti–al system. *Acta Materialia*, 48(3):589–623.

[119] R. Nassif, Y. Boughaleb, A. Hekkouri, J.F. Gouyet, and M. Kolb. Ionic diffusion on a lattice: Effects of the order-disorder transition on the dynamics of non-equilibrium systems. *Eur. Phys. J. B*, 1(4):453–464.

[120] A. B. Kuper, D. Lazarus, J. R. Manning, and C. T. Tomizuka. Diffusion in ordered and disordered copper-zinc. *Phys. Rev.*, 104(6):1536–1541.

[121] Shijun Zhao, Yuri Osetsky, and Yanwen Zhang. Diffusion of point defects in ordered and disordered ni–fe alloys. *Journal of Alloys and Compounds*, 805:1175–1183.

[122] Shubham Pandey, Robert J. Koch, Guangfang Li, Scott T. Misture, Hui Wang, and Simon R. Phillpot. Thermodynamics and kinetics of ordered and disordered cu/au alloys from first principles calculations. *Journal of Alloys and Compounds*, 809:151615.

[123] G. R Love. Dislocation pipe diffusion. *Acta Metallurgica*, 12(6):731–737.

[124] J. Carter Stotts, Rofiques Salehin, Ian N. Bakst, Gregory B. Thompson, and Christopher R. Weinberger. Hydrogen diffusion and storage in substoichiometric TiC. *International Journal of Hydrogen Energy*.

[125] Weidong Li, Di Xie, Dongyue Li, Yong Zhang, Yanfei Gao, and Peter K. Liaw. Mechanical behavior of high-entropy alloys. *Progress in Materials Science*, 118:100777.

[126] I. A. Leonidov, O. N. Leonidova, L. A. Perelyaeva, R. F. Samigullina, S. A. Kovyazina, and M. V. Patrakeev. Structure, ionic conduction, and phase transformations in lithium titanate li4ti5o12. *Phys. Solid State*, 45(11):2183–2188.

[127] N. Balke, S. Jesse, A. N. Morozovska, E. Eliseev, D. W. Chung, Y. Kim, L. Adamczyk, R. E. García, N. Dudney, and S. V. Kalinin. Nanoscale mapping of ion diffusion in a lithium-ion battery cathode. *Nature Nanotech*, 5(10):749–754. Number: 10 Publisher: Nature Publishing Group.

[128] Y.C. Chen, C.Y. Ouyang, L.J. Song, and Z.L. Sun. Lithium ion diffusion in li4+xTi5o12: From ab initio studies. *Electrochimica Acta*, 56(17):6084–6088.

[129] Marnix Wagemaker, Ernst R. H. Van Eck, Arno P. M. Kentgens, and Fokko M. Mulder. Li-ion diffusion in the equilibrium nanomorphology of spinel li $_{4+x}$ ti $_{5}$ o $_{12}$. *J. Phys. Chem. B*, 113(1):224–230.

[130] Navaratnarajah Kuganathan, Apostolos Kordatos, and Alexander Chroneos. Defect chemistry and li-ion diffusion in li2ruo3. *Sci Rep*, 9(1):550. Number: 1 Publisher: Nature Publishing Group.

[131] A. Van Der Ven, M. K. Aydinol, G. Ceder, G. Kresse, and J. Hafner. First-principles investigation of phase stability in li x CoO 2. *Phys. Rev. B*, 58(6):2975–2987.

[132] A. Van Der Ven, G. Ceder, M. Asta, and P. D. Tepesch. First-principles theory of ionic diffusion with nondilute carriers. *Phys. Rev. B*, 64(18):184307.

[133] Anton Van Der Ven, Jishnu Bhattacharya, and Anna A. Belak. Understanding li diffusion in li-intercalation compounds. *Acc. Chem. Res.*, 46(5):1216–1225.

[134] Young-Il Jang, Bernd J. Neudecker, and Nancy J. Dudney. Lithium diffusion in li x CoO2 (0.45 < x < 0.7) intercalation cathodes. *Electrochem. Solid-State Lett.*, 4(6):A74. Publisher: IOP Publishing.

[135] Hui Xia, Li Lu, and G. Ceder. Li diffusion in LiCoO2 thin films prepared by pulsed laser deposition. *Journal of Power Sources*, 159(2):1422–1427.

[136] Aleksandr I. Gusev and Svetlana Z. Nazarova. Magnetic susceptibility of nonstoichiometric compounds of transition d-metals. *Phys.-Usp.*, 48(7):651. Publisher: IOP Publishing.

[137] V. N. Lipatnikov, A. A. Rempel, and A. I. Gusev. Atomic ordering and hardness of nonstoichiometric titanium carbide. *International Journal of Refractory Metals and Hard Materials*, 15(1):61–64.

[138] Theresa Davey and Ying Chen. Vacancy ordering in substoichiometric zirconium carbide: A review. *International Journal of Ceramic Engineering & Science*, 4(3):134–157. _eprint: https://onlinelibrary.wiley.com/doi/pdf/10.1002/ces2.10126.

[139] A. I. Gusev and A. N. Zyryanova. Atomic-vacancy ordering and magnetic susceptibility of nonstoichiometric hafnium carbide. *Jetp Lett.*, 69(4):324–329.

[140] A. I. Gusev and A. A. Rempel. Phase diagrams of metal–carbon and metal–nitrogen systems and ordering in strongly nonstoichiometric carbides and nitrides. *physica status solidi (a)*, 163(2):273–304. _eprint: https://onlinelibrary.wiley.com/doi/pdf/10.1002/1521-396X%28199710%29163%3A2%3C273%3A%3AAID-PSSA273%3E3.0.CO%3B2-U.

[141] A. I. Gusev. Disorder and long-range order in non-stoichiometric interstitial compounds transition metal carbides, nitrides, and oxides. *physica status solidi (b)*, 163(1):17–54. _eprint: https://onlinelibrary.wiley.com/doi/pdf/10.1002/pssb.2221630102.

[142] Aleksandr I. Gusev. Order–disorder transformations and phase equilibria in strongly nonstoichiometric compounds. *Phys.-Usp.*, 43(1):1. Publisher: IOP Publishing.

[143] Corey Oses, Cormac Toher, and Stefano Curtarolo. High-entropy ceramics. *Nat Rev Mater*, 5(4):295–309. Number: 4 Publisher: Nature Publishing Group.

[144] Rui-Zhi Zhang and Michael J. Reece. Review of high entropy ceramics: design, synthesis, structure and properties. *J. Mater. Chem. A*, 7(39):22148–22162.

[145] Saeid Akrami, Parisa Edalati, Masayoshi Fuji, and Kaveh Edalati. High-entropy ceramics: Review of principles, production and applications. *Materials Science and Engineering: R: Reports*, 146:100644.

[146] Huimin Xiang, Yan Xing, Fu-zhi Dai, Hongjie Wang, Lei Su, Lei Miao, Guojun Zhang, Yiguang Wang, Xiwei Qi, Lei Yao, Hailong Wang, Biao Zhao, Jianqiang Li, and Yanchun Zhou. High-entropy ceramics: Present status, challenges, and a look forward. *J Adv Ceram*, 10(3):385–441.

[147] O. N. Senkov, G. B. Wilks, D. B. Miracle, C. P. Chuang, and P. K. Liaw. Refractory high-entropy alloys. *Intermetallics*, 18(9):1758–1765.

[148] Zezhou Li, Shiteng Zhao, Robert O. Ritchie, and Marc A. Meyers. Mechanical properties of high-entropy alloys with emphasis on face-centered cubic alloys. *Progress in Materials Science*, 102:296–345.

[149] Yong Zhang, Ting Ting Zuo, Zhi Tang, Michael C. Gao, Karin A. Dahmen, Peter K. Liaw, and Zhao Ping Lu. Microstructures and properties of high-entropy alloys. *Progress in Materials Science*, 61:1–93.

[150] D. B. Miracle and O. N. Senkov. A critical review of high entropy alloys and related concepts. *Acta Materialia*, 122:448–511.

[151] Xiaochuan Tang, Rofiques Salehin, Gregory B. Thompson, and Christopher R. Weinberger. Statistical study of vacancy diffusion in TiC and TaC. *Phys. Rev. Materials*, 4(9):093602.

[152] D. B. Miracle. High entropy alloys as a bold step forward in alloy development. *Nat Commun*, 10(1):1805. Number: 1 Publisher: Nature Publishing Group.

[153] E. P. George, W. A. Curtin, and C. C. Tasan. High entropy alloys: A focused review of mechanical properties and deformation mechanisms. *Acta Materialia*, 188:435–474.

[154] Easo P. George, Dierk Raabe, and Robert O. Ritchie. High-entropy alloys. *Nat Rev Mater*, 4(8):515–534. Publisher: Nature Publishing Group.

[155] Hang Li, Weibo Hua, Xinyang Liu-Théato, Qiang Fu, Morgane Desmau, Alexander Missyul, Michael Knapp, Helmut Ehrenberg, and Sylvio Indris. New insights into lithium hopping and ordering in LiNiO2 cathodes during li (de)intercalation. *Chem. Mater.*, 33(24):9546–9559. Publisher: American Chemical Society.

[156] D. L. Beke and G. Erdélyi. On the diffusion in high-entropy alloys. *Materials Letters*, 164:111–113.

[157] Juliusz Dąbrowa, Marek Zajusz, Witold Kucza, Grzegorz Cieślak, Katarzyna Berent, Tomasz Czeppe, Tadeusz Kulik, and Marek Danielewski. Demystifying the sluggish diffusion effect in high entropy alloys. *Journal of Alloys and Compounds*, 783:193–207.

[158] J.-W. Yeh, S.-K. Chen, S.-J. Lin, J.-Y. Gan, T.-S. Chin, T.-T. Shun, C.-H. Tsau, and S.-Y. Chang. Nanostructured high-entropy alloys with multiple principal elements: Novel alloy design concepts and outcomes. *Advanced Engineering Materials*, 6(5):299–303. _eprint: https://onlinelibrary.wiley.com/doi/pdf/10.1002/adem.200300567.

[159] I. Vattulainen, S. C. Ying, T. Ala-Nissila, and J. Merikoski. Memory effects and coverage dependence of surface diffusion in a model adsorption system. *Phys. Rev. B*, 59(11):7697–7707. Publisher: American Physical Society.

[160] S. C. Ying, I. Vattulainen, J. Merikoski, T. Hjelt, and T. Ala-Nissila. Memory expansion for diffusion coefficients. *Phys. Rev. B*, 58(4):2170–2178. Publisher: American Physical Society.

[161] Miguel A. Gosálvez and Joseba Alberdi-Rodriguez. Microscopic origin of the apparent activation energy in diffusion-mediated monolayer growth of two-dimensional materials. *J. Phys. Chem. C*, 121(37):20315–20322. Publisher: American Chemical Society.

[162] Joseba Alberdi-Rodriguez, Shree Ram Acharya, Talat S. Rahman, Andres Arnau, and Miguel A. Gosálvez. Dominant contributions to the apparent activation energy in two-dimensional submonolayer growth: comparison between cu/ni(111) and ni/cu(111). *Journal of Physics: Condensed Matter*, 32(44):445002. Publisher: IOP Publishing.

[163] Miguel Angel Gosalvez and Joseba Alberdi-Rodriguez. A microscopic perspective on heterogeneous catalysis. type: article.

[164] Barry A. Cipra. An introduction to the ising model. *The American Mathematical Monthly*, 94(10):937–959.

[165] B. C. S. Grandi and W. Figueiredo. Monte carlo simulation of an ising antiferromagnet with competing glauber and kawasaki dynamics. *Phys. Rev. E*, 56(5):5240–5244.

[166] B. C. S. Grandi and W. Figueiredo. Monte carlo simulation of an antiferromagnetic ising model at two competing temperatures. *Phys. Rev. E*, 59(5):4992–4996.

[167] A Kalz, A Honecker, S Fuchs, and T Pruschke. Monte carlo studies of the ising square lattice with competing interactions. *J. Phys.: Conf. Ser.*, 145:012051.

[168] Songbo Jin, Arnab Sen, Wenan Guo, and Anders W. Sandvik. Phase transitions in the frustrated ising model on the square lattice. *Phys. Rev. B*, 87(14):144406.

[169] Kyozi Kawasaki. Diffusion constants near the critical point for time-dependent ising models. i. *Phys. Rev.*, 145(1):224–230.

[170] M. G. Evans and M. Polanyi. Inertia and driving force of chemical reactions. *Trans. Faraday Soc.*, 34(0):11–24. Publisher: The Royal Society of Chemistry.

[171] J. M. Cowley. An approximate theory of order in alloys. *Phys. Rev.*, 77(5):669–675.

[172] J. M. Cowley. Short-range order and long-range order parameters. *Phys. Rev.*, 138(5):A1384–A1389.

[173] Richard A. Swalin. *Thermodynamics of solids*. Wiley series on the science and technology of materials. J. Wiley, 2d ed edition.

[174] Lars Onsager. Crystal statistics. i. a two-dimensional model with an order-disorder transition. *Phys. Rev.*, 65(3):117–149.

[175] Davide Di Stefano, Roman Nazarov, Tilmann Hickel, Jörg Neugebauer, Matous Mrovec, and Christian Elsässer. First-principles investigation of hydrogen interaction with TiC precipitates in -fe. *Phys. Rev. B*, 93(18):184108.

[176] V. N. Lipatnikov and A. I. Gusev. Effect of ordering on the structure and specific heat of nonstoichiometric titanium carbide. *Jetp Lett.*, 69(9):669–675.

[177] Hannes J?nsson, Greg Mills, and Karsten W. Jacobsen. Nudged elastic band method for finding minimum energy paths of transitions. In *Classical and Quantum Dynamics in Condensed Phase Simulations*, pages 385–404. WORLD SCIENTIFIC.

[178] F. J. J. Van Loo, W. Wakelkamp, G. F. Bastin, and R. Metselaar. Diffusion of carbon in TiC1y and ZrC1y. *Solid State Ionics*, 32-33:824–832.

[179] Shen J. Dillon and Martin P. Harmer. Multiple grain boundary transitions in ceramics: A case study of alumina. *Acta Materialia*, 55(15):5247–5254.

[180] Boris Straumal, Eugen Rabkin, Gabriel A. Lopez, Anna Korneva, Alexei Kuzmin, Alena Gornakova, Alexander Straumal, and Brigitte Baretzky. Grain boundary wetting phenomena in high entropy alloys containing nitrides, carbides, borides, silicides, and hydrogen: A review. *Crystals*, 11(12):1540. Number: 12 Publisher: Multidisciplinary Digital Publishing Institute.

[181] E. Rabkin. Thin films on grain boundaries in metals and ceramics and their importance for the properties of the materials. In Janusz Nowotny, editor, *Materials Science Monographs*, volume 81 of *Science of Ceramic Interfaces II*, pages 371–398. Elsevier.

[182] Ming Tang, W. Craig Carter, and Rowland M. Cannon. Grain boundary order-disorder transitions. *J Mater Sci*, 41(23):7691–7695.